HAL
open science

RANS and LES of multi-hole sprays for the mixture formation in piston engines

Muhammad Khan

To cite this version:

Muhammad Khan. RANS and LES of multi-hole sprays for the mixture formation in piston engines. Other. Ecole Centrale de Lyon, 2014. English. NNT : 2014ECDL0002 . tel-01002111

HAL Id: tel-01002111

https://theses.hal.science/tel-01002111v1

Submitted on 5 Jun 2014

HAL is a multi-disciplinary open access archive for the deposit and dissemination of scientific research documents, whether they are published or not. The documents may come from teaching and research institutions in France or abroad, or from public or private research centers.

L'archive ouverte pluridisciplinaire **HAL**, est destinée au dépôt et à la diffusion de documents scientifiques de niveau recherche, publiés ou non, émanant des établissements d'enseignement et de recherche français ou étrangers, des laboratoires publics ou privés.

Thèse de l'université de Lyon

délivrée par **l'Ecole Centrale de Lyon**

École doctorale de Mécanique, Energétique, Génie civil, Acoustique

Spécialité : Mécanique des fluides

Le titre de Docteur

préparée au

Laboratoire de Mécanique des Fluides et d'Acoustique

par

Muhammad Mahabat Khan

RANS and LES of multi-hole sprays for the mixture formation in piston engines

Soutenance le 20 janvier 2014 à l'Ecole Centrale de Lyon

JURY

François-Xavier Demoulin	Examinateur
Francis Dupoirieux	Rapporteur
MikhaelGorokhovski	Directeur de thèse
JérômeHélie	Co-encadrante
Richard Perkins	Examinateur
Anne Taniere	Rapporteur

RANS and LES of multi-hole sprays for the mixture formation in piston engines

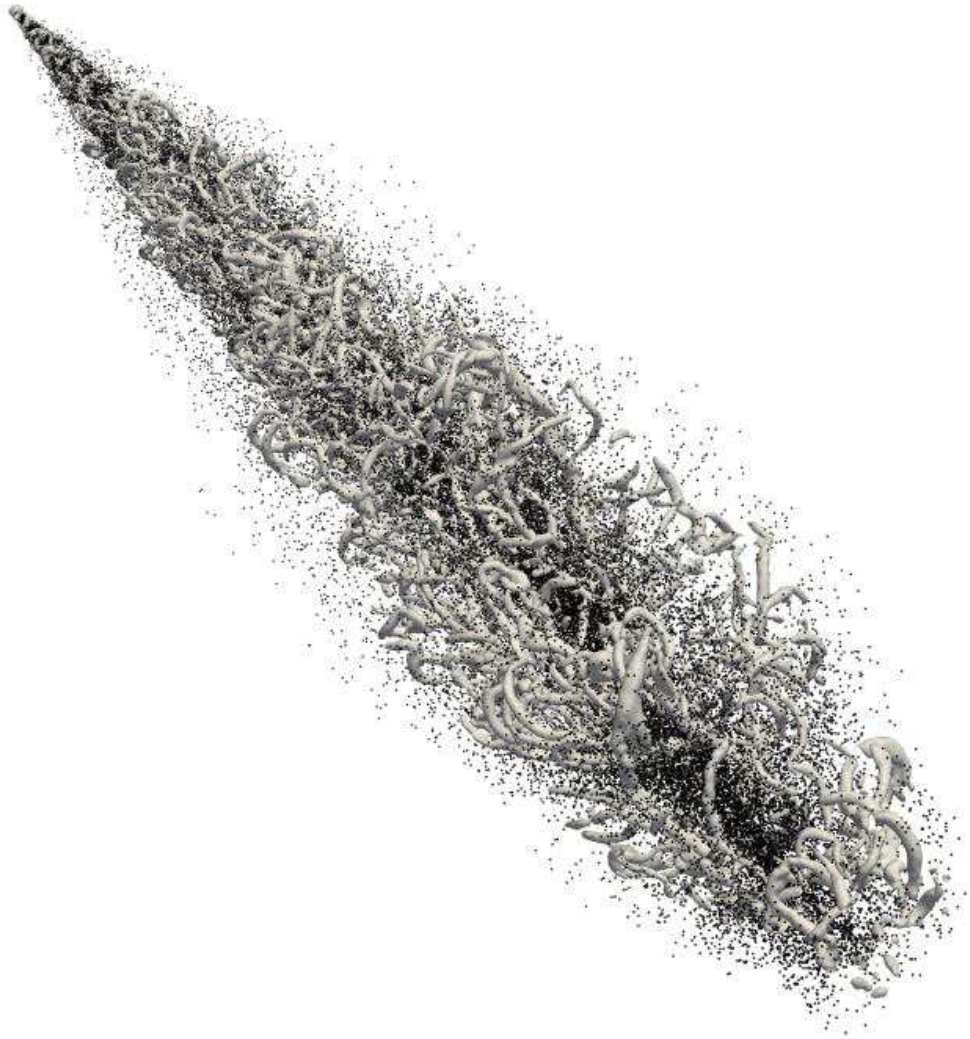

Muhammad Mahabat Khan

Laboratoire de Mécanique des Fluides et d'Acoustique

Ecole Centrale de Lyon

Résumé

Cette thèse porte sur la simulation des jets de gouttes générés par des pulvérisateurs essence haute pression, pulvérisateurs qui sont un point clef des systèmes de combustion automobile de la présente et future génération devant diminuer les émissions de CO_2 et de polluants.

Dans un premier temps les jets de gouttes (« sprays ») sont simulés par simulation moyennée. Les résultats de simulation d'un jet donnant des résultats en moyenne satisfaisant, l'interaction de jets en injecteurs multi-trous est alors simulée. Les résultats sont cohérents par rapport aux mesures d'entraînement d'air. La simulation permettant d'avoir accès au champ complet 3D, le mécanisme d'interaction jet à jet et de développement instationnaire du spray est décris en détail. La formation d'un mouvement descendant au centre du spray et celle d'un point d'arrêt central sont trouvés. Finalement,

Ces résultats sont étendus au cas surchauffé, cas où la pression dans la chambre est inférieure à la pression de vapeur saturante. Un modèle simple semi-empirique est proposé pour tenir compte de la modification des conditions proches de la buse d'injection. Le modèle prédit correctement les tendances des variations de paramètres et capture la forme générale du spray qui se referme sur lui-même.

La seconde grande partie est consacrée au développement d'un modèle de spray par l'approche des grandes échelles (SGE), limité ici aux cas non évaporant. Il comprend la modélisation de sous-maille de la dispersion turbulente, des collisions-coalescence et des termes d'échange de quantité de mouvement de sous-maille. L'effet du choix du modèle de sous-maille pour la viscosité turbulente de sous-maille est montré, le choix retenu étant le modèle de Smagorinski dynamique.

Afin d'améliorer la représentativité cruciale des conditions d'injections, un couplage faible est réalisé à partir de résultats de simulations existantes de l'écoulement interne aux buses. Les fonctions densité de probabilité simple et jointes extraits des résultats de simulations sont validés par rapport aux mesures PDA en situation pseudo-stationnaire et la pénétration liquide et la forme du spray est comparée aux visualisations par ombroscopie. Enfin, différentes zones caractéristiques sont identifies et des longueurs sont notées pour les cas d'injection à 100 et 200bar.

Mots clés:

Injecteur à trous multiples, pulvériser, atomisation, entraînement d'air, interaction jet à jet, flash boiling, turbulence, Reynolds moyennées de Navier Stokes, simulations des grandes échelles.

Abstract

Over the years numerical modelling and simulation techniques have constantly been improved with the increase in their use. While keeping the computational resources in mind, numerical simulations are usually adapted to the required degree of accuracy and quality of results. The conventional Reynolds Average Navier Stokes (RANS) is a robust, cheap but less accurate approach. Large Eddy Simulation (LES) provides very detailed and accurate results to the some of the most complex turbulence cases but at higher computational cost. On the other hand, Direct Numerical Simulation (DNS) is although the most accurate of the three approaches but at the same time it is computationally very expensive which makes it very difficult to be applied to the most of the complex industrial problems.

The current work is aimed to develop a deeper understanding of multi-hole Gasoline Direct Injection (GDI) sprays which pose many complexities such as; air entrainment in the multi-hole spray cone, Jet-to-Jet interactions, and changes in the spray dynamics due to the internal flow of the injector. RANS approach is used to study multi-hole injector under cold, hot and superheated conditions. Whereas, LES is utilized to investigate the changes in the dynamics of the single spray plume due to the internal flow of the GDI injector. To reduce computational cost of the simulations, dynamic mesh refinement has been incorporated for both LES and RANS simulation.

A thorough investigation of air entrainment in three and six hole GDI injectors has been carried out using RANS approach under non superheated and superheated conditions. The inter plume interactions caused by the air entrainment effects have been analysed and compared to the experimental results. Moreover, the tendencies of semi collapse and full collapse of multi-hole sprays under non superheated and superheated conditions have been investigated in detail as well.

A methodology of LES has been established using different injection strategies along with various subgrid scale models for a single spray plume. In GDI multi-hole sprays, the internal flow of the injector plays a very crucial role in the outcome the spray plume. A separate already available internal flow LES simulation of the injector has been coupled with the external spray simulation in

order to include the effect of nozzle geometry and the cavitation phenomenon which completely change the dynamics of the spray.

Keywords

Multihole injector, spray, atomisation, air entrainment, jet to jet interaction, flash boiling, turbulence, Reynolds Average Navier Stokes, Large Eddy Simulation.

Acknowledgement

I wish to express my heartfelt admiration to my supervisors, Prof. Mikhael Gorokhovski[1] and Dr. Jerome Helie[2], for the incredible amount of time and valuable knowledge they have provided during the course of this thesis. It has been an exceptionally rewarding experience.

I would like to thank all the members of MAGIE project and especially: Prof. Graham Wigley, Mehdi Mojtabi and Andrew Woods[3] for providing Phase Doppler Anemometry (PDA) experimental Data, Julian Kashdan and Jean Paul Dumas[4] who were involved in the experimental measurements of Particle Image Velocimetry (PIV) and Mie Scattering images. I also want to thank and appreciate my friend and colleague Samir Makhlouf who provided me the spray close up images.

A special thanks to everybody at Continental Automotive who provided great help during the past three years. I thank Dr. Jeremy Chesnel, who supported me in resolving many issues regarding Linux and OpenFOAM and most importantly for providing the data for internal flow simulation of the injector and Dr. Nicolas Lamarque, whose encouragement and help regarding different numerical issues. I also thank my colleagues whom I shared the office with.

Finally, I would like to thank my family for their constant love and encouragement. For my parents who raised me with devotion, care and affection and their continuous support helped me to pursue my goals. For my beloved sister and brothers and my late grandparents who always encouraged me to chase my dreams. For my loving, supportive, encouraging, and patient wife, Ameena whose faithful support during the final stages of this Ph.D. is so appreciated. Most of all for my beautiful little daughter, Alina whose beautiful smile kept me fresh even in most tiring times. Thank you.

Muhammad Mahabat Khan

---

[1] Ecole Centrale de Lyon, Lyon, France
[2] Continental Automotive Corporation, Toulouse, France
[3] Laughborough University, Laughborough, UK
[4] IFP Énergies Nouvelles, Paris, France

Table of Contents

RÉSUMÉ ..... **I**

ABSTRACT ..... **III**

ACKNOWLEDGEMENT ..... **V**

LIST OF FIGURES ..... **XIII**

LIST OF TABLES ..... **XIX**

NOMENCLATURE ..... **XXI**

CHAPTER 1 INTRODUCTION **1**

1.1 Objectives and outline of the thesis **5**

1.2 Overview of thesis chapters: **7**

CHAPTER 2 TURBULENCE AND SPRAY MODELLING **9**

2.1 Conservation equation: **9**

2.1.1 The total mass conservation equation: 10

2.1.2 Momentum conservation equation for fluid mixture: 10

2.1.3 Energy conservation equation: 10

2.1 Turbulence modelling: **10**

2.2.1 Carrier phase equations: 13

2.2.1.1 Reynolds Average Navier Stokes: 13

2.2.1.2 Large Eddy Simulation: 14

2.2.2 Liquid phase equations: 15

2.2.3 Two way coupling, effect of droplets on the gas phase: 16

Table of Contents

2.2 Spray modelling: 17

2.3.1 Liquid injection model: 17

2.3.2 Secondary droplet breakup model: 18

2.3.3 Stochastic droplet dispersion model: 21

2.3.4 Droplet tracking model: 24

2.3.5 Droplet collision model: 25

2.3.6 Evaporation and heat transfer models: 26

2.3 Conclusion: 28

CHAPTER 3 REYNOLDS AVERAGE NAVIER STOKES SIMULATIONS 29

3.1 Turbulence Model: 30

3.2 Numerical setup and Operational conditions: 31

3.2.1 Numerical solver: 31

3.2.2 Numerical schemes: 31

3.2.3 Two phase numerics: 32

3.2.4 Computational domain: 32

3.2.5 Injector Design: 33

3.2.6 Mass flow rate profile: 33

3.2.7 Operating conditions: 34

3.3 Results & Discussion: 35

3.3.1 Basic validations: 35

3.3.1.1 Non-evaporating conditions: 35

3.3.1.2 Evaporating conditions: 37

3.3.1.2.1 Axial liquid penetration of the spray: 37

3.3.1.2.2 Air entrainment between the two jets: 38

3.3.2 Jet-to-jet interactions: 39

3.3.2.1 Spatial evolution of vapour phase: 40

3.3.2.2 Axial gas velocity: 43

3.3.2.3 Comparison of spray angles: 44

3.3.2.4 Radial gas velocity: 45

3.3.2.5 Flux Balance: 46

3.4 Flash Boiling: 48

3.4.1 Modelling of the radial expansion of the spray, “Bell Shape”: 51
3.4.2 Results and discussion: 54
3.4.2.1 Improvement in spray shape: 54
3.4.2.2 Temporal evolution of the spray collapse: 55
3.4.2.3 Role of injector design parameters in flash boiling conditions: 57
3.4.2.3.1 Hole to hole distance: 57
3.4.2.3.2 Injection opening velocity: 59

3.5 Conclusion: 60
3.5.1 Spray behaviour under non-flashing conditions: 60
3.5.2 Spray behaviour under flashing conditions 60

CHAPTER 4 LARGE EDDY SIMULATIONS OF HIGH PRESSURE SPRAY 63

4.1 Large Eddy Simulations Modelling: 65
4.1.1 Carrier phase; Subgrid viscosity models: 65
4.1.2 Lagrangian equations 66
4.1.3 Two phase coupling models 66
4.1.4 Two phase Subgrid models 67
4.1.5 Two-way subgrid scales coupling 68
4.1.6 Rarefaction and Compressibility Effect: 69

4.2 Numerical Approach 70
4.2.1 Numerical Solver 70

4.3 Initial tests 71
4.3.1 Initial Tests Setup 71
4.3.1.1 Geometry 71
4.3.1.2 Liquid injection 73
4.3.2 Test cases 75
4.3.3 Results & discussion 77
4.3.3.1 Input excitations 77
4.3.3.2 Carrier phase Subgrid model effect: 79
4.3.3.2.1 Energy Spectra of carrier phase velocity: 79
4.3.3.2.2 Subgrid scale viscosity fields: 81
4.3.3.2.3 Shear layer structures: 82
4.3.3.2.4 Fluctuating velocity profiles: 83

4.3.3.3 Injection profile effect: 85
4.3.3.4 Instabilities and transition 87
4.3.3.5 Developed turbulence 90
4.3.3.6 Comparison of Simulation and experimental data: 95

4.4 Conclusion 96

CHAPTER 5 LES OF SINGLE SPRAY PLUME OF GDI INJECTOR 99

5.1 Nozzle Flow Dynamics: 100

5.2 Coupling of VOF and lagrangian simulation: 103

5.3 Studied Cases and numerical setup: 104

5.4 Steady State Results 105
5.5.1 Comparison of PDA and LES data: 105
5.5.1.1 Probability Density Function comparison of LES and PDA at 100 bar: 105
5.5.1.2 Joint Probability Density Function comparison of LES and PDA at 100 bar: 107
5.5.1.3 PDF comparison of LES and PDA at 200 bar: 110
5.5.1.4 JPDF comparison of LES and PDA at 200 bar: 111
5.5.2.1 Centreline gas velocity profile: 114
5.5.2.2 Charecterization of Spray half width: 115
5.5.2.3 Spray half width evolution 116
5.5.2.4 Mean velocity profiles: 118
5.5.2.4.1 Mean gas velocity profiles on Asymmetric zone: 118
5.5.2.4.2 Mean gas velocity profiles on Symmetric zone: 119
5.5.2.4.3 Mean liquid velocity profile on Asymmetric zone: 121
5.5.2.4.4 Mean liquid velocity profile on Symmetric zone: 122
5.5.2.4.5 Liquid Mass distribution: 123
5.5.2.5 RMS Fluctuations of Carrier Phase: 124
5.5.2.6 RMS fluctuations of dispersed phase: 126
5.5.2.7 Anisotropy: 127
5.5.2.8 Stokes Numbers: 129

5.5 Unsteady state results 131
5.5.1 Temporal spray evolution and dynamics: 131

5.5.2 Spray Penetration and plume angle: 132

5.6 Conclusion: 134

SUMMARY & CONCLUSION: 135

FUTURE WORK: 139

APPENDIX A EXPERIMENTAL SET-UP 141

A.1 Experimental set-up of PDA test bench: 141

A.2 Experimental set-up of PIV test bench: 142

A.3 Experimental setup high zoom shadowgraphy 143

APPENDIX B INPUT QUANTITIES FROM SEPARATE EXISTING LES-VOLUME OF FLUID SIMULATIONS 145

APPENDIX C A REMINDER TO THE NUMERICAL SCHEMES 149

C.1 Spatial Discretisation of the terms: 150

C.1.1 Convection term: 151

C.1.2 Convection differencing scheme: 151

C.1.3 Diffusion Term: 152

C.1.4 Source Terms: 154

C.2 Time Discretisation: 154

C.2.1 Euler Implicit Scheme: 155

C.2.2 Backward Implicit Scheme: 156

APPENDIX D RESEARCH PAPERS 157

Research Paper # 1 157

POD Application for the Flow Characterization at the Exit of a Low Pressure Gasoline Nozzle 157

Research Paper # 2 174

Table of Contents

Numerical Analysis of Multihole Gasoline Direct Injection Sprays..... 174

BIBLIOGRAPHY 190

List of Figures

Figure 1: CO_2 emission standards 2
Figure 2: Global PV/LV Engine Production (2012-2025) 4
Figure 3: Cross-sectional view of GDI injector (current XL3 injector) (scoltock, 2012) 4
Figure 4: Enlarged spray structure of two-hole-type injector (a) Point 1(b) Point2, (c) Point 3 (Ashgriz, 2011) 5
Figure 5: Comparison of different turbulence modelling techniques (Bakker, 2006) 12
Figure 6: Breakup mechanism; adapted from (Pilch & Erdman, 1987) 19
Figure 7: Calculated (N, = 1000, at = 0.1) drop positions at times (a) 10.0 (b) 30.0 (c) 50.0 (O'Rouke, 1989) 24
Figure 8: Motion of the particle with the face crossings (Macpherson, Nordin, & Weller, 2009) 25
Figure 9: The particles collision (Nordin, 2001) 26
Figure 10: Injector design 33
Figure 11: Mass Flow Rate Profile of the injector at 100 and 200 Bar Injection Pressure for 6-hole injector 34
Figure 12: Experimental and simulation results of 3-hole injector; (a) Mean droplet diameter (D_{10}) at different axial locations ,(b) PDF of droplet distribution at 40mm axial location 36
Figure 13: Comparison of penetration curves under evaporating conditions for 3-hole and 6-hole injectors 37
Figure 14: 2D vector flow fields showing air entrainment at 1.4ms ASOI for the 3-hole injector (a) Experimental (b), Simulation (c), Difference between Experimental & Simulated results; and for the 6-hole injector (d) Experimental (e), Simulation (f), Difference between Experimental & Simulated results 39
Figure 15: Liquid phase spray images of the sprays under evaporating conditions at 1.75ms ASOI; (a) Experimental result (high-speed Mie scattering) of 3-hole injector (b) Simulation result of 3-hole injector (c) experimental result (high-speed Mie scattering) of 6-hole injector (d) Simulation result of 6-hole injector 40
Figure 16: Simulation results of fuel vapour mass fraction at (a) 1.75ms ASOI and (b) 3.1ms ASOI (Part1) 41
Figure 17: Simulation results of fuel vapour mass fraction at (a) 1.75ms ASOI and (b) 3.1ms ASOI;(Part 2) 42
Figure 18: 2D velocity vector plots of simulated air and gas entrainment; (a) 1.75ms ASOI, (b) 3.10ms ASOI 44
Figure 19: Comparison of spray plumes at 1.8ms ASOI; (a) Simulation result (b), experimental result 45
Figure 20: Radial velocity vector plot of the simulated air entrainments at 3.10ms ASOI at downstream locations; (a) 20mm (b) 30mm (c) 40mm (d) 50mm (e), 60mm (f), 70mm 46
Figure 21: Schematic of Air entrainment in a control volume 47
Figure 22: Air flux balance in the control volume 47
Figure 23: Phase change diagram 48

List of Figures

FIGURE 24: SO-CALLED "FLASH BOILING" PROCESS FOR ATOMIZING SUPERHEATED FLOW. (A): A SCHEMATIC VIEW; IN-ENGINE VISUALISATION IN LOTUS ENGINE IN LOUGHBOROUGH UNIVERSITY (B) WIDE OPEN THROTTLE (C): 2.7BAR INDICATED MEAN EFFECTIVE PRESSURE 49

FIGURE 25: OBSERVED CHANGE IN THE SPRAY SHAPE WITH A 6 HOLES AND DIFFERENT CHAMBER PRESSURES, 60 DEG NOMINAL SPRAY PLUME ANGLE AT 100BAR, TOPS: SIDE VIEW BY SHADOWGRAPHY. BOTTOMS: BOTTOM VIEW BY MIE SCATTERING. (MOJTABI, CHADWICK, WIGLEY, & HELIE, 2008; MOJTABI, 2011) 50

FIGURE 26: SCHEMATIC OF THE PRESENT APPROACH. STEP 1: ATOMIZED SPRAY INCLUDING BUBBLES; STEP 2: SUPPLEMENTARY DISINTEGRATION; STEP 3: RESULTING REDUCED DROP SIZE AND ADDITIONAL KINETIC ENERGY (DASHED LINE) 52

FIGURE 27: EXPERIMENTAL IMAGE OF FLASH BOILING SPRAY AT 1MS ASOI WITH $Pinj = 50bar$, $P\ chamber = 0.4\ bar$, $Tfuel = Tchamber = 60°C$ 52

FIGURE 28: SPRAY UNDER FLASH BOILING CONDITIONS AT 0.5MS ASOI (A) EXPERIMENT, (B) SIMULATION WITHOUT RADIAL EXPANSION MODELLING (C) SIMULATION WITH RADIAL EXPANSION MODELLING; $Pinj = 50bar$, $P\ chamber = 0.4\ bar$, $Tfuel = Tchamber = 60°C$ 54

FIGURE 29: SPRAY PENETRATION COMPARISON AT $Pinj = 50bar$, $P\ chamber = 0.4\ bar$, $Tfuel = Tchamber = 60°C$; (A) 0.5MS ASOI; EXPERIMENT, SIMULATION (B) 1MS ASOI; EXPERIMENT, SIMULATION (C) 1.5MS ASOI; EXPERIMENT, SIMULATION; 55

FIGURE 30: VERTICAL PLANAR CUT OF VAPOUR MASS FRACTION (IN COLOUR) SUPER IMPOSED BY AXIAL GAS VELOCITY VECTORS FOR THE SPRAY WITH $Pinj = 50bar$, $P\ chamber = 0.4\ bar$, $Tfuel = Tchamber = 60°C$; (A) 0.2MS ASOI (B) 0.5MS ASOI (C) 1MS ASOI (D) 1.5MS ASOI 56

FIGURE 31: HORIZONTAL PLANAR CUT OF VAPOUR MASS FRACTION (IN COLOUR) SUPER IMPOSED BY RADIAL GAS VELOCITY VECTORS FOR THE SPRAY AT 1.5MS ASOL WITH $Pinj = 50bar$, $P\ chamber = 0.4\ bar$, $Tfuel = Tchamber = 60°C$; (A) 10MM(B) 20MM (C) 30MM 57

FIGURE 32: 6-HOLE INJECTOR WITH INDICATION OF HOLE TO HOLE DISTANCE 58

FIGURE 33: SPRAY UNDER FLASH BOILING CONDITIONS WITH $Pinj = 50bar$, $P\ chamber = 0.4\ bar$, $Tfuel = Tchamber = 60°C$; WITH DIFFERENT HOLE TO HOLE DISTANCES, AT 1.5MS ASOI (A) NOMINAL (B) REDUCED BY 13%,(C) REDUCED BY 19% (D) REDUCED BY 32% 58

FIGURE 34: SPRAY UNDER FLASH BOILING CONDITIONS WITH $Pinj = 50bar$, $P\ chamber = 0.4\ bar$, $Tfuel = Tchamber = 60°C$; (A) EXPERIMENT WITH $Ulo = 45m/s$ (B) SIMULATION WITH $Ulo = 45m/s$ (C) EXPERIMENT WITH $Ulo = 90m/s$ (D) SIMULATION WITH $Ulo = 90m/s$ 59

FIGURE 35: MODIFICATION OF THE DRAG COEFFICIENT DUE TO RAREFACTION AND COMPRESSIBILITY EFFECTS FOR SMALL AND LARGE PARTICLES OF ( ) 0.4 MA, ( ) 0.5 MA, ( ) 0.6 MA, ( ) 0.7 MA, ( ) 0.8 MA, ( ) 0.9 MA,( )1MA.... 70

FIGURE 36: COMPUTATIONAL DOMAIN, BOUNDARY CONDITIONS AND MESH WITH SUPERIMPOSED STREAMWISE GAS VELOCITY NON DIMENSIONED BY THE LIQUID INJECTION VELOCITY. INSIDE THE VELOCITY SHAPE, THE MESH CELL SIZE REMAINS CONSTANT TO THE HIGHEST LEVEL OF REFINEMENT. 72

FIGURE 37: (A) INPUT EXCITATION SIGNAL (B) FFT OF THE INPUT EXCITATIONS 74

List of Figures

FIGURE 38: SCHEMATIC FOR THE DROPLET INJECTION STRATEGY 75

FIGURE 39: FOURIER TRANSFORM OF THE NORMALIZED VELOCITY FIELD AT AXIAL DOWNSTREAM LOCATIONS OF; 12.5DI (A) INPUT EXCITATIONS UNTIL THE END OF INJECTION (B) INPUT EXCITATIONS UNTIL 100TI, (C) NO INPUT EXCITATIONS; 50DI (D) INPUT EXCITATIONS UNTIL THE END OF INJECTION (E) INPUT EXCITATIONS UNTIL 100TI, (F) NO INPUT EXCITATIONS 78

FIGURE 40: ENERGY SPECTRUM USING AT 200Di WITH INPUT EXCITATIONS CUTOFF AT 100TiMS FOR (A) STANDARD SMAGORINSKY (B)ONE EQUATION EDDY (C) DYNAMIC SMAGORINSKY (D) IMPLICIT 80

FIGURE 41: STREAMWISE CROSS-SECTION OF NORMALIZED SUBGRID SCALE VISCOSITY, ISOLEVELS (A) ONE EQUATION EDDY MODEL (B) STANDARD SMAGORINSKY (C) DYNAMIC SMAGORINSKY 81

FIGURE 42 : CLOSE UP INSTANTANEOUS VIEW ON THE TOP HALF DOMAIN OF ISO-SURFACES OF Q CRITERIUM (QN=0.1) COLORED BY NORMALIZED HELICITY (A) STANDARD SMAGORINSKY (B) ONE EQUATION (C) DYNAMIC SMAGORINSKY (D) IMPLICIT 82

FIGURE 43: NORMALIZED STREAMWISE RADIAL PROFILES (HOLLOW) FILTERED FLUCTUATING VELOCITY (FILLED) TOTAL FLUCTUATING VELOCITY AT; 50Di (–○–), 100Di (–☆–), 150Di (–□–), 200Di (–◇–), 250Di(–▽–) (A) STANDARD SMAGORINSKY (B) ONE EQUATION EDDY (C) DYNAMIC SMAGORINSKY (D) IMPLICIT 84

FIGURE 44: MEAN RADIAL DISTRIBUTION OF LIQUID MASS NORMALIZED BY MAXIMUM LIQUID MASS AT THE CENTRELINE AT; 50Di (–○–), 100Di (–☆–), 150Di (–□–), 200Di (–◇–), 250Di(–▽–) WITH INJECTION MODELS OF (A) G-L (B) G-R (C) R-R 86

FIGURE 45: SPRAY PLUMES IN THE TOTAL COMPUTATIONAL DOMAIN WITH INJECTION MODELS OF; (A) G-L; (B) G-R (C) R-R, TRAVERSE CROSS-SECTIONAL PLANES ARE TAKEN AT A DOWNSTREAM LOCATION OF 200 Di 86

FIGURE 46: NORMALIZED GAS FILTERED STREAMWISE VELOCITY ALONG THE CENTRELINE VERSUS DISTANCE UNTIL 50Di (SOLID LINE) MEAN VELOCITY (DASHED LINE) INSTANTANEOUS VELOCITY 87

FIGURE 47 : NORMALIZED VORTICITY BASED ON THE FLUCTUATING VELOCITY (A) PLANAR CUT 100 X/ Di; (B & C) SUPERIMPOSED BY FLUCTUATING VELOCITY VECTORS 88

FIGURE 48: ISO-SURFACES OF QN=0.25 COLORED BY HELICITY 89

FIGURE 49: STREAMWISE PROFILES OF FILTERED NORMAL STRESS COMPONENTS (A) $u'u'$ (B) $v'v'$ (C) $w'w'$ NORMALIZED BY THE CENTRELINE VELOCITY AT 50Di (–○–), 100Di (–☆–), 150Di (–□–), 200Di (–◇–), 250Di(–▽–) 90

FIGURE 50: STREAMWISE PROFILES OF FILTERED SHEAR STRESS COMPONENT $v'w'$ NORMALIZED BY THE CENTRELINE VELOCITY 50Di (–○–), 100Di (–☆–), 150Di (–□–), 200Di (–◇–), 250Di(–▽–) 91

FIGURE 51 : NORMALIZED VELOCITY ALONG THE CENTRELINES VERSUS DISTANCE WITH DYNAMIC SMAGORINSKY MODE, (SOLID LINE) MEAN VELOCITY (DOTTED LINE) INSTANTANEOUS VELOCITY (DASHED LINE) WANG, FRÖHLICH, MICHELASSI, & RODI, 2008 91

FIGURE 52: NORMALIZED PLUME HALF WIDTH ALONG THE CENTRELINES VERSUS DISTANCE WITH DYNAMIC SMAGORINSKY MODEL, DASHED LINE REPRESENTS THE SLOPE OF THE GAS JET HALF WIDTH (WANG, FRÖHLICH, MICHELASSI, & RODI, 2008) 92

FIGURE 53: RADIAL DISTRIBUTION OF (A) GAS VELOCITY; WITH DYNAMIC SMAGORINSKY MODEL DOWNSTREAM AT 50Di (–○–), 100Di (–☆–), 150Di (–□–), 200Di (–◇–), 250Di(–▽–); SOLID LINE, GAUSSIAN FIT WITH MEAN =0 AND STANDARD DEVIATION OF 1. 92

List of Figures

FIGURE 54: NORMALIZED RADIAL PROFILES OF STREAMWISE FLUCTUATING VELOCITY (A) DISPERSED PHASE (B) SLIP VELOCITY; WITH DYNAMIC SMAGORINSKY MODEL AT DOWNSTREAM LOCATIONS OF; $50Di$ (—○—), $100Di$ (—☆—), $150Di$ (—□—), $200Di$ (—◇—), $250Di$(—▽—) 93

FIGURE 55: STOKE NUMBERS AT (A) FILTER SCALE Δ (B)KOLMOGOROV SCALE H ; WITH DYNAMIC SMAGORINSKY MODEL IN..... 94

FIGURE 56: PDF COMPARISON, 40MM DOWNSTREAM AT SPRAY PLUME CENTRE , (A) DIAMETER (B) AXIAL VELOCITY (C) RADIAL VELOCITY(FILLED) EXPERIMENTAL (HOLLOW) NUMERICAL..... 95

FIGURE 57: VOF RESULTS; (A) ISO-SURFACE OF LIQUID; (B) CROSS-SECTION OF THE LIQUID TO GAS VOLUME RATIO 100

FIGURE 58: VOLUME OF FLUID SIMULATION, CROSS-SECTION OF LIQUID TO GAS RATIO AT THE NOZZLE OUTLET (A) MEAN (B) RMS 100

FIGURE 59: VOLUME OF FLUID SIMULATION, CROSS-SECTION OF MEAN LIQUID VELOCITY NORMALIZED IN TERMS OF MACH NUMBER OF AT THE NOZZLE OUTLET (A) MEAN (B) RMS 101

FIGURE 60: VOLUME OF FLUID SIMULATION, CROSS-SECTION OF THE LIQUID ANGLE FROM THE CENTRELINE OF NOZZLE (A) RADIAL (B) AZIMUTHAL 102

FIGURE 61: DROP SIZE DISTRIBUTION ON THE CAVITATION SIDE, DASHED LINE REPRESENTS THE LOGNORMAL DISTRIBUTION WITH A MEAN VALUE OF 1.35 AND STANDARD DEVIATION OF 0.375 102

FIGURE 62: VOLUME OF FLUID SIMULATION, CROSS-SECTION OF DROP SIZE DISTRIBUTION (A) D10 (B) SMD 103

FIGURE 63: PDF DISTRIBUTIONS FOR $Pi = 100\ bar$ AT A DOWNSTREAM LOCATION OF $250Di$; AT SPRAY PLUME CENTRE, (A) DIAMETER (B) AXIAL VELOCITY (C) RADIAL VELOCITY; AT PERIPHERY (D) DIAMETER (E) AXIAL VELOCITY (F) RADIAL VELOCITY; (FILLED) EXPERIMENTAL (HOLLOW) NUMERICAL..... 106

FIGURE 64: JOINT PDF DISTRIBUTIONS FOR $Pi = 100\ bar$ AT A DOWNSTREAM LOCATION OF $250Di$; AT SPRAY PLUME CENTRE, FOR DIAMETER & AXIAL VELOCITY (A) EXPERIMENTAL (B) NUMERICAL; DIAMETER & RADIAL VELOCITY (C) EXPERIMENTAL (D) NUMERICAL (GRAY SCALE INVERTED, BLACK DENOTES MAXIMUM) 108

FIGURE 65: JOINT PDF DISTRIBUTIONS FOR $Pi = 100\ bar$ AT A DOWNSTREAM LOCATION OF $250Di$; AT SPRAY PLUME PERIPHERY, FOR DIAMETER & AXIAL VELOCITY (A) EXPERIMENTAL (B) NUMERICAL; DIAMETER & RADIAL VELOCITY (C) EXPERIMENTAL (D) NUMERICAL (GRAY SCALE INVERTED, BLACK DENOTES MAXIMUM) 109

FIGURE 66: JOINT PDF DISTRIBUTIONS OF RADIAL & AXIAL VELOCITY FOR $Pi = 100\ bar$ AT A DOWNSTREAM LOCATION OF $250Di$; AT SPRAY PLUME CENTRE, FOR (A) EXPERIMENTAL (B) NUMERICAL; SPRAY PLUME PERIPHERY (C) EXPERIMENTAL (D) NUMERICAL (GRAY SCALE INVERTED, BLACK DENOTES MAXIMUM) 110

FIGURE 67: PDF DISTRIBUTIONS FOR $Pi = 200\ bar$ AT A DOWNSTREAM LOCATION OF $250Di$; AT SPRAY PLUME CENTRE, (A) DIAMETER (B) AXIAL VELOCITY (C) RADIAL VELOCITY; AT PERIPHERY (D) DIAMETER (E) AXIAL VELOCITY (F) RADIAL VELOCITY; (FILLED) EXPERIMENTAL (HOLLOW) NUMERICAL..... 111

FIGURE 68: JOINT PDF DISTRIBUTIONS FOR $Pi = 200\ bar$ AT A DOWNSTREAM LOCATION OF $250Di$; AT SPRAY PLUME CENTRE, FOR DIAMETER & AXIAL VELOCITY (A) EXPERIMENTAL (B) NUMERICAL; DIAMETER & RADIAL VELOCITY (C) EXPERIMENTAL (D) NUMERICAL (GRAY SCALE INVERTED, BLACK DENOTES MAXIMUM) 112

List of Figures

FIGURE 69: JOINT PDF DISTRIBUTIONS FOR $Pi = 200\ bar$ AT A DOWNSTREAM LOCATION OF $250Di$; AT SPRAY PLUME PERIPHERY, FOR DIAMETER & AXIAL VELOCITY (A) EXPERIMENTAL (B) NUMERICAL; DIAMETER & RADIAL VELOCITY (C) EXPERIMENTAL (D) NUMERICAL (GRAY SCALE INVERTED, BLACK DENOTES MAXIMUM) 113

FIGURE 70: JOINT PDF DISTRIBUTIONS OF RADIAL & AXIAL VELOCITY FOR $Pi = 200\ bar$ AT A DOWNSTREAM LOCATION OF $250Di$; AT SPRAY PLUME CENTRE, FOR (A) EXPERIMENTAL (B) NUMERICAL; SPRAY PLUME PERIPHERY (A) EXPERIMENTAL (B) NUMERICAL (GRAY SCALE INVERTED, BLACK DENOTES MAXIMUM) DEVELOPED TURBULENCE AT 100 BAR AND 200 BAR: 114

FIGURE 71 : NORMALIZED GAS VELOCITY ALONG THE CENTRELINES IN DOWNSTREAM DIRECTION AT THE INJECTION PRESSURE OF (A) 100 BAR (B) 200 BAR, (SOLID LINE) MEAN VELOCITY (DOTTED LINE) INSTANTANEOUS VELOCITY 115

FIGURE 72: CROSS-SECTION OF SPRAY PLUME AT 100BAR INJECTION PRESSURE 116

FIGURE 73: DOWNSTREAM EVOLUTION OF NORMALIZED HALF WIDTH AT THE INJECTION PRESSURE OF (A) 100 BAR (B) 200 BAR; (—)Lha (– –) Lhc (...) $Lhnc$ (–·–)Lhs 117

FIGURE 74: RADIAL DISTRIBUTION OF MEAN VELOCITY IN ASYMMETRIC ZONE, NORMALIZED BY INJECTION VELOCITY (A) $Pi = 100\ bar$ (B) $Pi = 200\ bar$; NORMALIZED BY CENTRELINE VELOCITY (C) $Pi = 100\ bar$ (D) $Pi = 200\ bar$; $50Di$ (–○–), $100Di$ (–☆–), $150Di$ (–□–), $200Di$ (–◇–), $250Di$(–▽–) (DASHED LINE, GAUSSIAN FIT WITH MEAN =0 AND STANDARD DEVIATION OF 0.8. 119

FIGURE 75: RADIAL DISTRIBUTION OF MEAN VELOCITY IN SYMMETRIC ZONE; NORMALIZED BY INJECTION VELOCITY (A) $Pi = 100\ bar$ (B) $Pi = 200\ bar$; NORMALIZED BY CENTRELINE VELOCITY (C) $Pi = 100\ bar$ (D) $Pi = 200\ bar$; AT DOWNSTREAM LOCATIONS OF $50Di$ (–○–), $100Di$ (–☆–), $150Di$ (–□–), $200Di$ (–◇–), $250Di$(–▽–) (SOLID LINE, GAUSSIAN FIT WITH MEAN =0 AND STANDARD DEVIATION OF 0.75. 120

FIGURE 76: RADIAL DISTRIBUTION OF MEAN LIQUID VELOCITY IN ASYMMETRIC ZONE; NORMALIZED BY INJECTION VELOCITY (A) $Pi = 100\ bar$ (B) $Pi = 200\ bar$; NORMALIZED BY CENTRELINE VELOCITY (C) $Pi = 100\ bar$ (D) $Pi = 200\ bar$; AT DOWNSTREAM LOCATIONS OF $50Di$ (–○–), $100Di$ (–☆–), $150Di$ (–□–), $200Di$ (–◇–), $250Di$(–▽–) (SOLID LINE, GAUSSIAN FIT WITH MEAN =0 AND STANDARD DEVIATION OF 0.75. 121

FIGURE 77: RADIAL DISTRIBUTION OF MEAN LIQUID VELOCITY DISTRIBUTION PROFILES IN SYMMETRIC ZONE; NORMALIZED BY INJECTION VELOCITY (A) $Pi = 100\ bar$ (B) $Pi = 200\ bar$; NORMALIZED BY CENTRELINE VELOCITY (C) $Pi = 100\ bar$ (D) $Pi = 200\ bar$; AT DOWNSTREAM LOCATIONS OF $50Di$ (–○–), $100Di$ (–☆–), $150Di$ (–□–), $200Di$ (–◇–), $250Di$(–▽–) (SOLID LINE, GAUSSIAN FIT WITH MEAN =0 AND STANDARD DEVIATION OF 0.75. 122

FIGURE 78: RADIAL DISTRIBUTION OF MEAN LIQUID TO GAS MASS RATIO IN; ASYMMETRIC ZONE; (A) $Pi = 100\ bar$ (B) $Pi = 200\ bar$; SYMMETRIC ZONE; (C) $Pi = 100\ bar$ (D) $Pi = 200\ bar$; AT DOWNSTREAM LOCATIONS OF $50Di$ (–○–), $100Di$ (–☆–), $150Di$ (–□–), $200Di$ (–◇–), $250Di$(–▽–) (SOLID LINE, GAUSSIAN FIT WITH MEAN =0 AND STANDARD DEVIATION OF 0.75. 124

FIGURE 79: STREAMWISE RMS CARRIER PHASE VELOCITY FLUCTUATIONS AT $Pi = 100\ bar$ (A) RESOLVED (B) TOTAL; AND AT $Pi = 200\ bar$ (C) RESOLVED (D) TOTAL; AT THE DOWNSTREAM LOCATIONS OF $50Di$ (–○–), $100Di$ (–☆–), $150Di$ (–□–), $200Di$ (–◇–), $250Di$(–▽–) 125

List of Figures

FIGURE 80: STREAMWISE RMS DISPERSED PHASE VELOCITY FLUCTUATIONS FOR Pi OF (A) 100 BAR (B) 200 BAR AT THE DOWNSTREAM LOCATIONS OF $50Di$ (—⊙—), $100Di$ (—☆—), $150Di$ (—□—), $200Di$ (—◇—), $250Di$(—▽—) 126

FIGURE 81: STREAMWISE PROFILES OF FILTERED NORMAL STRESS COMPONENT $u'u'$ NORMALIZED BY CENTRELINE VELOCITY AT INJECTION PRESSURE (A) 100 BAR (B) 200 BAR; $50Di$ (—⊙—), $100Di$ (—☆—), $150Di$ (—□—), $200Di$ (—◇—), $250Di$(—▽—) 127

FIGURE 82: STREAMWISE PROFILES OF FILTERED NORMAL STRESS COMPONENT $v'v'$ NORMALIZED BY CENTRELINE VELOCITY AT INJECTION PRESSURE (A) 100 BAR (B) 200 BAR; $50Di$ (—⊙—), $100Di$ (—☆—), $150Di$ (—□—), $200Di$ (—◇—), $250Di$(—▽—) 128

FIGURE 83: STREAMWISE PROFILES OF FILTERED NORMAL STRESS COMPONENT $w'w'$ NORMALIZED BY CENTRELINE VELOCITY AT INJECTION PRESSURE (A) 100 BAR (B) 200 BAR; $50Di$ (—⊙—), $100Di$ (—☆—), $150Di$ (—□—), $200Di$ (—◇—), $250Di$(—▽—) 128

FIGURE 84: STREAMWISE PROFILES OF FILTERED SHEAR STRESS COMPONENT $u'w'$ NORMALIZED BY CENTRELINE VELOCITY AT INJECTION PRESSURE (A) 100 BAR (B) 200 BAR; $50Di$ (—⊙—), $100Di$ (—☆—), $150Di$ (—□—), $200Di$ (—◇—), $250Di$(—▽—) 129

FIGURE 85: STREAMWISE PROFILES OF FILTERED SHEAR STRESS COMPONENT $v'w'$ NORMALIZED BY CENTRELINE VELOCITY AT INJECTION PRESSURE (A) 100 BAR (B) 200 BAR; $50Di$ (—⊙—), $100Di$ (—☆—), $150Di$ (—□—), $200Di$ (—◇—), $250Di$(—▽—) 129

FIGURE 86: STOKE NUMBERS AT SEVERAL DOWNSTREAM LOCATIONS FOR $Pi = 100\ bar$ (A) KOLMOGOROV SCALE H (B) FILTER SCALE Δ; AND $Pi = 200\ bar$ (C) KOLMOGOROV SCALE H (D) FILTER SCALE Δ; WITH DYNAMIC SMAGORINSKY MODEL IN THE DOWNSTREAM DIRECTION AT (—△—) CENTRELINE (—□—) SHEAR LAYER..... 130

FIGURE 87: TEMPORAL SPRAY EVOLUTION OF EXPERIMENT ON LEFT AND SIMULATION ON RIGHT; FOR $Pi = 100\ bar$ AT THE INJECTION TIME, $Tinj$ OF (A) 0.8MS (B) 1.1MS (C) 1.4MS (D) 1.7MS (E) 2 (F) 2.3MS (INCLUDING THE DELAY IN OPENING OF INJECTOR OF 0.433MS AND 0.490MS FOR 100 BAR AND 200 BAR RESPECTIVELY) 132

FIGURE 88: SPRAY PENETRATION VERSUS INJECTION TIME (△) EXP 100 BAR (□) EXP 200 BAR (▬) NUM 100 BAR (- -) NUM 200 BAR 133

FIGURE 89: SPRAY PLUME ANGLE; AT 100 BAR (A) EXPERIMENT (B) NUMERICAL 134

FIGURE 90: INJECTOR SPRAY GEOMETRY AND PDA LASER BEAM ALIGNMENT (MOJTABI, WIGLEY, & HELIE, 2010) 142

FIGURE 91: PIV SETUP OF THE AIR ENTRAINMENT BETWEEN THE TWO JETS FOR (A) XL 3-HOLES INJECTOR (B) 6-HOLES INJECTOR [COURTESY IFPEN] 143

FIGURE 92: SPRAY TEST BENCH SET-UP FOR CLOSE-UP SPRAY IMAGING [COURTESY SAMIR MAKHLOUF, PHD STUDENT] 144

FIGURE 93: (A) TYPICAL SIMULATION, RED: CAVITATION SURFACE IN THE METERING HOLE RED ; LIGHT BLUE: ATOMIZATION SURFACE IN THE EXTERNAL DOMAIN. (B) PLANE USED FOR PRIMARY ATOMISATION ANALYSIS OF THE CONTINUOUS CORE. 145

FIGURE 94: LIGAMENTS ANALYSIS ROUGH PRINCIPLE 146

FIGURE 95: LIGAMENTS ANALYSIS PROCESS. (A) INITIAL INSTANTANEOUS FILED (B) DISTANCE FUNCTION (C): DEDUCED ARITHMETIC AVERAGE OF THE EXPECTED DROP SIZE ON THIS FIELD (BEFORE WAVE ANALYSIS HERE) 147

FIGURE 96: CONTROL VOLUME FOR FINITE VOLUME DISCRETISATION; ADAPTED FROM (VILLIERS, 2006) 149

FIGURE 97: FACE INTERPOLATION 152

FIGURE 98: DECOMPOSITION OF FACE AREA VECTOR IN ORTHOGONAL AND NON-ORTHOGONAL PARTS. 153

List of Tables

TABLE 1: EU EMISSIONS STANDARDS FOR PASSENGER CARS (** APPLIES ONLY TO VEHICLES WITH DIRECT INJECTION ENGINES) 3
TABLE 2: INJECTOR DESIGN PARAMETERS 33
TABLE 3: OPERATING CONDITIONS OF EXPERIMENTS (PDA AND PIV) AND SIMULATIONS 34
TABLE 4: ANGLES OF CLOSE-UP AND DEFLECTED PART OF THE SPRAY AT TIME 1.75MS AND 3.10MS 45
TABLE 5: COMPARISON OF AXIAL AND MAXIMUM PENETRATION FOR THE CASES WITH DIFFERENT HOLE TO HOLE DISTANCE CONFIGURATIONS 58
TABLE 6 : SUBGRID SCALE MODELS WITH DIFFERENT INJECTION MODELS 73
TABLE 7 : INITIAL PARAMETERS 77
TABLE 8: INJECTION PARAMETERS 104
TABLE 9: SPRAY MAIN STREAM ANGLES 117

Nomenclature

Greek Symbols

$\boldsymbol{\alpha}$	Volume fraction	-
$\boldsymbol{\alpha_c}$	Spray cone angle close to the injection nozzle	degree
$\boldsymbol{\alpha_d}$	Deflected spray cone angle	degree
$\boldsymbol{\alpha_h}$	Geometrical half spray cone	degree
$\boldsymbol{\alpha_l}$	Liquid to gas mass ratio	-
$\boldsymbol{\alpha_{l_o}}$	Liquid to gas mass ratio at the injection surface	-
$\boldsymbol{\beta}$	Spray plume angle	degree
$\boldsymbol{\varepsilon}$	Dissipation	m^2/sec^3
$\boldsymbol{\eta}$	Kolmogorov scale	m
$\boldsymbol{\lambda}$	Taylor microascale	m
$\mathbf{\Delta t}$	Time-step	sec
$\boldsymbol{\mu_g}$	Gas viscosity	$kg/m\ sec$
$\boldsymbol{\mu_l}$	Liquid viscosity	$kg/m\ sec$
$\boldsymbol{\mu_t}$	Turbulent viscosity	$kg/m\ sec$
$\boldsymbol{\rho^*}$	Effective density	kg/m^3
$\boldsymbol{\rho_g}$	Gas density	kg/m^3
$\boldsymbol{\rho_l}$	Liquid density	kg/m^3
$\boldsymbol{\rho_p}$	Drop density	kg/m^3
$\boldsymbol{\rho_v}$	Vapour density	kg/m^3
$\boldsymbol{\sigma}$	Surface tension	kg/sec^2
$\boldsymbol{\tau_e}$	Evaporation time scale	sec
$\boldsymbol{\tau_h}$	Heat transfer relaxation time	sec
$\boldsymbol{\omega}$	Vorticity	sec^{-1}

Nomenclature

Roman Symbols

c_{ps}	Emperical constant	
C_D	Coefficient of drag	-
C_{fb}	Coefficient of flash boiling	-
d_p	Droplet or Particle diameter	m
$\mathcal{D}$	Mass Diffusivity Coefficent	-
D_i	Injection or inlet diameter of the nozzle hole	m
D_{10}	Mean diameter $= < d_p >$	m
g	Gravity	m/sec^2
l_I	Integral length scale	m
k	Kinetic energy	$kg\ m^2/sec^2$
k_{sgs}	Subgrid scale kinetic energy	$kg\ m^2/sec^2$
l_{turb}	Turbulence length scale	m
L_h	Spray plume half width	m
$L_{h,nc}$	Spray plume half width on non-cavitation side	m
$L_{h,c}$	Spray plume half width on cavitation side	m
$L_{h,z}$	Spray plume half width on symmetric side	m
m_p	Droplet or Particle mass	kg
n_{rand}	Random number	-
Ma	Mach number	-
Nu	Nusselt Number	-
$P_{ambient}$	Ambient pressure	bar /10^5Pa
$P_{chamber}$	Chamber pressure	bar /10^5Pa
P_{inj}	Injection Pressure	bar /10^5Pa
Pr	Prandtl Number	-
q	Spread factor for Rosin Rammler	-
Re	Reynolds number	-
Re_p	Drop or particle Reynolds number	-
S_c	Schmidt Number	-
S_{energy}	Energy source term	$kg\ m^2/sec^2$
S_h	Sherwood Number	-

Nomenclature

$\boldsymbol{S_{ij}}$	is the rate of strain tensor	sec^{-1}
$\mathbf{S_{mass}}$	Mass source term	kg
$\mathbf{S_{mom}}$	Momentum source term	$kg\ m/_{sec^2}$
$\boldsymbol{S_t}$	Stokes number	-
$\boldsymbol{S_{ti}}$	Inlet Stokes number, based on inlet velocity	-
$\boldsymbol{S_{td}}$	Standard deviation	-
SMD	Sauter mean diameter, $D_{32} = < d_p{}^3/d_p{}^2 >$	m
$\boldsymbol{t_{turb}}$	Turbulence correlation time	sec
$\mathbf{T_i}$	Inlet time based on inlet velocity and inlet diameter	sec
Ta	Taylor number	-
u, U	Velocity	$m/_{sec}$
$\mathbf{U_c}$	Centreline gas velocity	$m/_{sec}$
$\mathbf{U_i}$	Inlet velocity	$m/_{sec}$
$\mathbf{U_{l_o}}$	Liquid velocity at the inlet	$m/_{sec}$
$\mathbf{u_g}$	Gas velocity	$m/_{sec}$
$\mathbf{u_p}$	Droplet velocity	$m/_{sec}$
$\mathbf{u_{pa}}$	Droplet axial velocity	$m/_{sec}$
$\mathbf{u_{pr}}$	Droplet radial velocity	$m/_{sec}$
$\mathbf{U_p}$	Liquid velocity	$m/_{sec}$
$\mathbf{U_{pc}}$	Centreline liquid velocity	$m/_{sec}$
We	Weber Number	-
$\mathbf{We_p}$	Droplet Weber number	-
$\mathbf{We_l}$	Liquid Weber number	-
$\mathbf{X_{\upsilon,s}}$	Mass fraction of fuel vapour at droplet surface	-
$\mathbf{X_{\upsilon,\infty}}$	Mass fraction of fuel vapour far away	-
$\mathbf{Y_f}$	Evaporation mass fraction	-

Chapter 1 Introduction

The engines of current generation automobiles are quite different from what they used to be a few decades back. The basic process of engine combustion is still the same as before but the injection strategies have evolved massively. Modern engines have new electronically controlled injection systems along with mechanisms to compress air which helps in better combustion while cylinder deactivation makes sure the engine uses only the amount of fuel that it requires.

As an estimate, during the past year almost 60 million passenger cars are produced which makes it 165, 000 cars produced per day. More than 50% of the cars are produced in Asia and Oceania, whereas Europe produces almost one third of the total number of cars in the world. In last decade the total number of cars produced annually has increased by 20 millions. This has increased the pollutants by a quite a huge percentage which poses a great threat to the environment. All the emission regulatory bodies around the world have been striving constantly in order to reduce the amount of pollutants emitted by the vehicles. The emissions from gasoline and diesel combustion engines include carbon dioxide (CO_2) and carbon monoxide (CO). Partially burnt fuel present in the exhaust gases forms a complex mixture of hydrocarbons (HCs) such as methane (CH4). Particulate matter (PM) and nitrogen oxides (NOx) are also produced which is common in diesel exhaust.

The regulations on the emissions are getting tougher and tougher with passage of time e.g. it is planned to reduce the emission of CO_2 from the passenger cars to an order of 100 mg/km by year 2025 for all the major regulations across the world. Although carbon dioxide is a non-toxic gas but yet, it is very dangerous for the environment simply due to greenhouse effect. An annual release of carbon dioxide is estimated to be around 30 billion tonnes due to various human activities across the world. The concentration of carbon dioxide (from all sources) has increased by 31% since 1750.

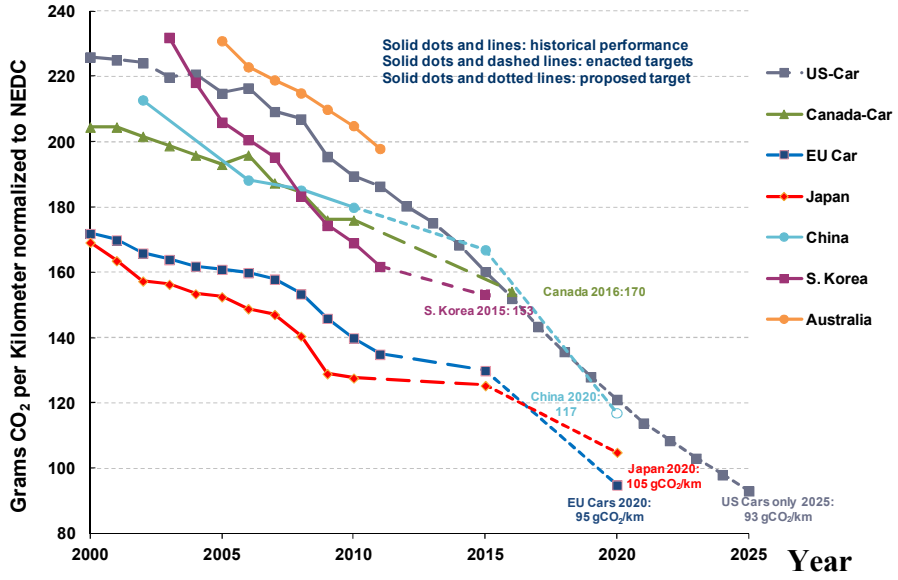

Figure 1: CO_2 emission standards

Euro 5 emission regulations came into force on 1st of September 2009 and were applied to all new vehicles from 1st of January 2011. Euro 6 regulations which are much tougher than that of Euro 5 will come into force on 1st of September 2014 and shall apply to all new vehicles from 1st January 2015. Therefore it is absolutely necessary to improve the quality of engine combustion which in turn is controlled by the injection system. The emission regulations in the past present and in future are presented in Table 1.

Modern day internal combustion engines use highly advanced fuel injectors to deliver fuel to the engine in most efficient way. There are various types of fuel injection systems available depending on the type of engine. In spark-ignition (SI) engines, port fuel injection (PFI) and direct injection (DI) are most commonly used. In compression ignition (CI) engines, injection consists of port injection as in homogeneous-charge compression ignition (HCCI) engines or direct injection as in conventional diesel engines. In SI engines the injection pressures vary from 2 to 3 bar in PFI engines to 100 to 200 bars in the direct-injection spark-ignition (DISI) engines. Whereas, DI diesel engines work at much higher pressures of around 10 or more times higher than spark-ignition DI engines. Injection systems are usually controlled electronically in order to open and close the injectors immediately and thus reduce the wastage of the fuel.

Euro Standard	Implementation date*	CO (g/km)	THC (g/km)	NMHC (g/km)	NOx (g/km)	HC=NOx (g/km)	PM (g/km)
Diesel							
Euro I	July 1993	2.72	-	-	-	0.97	0.14
Euro II	January 1997	1.00	-	-	-	0.70	0.08
Euro III	January 2001	0.64	-	-	0.50	0.56	0.05
Euro IV	January 2006	0.50	-	-	0.25	0.30	0.025
Euro V	September 2010	0.500	-	-	0.180	0.230	0.005
Euro VI	September 2015	0.500	-	-	0.080	0.170	0.005
Gasoline							
Euro I	July 1993	2.72	-	-	-	0.97	-
Euro II	January 1997	2.20	-	-	-	0.50	-
Euro III	January 2001	2.30	0.20	-	0.15	-	-
Euro IV	January 2006	1.00	0.10	-	0.08	-	-
Euro V	September 2010	1.000	0.100	0.068	0.060	-	0.005**
Euro VI	September 2015	0.100	0.100	0.068	0.060	-	0.005**

*Table 1: EU emissions standards for passenger cars (** Applies only to vehicles with direct injection engines)*

In case of gasoline engines, Figure 2 predicts an increase in the production of the GDI engines and a steady demise in the production of engines based on port fuel injection system. In gasoline direct injection (GDI) engines, also referred as DISI engines, the fuel is directly injected into the cylinder during the intake or compression stroke of the engine cycle. The fuel is injected in the engine according to the engine load conditions. At the high load operational conditions, fuel is injected during the intake stroke and engine operates like a homogeneous-charge stoichiometric SI engine. At the lower load conditions the fuel injection is delayed according to the required load and the air fuel mixture tends to be lean and stratified. The GDI engines are 15% more efficient in the fuel consumption than the PFI engine due to reduced pumping loss, lean-burn, lower heat losses, and higher compression ratio of GDI in relation to PFI (Alkidas & El-Tahry, 2003).

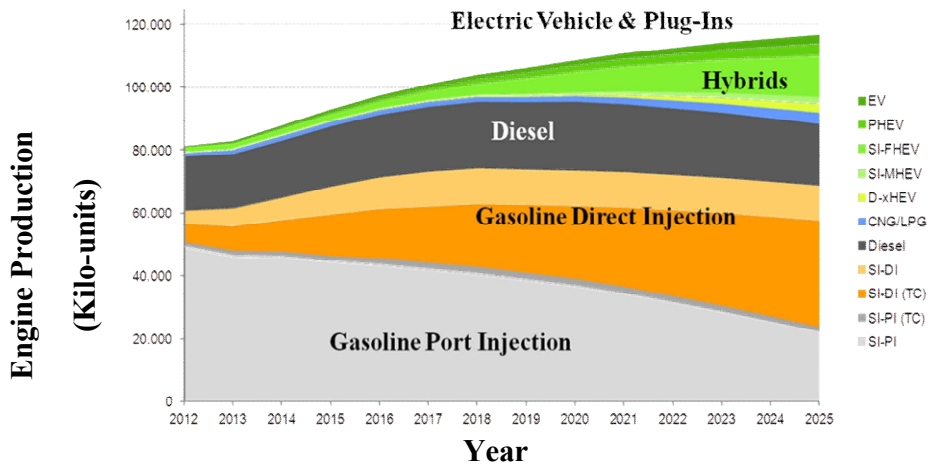

Figure 2: Global PV/LV Engine Production (2012-2025)

In GDI engines, fuel is injected directly from the multi-hole injectors usually at 200 bar injection pressure. A cross-sectional view of Continental's current XL3 injector is presented in Figure 3. Depending on the engine application, multi-hole injectors can have 5 to 7 cylindrical or conical holes of diameter ranging from 150 µm to 250 µm. The injectors are controlled electronically by a solenoid actuator, which can withstand a pressure of 270 bar. The actuator lifts the needle to open the valve at the precise time to releases a metered amount of fuel in the engine. The spray plumes directions and injector opening timings are adjusted according to engine design and application which ensures no or a minimum amount of the spray plumes come in contact with engine cylinder walls, piston or the valves.

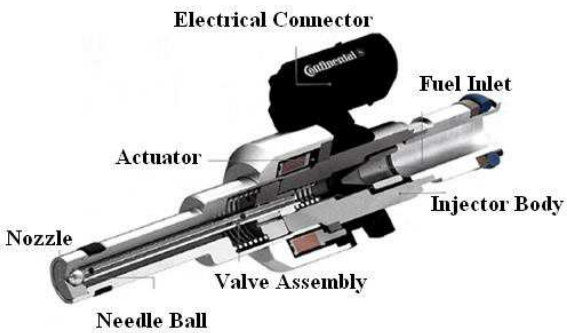

Figure 3: Cross-sectional view of GDI injector (current XL3 injector) (scoltock, 2012)

1.1 Objectives and outline of the thesis

The spray structure of a multi-hole GDI injector is a combination of liquid ligaments and drops of various sizes usually dependent on the injection pressure. When the liquid is injected in the engine it creates a ring shape of the spray. Usually liquid ligaments are formed upstream in the nozzle vicinity and the ligaments break into droplets downstream due of air liquid interaction which promotes the growth of instabilities on the liquid surface. The droplets breakup continues further downstream which encourages evaporation.

Multi-hole injectors are usually very complex in nature due to the phenomenon like je-to-jet interaction; cavitation inside the nozzle of the injector. Jet-to-jet interactions are observed at high load conditions in which high vapour concentration enhances the jet-to-jet interactions. This behaviour of the multi-hole spray can also be noticed in the experiments but the spray cone is so dense that it is almost impossible to see across the thick fog of droplets. Under flashing i.e. superheated conditions multi-hole the behaviour of the multi-hole injectors becomes very strange due immense jet to jet interaction and rapid expansion of the spray plumes. Similarly, cavitation in multi-hole injectors is usually observed on the outer region of the spray and it leads to a sudden increase in the angle of the spray very close to the injection nozzle. Moreover it also forces the liquid inside the injection hole to be distributed unevenly which lead to unpredictable behaviour of the spray plumes.

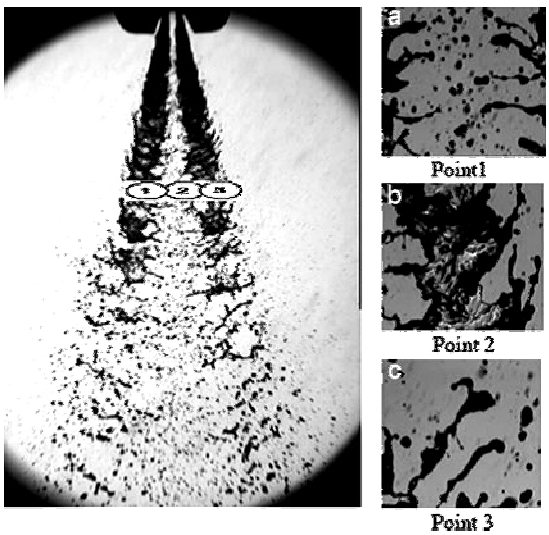

Figure 4: Enlarged spray structure of two-hole-type injector (a) Point 1(b) Point2, (c) Point 3 (Ashgriz, 2011)

The information obtained from the experimental results is certainly not enough to draw clear conclusion which could help in design improvement of the injector. However, simulation techniques which are sufficiently advanced these days and can provide more insight to the posed problems. There are usually three different simulation approaches: Direct numerical Simulations, DNS; Large Eddy Simulations, LES and Reynolds Average Navier Stokes, RANS. DNS and LES both are the transient simulation techniques while RANS only gives the averaged solution. DNS is the most accurate but at the same time most expensive in terms of computational time and resources. On the other hand LES is reasonably accurate and yet not too expensive like DNS and it serves the purpose well in most of the applications. Whereas, RANS is least accurate of all three approaches but it is the cheapest approach of the three.

Despite of the all the advancements in the information technology, it is still not possible to have sufficient computational resources at a reasonable cost. This is the reason why we have so many computational techniques these days. Some it is not always possible to perform very complex simulations with limited resources. Such is the case of a multi-hole injector which requires huge computational resources to perform LES of a full injector. But RANS on the other hand can perform such simulation in a reasonable time and limited computational resources. Therefore this thesis is divided in to two major parts (1) RANS simulations of the complete injectors in order to study jet-to-jet interactions under various surrounding conditions (2) LES of a single GDI spray to study the variations in the spray dynamics due to the various effects at the injector's outlet e.g. cavitation etc.

RANS simulation of multi-hole injector provides a very useful insight to the air entrainment in the spray cone and jet-to-jet interactions. The effects of surrounding conditions are also investigated on the spray plume interactions. Under superheated conditions the spray plumes expands enormously giving rise to severe jet-to-jet interactions which makes it very difficult to be captured by the ordinary RANS simulation. A special formulism for is introduced in the RANS to capture the spray behaviour under flash boiling conditions.

LES of a single spray plumes helps to investigate different spray injection conditions which lead to different spray structures and properties. The role of different turbulence models are also studied

which could artificially influence the spray simulations. Moreover, a methodology to couple the internal LES of Volume Of Fluid (VOF) simulation results with the Lagrangian LES spray simulation that takes the internal flow's organizational information along with cavitation effect at the exit hole has also been developed.

1.2 Overview of thesis chapters:

This thesis is divided into five chapters.

The first and present chapter is dedicated to the introduction of the topic and the objective of thesis.

A general introduction to the numerical tools, models and schemes used for the spray simulations are discussed in the chapter 2. The Euler-Lagrange formulation is used for the numerical simulation of the spray in which gas is treated in the Eulerian framework and the liquid in the lagrangian framework. This chapter is further divided into two main sections: (1) Turbulence modelling (2) Spray Modelling. Turbulence modelling section includes the overview of the different scales of turbulence present in a flow and the different turbulence modelling techniques. The second part deals with spray modelling. Spray modelling which covers the major part of this chapter includes detailed explanation of spray droplets injection model, breakup model, drag model, collision model, dispersion model, heat transfer model and evaporation model.

The next chapter deals with the simulation of 3-hole and 6-hole multi-hole injectors' sprays using RANS methodology under non superheated and superheated conditions. The air entrainment of both 3-hole and 6-hole injectors are compared with the experimental data. A detailed study of multiple two phase jet interactions under high load conditions is performed for both 3-hole and 6-hole injectors. The role of surrounding conditions is also studied in detail which leads to increase or decrease in the amount of jet-to-jet interactions. Under super heated conditions the spray behaviour is usually very bizarre and it is extremely difficult to be captured by the ordinary simulation technique. A new injection model for spray under superheated conditions, based on mathematical relationships and the experimental observations, is introduced and test against experimental shadowgraphy.

The next two chapters are devoted to transient spray simulations of a single spray plume. A thorough investigation in order to choose best suitable numerical and turbulence models for the spray simulation is discussed in chapter 4. The effects of various input excitation levels at the inlet along with different injection models are investigated. Moreover, the performance of turbulence models which directly influence on spray development is studied very deeply.

The last and final chapter includes the coupling of the internal flow LES-VOF simulation of a real injector with Lagrangian LES spray simulation. The coupling of the internal flow simulation removes the dependency of usual fixed input parameters and provides a priori to more realistic spray injection conditions. The steady state and unsteady state results are compared with the available experimental data.

Chapter 2 Turbulence and Spray Modelling

The methods based on the continuum transport have been known for the long time. In the past, it was not so easy to apply this methodology to highly turbulent flows due to lack of computational advancements. During the last two decades, new developments in the field of computations made it possible now to apply these methods to even most complex flows. One such area of study that has made a big progress over the years is "Spray Modelling". Different methodologies have been developed to study this complex flow but the most widely used approaches are: Eulerian for the gas phase and Lagrangian for disperse phase.

2.1 Conservation equation:

A general conservation equation which governs the motion of a fluid in the Eulerian framework, based on the concepts of divergence theorem and Reynolds transport theorem, has been represented in equation (1).

$$\frac{\partial X}{\partial t} = P + S + F \tag{1}$$

In the equation above a rate of change of physical quantity (X) is balanced by the production term P, supply term S and Flux term F. Production term can be referred to source or sink term. Supply term S originates due to the body forces in the flow like gravity etc. Lastly the flux term F comes into play due to the surface stresses on the fluid body or from heat flux through surfaces.

Similarly, the conservation equations for a specific physical quantity can easily be explained by the equations of the motion of a fluid with density (ρ), velocity $(\mathbf{u})$, and internal energy (e).

2.1.1 The total mass conservation equation:

$$\frac{\partial \rho}{\partial t} + \nabla.(\rho \mathbf{u}) = S_{mass} \tag{2}$$

S_{mass} is the change of mass density

2.1.2 Momentum conservation equation for fluid mixture:

$$\frac{\partial \rho \mathbf{u}}{\partial t} + \nabla.(\rho \mathbf{u}\mathbf{u}) = \rho g - \nabla.(\tau) + S_{mom} \tag{3}$$

S_{mom} is the rate of momentum exchange with spray per unit volume.

2.1.3 Energy conservation equation:

$$\frac{\partial \rho e}{\partial t} + \nabla.(\rho \mathbf{u} e) = -\nabla(\mathbf{q}) + (\nabla \mathbf{u} : \tau) + S_{energy} \tag{4}$$

here q is the specific heat flux and can be explained by the simple Fourier law of heat transfer, the expression $\nabla u : \tau$ represents the double inner product of gradient of u with Cauchy's stress tensor. The source term S_{energy} due to interaction with spray will be defined later.

Cauchy stress tensor (τ), used in the above equations, is defined as:

$$\tau = -p\mathbf{I} - \mu\left[(\nabla \mathbf{u} + \nabla \mathbf{u}^{T}) - \frac{2}{3}\nabla \mathbf{u}\mathbf{I}\right] \tag{5}$$

2.1 Turbulence modelling:

First, let us remind ourselves with the background of modern engineering approaches in turbulence modelling, namely, the Kolmogorov's homogeneous isotropic statistically stationary turbulence at a

high Reynolds number. On the basis of a simple scenario of energy transfer from the large energetic unstable eddy to scales on which this energy is dissipating into molecular motion, and employing the dimensionality analysis, this theory gives universal relations between parameters of turbulence. Thus, we start by characterizing typical velocity fluctuation $u' = \Delta_l u$ and the velocity increment between two points lying at the distance l_{turb} much smaller than the geometric spatial scale of flow $L \gg l_{turb}$.

Kolmogorov assumed that the energy decay rate is independent of this distance l and is also independent of the viscosity of fluid. Denoting this rate by ε, as a sole parameter of turbulent cascade, the Kolmogorov's scenario reads:

$$\frac{(\Delta_l u)^3}{l_{turb}} = \langle \varepsilon \rangle_{l_{turb}} = \varepsilon \tag{6}$$

where $\langle \varepsilon \rangle_{l_{turb}}$ is the averaged decay rate of kinetic energy estimated at spatial scale l_{turb}

On the other hand, on smallest spatial scales $\eta \ll l_{turb}$. The molecular viscosity should also be a parameter of energy transfer, along with ε. Then, again employing dimensionality analysis $l_{turb} \sim \eta$, we have:

$$l_{min} = l_{min}(v, \varepsilon) \equiv \eta \Longrightarrow \eta \sim \left(\frac{v^3}{\varepsilon}\right)^{1/4} \tag{7}$$

$$\Delta_\eta u \sim (\varepsilon v)^{1/4} \Longrightarrow = Re_\eta \Longrightarrow \frac{(\Delta_\eta u)\eta}{v} = 1 \tag{8}$$

That results in the following scaling law:

$$Re_L = \frac{(\Delta_L u)L}{v} = Re_\eta \left(\frac{L}{\eta}\right)^{4/3} \Longrightarrow \frac{L}{\eta} \sim Re_L{}^{3/4} \tag{9}$$

Two others corollaries from this are as follows.

Representing, $l_{turb} \sim \frac{1}{k}$, the density of turbulent energy in the space of wave numbers is

$$E(k) \sim \varepsilon^{2/3} k^{-5/3} \tag{10}$$

Denoting the turbulent energy by K, one yields the expression for turbulent viscosity:

$$\varepsilon \approx \frac{\Delta_L u^3}{L} \equiv \frac{K^{3/2}}{L}$$

$$\varepsilon \approx \nu_T \frac{\Delta_L u^2}{L^2} \equiv \nu_T \frac{K}{L^2} \tag{11}$$

$$\nu_T = C_\mu L K^{1/2}$$

These simple relations give rise to modern engineering approaches in turbulence modelling. Hereafter we will apply two of them: RANS with K-epsilon, and LES. The first approach is based on the Reynolds Averaged Navier-Stokes equations (RANS). All scales of turbulence, from L to η, are simulated in this approach. The second approach, referred to as Large Eddy Simulation (LES), integrates the filtered Navier-Stokes equations, with the width of filter comparable to the typical mesh size Δ. Then only subgrid turbulent scales are simulated in this approach, from Δ to η. The approach referred to as Direct Numerical Simulation (DNS) integrates the unfiltered Navier-Stokes equations; this approach employs the grid comparable to η, and is prone to resolve all turbulent sales. According to above written scaling, higher the Reynolds number is, higher is the spectrum of scales to be resolved, and consequently, higher the mesh density to be employed.

The different turbulence modelling techniques are compared in the Figure 5.

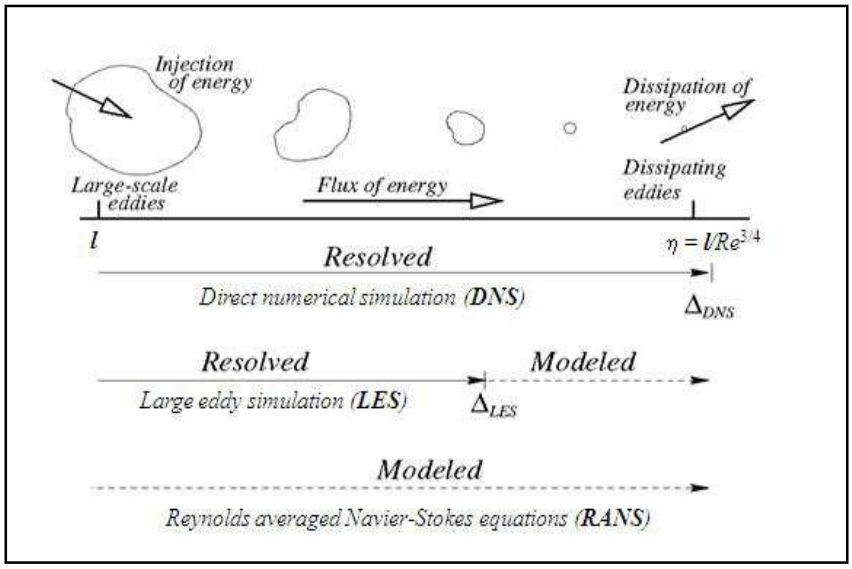

Figure 5: Comparison of different turbulence modelling techniques (Bakker, 2006)

2.2.1 Carrier phase equations:

2.2.1.1 Reynolds Average Navier Stokes:

The averaging in RANS is performed in a way that a flow field is divided in to two parts, one being the average part and other being the fluctuating part.

$$u_i(x_i, t) = \bar{u}_i(x_i, t) + \acute{u}_i(x_i, t) \tag{12}$$

The average part is obtained from the ensemble average, which is the average over a set of realizations of the given quantity being averaged.

$$\bar{u}_i(x_i, t) = \frac{1}{N}\sum_{n=1}^{N} u_i(x_i, t) \tag{13}$$

N is the number of the ensemble members.

This averaging technique when applied to the general conservation equations, it yields the averaged Navier-Stokes equations.

$$\frac{\partial \rho}{\partial t} + \frac{\partial \rho \bar{u}_i}{\partial x_i} = \bar{S}_{mass} \tag{14}$$

$$\frac{\partial \rho \bar{u}_i}{\partial t} + \frac{\partial \rho \bar{u}_i \bar{u}_j}{\partial x_j} = \rho g - \frac{\partial \bar{p}}{\partial x_i} + \frac{\partial \bar{\sigma}_{ij}}{\partial x_j} + \frac{\partial \tau_{ij}}{\partial x_j} + \bar{S}_{mom} \tag{15}$$

$$\frac{\partial \rho \bar{e}}{\partial t} + \frac{\partial \rho \bar{e} \bar{u}_j}{\partial x_j} = -\frac{\partial \bar{p} \bar{u}_j}{\partial x_i} + \frac{\partial \bar{u}_j \bar{\sigma}_{ij}}{\partial x_j} + \frac{\partial \bar{u}_j \tau_{ij}}{\partial x_j} + \bar{S}_{energy} \tag{16}$$

In the above equations S_{mass}, S_{mom} and S_{energy} are respectively the mass, momentum, and energy source terms from the dispersed phase. ρ denotes the density of the carrier phase, p represents the pressure and g is the gravity. The indices i and j represent the x, y and z directions, ∂ indicates the partial derivative and $\bar{\sigma}_{ij}$ represents the viscous stress tensor.

$$\bar{\sigma}_{ij} = \mu\left(\frac{\partial \bar{u}_i}{\partial x_j} + \frac{\partial \bar{u}_j}{\partial x_i} - \frac{2}{3}\frac{\partial \bar{u}_k}{\partial x_k}\delta_{ij}\right) \tag{17}$$

And τ_{ij} is the Reynolds stress term which is unknown and needs to be modelled in order to close the equations (15) and (16). Reynolds stress term is approximated by Boussinesq hypothesis (Hinze, 1975):

$$\tau_{ij} = \mu_t\left(\frac{\partial \bar{u}_i}{\partial x_j} + \frac{\partial \bar{u}_j}{\partial x_i} - \frac{2}{3}\frac{\partial \bar{u}_k}{\partial x_k}\delta_{ij}\right) - \frac{2}{3}\rho\delta_{ij}k \tag{18}$$

k is the turbulent kinetic energy described as $\frac{1}{2}\left(\overline{\acute{u}_i^{\,2}} + \overline{\acute{v}_i^{\,2}} + \overline{\acute{w}_i^{\,2}}\right)$ and μ_t is the turbulent viscosity.

2.2.1.2 Large Eddy Simulation:

Large eddy simulation resolves the large scales of the flow and only models the small scales, as explained in Figure 5. The large scales are produced due to the geometry of the flow and can vary for different geometries. On the other hand, small scales which are responsible for the dissipation of turbulent kinetic energy, tend to be universal and can be modelled easily.

In order to effectively filter out the small scale eddies form the large eddies a special filter of width Δ is utilized. The spatial filtering operation decomposes a flow field into two components i.e. resolved (filtered) and Sub-grid scale (residual).

$$u_i(x_i, t) = \tilde{u}_i(x_i, t) + \acute{u}_i(x_i, t) \tag{19}$$

The filtering operation of LES was first introduced by (Leonard, 1975) is defined by:

$$\tilde{u}(x, t) = \int_D G(r, x)\, u(x - r, t)\, dr \tag{20}$$

where D denotes domain of the flow field and G is a specified filter function and it satisfies normalization condition (Pope S. B., 2000):

$$\int G(r, x)\, dr = 1 \tag{21}$$

The continuity, momentum and the energy filtered Navier-Stokes equations after the filtration are:

$$\frac{\partial \rho}{\partial t} + \frac{\partial \rho \tilde{u}_i}{\partial x_i} = \tilde{S}_{mass} \tag{22}$$

$$\frac{\partial \rho \tilde{u}_i}{\partial t} + \frac{\partial \rho \tilde{u}_i \tilde{u}_j}{\partial x_j} = \rho g - \frac{\partial \tilde{p}}{\partial x_i} + \frac{\partial \tilde{\sigma}_{ij}}{\partial x_j} + \tilde{S}_{mom} \tag{23}$$

$$\frac{\partial \rho \tilde{e}}{\partial t} + \frac{\partial \rho \tilde{e} \tilde{u}_j}{\partial x_j} = -\frac{\partial \tilde{p} \tilde{u}_j}{\partial x_i} + \frac{\partial \tilde{u}_j \tilde{\sigma}_{ij}}{\partial x_j} + \tilde{S}_{energy} \tag{24}$$

The anisotropic part of subgrid-scale Reynolds stress which is unknown can be modelled though Boussinesq approach:

$$\tilde{\sigma}_{ij}{}^{s} - \frac{1}{3}\delta_{ij}\tilde{\sigma}_{kk}{}^{s} = -\mu_t \tilde{S}_{ij} \tag{25}$$

$\tilde{S}_{ij}$ is the rate of strain tensor at the filtered scale:

$$\tilde{S}_{ij} = \left(\frac{\partial \tilde{u}_i}{\partial x_j} + \frac{\partial \tilde{u}_j}{\partial x_i}\right). \tag{26}$$

The modelling of the subgrid scale viscosity μ_t will be discussed in the chapter 4.

2.2.2 Liquid phase equations:

The positions of the droplets are basically governed by Newton's equation of motion as introduced by (Stokes, 1850) and then later on some modifications were introduced by (Boussinesq, 1903) and (Maxey & Riley, Equation of motion for a small rigid sphere in a nonuniform flow, 1983).

$$\frac{1}{6}\rho_p \pi {d_p}^3 \frac{d\mathbf{u}_p}{dt} = \frac{1}{2}(\mathbf{u}_g - \mathbf{u}_p)|\mathbf{u}_g - \mathbf{u}_p|\rho_g C_D \frac{\pi {d_p}^2}{4} + \boldsymbol{F} \tag{27}$$

where, d_p is the droplet diameter, $\mathbf{u}_p$ is droplet velocity, $\mathbf{u}_g$ is the gas velocity and $\boldsymbol{F}$ is the sum of the Basset force, Faxen force, Saffman force, Magnus force and pressure gradient force. All these hydrodynamic forces are neglected and the motion equation of droplet is reduced to the Stokes drag:

$$\frac{d\mathbf{u}_p}{dt} = \frac{C_D}{\tau_p}\frac{Re_p}{24}\left(\mathbf{u}_g - \mathbf{u}_p\right) \tag{28}$$

$\mathrm{Re_p}$ is the droplet Reynolds number and τ_p is the droplet relaxation time. C_D is the coefficient of drag based on experimental correlations:

$$Re_p = \frac{\left|\mathbf{u}_\mathrm{g} - \mathbf{u}_\mathrm{p}\right| d_p}{\nu_g}, \quad \tau_p = \frac{4}{3}\frac{\rho_p d_p}{\rho_g C_D \left|\mathbf{u}_\mathrm{p} - \mathbf{u}_\mathrm{g}\right|} \tag{29}$$

$$C_D = \begin{cases} {}^{24}/_{Re_p} & Re_p < 0.1 \\ \dfrac{24\left(1 + \frac{1}{6} Re_p{}^{2/3}\right)}{Re_p} & 0.1 < Re_p < 1000 \\ 0.424 & Re_p > 1000 \end{cases} \tag{30}$$

2.2.3 Two way coupling, effect of droplets on the gas phase:

The droplets in a flow field alter the turbulence of the gas phase and it is necessary to take into account this effect. In equation, (14), (15) and (16), sources terms account for the contribution of the particles through the two-way coupling. The exact mass, momentum and energy source term can be expressed as:

$$S_{mass} = \frac{4}{3}\rho_p \pi \left(\frac{d_p}{2}\right)^3 \tag{31}$$

$$S_{mom} = \frac{4}{3}\rho_p \pi \left(\frac{d_p}{2}\right)^3 \left(\frac{d\mathbf{u}_\mathrm{p}}{dt} - \mathbf{g}\right) \tag{32}$$

$$S_{energy} = \frac{4}{3}\rho_p \pi \left(\frac{d_p}{2}\right)^3 \left(\left(H_g - H_p\right) + \left(\frac{P_g - P_{fv}}{\rho_p}\right)\right) \tag{33}$$

where H_g and H_p are the enthalpy gas and enthalpy of fluid respectively and P_g and P_{fv} are correspondingly the pressure of gas and fuel vapour pressure. In Euler Lagrange formulation of RANS all the source terms are averaged over the volume of the cell.

$$\bar{S}(x) = \frac{1}{V_{cell}} \sum_{p} S_i \tag{34}$$

2.2 Spray modelling:

When a liquid jet enters into gaseous environment it exchanges the momentum with the slowly moving gas generating a strong shear in the flow; thereby the turbulent flow around the spray is formed. The interaction between turbulent flow and liquid jet leads to its disintegration, and then the breakup of ligaments and big drops to the smaller droplets. This is the first of many phenomena to be modelled in spray. This phenomenon is very complex; its physics is not really understood. It is commonly recognized that this process is significantly affected by internal nozzle effects like cavitation and turbulence. Also, the sudden change in the boundary conditions for inner to outer flow has to be taken into account (Ashgriz, 2011).

As the spray plume moves away from the nozzle, the effect of drag, inter-droplet collisions, evaporation and heat transfer contribute to the complex physics of spray. Therefore, several sub models are needed to be included in spray modelling.

2.3.1 Liquid injection model:

In the present Lagrangian spray simulation the liquid is injected in the form of blobs with presumed mean size comparable to diameter of the injection nozzle orifice. The blobs are injected in the domain using a Rosin-Rammler distribution (Rosin & Rammler, 1933) sampled form the following expression:

$$d_{p_o} + d_p \left(-\ln\left(1 - n_{rand} k_R\right)\right)^{-q} \tag{35}$$

where k_R is defined as; $k_R = 1 - exp\left(\frac{\left(d_{p_{max}} - d_{p_o}\right)^q}{\langle d_p \rangle}\right)$ and n_{rand} is the random number. d_{p_o} is the minimum diameter, $d_{p_{max}}$ is the maximum diameter and $\langle d_p \rangle$ is the mean diameter. The spread factor of the distribution is controlled by q.

2.3.2 Secondary droplet breakup model:

When the liquid blobs are injected the main factors which govern the breakup of the droplets are the liquid and gas densities, the relative velocity between liquid and gas along with the liquid viscosity and surface tension. Weber number, defined as a ratio of fluid inertia to surface tension, therefore, becomes a crucial non-dimensional number for the breakup of the drops.

$$We_p = \frac{\rho_g \left|\mathbf{u}_g - \mathbf{u}_p\right|^2 r_p}{\sigma_p} \tag{36}$$

where the subscript "p" denotes the drop or liquid and subscript "g" stands for the gas. ρ symbolizes the density, and σ_p is surface tension of the drop.

In the literature five different breakup mechanisms of droplet breakup are usually referred (Pilch & Erdman, 1987) which are presented in the Figure 6 on next page.

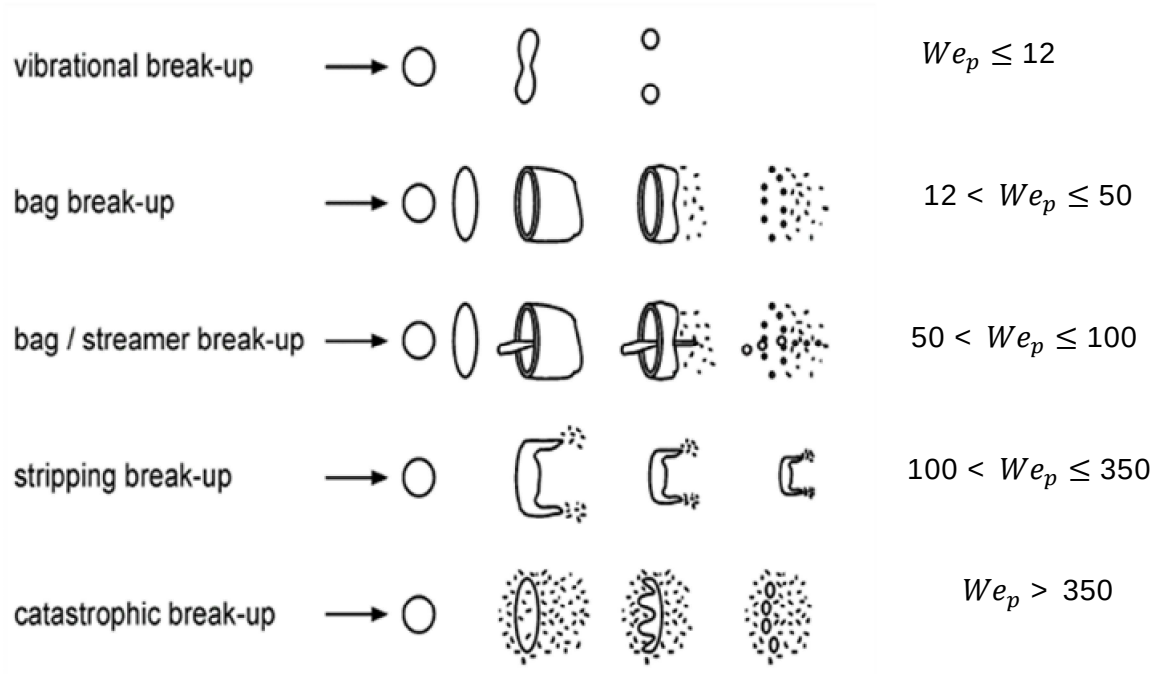

Figure 6: Breakup mechanism; adapted from (Pilch & Erdman, 1987)

In the present work the maximum Weber number does not exceed 350. Therefore, Enhanced Taylor Analogy Breakup (ETAB) model (Tanner, 1997) is chosen for the secondary breakup which utilizes the bag and stripping breakup mechanism. It is based on the same concept of droplet deformation as the classical TAB model (O'Rourke & Amsden, 1987) but with different relations for the breakup of parent droplet to child droplets.

The Taylor analogy breakup (TAB) model is based upon Taylor's analogy between an oscillating, distorting droplet and a spring mass system. It acts on a single droplet and it determines the droplet breakup by its shape deformation induced by the resonance of the droplet's surface.

$$m_p \frac{d^2x}{dt^2} + b\frac{dx}{dt} + kx = \boldsymbol{F} \tag{37}$$

The distortion of the droplet is represented by "x" which is actually the measure of deformation of the droplet from its original position, m_p is the mass of the droplet. The droplet viscous force is equivalent to the damping force b, surface tension forces are analogous to the spring force, k, and the

dynamic pressure force **F** is considered as the external force. The coefficients can be expressed in the following way:

$$\frac{b}{m_p} = C_\mu \frac{\mu_l}{\rho_p {r_p}^2} \tag{38}$$

$$\frac{k}{m_p} = C_w \frac{\sigma_p}{\rho_p {r_p}^3} \tag{39}$$

$$\frac{F}{m_p} = \frac{1}{3} \frac{\rho_g \left|\mathbf{u}_g - \mathbf{u}_p\right|^2}{\rho_p {r_p}^2} \tag{40}$$

where r_p is the radius of the droplet, ρ_g and ρ_p are the gas and liquid densities respectively, C_w and C_μ are the constants.

The distortion amplitude is non-dimensionalised by the radius of the drop.

$$y = \frac{x}{C_b r_p} \tag{41}$$

The breakup constant, C_b is chosen in a way that when y exceeds the unity, the "parent" droplet will breakup into a number of smaller "child" droplets.

The equation (37) can simply be solved for droplet distortion and oscillation in non-dimensional form at any given time using equations (38), (39), (40) and (41)

$$y(t) = We_{tmp} + e^{-t/t_d}\left[\left(y(0) - We_{tmp}\right)cos\omega t + \frac{1}{\omega}\left(\dot{y}(0) + \frac{y_0 - We_{tmp}}{t_p}\right)sin\omega t\right] \tag{42}$$

We_{tmp} is the temporal Weber number, $We_{tmp} = \frac{We_p}{We_{crtical}}$. A typical value of the critical Weber number, $We_{crtical}$ is 12. The coefficient t_p represents the characteristic viscous damping time of the droplet and it is proportional to drop surface, $t_d = \frac{2}{C_\mu}\frac{\rho_d {r_p}^2}{\mu_p}$. The oscillation frequency of the droplet is found from the constant of restoring force as $\omega^2 = C_w \frac{\sigma_p}{\rho_p {r_p}^3}\frac{1}{{t_p}^2}$

The rate of droplet creation in ETAB model is

$$\frac{d\overline{m}(t)}{dt} = -3K_{br}\overline{m}(t) \tag{43}$$

where $\overline{m}(t)$ is the mean mass of the child droplet distribution and K_{br} is a constant that depends on the droplet breakup regime. This leads to an exponential relation between the child droplet radius R_c and the parent droplet radius R_p.

$$R_c/R_p = e^{-K_{br}t} \; ; \; where \;\; K_{br} = \begin{cases} k_1 w & We \leq We_t \\ k_2 w\sqrt{We} & We > We_t \end{cases} \tag{44}$$

where w denotes the angular oscillation velocity of the droplet, k_1 and k_2 are the constants which are set to 0.2 and We_t is the transition Weber number which distinguishes the two regimes and is set to 100 for all cases.

2.3.3 Stochastic droplet dispersion model:

Particle dispersion, in average sense, based on the large scale flow structures governed by Stokes number was investigated by (Crowe C. T., 1982). (Lazaro & Lasheras, 1989; Lazaro & Lasheras, 1992a; Lazaro & Lasheras, 1992b) performed detailed experimental studies of particle dispersion in free shear flows under natural and forced boundary conditions. (Crowe, Chung, & Troutt, 1993) found that the gas turbulence can either increase or decrease depending on the particle size in the flow field.

A stochastic droplet dispersion model based on the initial work of (Dukowitz J. K., 1980) and (O'Rouke, 1989) has been utilized in the present work. In this model a fluctuation velocity component $\mathbf{u}'$ based on the turbulent kinetic energy, k is obtained from a Gaussian distribution

$$p(\mathbf{u}') = \frac{1}{\sqrt{2\pi}S_{td}} \exp\left(-\frac{\mathbf{u}'}{2S_{td}^{2}}\right) , \qquad \sigma = \sqrt{\frac{2}{3}k} \tag{45}$$

where, the standard divination (S_{td}) depends on the turbulent kinetic energy of the cell in which the particle is located. This fluctuation component is added to the mean gas velocity $(\bar{\mathbf{u}})$ to account for the particle dispersion.

Moreover this fluctuating velocity component $(\mathbf{u}')$ is a piecewise constant function, changing discontinuously at the passage of every turbulence correlation time (t_{turb}). Turbulence correlation time is defined as:

$$t_{turb} = \min\left(\frac{k}{\varepsilon}, c_{ps}\,\frac{k^{\frac{3}{2}}}{\varepsilon}\,\frac{1}{|\bar{\mathbf{u}} + \mathbf{u}'|}\right) \tag{46}$$

here, c_{ps} is an empirical constant with a value of 0.16432.

Therefore, t_{turb} represents the minimum of an eddy breakup time and a time required by a droplet to traverse or pass through an eddy. The sum of the mean and fluctuating velocity component $(\bar{\mathbf{u}} + \mathbf{u}')$ is the gas velocity which a particle sees during the computation of drag, mass transfer, momentum transfer, oscillations and breakup. The dispersion of each particle depends on whether the mean time step, Δt is smaller or greater than the turbulence correlation time, t_{turb}, i.e. (1) $\Delta t < t_{turb}$ (2) $\Delta t > t_{turb}$.

Case 1 $(\Delta t < t_{turb})$:

When the mean time step is smaller the turbulence correlation time, droplet velocity and position is simply calculated by the finite difference method. The position of the particle located in the momentum cell (i, j, k) are

$$t_{turb} = \min\left(\frac{k}{\varepsilon}, c_{ps}\,\frac{k^{\frac{3}{2}}}{\varepsilon}\,\frac{1}{|\bar{\mathbf{u}} + \boldsymbol{u}'|}\right) \tag{47}$$

$$\frac{x_p^B - x_p^n}{\Delta t} = \mathbf{u}_p^n \;; \qquad \frac{\mathbf{u}_p^B - \mathbf{u}_p^n}{\Delta t} = D_p\left(\mathbf{u}_{ijk}^B + \mathbf{u}'\right) \tag{48}$$

where, D_p is the drag function and gravity is neglected.

Case 2 ($\Delta t > t_{turb}$) :

When the mean time step is greater than turbulence correlation time then more than one value of $\mathbf{u}'$ is available in the single time step. To address this issue Δt can simply be forced every computational time step in order to be smaller than t_{turb} but this would increase simulation time. Remedy to this problem was proposed by (O'Rouke, 1989), by choosing a random position and velocity from a probability distribution given in equation (45). This makes the problem to be independent of t_{turb} and there will always be one value of position and velocity.

For detailed mathematical formulation to calculate variance for the droplet velocity and position readers should refer to (O'Rouke, 1989) .This formulation is based on the linear drag law which allows the droplet's position and velocity changes to be treated as independent.

$$\sigma_{u'}{}^2 = \frac{1 - \exp\left[-D_p\, t_{turb}\right]}{1 + \exp\left[-D_p\, t_{turb}\right]}\sigma^2 \tag{49}$$

$$\sigma_{x'}{}^2 = \left[t_{turb}\,\Delta t - \frac{2t_{turb}}{D_p}\left(1 - \exp\left[-D_p\,\Delta t\right] + \frac{\sigma_{u'}{}^2}{\sigma^2 D_p{}^2}\right)\right]\sigma^2 \tag{50}$$

Once the drop positon and the velocity is obtained from the probability function then again quite simply the position and the velocity of the drop is updated like in case 1.

$$\frac{x_p^B - x_p^n}{\Delta t} = \mathbf{u}_p^n + \frac{\delta\, x'}{\Delta t} \tag{51}$$

$$\frac{\mathbf{u}_p^B - \mathbf{u}_p^n}{\Delta t} = D_p\left(\mathbf{u}_{ijk}^B + \mathbf{u}'\right) + \mathbf{g} + \frac{\delta\,\mathbf{u}'}{\Delta t} \tag{52}$$

An example of dispersion of droplets from (O'Rouke, 1989) is reproduced here to show the behaviour of this model.

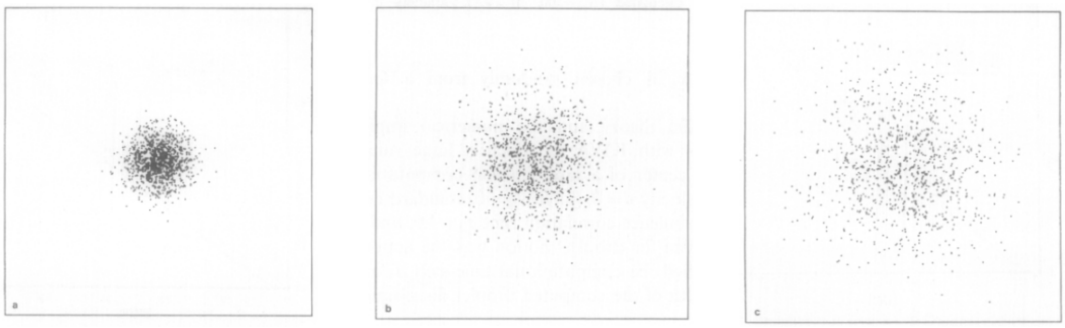

(a) *(b)* *(c)*

Figure 7: Calculated (N, = 1000, at = 0.1) drop positions at times (a) 10.0 (b) 30.0 (c) 50.0 (O'Rouke, 1989)

2.3.4 Droplet tracking model:

To account for the inter droplet collisions, trajectory model of (Macpherson, Nordin, & Weller, 2009) has been considered. To understand the working of this model, suppose a particle positioned at point '**a**' moves to point '**b**', as shown in Figure 8. The trajectory of the particle is such that it intersects two cells on its way to the final destination at point '**P**' and '**P'**' respectively. Now at every instant when a particle reaches the boundary of any cell then it needs to be treated as a separate segment. The distance from point '**a**' and point '**P**' is then calculated using

$$P = a + \lambda_a (b - a) \tag{53}$$

Every face of the grid cell can be used to judge a location of the particle on that face just by face centre 'C_f' along with a normal vector 'S'.

$$(P - C_f).S = 0 \tag{54}$$

By replacing the equation 1 in to equation 2 we get the value of λ_a

$$\lambda_a = \frac{(C_f - a).S}{(b - a).S} \tag{55}$$

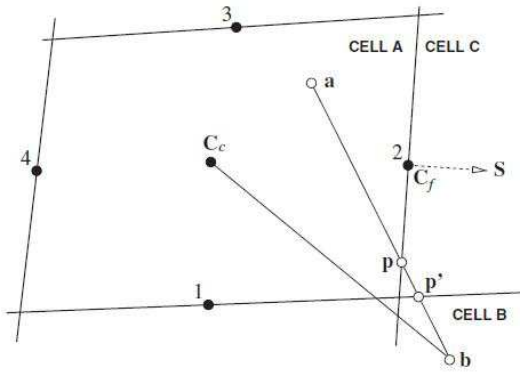

Figure 8: Motion of the particle with the face crossings (Macpherson, Nordin, & Weller, 2009)

There are usually few problems in particle tracking with this technique found mostly when the cell is non-planar. Thus the inclusion of the cell centres instead of the face centres in the calculations solves this problem (Macpherson, Nordin, & Weller, 2009). This model is unreliable in case of concave cells. It can go into an infinite loop if the particle enters in a domain with concave cells. Therefore, care must be taken in order to avoid this problem.

2.3.5 Droplet collision model:

This model utilizes the same concept of particle tracking in trajectory model. "*The collision between two particles occurs when their trajectories intersect and intersection point is reached at the same time and within the integration step*". (Nordin, 2001)

To avoid impossible collision a criterion is set for the particles to fulfil before they can collide. In order to have a collision the particles need to be travelling towards each other not away from one another.

$$\mathbf{U}_{align} = \boldsymbol{U}_{rel} \frac{(x_2 - x_1)}{|x_2 - x_1|} \tag{56}$$

where $\mathbf{U}_{rel} = (\mathbf{U}_2 - \mathbf{U}_1)$, is the relative velocity between the particles, x_2 and x_1 are the positions of the parcel. The distance between the two particles must be less than their relative displacement.

$$\mathbf{U}_{align}\Delta t > |x_2 - x_1| - (r_2 - r_1) \tag{57}$$

These two conditions are used to evaluate any possible collision. The collision takes place when random number $\zeta \in (0,1)$ is less than the probability $P_{collision}$.

$$P_{collision} = \left(\frac{r_2 + r_1}{max(r_2 + r_1, \Delta_{12})}\right)^{C_{space}} e^{\left(\frac{-C_{time}|\alpha_0 - \beta_0|}{\Delta t}\right)} \tag{58}$$

$\Delta_{12} = |p_2(\beta_0) - p_1(\alpha_0)|$, is the minimum distance between the two trajectories and p1 and p2 are the positions of the particles, α_0& β_0 are the constants, C_{space} & C_{time} are model constants related to spatial and temporal collision probability decay.

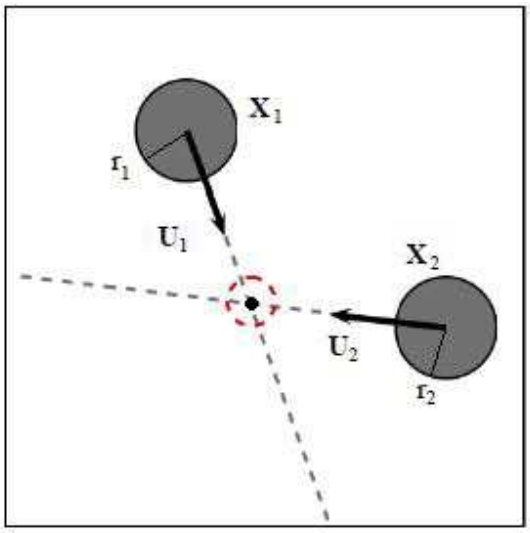

Figure 9: The particles collision (Nordin, 2001)

2.3.6 Evaporation and heat transfer models:

When a drop undergoes evaporation, the rate of change of mass, m_p of the drop is equal to the change in the volume of the drop.

$$\frac{dm_p}{dt} = \rho_p \frac{d}{dt}\left(\frac{4}{3}\pi\left(\frac{d_p}{2}\right)^3\right) \tag{59}$$

Further, the evaporation is assumed to follow a classical empirical $D^2 - \text{law}$ (Godsave, 1953; Spalding, 1953):

$$\frac{d}{dt}\left({d_p}^2\right) = C_e \tag{60}$$

where C_e is constant. From integration of above equation evaporation relaxation time (τ_e) is

$$\tau_e = \frac{{d_{p_i}}^2}{C_e} \tag{61}$$

The equation (59) is expressed as:

$$\frac{dm_p}{dt} = \rho_p \frac{\pi}{4} d_p C_e \tag{62}$$

Another way to express the time derivative of the mass of the droplet is presented by (Nordin, 2001):

$$\frac{dm_p}{dt} = -\pi d_p Sh\mathcal{D}\ \rho_v ln\left(\frac{p - p_{v,\infty}}{p - p_{v,s}}\right) \tag{63}$$

$$\frac{dm_p}{dt} = -\pi d_p Sh\ \mathcal{D}\rho_v ln\left(1 + \frac{X_{v,s} - X_{v,\infty}}{1 - X_{v,s}}\right) \tag{64}$$

where $\mathcal{D}$ is a mass diffusivity constant and ρ_v is the fuel vapour density. By equating equation (65) and (64) the coefficient C_e is determined very easily

$$C_e = -4Sh\mathcal{D}\ \frac{\rho_v}{\rho_p} ln\left(1 + \frac{X_{v,s} - X_{v,\infty}}{1 - X_{v,s}}\right) \tag{65}$$

The Sherwood number Sh is calculated using the Frössling correlation (Crowe, Sommerfeld, & Tsuji, 1998):

$$Sh = 2 + 0.6Re^{0.5}Sc^{0.333} \tag{66}$$

The equation (61) gives the evolution of droplet size characterized by the evaporation time scale (τ_e).

$$\tau_e = \frac{\rho_p {d_p}^2}{-4Sh\mathcal{D}\rho_v \, ln\left(1 + \frac{X_{v,s} - X_{v,\infty}}{1 - X_{v,s}}\right)} \tag{67}$$

Moreover heat transfer between the two phases can simply be obtained from the convection equation. The heat transfer relaxation time is:

$$\tau_h = \frac{\rho_l \, c_{pl} {d_p}^2}{6\kappa Nu} \tag{68}$$

where c_{pl} is the heat capacity of the liquid and Nu is the Nusselt number. Nu is obtained from the Ranz-Marshall Correlation (Ranz & Marshall, 1952)

$$Nu = 2 + 0.6 \, {Re_p}^{1/2} Pr^{1/3} \tag{69}$$

2.3 Conclusion:

This chapter mainly deals with the theoretical background of turbulence and spray modelling. The scales of turbulence from largest to the smallest are discussed along with their relationships. The spray modelling is based on Euler-Lagrange framework. The carrier phase is represented in the Eulerian framework, whereas, liquid phase is treated in the Lagrangian framework. The turbulence models of RANS and LES are also discussed in this chapter in a general way. The detailed explanation of the turbulence models will be given in the coming chapters.

The second part deals with spray modelling in detail. Spray injection model, which injects blobs of mean size of the order of injection hole and the variation of the blob size is controlled by the Rosin Rammler distribution. The droplet breakup model is Enhanced Taylor Breakup Model (ETAB) which estimates the droplet breakup into smaller drops in a similar way to classical Taylor Breakup Model (TAB) but with slight modifications in prediction of child drops. The droplet dispersion is modelled by the stochastic dispersion model, which is based on the eddy turn over time. Droplet tracking and collision model are achieved by the trajectory model which calculates the trajectory of the drops before the collision.

Chapter 3 Reynolds Average Navier Stokes Simulations

Typically a multi-hole GDI injector provides a more efficient way to inject the fuel. It reduces fuel injection timing, penetration and increases the fuel-air mixture quality with sufficient vapour homogeneity for better combustion in the engines provided that intended spray cone angle, desired spray plumes' path and optimum atomization of the droplets are achieved (Befrui, Corbinelli, D'Onofrio, & Varble, 2011). But in reality multi-hole GDI injectors are very complex in nature because of the several closely spaced spray plumes which are usually very unpredictable at high load conditions. This unpredictability of closely spaced spray plumes give rise to plume interactions also known as jet-to-jet interactions which, unless studied thoroughly, can prove to be a weak link for these types of injectors. At high load conditions it becomes very difficult to keep the intended spray targeting in the engine. Moreover under superheated conditions the jet-to-jet interactions appear to be uncontrollable and can cause whole spray cone to just collapse.

Multi-hole GDI injectors are studied in (Rotondi, Hélie, Leger, & Wigley, 2010) regarding spray plume angle variations and droplet sizing. The effects of gas entrainment on the mixture formation of GDI hollow cone injector under various injection pressures are highlighted experimentally using PIV (Particle Image Velocimetry) in (Prosperi, Helie, & Bazile, 2007). Another interesting experimental investigation using PIV is done on the air entrainment variations induced by the injection fluctuations in (Delay, Bazile, Charnay, & Nuglisch, 2004). A numerical and experimental analysis on GDI annular orifice spray shows the effect of air entrainment on the spray structure (Seibel, Gartung, Arndt, & Weigand, 2003). Multi-hole evaporating sprays are studied in (Skogsberg, Dahlander, Lindgren, & Denbratt, 2005) which show the air entrainment and vapour accumulation inside the spray cone experimentally but it does not explain the phenomena of air entrainment and its effects on the spray behaviour.

A thorough investigation of such complex phenomena, which often occur in GDI injectors, is performed both experimentally and numerically. Experimental PDA measurements of droplets sizes are carried out in Loughborough University under cold conditions for 3 holes injector only. Whereas PIV air entrainment fields are captured experimentally at IFPEN for both 3 and 6 holes injectors in hot conditions. The experimental setups of PDA and PIV are well explained in in Appendix A. RANS approach is utilized for the simulation of the 3 hole and 6 hole injector which highlights many interesting points regarding spray plume interactions which cannot be observed in the experiments.

3.1 Turbulence Model:

Standard K-epsilon turbulence model (Launder & Spalding, 1972) solves two transport equations, one for the turbulent kinetic energy (k) derived from the exact equation and one for the dissipation rate (ε) obtained more by the interpretation of physical laws rather than any mathematical equation. The equation for the turbulent kinetic energy and the dissipation rate are presented in equations (70) and (71).

$$\frac{\partial \rho k}{\partial t} + \frac{\partial \rho \bar{u}_i k}{\partial x_j} = \frac{\partial}{\partial x_j}\left[\left(\mu + \frac{\mu_t}{\sigma_k}\right)\frac{\partial k}{\partial x_j}\right] + G - \frac{2}{3}\rho k \delta_{ij}\frac{\partial \bar{u}_i}{\partial x_j} - \rho\varepsilon \tag{70}$$

$$\frac{\partial \rho \varepsilon}{\partial t} + \frac{\partial \rho \bar{u}_i \varepsilon}{\partial x_j} - \frac{\partial}{\partial x_j}\left[\left(\mu + \frac{\mu_t}{\sigma_\varepsilon}\right)\frac{\partial \varepsilon}{\partial x_j}\right] = \frac{C_1 \varepsilon}{k} G - \left[\left(\frac{2}{3}C_1 - C_3\right)\rho\varepsilon\delta_{ij}\frac{\partial \bar{u}_i}{\partial x_j}\right] - C_2 \rho \frac{\varepsilon^2}{k} \tag{71}$$

where $\sigma_k = 1, \sigma_\varepsilon = 1.3,\ C_1 = 1.44, C_2 = 1.92, C_3 = -0.33$ and $G = \mu_t\left(\frac{\partial \bar{u}_i}{\partial x_j} + \frac{\partial \bar{u}_j}{\partial x_i}\right)\frac{\partial \bar{u}_i}{\partial x_j}$. The turbulent viscosity (μ_t) is defined as:

$$\mu_t = \frac{\rho C_\mu k^2}{\varepsilon} \tag{72}$$

C_μ is also a constant and usually its value is 0.09. To avoid dividing by k=0, the values of k and ε are bounded to minimum values $(k \geq k_{min})$ and $(\varepsilon \geq \varepsilon_{min})$ respectively.

3.2 Numerical setup and Operational conditions:

The simulation set up used for all the RANS calculations is presented in this section

3.2.1 Numerical solver:

The Reynolds Average Navier Stokes (RANS) simulations are performed on OpenFOAM ® (Weller, Tabor, Jasak, & Fureby, 1998) version 1.7.1, where the gaseous phase is modelled by the standard K-Epsilon approach and the liquid phase is modelled by the Lagrangian approach. A pseudo-compressible variable density spray solver is used. The solver does not include the density balance equation of $D\rho/Dt = 0$ and it does not capture any acoustic waves. It is based on the standard "dieselFoam" solver along with automatic mesh refinement (AMR) of "interDyMFoam". This solver is implemented in OpenFOAM ® with the help of (Kosters, 2010) which gives the solver a capability of AMR.

3.2.2 Numerical schemes:

Pressure velocity coupling of the carrier phase is achieved by PISO (pressure implicit with splitting off operators) like algorithm (Demirdžić, Lilek, & Perić, 1993) with two loop iterations PISO loop for the predictor correction. A second order setup for the space discretisation and first order setup for time discretisation is utilized. Gauss limited linear scheme is a second order bounded scheme which is utilized for the convective operators. Gauss linear corrected scheme, a second order unbounded conservative scheme, is used for diffusion operators. Euler Implicit scheme which is first order accurate in time and is dependent on the courant number for the stability is used. All the numerical schemes are described in the appendix C.

Automatic time step adjustment is also included to keep local courant number to be less than 0.5 with initial time step of 10^{-7} sec. Preconditioned bi-conjugate gradient method (Hestens & Stiefel, 1952) with Diagonal incomplete-Cholesky (symmetric) preconditioner (DIC) for pressure equation and

Diagonal incomplete-LU (asymmetric) for the equations of the rest of the quantities like velocity, kinetic energy etc are used with a local accuracy of 10^{-7} at every time step.

3.2.3 Two phase numerics:

In spray simulations, the number of drops can range from few thousands to several millions (Apte, Mahesh, Gorokhovski, & Moin, 2009). Therefore, it would become almost impossible to track the trajectory of each drop in the computational domain. A remedy to this problem was proposed by the (O'Rourke & Bracco, 1980) by introducing "discrete-parcel model" to represent drops in the sprays. In this approach a group of droplets with similar characteristics of diameter, velocity and temperature are represented by a parcel. This makes the computation easier to be managed, since, instead of tracking a single drop a group of drops are tracked at once.

A lagrangian time step is defined per parcel on the basis of the time taken by the particle to leave the cell it resided in. Therefore, a lagrangian sub-iteration time loop can occur. The gas velocity, acceleration and vorticity calculated in the eulerian frame are interpolated to the lagrangian frame in order to calculate the drag force on the particle which will eventually allows computing the particle velocity and position. A linear interpolation scheme which is based on second order central differencing scheme is utilized. Two different ways to evaluate the gaseous properties at the parcel position are used. Cell-to-Point-to-Face interpolation scheme interpolates the gas velocity at the particle position. The gaseous velocity is first interpolated to the nodes of the cell and then to face-centres and the tetrahedral used for interpolation will consist of cell-centre, face-centre and two cell nodes.

3.2.4 Computational domain:

A computational domain of size 112mm x 112mm x 112mm with an initial cell size of 1.5mm is used for the simulations with a mesh refinement interval of 2 and maximum cell limit of 5 million. The initial cell size after being refined twice reduces to a minimum cell size of 0.375mm. Maximum limit of cells ensures the cell size doesn't increase beyond the computational resources. AMR is based on the scalar fields of kinetic energy and vapour mass fraction for non-evaporating and evaporating conditions, respectively.

3.2.5 Injector Design:

In the current work two of the Continental's XL3 multi-hole injectors with 3 holes and 6 holes are used. A diagram in the Figure 10 highlights the important design parameters of a multi-hole injector. All the design parameters for 3-hole and 6-hole injector are presented in the Table 2, where β denotes the angle of injection from the central axis of the injector. L_i is length of the injection hole and D_i is the diameter of the injection hole. The ratio of L_i/D_i is a very important parameter of a GDI injector's design because it influences the organization of the internal flow at the exit of the injection hole and eventually affects the spray formation (Dahlander & Lindgren, 2009). In GDI injectors usually L_i/D_i ratio of unity is used. It should be noted here that the injection hole length is not required in the lagrangian simulation. Qs denotes the static Mass flow rate of a given injector at 100bar (10MPa) injection pressure with n-Heptane.

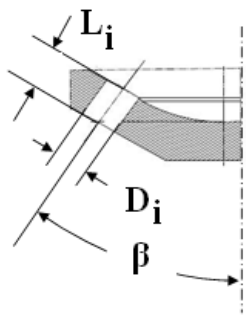

Figure 10: Injector design

XL3 Injector	β	L_i/D_i (mm)	Qs (g/s)
3-hole	38°	L/Di = 0.221 / 0.200 =1.1	5.7
6-hole	23°	L/Di = 0.224 / 0.200 =1.1	11.4

Table 2: Injector design parameters

3.2.6 Mass flow rate profile:

Mass flow rate profiles under non-evaporating conditions for six hole injector at 100bar (10MPa) and 200bar (20MPa) is presented in Figure 11.

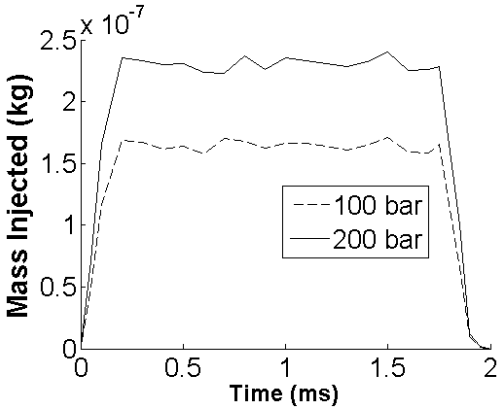

Figure 11: Mass Flow Rate Profile of the injector at 100 and 200 Bar Injection Pressure for 6-hole injector

3.2.7 Operating conditions:

The operating conditions for both the XL3 3-hole 90° cone angle (CA) and XL3 6-hole 60° CA injectors are presented in the table below:

Conditions and Experiment type	Injectors	Injection Pressure (P_i) (bar)	Fuel Temperature (T_f) (°C)	Chamber Pressure (P_c) (bar)	Chamber Temperature (T_c) (°C)	Injection Duration (ms)	Total Injected Mass (mg)	Fuel Type
Non-evaporating-PDA	3-hole	100	20	1	20	2.0	15	Gasoline
Evaporating-PIV	3-hole	200	90	1.54	33	3.32	24.9	Iso-Octane
Evaporating-PIV	6-hole	200	90	1.54	33	3.387	49.8	Iso-Octane

Table 3: Operating conditions of experiments (PDA and PIV) and Simulations

3.3 Results & Discussion:

3.3.1 Basic validations:

Some of the basic validations of simulations of the 3-hole and 6-hole injectors are presented under non-evaporating and evaporating conditions.

3.3.1.1 Non-evaporating conditions:

The simulation results of droplet size distributions of 3-hole injectors are compared with experimental PDA results, under non-evaporating conditions presented in the Table 3. The plot in Figure 12 (a) shows a comparison between the simulation and experimental results for the average droplets size (D_{10}) at different axial locations at the centre of a single plume for a time interval of 1.6ms to 2ms. The mean droplet sizes at 10mm downstream location at the centre of the plumes are 7.55µm and 7.43µm for the experiment and simulation, respectively. The mean droplet size reduces to 5.89µm at 40mm location in the experiments whereas in simulation it is 6.55µm in Figure 12 (b). The Probability Density Function (PDF) of droplet size distribution, at 40mm downstream location at the centre of a single separated plume, also shows a good agreement. The experimental and numerical drop size distributions are compared with two standard particle distribution functions commonly found in the literature, namely log normal and Rosin Rammler distribution functions.

The log normal distribution function (Johnson, Kotz, & Balakrishnan, 1994) is defined by:

$$pdf = \frac{1}{d_p S_{td}\sqrt{2\pi}} e^{-\left[\frac{\left(ln(d_p)-M_n\right)^2}{2{S_{td}}^2}\right]} \tag{73}$$

where M_n is the mean and S_{td} is the standard diviation, which were adjusted empirically in order to fit the experimental and numerical data in the best possible way. The values were M_n and S_{td} are chosen to be 1.85 and 0.5 respectively.

The Rosin Rammler distribution defined here contains the same variables as in equation (35) which used at the injection input, but it is formulated slightly differently:

$$pdf = q\langle d_p\rangle^{-q} {d_p}^{q-1} e^{-\left(\frac{d_p}{\langle d_p\rangle}\right)^q} \tag{74}$$

here the mean diameter $\langle d_p\rangle$ is set to be 6.5 and spread factor q of 2.2.

Both of the distribution functions fit reasonably well with the experimental and numerical data, however, both of the functions are not perfect. Log normal distribution function misses the small drops but captures most of the larger drops. On the contrary Rosin Rammler profile captures the small drops very well but fails to capture some of the larger drops. Therefore both of these distribution functions can be very useful in comparison of the drop distribution at various downstream locations. Log normal distribution function could be a better choice in near injection regions where the probability of the larger drops would be certainly higher than smaller drops. Whereas, Rosin Ramler distribution function could be useful in downstream locations were the drop sizes tend to be smaller due to the droplet breakup and evaporation.

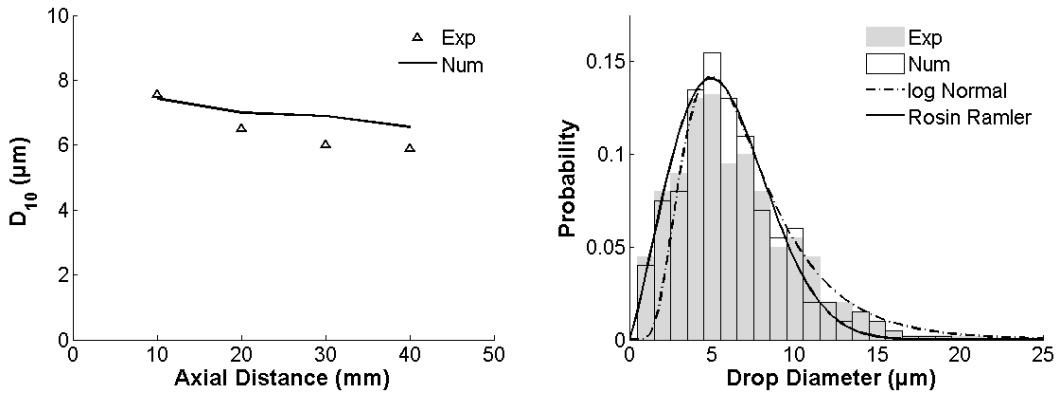

(a) *(b)*

Figure 12: Experimental and simulation results of 3-hole injector; (a) Mean droplet diameter (D_{10}) at different axial locations ,(b) PDF of droplet distribution at 40mm axial location

3.3.1.2 Evaporating conditions:

Some of basic validations of simulation results against the experimental data, regarding the air entrainment in the spray, under evaporation conditions, listed in the Table 3, are presented in this section.

3.3.1.2.1 Axial liquid penetration of the spray:

Axial liquid penetration rates of the spray are compared for both the 3-hole and 6-hole injectors experimentally and numerically under evaporating conditions presented in Table 3. The results in Figure 13 reveal that both injectors have similar penetration rates despite the fact that the nominal nozzle geometries differ significantly between the two injectors. The numerical prediction of the global spray penetration is comparable with the experimental data. A delay of 400µs is observed for the experiments between the electrical start (injector trigger) and the physical start of injection (first appearance of liquid at the nozzle exit). This delay incorporates the electrical delay (solenoid activation) and hydraulic delay (internal nozzle fluid flow). This delay is also included in the simulations to have the same starting time of fuel injection.

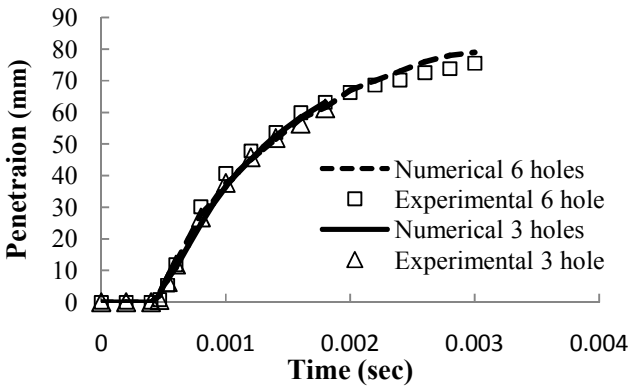

Figure 13: Comparison of penetration curves under evaporating conditions for 3-hole and 6-hole injectors

3.3.1.2.2 Air entrainment between the two jets:

A comparison of the 2D flow fields, measured experimentally and simulated numerically, under the evaporating conditions has been presented below. The air entrainment characteristics for the 3-hole and 6-hole injectors are shown in Figure 14 on top and bottom respectively, at a time 1.4ms *After Start Of Injection* (ASOI). In both cases the numerical results show satisfactory agreement with the experimental data. The air entrainment is relatively high in the near nozzle region and at the spray tip leading edge as a result of the high spray momentum for both the 3 and 6-hole injectors.

On the contrary to the 3-hole case, the 6-hole injector reveals a specific structure. Experimental measurements show that the spray cone collapses compared to the 3-hole injector. The spray cone collapse is believed to be linked to the more significant jet-jet interactions: the air entrainment due to momentum transferred from droplets to air in a given plume is affected by air entrainment into neighbouring plume. This may modify the spray structure and dynamics. Unfortunately PIV data could not be acquired in the inter-jet spacing for the 6-hole injector due to spray collapse and the resulting formation of what appears to be a continuous spray plume. The air entrainment, in between the jets, is discussed in more detail in the next sections. The resulting difference between the experimental and computational results as shown on Figure 14 (a, d) does not exceed 2.5m/s and mostly the error appears to be local or linked to the main direction of the flow more than the absolute value i.e. the error vectors are mainly perpendicular to the main direction from experimental.

The error, as shown is Figure 14 (c, f), remains low (less than 2.5m/s). Usually the error seems to be local, or linked to the main direction more than the absolute value (the error vectors are mainly perpendicular to the main direction from experimental).

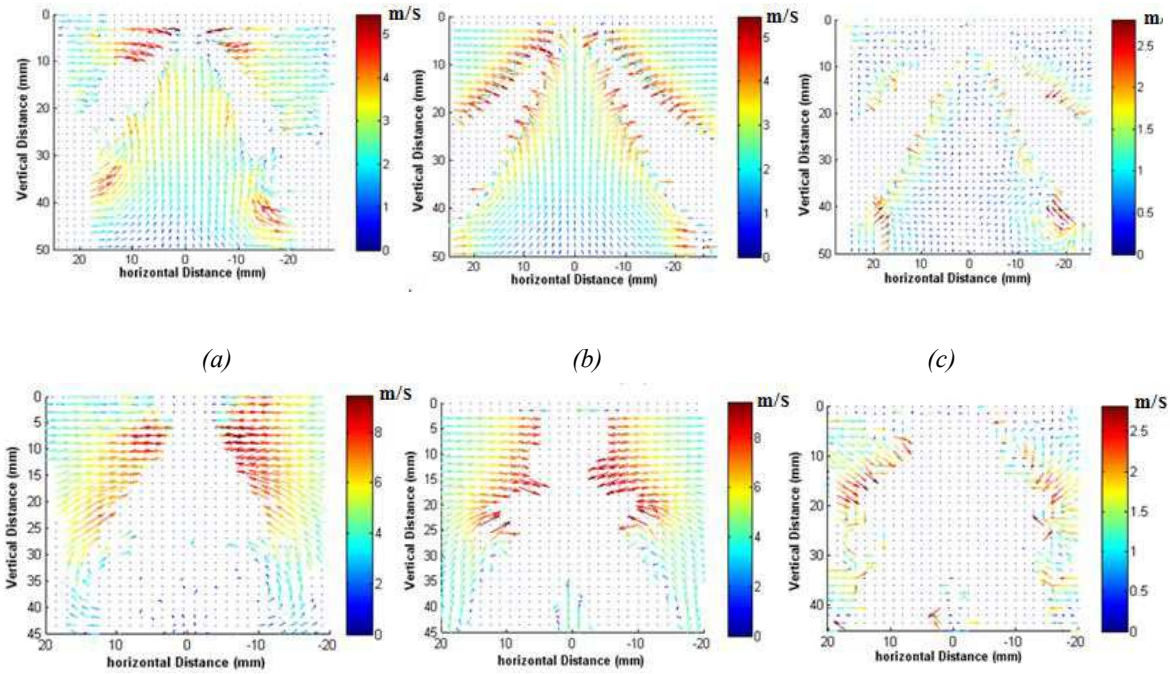

(a) *(b)* *(c)*

(d) *(e)* *(f)*

Figure 14: 2D vector flow fields showing air entrainment at 1.4ms ASOI for the 3-hole injector (a) Experimental (b), Simulation (c), Difference between Experimental & Simulated results; and for the 6-hole injector (d) Experimental (e), Simulation (f), Difference between Experimental & Simulated results

3.3.2 Jet-to-jet interactions:

Jet-to-jet interactions can be significant for multi-hole injectors and as a result have an effect on the global spray structure. The simulation results obtained for the 6-hole injector under the evaporating conditions presented in Table 3, reveals the presence of what appear to be jet-to-jet interactions causing a modification in terms of the trajectory of the individual spray plumes as shown in Figure 15. In contrast, the spray plumes are well separated in the case of the 3-hole injector. Moreover the 6-hole injector reveals a continuous spray structure, due to the presence of droplets and it becomes difficult to identify individual plumes. One would expect that significant interactions occur between adjacent jets, modifying the air entrainment and subsequently the fuel-air mixture distribution. Such aspects are studied in more detail by analysing the results of numerical simulations.

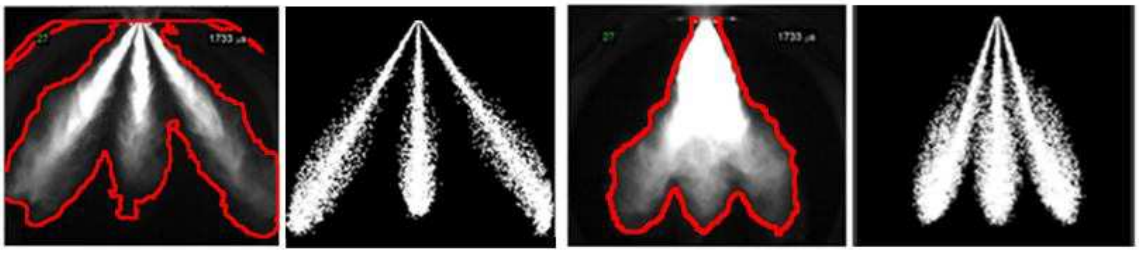

(a) (b) (c) (d)

Figure 15: Liquid phase spray images of the sprays under evaporating conditions at 1.75ms ASOI; (a) Experimental result (high-speed Mie scattering) of 3-hole injector (b) Simulation result of 3-hole injector (c) experimental result (high-speed Mie scattering) of 6-hole injector (d) Simulation result of 6-hole injector

3.3.2.1 Spatial evolution of vapour phase:

The simulation results of the vapour phase of 6-hole injector under evaporating conditions provide further insight to the process involved in the spray propagation, structure and mixture formation. A sequence of images containing various cross-sectional planes of the vapour mass fraction along the axial direction of the spray plumes is presented below in Figure 16 and Figure 17, at time steps of 1.75ms ASOI and 3.10ms ASOI. The cross-sections near the nozzle spray region reveal a star shape of the spray plumes which are well separated from one another. The images also divulge vapour phase fuel in the central region of the spray. Moving further downstream the vapour phase fuel surrounding the plumes tends to merge into one other. At this point the star shape transforms into a closed ring structure and the spray reveals a hollow cone spray structure. It is at this stage where the spray plumes tend to deflect resulting in a notable change in spray angle. This process takes places throughout the spray propagation. In order to better understand the observed behaviour, an analysis of the air entrainment characteristics has been performed.

	Time = 1.75ms	Time = 3.10ms	
Vertical Cross-section (x-z)	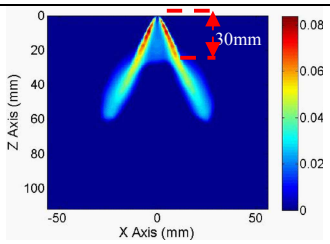	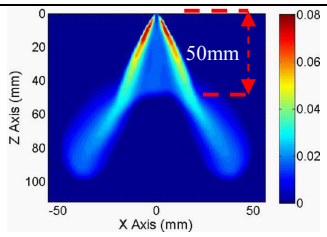	Distance from nozzle tip (mm)
Traverse cross-section (x-y)	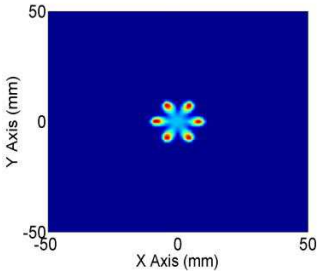	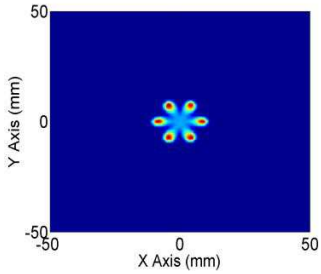	20
	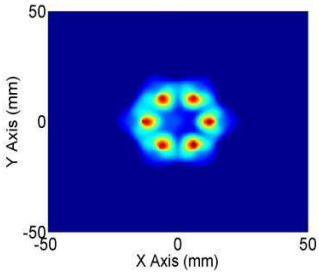	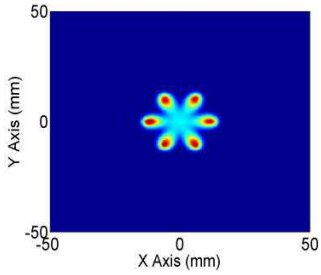	30

(a) *(b)*

Figure 16: Simulation results of fuel vapour mass fraction at (a) 1.75ms ASOI and (b) 3.1ms ASOI (Part1)

	Time = 1.75ms	Time = 3.10ms	
	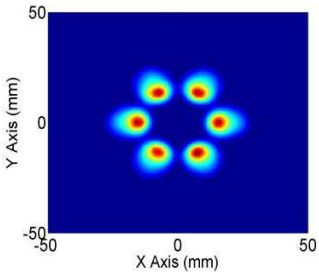	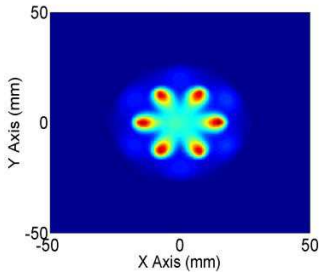	40
	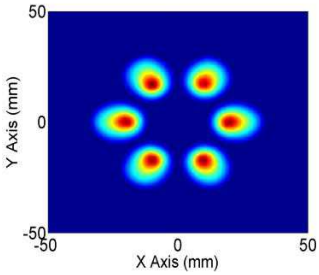	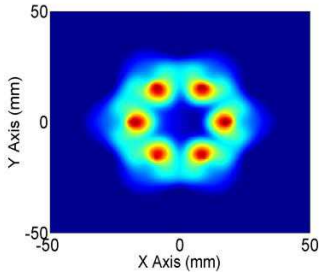	50
		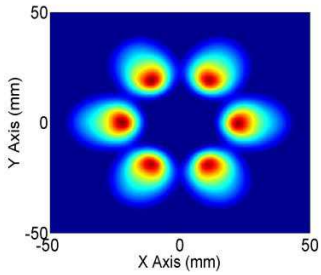	60
		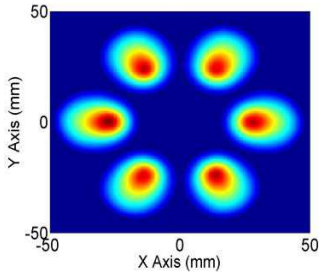	70

(a) *(b)*

Figure 17: Simulation results of fuel vapour mass fraction at (a) 1.75ms ASOI and (b) 3.1ms ASOI;(Part 2)

3.3.2.2 Axial gas velocity:

For a typical case of a single spray plume, a large-scale head vortex is formed by the high-speed spray. In the upper part of spray, this may induce a strong air entrainment (air sucked from the outer region), while in the bottom part of spray, droplets which are behind the spray tip, move in the sheared outwards directed radial flow. Consequently, such droplets are dispersed radially along with spray penetration in the downstream direction. Considering the multi-hole case, the large-scale vortical structures stem from interaction with each spray plume; every spray plume is subject to such a collective flow, whence interaction between plumes takes place. The gas entrainment between two adjacent plumes (vertical cross-sections (x-z)) of 6-hole injector at 1.75ms and 3.10ms ASOI is presented in Figure 18. Typically gas entrainment into the spray plumes can be divided into two sections: (i) air sucked into the near nozzle region; (ii) gas (air and vapour) pushed downwards in the direction of the spray tip penetration (Prosperi, Helie, & Bazile, 2007; M, P, R, & Denbratt, 2005). These two phenomena can be observed in Figure 18 with vapour being sucked in towards the injector tip and pushed out at the spray.

The gas between the two jets is pushed downwards in the upper half of the spray cone (close to the injector tip). This is usually not observed in the sprays with spatially well separated plumes and wide cone angles as is the case of 3-hole injector. The internal downward gas flow in the upper half of the spray cone encounters an inverse flow, originating from each tip of plumes, which may be referred to as internal air entrainment. Two flows shear each other at 30mm at 1.75ms ASOI and 50mm at 3.10ms ASOI, forming a stagnation plane. Consequently a high radial flow toward the external side can be observed in Figure 18. This radial flow contributes to the spray plumes deviation from their original paths, with a noticeable change in the angles; thereby plumes are separated from each other which can also be observed in Figure 16 and Figure 17.

Moreover a second difference observed in the 6-hole spray compared to 3-hole spray is on bottom half part of the spray cone (far away from the injector needle). Here the spray tip recirculation area is strongly reduced in its central part. This reduction is approximately compensated by an increased recirculation area on the external side. This asymmetry external/internal is observed when the jet plumes are widely separated.

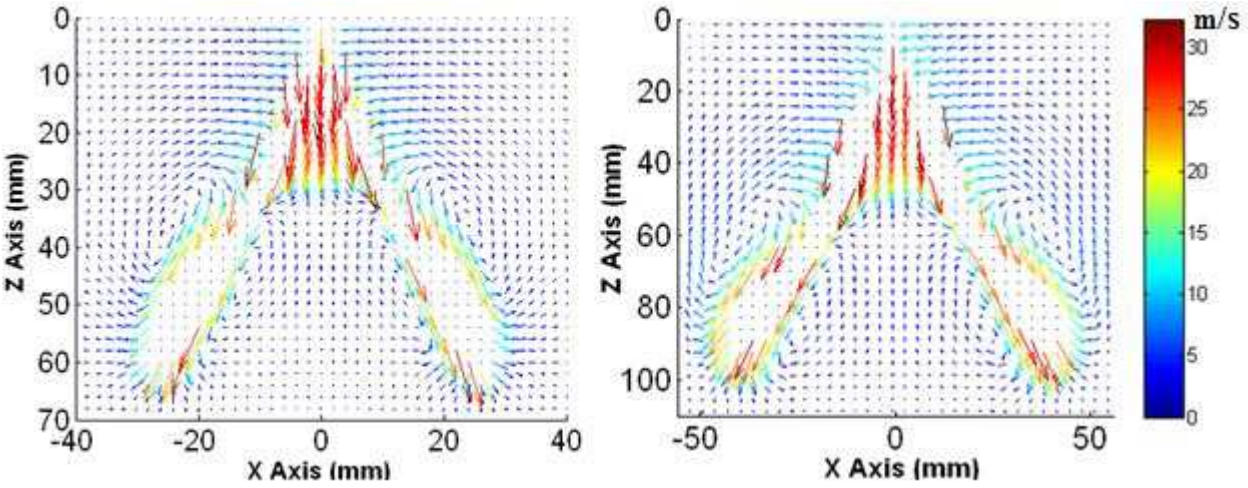

(a) *(b)*

Figure 18: 2D velocity vector plots of simulated air and gas entrainment; (a) 1.75ms ASOI, (b) 3.10ms ASOI

3.3.2.3 Comparison of spray angles:

A modification of the global spray angle is observed experimentally from high-speed spray imaging performed in the high pressure and high temperature (HPHT) chamber at IFPEN on the XL3 6-hole 60° CA injector. The simulation and experimental data is shown in Figure 19 (a) and (b) respectively, for this particular case. The spray cone can be divided into two regions corresponding firstly, to a close-up, near nozzle zone and secondly, to a downstream region where one observes a modification of the spray angle as shown in Figure 19 (a). The angles are measured by capturing images of the simulated spray in the x-z plane. These spray images at two time steps corresponding to 1.75 and 3.10ms ASOI are analysed by "imageJ" software (Abramoff, Magalhaes, & Ram, 2004) which is a simple java based image processing. The angle of the near nozzle zone (α_c) at 1.75ms and at 3.10ms ASOI is approximately 42°.

These near nozzle angles in Table 4 suggest that the measured spray cone angle is in fact narrower than the nominal cone angle of 60°. The near angles are measured from plume centre to plume centre which implies that taking account of the half plume angle (6°) of each of the two spray plumes, the total cone angle will be approximately 54°. A difference of approximately 6° between the nominal angle and the measured, near nozzle angle indicates the spray partially collapse in the close up

(upper) region. In the downstream zone of the spray, at 1.75ms ASOI, the deflected spray angle (α_d) is approximately 48° which increases to 51° at 3.10ms ASOI.

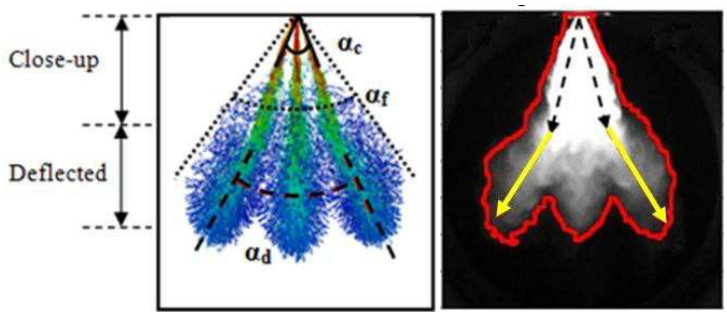

(a) *(b)*

Figure 19: Comparison of spray plumes at 1.8ms ASOI; (a) Simulation result (b), experimental result

The spray cone is thus deflected by 6 ° and 9 ° at 1.75ms and 3.10ms ASOI respectively. Although the spray far cone angles (α_f) of both experimental and numerical results show a good agreement, the spray plumes manifest two different angles, near and far from the injector nozzle. That means the overall spray cone angle is not a pure indicator of the spray directions when there are strong jet-to-jet interactions.

Time (ms)	**Simulated Close up Angle (α_c)**	**Simulated Deflected Part Angle (α_d)**	**Simulated Far cone angle (α_f)**	**Experimental Far cone angle (α_f)**
1.75	42°	48°	66°	65°
3.10	42°	51°	65°	65°

Table 4: Angles of close-up and deflected part of the spray at time 1.75ms and 3.10ms

3.3.2.4 Radial gas velocity:

Horizontal planes of radial velocity vector plots of air entrainment at different axial locations at 3.10ms ASOI are shown in Figure 20. The complex and interesting flow structures, which are different from one axial section to another, are also observed. The upper part of the spray is characterized by the strong air-entrainment towards the spray which is clearly seen until 40mm downstream. Simultaneously, by the radial spreading of injected high-speed droplets, the air is pushed out in radial direction. Similar to planar jet flow, this contributes to air entrainment in

between plumes of spray. As to further downstream sections, the radial outwards motion can be observed due to counter-flow shearing, between pushed downstream gas (by upper dense core of the spray) and internal air-entrainment induced by leading region of each plume. Such radial flow is relatively larger than the air entrainment from outside the spray cone. This causes the spray to bend from their original path.

It is seen in the Figure 20 (bottom jet-to-jet) that at 50mm downstream there is a ring of gas pushing outwards produced by the interactions of opposite gas velocity in the core of spray cone. As expected, at 70mm downstream position the radial velocity is a projection of the air entrained in the spray, with a large external recirculation around the jets.

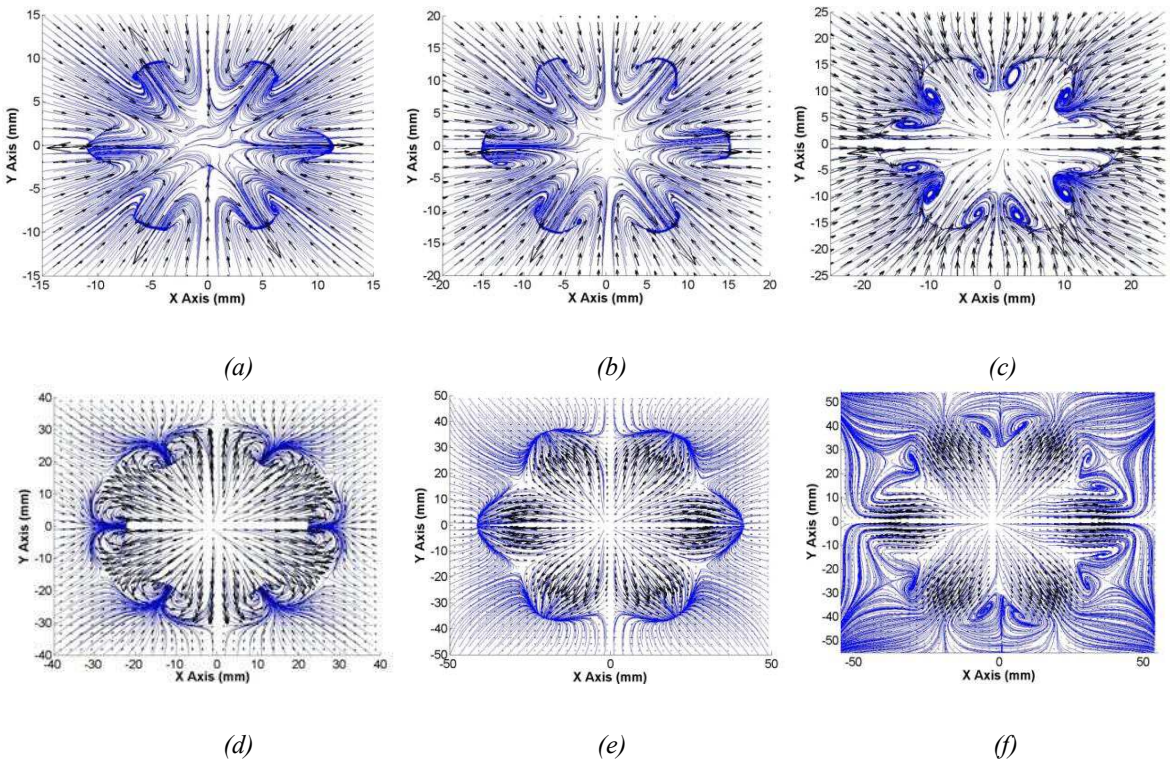

Figure 20: Radial velocity vector plot of the simulated air entrainments at 3.10ms ASOI at downstream locations; (a) 20mm (b) 30mm (c) 40mm (d) 50mm (e), 60mm (f), 70mm

3.3.2.5 Flux Balance:

The total air flux entering the spray cone cannot immediately be entrained back in the spray plumes at the inner side. Large part of the air entrained is pushed down until the stagnation plane is

approached. Air flux balance can indicate the percentage of air, which is immediately entrained by the plumes and which cannot be entrained in the plumes. A schematic of the control volume which is considered at the location where the deflection of spray cone occurs is presented in Figure 21. There are three main fluxes in the control volume: (1) Air coming from the centre of spray cone and from outside the spray cone (2) Air entrained by the spray plumes (3) air which could not be entrained and is pushed instead. The Figure 22 reveals that 60% of the air flux could not be entrained by the spray plumes.

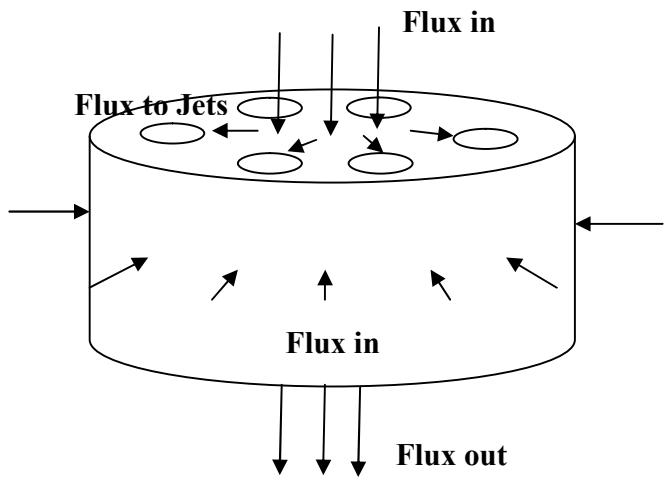

Figure 21: Schematic of Air entrainment in a control volume

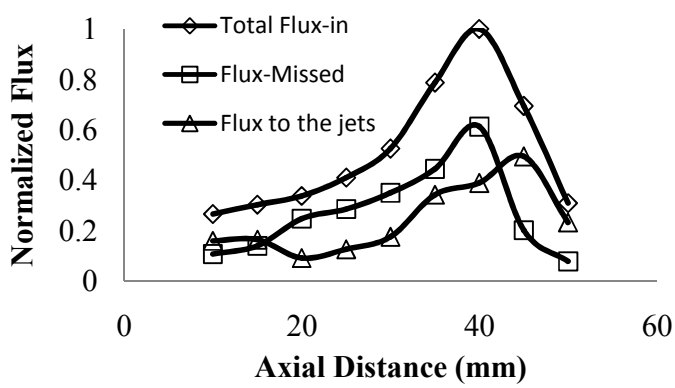

Figure 22: Air flux balance in the control volume

3.4 Flash Boiling:

Flash boiling occurs when a pressurised upstream superheated fuel is injected into a downstream domain with low surrounding pressure. A phase change occurs due to temperature variation which is limited by the heat transfer characteristic time. On the contrary, pressure drop depends on the geometrical and flow conditions and also on elevated speed of sound as presented in phase change diagram in Figure 23. The surrounding conditions quickly evolve to superheating conditions B'. As noticed by (Schmidt, Cavitation in diesel fuel injector nozzles, 1997), the thermodynamics of the phase change process can be not at equilibrium.

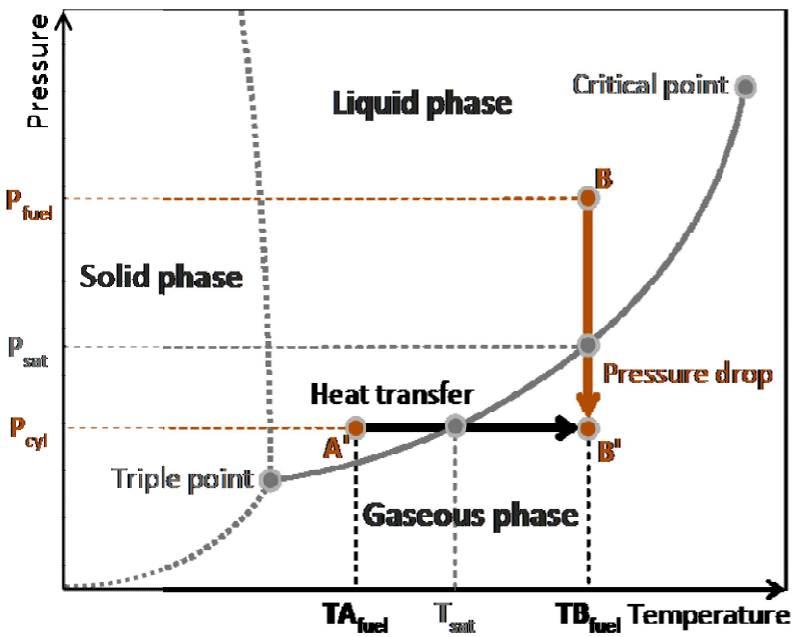

Figure 23: Phase change diagram

Whatever the complexity of this evolution, in this process a part of the fuel is converted to vapour forming bubbles in the liquid (Lin, Storey, & Szeri, 2002). These bubbles grow quite quickly and then eventually explode. The explosions of the bubbles within the liquid fuel cause rapid atomization of the fuel along with sudden radial expansion of the spray as shown in Figure 24 (a).

A detailed study has been performed in the past regarding the atomization enhancement in the flashing sprays compared to non flashing sprays (Suma & Koizumi, 1977; Reitz, 1990; Park & Lee,

1994; Sher, Bar Kohany, & Rashkovan, 2008; She, 2010). Regarding the atomization and vaporization under flash boiling conditions, ratio of ambient to saturation pressure or temperature are used as the main dimensionless numbers governing the flash boiling intensity (Zeng, Xu, Zhang, Zhang, & Cleary, 2012). However, a general and complete understanding for high pressure atomizing flash-boiling spray still lacks.

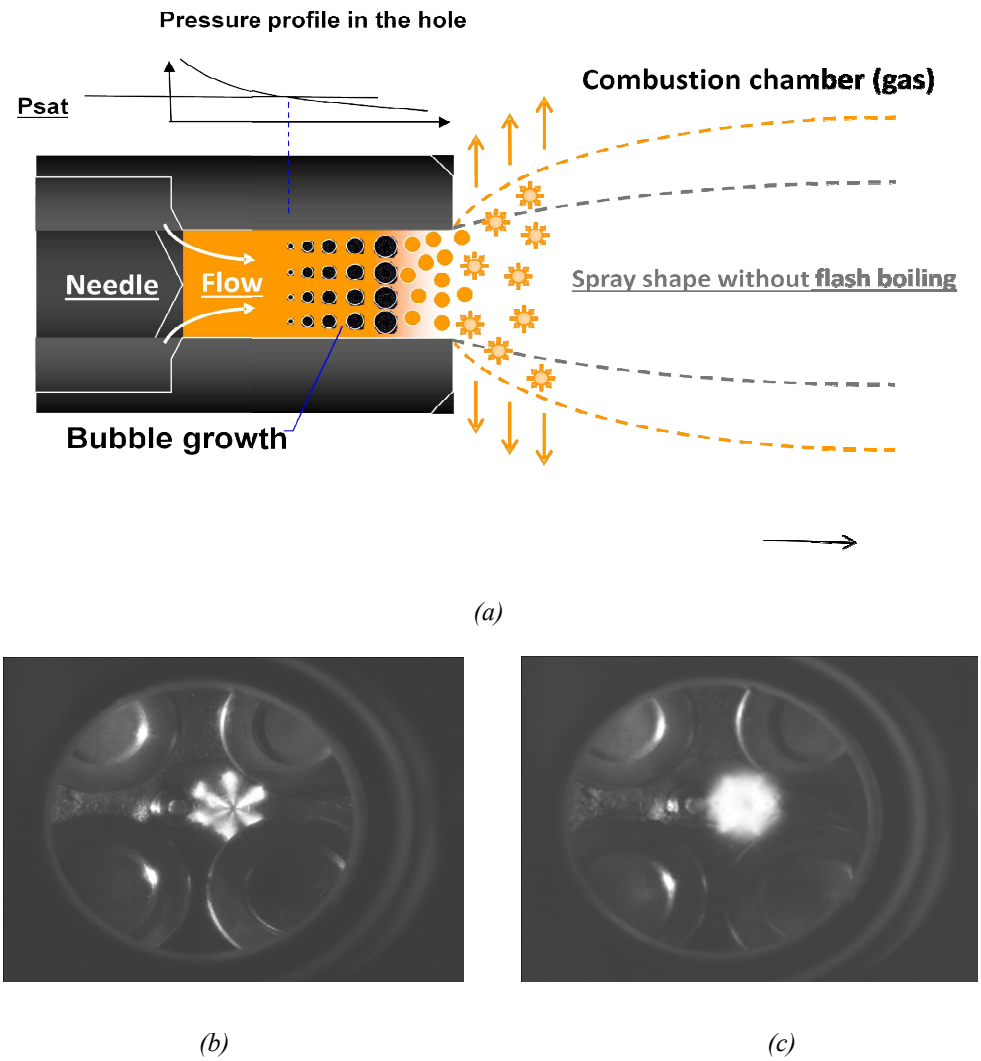

Figure 24: So-called "Flash boiling" process for atomizing superheated flow. (a): A schematic view; in-engine visualisation in Lotus engine in Loughborough University (b) wide open throttle (c): 2.7bar Indicated Mean Effective Pressure

In engines, flash-boiling can improve in general the performance of the atomizer by decreasing drop size, increasing overall liquid dispersion, and enhancing evaporation; and linked to this by reducing the penetration of the liquid Figure 24 (b & c).

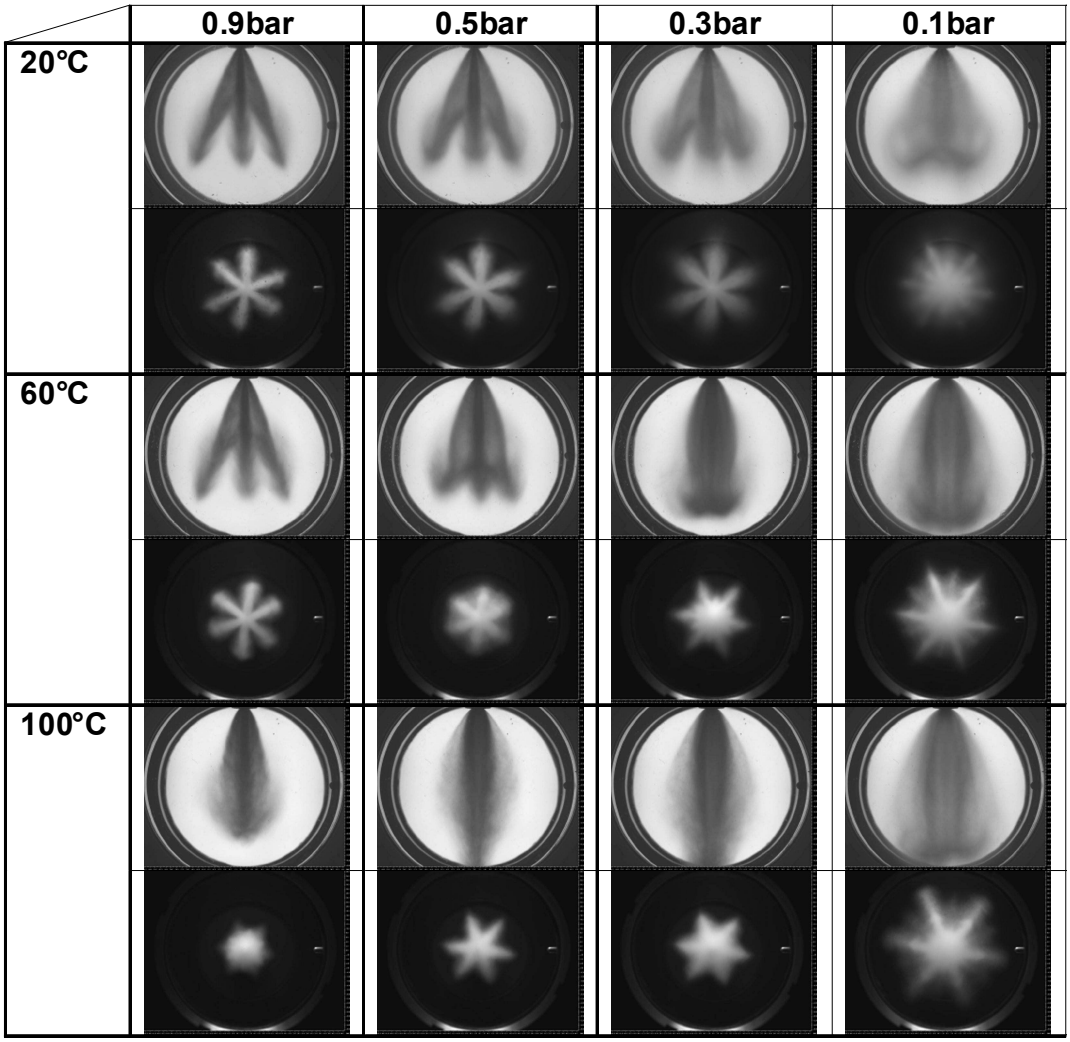

Figure 25: Observed change in the spray shape with a 6 holes and different chamber pressures, 60 deg nominal spray plume angle at 100bar, Tops: side view by shadowgraphy. Bottoms: bottom view by Mie scattering. (Mojtabi, Chadwick, Wigley, & Helie, 2008; Mojtabi, 2011)

The shadowgraphy and Mie images in Figure 25 of the spray from 6-hole injector under flash-boiling conditions exhibits: (Mojtabi, 2011; Wood, Wigley, & Helie, 2013)

- For ambient pressure below the saturation pressure, no effects (enhanced evaporation only).
- For moderate superheating, wide injection angle and enhanced evaporation. (Zhang, Xu, Zhang, & Zhang, 2010) have also highlighted swift atomization process and the large radial expansion of the multi-hole sprays.

- Strong change in the spray shape, with possible collapse: the spray plumes interact massively and eventually collapse to form thick fog of drops with reduced angle.
- In between the plumes, liquid re-appears, clearly visible on the Mie imaging (bottom views)
- Later in penetration, the final spray shape and penetration distance depend on the spray collapse and on the evaporation (from the available enthalpy).

Considering modelling and simulation, there are less number of studies performed regarding the modelling of spray near the injection nozzle for recent high pressure geometries, except (Schmidt, Cavitation in diesel fuel injector nozzles, 1997; Negro, Brusiani, & Bianchi, 2011). An improvement in the atomization modelling of the spray in swirl injector under flash boiling conditions has also been reported by (Chang, Lee, & Fon, 2005) using a simplified bubble growth model. Due to the lack of knowledge of the internal flow of multi-hole nozzles under flash boiling conditions, it becomes extremely difficult and important to figure out right input conditions of the spray which could mimic flash boiling conditions. As it is not the purpose of this thesis to model the internal flow of the injector, under flash boiling conditions; therefore, the nozzle output conditions i.e. spray input conditions have to be determined by simulations and modelling from the literature or, if not possible, by empirical adjustment of the spray inputs in terms of enhanced atomization.

3.4.1 Modelling of the radial expansion of the spray, "Bell Shape":

The present approach focuses on the modification of the atomized spray at nozzle vicinity. As explained earlier, the presence of bubbles under flash boiling conditions generates:

- A reduced drop sizing
- A large radial expansion making the spray plumes to acquire a kind of bell shape near the nozzle.

These observed features fit with the proposed modelling approach in Figure 26. The atomization "as usual" is assumed to be quasi-immediate at the injector outlet. The drops are assumed to entrained bubbles inside. These bubbles undergo a rapid expansion process and eventually explode and disintegrate into smaller drops, as proposed by (Kawano, Ishii, Suzuki, Goto, Odaka, & Senda, 2006).

It results not only in smaller drops but also in the additional kinetic energy. The injection of vapor at the nozzle position is neglected in the present study.

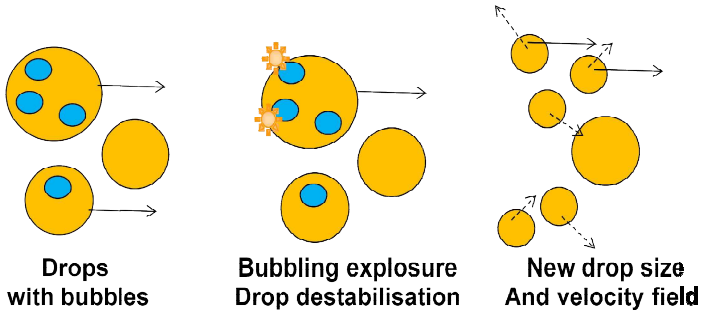

Figure 26: Schematic of the present approach. Step 1: atomized spray including bubbles; Step 2: supplementary disintegration; Step 3: resulting reduced drop size and additional kinetic energy (dashed line)

The velocity of a droplet is decomposed into two main parts, the velocity based on the liquid flow (without flash boiling), u_p^{nf} and an additional radial velocity due to the flash boiling u_p^{fb}.

$$u_p = u_p^{nf} + u_p^{fb} \tag{75}$$

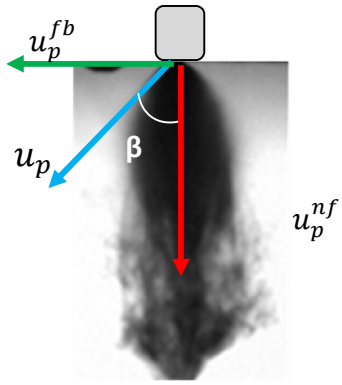

Figure 27: Experimental image of flash boiling spray at 1ms ASOI with $P_{inj} = 50bar$, $P_{chamber} = 0.4\ bar$, $T_{fuel} = T_{chamber} = 60°C$

We propose to consider a simple proportionality relationship between this additional kinetic energy and the additional energy surface:

$$\rho_l u_p^{fb^2} \approx \left(\frac{\sigma_l}{d_{p_i}} - \frac{\sigma_l}{d^*_{p_i}}\right) \tag{76}$$

This explosion of the bubbles in the proposed model approach (Figure 26) should be isotropic: it should not depend on the direction. From the above equations, a dependency of the injection angle, β and drop diameter, d_p can easily be deduced from the non flash boiling velocity component and flash boiling velocity component.

$$\beta = \tan^{-1}\left(\frac{u_p^{fb}}{u_p^{nf}}\right) \tag{77}$$

Therefore, the proposed model reads:

$$\text{Additional angle } \beta = \tan^{-1}\left(\sqrt{C_{fb}\left(\frac{1}{d_{p_i}} - \frac{1}{d^*_{p_i}}\right)}\right) \tag{78}$$

where C_{fb} is a new introduced constant (with dimension of a length) assumed to be constant and especially not depending on the flash boiling conditions. The sauter mean diameter d_{p_i} is reduced to $d^*_{p_i}$ depending on the superheating degree. It can also depend on the geometry of the injector, e.g. if a metering hole is followed by a larger hole, a so-called “step-hole”. The value of the constant will increase with the increase of the step-hole diameter to length ratio.

As stated earlier, it is emphasized again that the present thesis is not dedicated to the study the internal flow of the nozzle. Therefore, the drop size reduction depending on the superheating degree and the fixed value of the constant is assumed. The interest of the present work is to verify if:

1. A simple model as proposed can reproduce the observed flow near the nozzle – at least for a moderate superheating degree (realistic of engine conditions).
2. The temporal dynamic of the injector can be reproduced
3. The sensitivity to spray injection change can be reproduced
4. And lastly, how the collapse is occurring.

3.4.2 Results and discussion:

3.4.2.1 Improvement in spray shape:

Spray under flash boiling conditions with injection pressure, $P_{inj} = 50bar$, chamber or back pressure, $P_{chamber} = 0.4$ bar and the fuel and chamber temperatures, $T_{fuel} = T_{chamber} = 60°C$ respectively have been studied both numerically and experimentally. These highly evaporating conditions produce highly collapsing spray. Experimentally the process of the spray collapse has been observed to begin with a formation of tulip shape spray in first few hundred micro-seconds after the start of injection. This tulip shape formation is usually a result of sudden burst of bubbles in the flashing sprays generating finely atomized drops along with huge radial expansion leading to dramatic collapse of spray due to the high evaporation and jet-to-jet interactions.

To account for the enhanced atomization effect in the simulation SMD of the droplet at the injection was reduced to 20µm which is coherent to what experimental PDA data close to the injector tip shows (Wood, Wigley, & Helie, 2013). The flash boiling coefficient C_{fb} was chosen to be 2.5 for all the studied cases. This triggers a spray collapse due to the high evaporation and jet-to-jet interactions but without recovering the tulip shape near the injector tip, as presented in the Figure 28 (b). This means that the radial expansion of the spray cannot be neglected in the lagrangian spray simulation of the flashing spray. The simulation utilizing the equation (78) captures the tulip shape of the collapsing spray reasonably well as presented in Figure 28 (c).

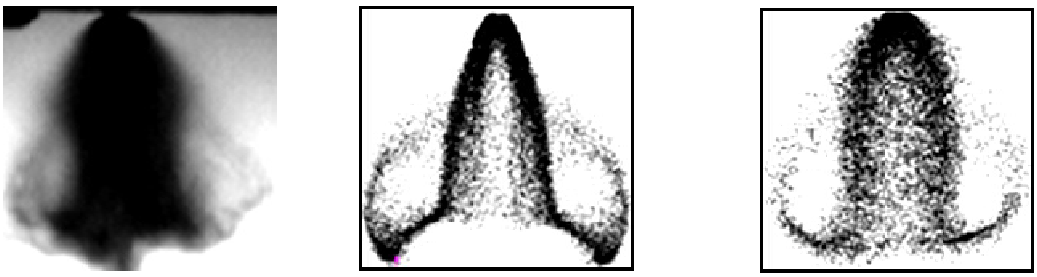

(a) *(b)* *(c)*

Figure 28: Spray under flash boiling conditions at 0.5ms ASOI (a) experiment, (b) simulation without radial expansion modelling (c) simulation with radial expansion modelling; $P_{inj} = 50bar$, $P_{chamber} = 0.4\ bar$, $T_{fuel} = T_{chamber} = 60°C$

3.4.2.2 Temporal evolution of the spray collapse:

The spray after the tulip shape formation collapses further in time while keeping the liquid core intact. In the Figure 29, the simulation captures the shape and penetration well. The small drops on the periphery also get engulfed in the collapsing spray cone, which contribute more to the already high vapour concentration region. The presence of high amount of drops and vapour in the core of the spray cone leads to high penetration of the flash boiling sprays as compared to non flashing sprays.

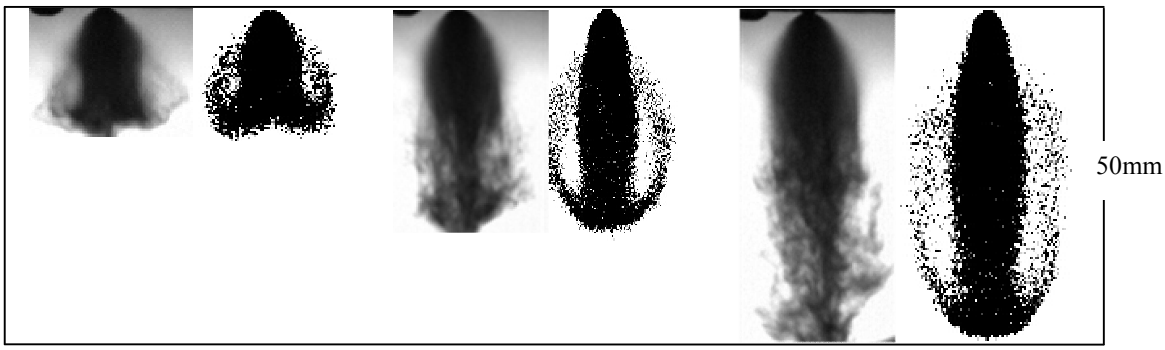

(a) *(b)* *(c)*

Figure 29: Spray penetration comparison at P_{inj} = 50bar, $P_{chamber}$ = 0.4 bar, T_{fuel} = $T_{chamber}$ = 60°C; (a) 0.5ms ASOI; experiment, simulation (b) 1ms ASOI; experiment, simulation (c) 1.5ms ASOI; experiment, simulation;

The jet-to-jet interactions are more severe than in the non flashing or partially flashing sprays, presented in the earlier section 6. The air inside the spray cone is pushed downwards along with the vapour which prohibits the spray to disperse which is also confirmed in (Xu, Zhang, Zeng, Zhang, & Zhang, 2013). Jet-to-jet interactions are very strong even from the start of injection. At 0.2ms it can be noticed that a high amount of vapour has already been generated inside the spray cone. At 0.5ms, some part of the vapour is sucked away from the core of the spray cone by the re-circulations at the tip of the spray, producing a tulip shape spray. But as the spray progresses further the vapour concentration increases at the centre of the spray cone. The vapour at the centre of spray cone is concentrated until the tip of the spray even at 1ms ASOI which forces the spray to penetrate more and stops any gas entrainment from the bottom half of the spray. At 1.5ms ASOI the continuous vapour core is disrupted at 35mm downstream by the growing spray tip vortices giving rise to the high vapour concentration region at the tip of the spray. This makes the spray core to become thinner and more penetrating in the flashing sprays.

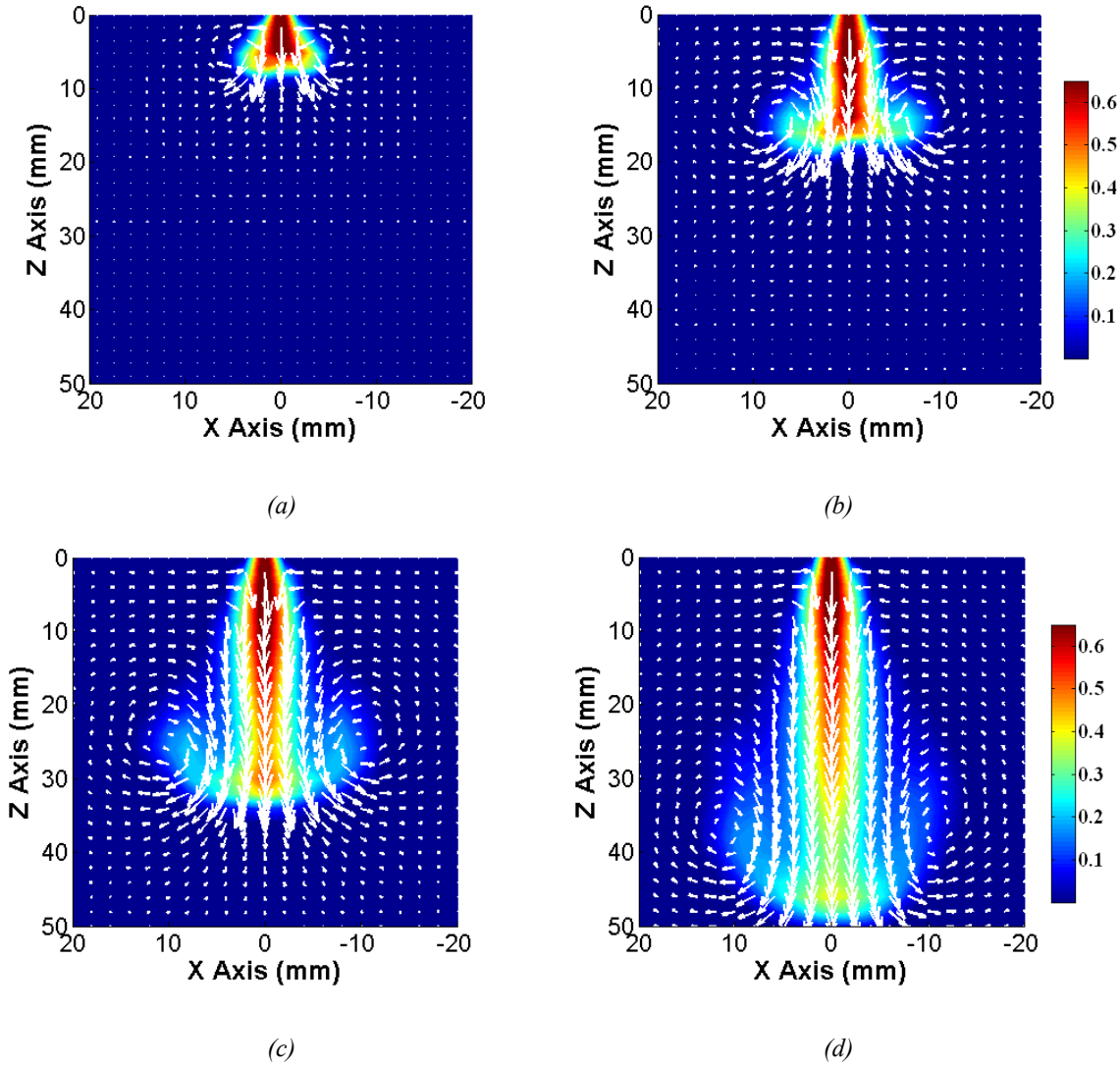

Figure 30: Vertical planar cut of vapour mass fraction (in colour) super imposed by axial gas velocity vectors for the spray with P_{inj} = 50bar, $P_{chamber}$ = 0.4 bar, T_{fuel} = $T_{chamber}$ = 60°C; (a) 0.2ms ASOI (b) 0.5ms ASOI (c) 1ms ASOI (d) 1.5ms ASOI

The Horizontal planer cuts of the vapour mass fraction superimposed by the radial gas velocity vectors in Figure 31 reveal that the plumes merge quite quickly in flash boiling conditions. The plumes do not appear to be segregated at all even at 10mm downstream. Any gas which is entrained inside the spray is immediately pushed downwards. This process continues from the injection nozzle tip to spray tip.

In multi-hole sprays, the spray segregation is more dependent on the spray tip vortices at the inside and the outside of the plumes which keeps the direction of the spray plume balanced. This requires

the gas entrainment inside the spray cone from the bottom half of the spray which is not possible in fully collapsing spray. In other words, once the spray plumes merge and collapse fully then there is no chance to separate the plumes again, therefore it is necessary to reduce the strong jet-to-jet interactions near the injection region.

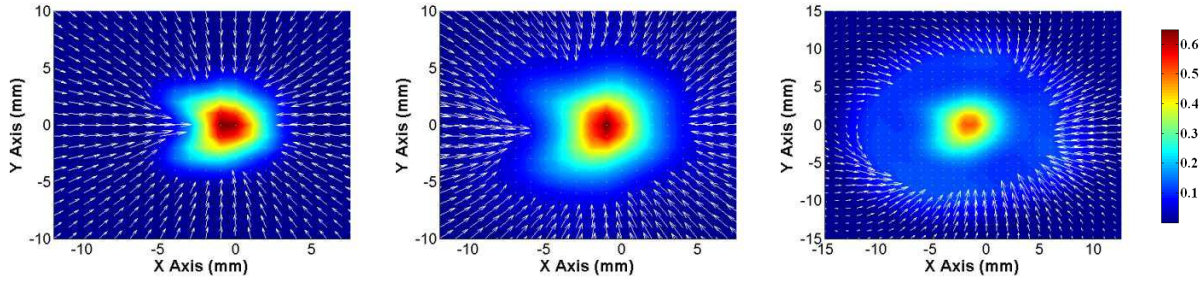

(a) *(b)* *(c)*

Figure 31: Horizontal planar cut of vapour mass fraction (in colour) super imposed by radial gas velocity vectors for the spray at 1.5ms ASOL with $P_{inj} = 50bar$, $P_{chamber} = 0.4\ bar$, $T_{fuel} = T_{chamber} = 60°C$; *(a) 10mm(b) 20mm (c) 30mm*

3.4.2.3 Role of injector design parameters in flash boiling conditions:

In multi-hole injectors in addition to the external factors such as, fuel and chamber pressures and temperatures, there are some factors linked to the injector design which can prevent, delay or initiate the spray collapse. One of these factors is distance between the injection holes and the other is injection velocity at opening of the injector.

3.4.2.3.1 Hole to hole distance:

The distance between the holes of the injector denoted by L_d in Figure 32, play a critical role in the spray collapse under flash boiling conditions. As explained in the previous section, high evaporation rate and jet-to-jet interactions cause the spray plume in multi-hole injectors to merge and collapse. Spray collapse intensity can be partially controlled by increasing or decreasing the distance between the injection holes. Four cases with different hole to hole distances have been studied numerically. Here the ratio of the hole to hole distance to the hole diameter L_d / D_i for the nominal case is equal to

1.1. It is apparent in the Figure 33 (from left to right) that a small decrease in the distance between the injection holes leads to dramatic collapse of the spray. The axial penetration increases with increase in spray collapse intensity, slowly until the point where the spray collapse: the spray collapse leads to a high value of penetration.

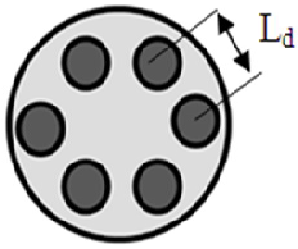

Figure 32: 6-hole injector with indication of hole to hole distance

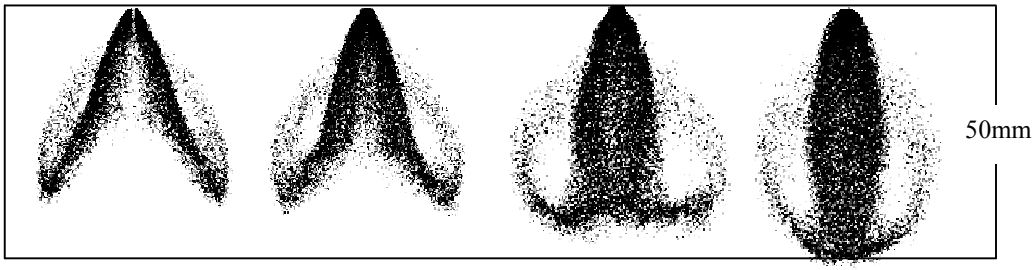

(a) (b) (c) (d)

Figure 33: Spray under flash boiling conditions with P_{inj} = 50bar, $P_{chamber}$ = 0.4 bar, T_{fuel} = $T_{chamber}$ = 60°C; with different hole to hole distances, at 1.5ms ASOI (a) nominal (b) reduced by 13%,(c) reduced by 19% (d) reduced by 32%

Cases	Axial Penetration	Maximum Penetration
nominal	39	45
reduced by 13%	41	46
reduced by 19%	45	48
reduced by 32%	50	50

Table 5: Comparison of axial and maximum penetration for the cases with different hole to hole distance configurations

3.4.2.3.2 Injection opening velocity:

The injection opening velocity is driven by the needle movement of the injector. The needle of the injector can be quick or slow in responce to the electrical signal for the opening of injector which will eventually have an effect on the quality of spray mixture formation specially in flash boiling conditions.

Two cases with injection opening velocities of 45m/s (corresponding to the slow opening of the injector) and 90 m/s (corresponding to the fast opening of the injector) have been studied experimentally and numerically with the same injection and surrounding conditions as in section 3.4.2.1 except the chamber pressure, which is 0.5 bar in this case. The injector with slower opening velocity produces more droplets in the centre of the spray cone and the overall spray cone appears to be thicker. The higher injection opening velocity keeps the spray plumes partially segregated in the begining. Even though the spray plumes are segregated initially but the spray collapse tedency doesnot vanish. The spray plumes are recognizable even after the spray collapse in the case of faster injection opening velocity whereas, the slower injection opening velocity can lead to more intense jet-to-jet interactions near the injection region.

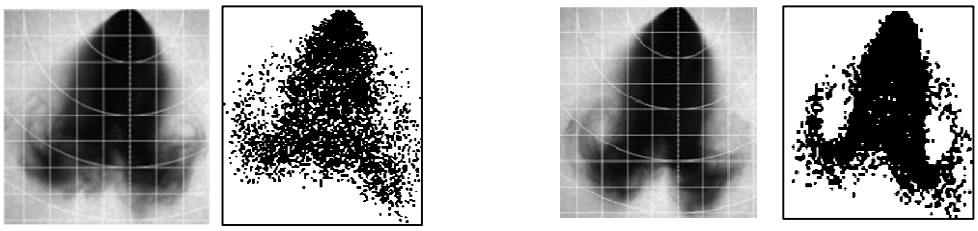

(a) *(b)* *(c)* *(d)*

Figure 34: Spray under flash boiling conditions with $P_{inj} = 50bar$, $P_{chamber} = 0.4\ bar$, $T_{fuel} = T_{chamber} = 60°C$; *(a) experiment with* $U_{lo} = 45m/s$ *(b) simulation with* $U_{lo} = 45m/s$ *(c) experiment with* $U_{lo} = 90m/s$ *(d) simulation with* $U_{lo} = 90m/s$

3.5 Conclusion:

The conclusion of this chapter has been divided into two main parts namely, Spray behaviour under non-flashing conditions and Spray behaviour under flashing conditions.

3.5.1 Spray behaviour under non-flashing conditions:

Numerical results with standard spray models and AMR approach show a good agreement for the both 3 and 6-hole GDI injectors compared to high-speed Mie scattering, PDA and PIV experimental data which have been performed in non-evaporating and evaporating conditions. The droplet size comparison between the experiments and numerical results at the centre of the spray plume reveals a difference of less than 1μm in D_{10}. PDF of droplet distribution shows a good agreement. The penetration and vector fields of air entrainment for both injectors are very well captured. The air entrainment effects on the spray jets are observed and appear to be very pronounced. Jet to jet interaction appears to be linked with the reorganization of the flow due to the compact geometry. As spray is penetrating downstream, the dense core of the spray may cause the air near the nozzle to be pushed downwards, while leading regions of each spray plume induce inter-plume air-entrainment. The resulting counter flow shear gives rise to radial flow, which makes the spray plumes to deflect from their original path. At the deflection point a ring of vapour appears which is pushed along with the radial flow from the centre of the spray cone. The cone deflection angle in the simulations is measured roughly to be between 6° to 9°.

3.5.2 Spray behaviour under flashing conditions

Spray shape is recovered well with radial expansion model in flash boiling conditions. The spray penetration is also quite comparable to the experiments and the spray penetration has been observed to increase in case of fully collapsing sprays in comparison to partially collapsing sprays. The gas entrainment and vapour mass fraction results highlight the increase in the penetration of the fully collapsing sprays. High vapour concentration, along with gas being pushed down inside the spray cone contributes to the high penetration of the fully collapsing sprays. The spray collapse tendency has been found to be reduced with increase in hole to hole distance and the injection opening

velocity. The increase in hole to hole distances reduce the spray plume interactions close to the injector and the injection opening velocity keeps the spray plume segregated further downstream.

Chapter 4 Large Eddy Simulations of High Pressure Spray

As explained earlier, Euler-Euler approach is well established for dense particle flows but Euler-Lagrange approach presents many advantages, especially for intrinsically capturing poly-disperse particle flow. Additionally, macroscopic Euler-Euler approach requires immense effort to close the unknown terms, along with some open questions on the universality of the closure and the values of the constant. For more details on these approaches, readers can, for instance, refer to (Sirignano, 2000; Kaufmann, Moreau, Simonin, & Helie, 2008; Moreau, Simonin, & Bédat, 2010). The present work focus on Euler-Lagrange point force approach in the Large Eddy Simulations (LES) formalism.

Different studies have used various subgrid scale models for the Euler-Lagrange simulations but mostly in the context of particle laden jets. (Bini & Jones, 2008; Apte, Mahesh, Moin, & Oefelein, 2003; Vuorinen, 2010) have used classical Smagorinsky model, dynamic Smagorinsky and implicit models respectively. In the framework of LES of spray (Kosaka & Kimura, 2006) studied the effect of two way coupling on the diesel spray evaluation and mixing by using classical Smagorinsky model under non evaporating conditions. On the other hand (Bharadwaj, Rutland, & Chang, 2009) used one equation turbulence models but mainly in highly evaporating conditions. Therefore, there is lack of understanding regarding the choice of the subgrid scale model for LES of spray.

(Boivin, Simonin, & Squires, 2000) tested a priori on various classical single-phase subgrid scale turbulence models on the results obtained from the DNS of incompressible, isotropic, forced homogeneous, turbulent flow. The classical Smagorinsky model demonstrated approximately correct overall results, with the same limits found on single-phase turbulent flow (Sagaut, 2006) but the dynamic Smagorinsky model was found to return more accurate results, with mesh-independency. Despite some of these early works, only a small number of applications to classical flows have been published. In the literature, a large part of the studies is found to be focused on channel flow, where

particle-wall interactions are difficult to capture (Vinkovic, Aguirre, Simoens, & Gorokhovskhi, 2005). Also, there are quite a few studies dedicated to the particle-laden jets, which represent ideal test cases for either one-way coupling or with a limited backward influence on the turbulence modulation.

Most of the literature of Large Eddy Simulations of spray deals with a simplified approach.

Some works deal with two-phase flow regimes where the subgrid contribution is negligible and therefore, subgrid scales effects are usually neglected as in (Vuorinen, 2010). Despite these simplifications, often a large part of the physics is represented, and the validation results are not unsatisfactory, as the purpose of Large Eddy Simulations is to solve explicitly a large part of the flow features evolving at the resolved scales. In real flow the subgrid terms cannot always be assumed to be negligible, thus, further analysis is required to clarify this point.

A second category of previous works is concerned with extremely poor resolution for LES, mostly due to complex geometry, moving mesh, in-engine combustion applications as in (Bharadwaj, Rutland, & Chang, 2009). Usually, the results are RANS-like, and such spray simulations appear to be used more as a vapour generator rather than being really predictive. For instance, these approaches cannot accurately predict the spray angle and mass load in the spray.

To our knowledge no clear methodology and systematic tests have been presented for dense laden jets or sprays – as it was presented for single-phase in (Sagaut, 2006). Even in the case of single-phase flow the influence of the choice the subgrid carrier phase model on the subgrid dispersion, subgrid two-phase coupling, and the sensitivity of input conditions, has still not been reported in detail.

The present study focuses on spray generated by liquid high pressure atomizers. These two-phase jets do not deal with wall interaction, but with pure second phase injection, without the assistance of carrier phase injection. The flow dynamics are generated only from the momentum exchange. Therefore, it can be considered as a more complex case, in comparison to dilute particle laden jets.

A systematic methodology is progressively built in the current work. For simplification, secondary breakup, thermal or mass exchanges are not considered. The study focuses initially on steady state in

order to remain uninfluenced by transient injection flow. Secondary break-up and collisions are introduced at the end of the present chapter, whereas the application of the drag correction for high velocity (part 4.1.6) will only be applied in the next chapter.

4.1 Large Eddy Simulations Modelling:

The LES equations are presented in the chapter 2 from equations (22) to (25).

4.1.1 Carrier phase; Subgrid viscosity models:

Four different subgrid scale models for turbulent viscosity μ_t have been used: standard Smagorinsky model, one equation eddy model, dynamic Smagorinsky model and the implicit model. By inserting the mesh size Δ in the place of geometrical scale of turbulence L in the equation (11) of chapter 2 and characterising the turbulent energy of fluctuations by; $\Delta\,|S_{ij}\,|$, where, $|S_{ij}\,|$ is the mean strain rate tensor, the Smagorinsky model (Smagorinsky, 1963) for turbulent subgrid viscosity is written as:

$$\mu_t = \rho\left(\Delta {C_s}^2\right)\sqrt{\tilde{S}_{ij}\,\tilde{S}_{ij}} \tag{79}$$

The standard value of the constant is $C_s = 0.02$. This constant C_s is not universal (Meldi, Lucor, & Sagaut, 2011). A dynamic approach, introduced by (Germano, Piomelli, Moin, & Cabot, 1991) and subsequently modified by (Lilly, 1992), estimates the Smagorinsky constant locally in a flow field. In dynamic Smagorinsky model, in addition to the grid filter, a second filter named as test-filter, which is twice the size of grid filter, is applied to the equations of motion. Both filters produce a resolved flow field and their difference gives the contribution of the small scales with the size in between the grid filter and the test-filter, in such a way that locally, the Kolmogorov's scaling is verified. The constant C_s is then calculated by the least square analysis of (Lilly, 1992). The implicit model assumes that the numerical dissipation is equal or superior to the subgrid contribution, therefore, the constant is set to zero and no additional subgrid viscosity is introduced (Vuorinen, 2010).

In addition to zero equation eddy viscosity models, there is also one equation model which solves transport equation for subgrid scale kinetic energy, k_{sgs} (Yoshizawa, 1985; Dejoan & Schiestel, 2002; Krajnović & Davidson, 2002). One-equation model (Yoshizawa, 1985) is also investigated

$$\frac{\partial \rho k_{sgs}}{\partial t} + \nabla.\left(\rho k_{sgs}\bar{u}\right) = \nabla.\left((\mu + \mu_t)\nabla k_{sgs}\right) - \rho(\tau:\bar{S}) - \epsilon \tag{80}$$

where μ_t is the subgrid scale viscosity and ϵ is the dissipation modelled respectively as $\mu_{sgs} = C_k k_{sgs}^{\frac{1}{2}}\Delta$ and $\epsilon = C_e k_{sgs}^{\frac{3}{2}}\Delta^{-1}$. C_k and C_e are the constants with values of 0.094 and 1.048.

4.1.2 Lagrangian equations

The solved lagrangian equations have been introduced in the previous chapter in equation (28). The values of constants, in physical sub models of drops, have not been altered in comparison to average simulations. In Eulrer-lagrangian point-source Large Eddy Simulations, the lagrangian tracking is based on the total (assumed to be exact) drop motion and the filtered gas at the drop position. The equation (28) will take the form:

$$\frac{d\mathbf{u}_p}{dt} = \frac{C_D}{\tau_p}\frac{Re_p}{24}\left(\tilde{\mathbf{u}}_g - \mathbf{u}_p\right) \tag{81}$$

The difference between the above exact equation and the previous one in equation (28) is the filtered gas velocity which is treated by an additional subgrid dispersion model that will be presented in the next part. Also, the droplet Reynolds number is estimated with the filtered gas characteristics.

4.1.3 Two phase coupling models

In Euler-Lagrange formulation of two-phase flow, the exact source terms are not resolved and thus, are filtered explicitly:

$$\tilde{S}(x) = \frac{1}{\Delta^3}\sum_{p}\int_{V} S_p\,\delta(x_p - y)\,G(x - y, \Delta(x))\,dy \tag{82}$$

In the present work, the filter G represents a Top-hat filter of size Δ, which means that the filtering reduces simply to a volume average of the individual contributions (Bini & Jones, 2008).

When the inter-drop collisions are considered, the trajectory model of (Macpherson, Nordin, & Weller, 2009) is used in the simulations, which is based on the O'Rourke collision model (O'Rouke, 1989) with some modifications. The short coming of the original model of O'Rourke is that it only considers the probability of the particles to be found in the same cell for the collision without any dependence of the particle directions. This problem is addressed in the trajectory model which calculates the trajectory of the particle and allows collision when these trajectories coincide, otherwise droplets do not collide.

4.1.4 Two phase Subgrid models

In equation (81) the velocity of the gas "seen" by the particle is unknown, since, typically it is the velocity on residual (or unresolved) scales. Therefore, for resolving particle acceleration, equation (81) has to be completed by modelling of this equation. The simple eddy turn over algebraic model, presented in detail in section 2.3.3 in chapter 2 for RANS, has been modified, in terms of subgrid scale model for LES, by using subgrid scale kinetic energy. A subgrid velocity is estimated each eddy turnover time by:

$$u^*{}_p = \frac{\sqrt{k_{sgs}}}{\tau_p} \tag{83}$$

This additional subgrid scale velocity is added to the gas velocity and hence it accounts for the effect of turbulence on the particle by modifying the slip velocity. Subgrid two way coupling has to be considered to account for the following work acting on the carrier phase.

4.1.5 Two-way subgrid scales coupling

In dispersed two phase flow, particles and fluid both influence each other through interphase mass, momentum or energy exchange. In the present study, the two-way coupling has been based on the transfer of momentum between the two phases. The mean carrier phase velocity field is affected by the presence of the particles. The particles modify the overall momentum and turbulence of the carrier phase. These changes depend on the number of particles in the domain.

The particles closely follow the fluid flow field when they are quite small and move with the same velocity as the continuous phase. This information is provided by the particle Stokes number St, which is the ratio of particle response time to the fluid response time. When the particle Stokes number is sufficiently smaller than 1, the particles and continuous phase move with unison. In this situation a two-phase flow may be modelled as continuous; thereby coupling gas and droplets may be viewed in terms of effective compressibility.

The effective density (ρ^*) can be defined simply as the mass of the dispersed phase and carrier phase per unit volume. In terms of volume fraction α, which is the ratio of the particle to the fluid volume in a given, the equation reads:

$$\rho^* = \rho_g \alpha + \rho_l (1 - \alpha) \tag{84}$$

In context of LES this equation for modified density is introduced in the turbulent subgrid scale viscosity in equation (79). The Stokes number at filter size St_Δ which is defined as the ratio of particle response time to the fluid response time at the filter scale, is used as a limiting criterion. The effective density equation is used for the drops with $St_\Delta < 0.2$.

When particles are non-inertial, they respond to small scale vortex features resulting in significant relative velocity fluctuations. This leads to another dominant mechanism is the turbulence dispersion of the carrier phase. The loss of the turbulent kinetic energy of the carrier phase depends on the transfer of fluid fluctuating energy to the particle fluctuating energy and viscous dissipation (Loth, 2008).

In order to change the path of a particle, carrier phase fluid needs to apply a certain amount of force on that particle, and the main one is the drag force. Since this fluid force comes from the fluctuating flow, therefore, its impact on particle motion and direction is fluctuating as well.

The turbulent fluctuations of velocity in the flow surrounding a given particle may be characterized locally by the subgrid kinetic energy. Therefore, when the linear drag is assumed, the subgrid scale kinetic energy in a given cell may be employed for simulation. As an approximation, the rate of fluid energy loss may be considered as:

$$E_L = \left(m^* \tau_p^{-1} \sqrt{\frac{2}{3} k_{sgs}} \right) u^*_p \tag{85}$$

where u^*_p is the particle fluctuating velocity estimated from the dispersion model and m^* is the effective mass which actually corresponds to a total mass of the particles in a cell i.e. for "n" number of particles in a cell, $m^* = \sum_{i=1}^{n} (4/3) \rho_p \pi \left(d_{p,i}/2\right)^3$. The loss of TKE due to the viscous losses can simply be considered as the dissipation of the energy at the Kolmogorov scale, η. Both these mechanisms participate to the dissipation of the fluid kinetic energy at the sub grid scale along with the change of effective density in subgrid scale viscosity.

4.1.6 Rarefaction and Compressibility Effect:

The drag on the particles under certain conditions can either reduce or increase. The effects which deal with reduction or enhancement of drag on the particles are usually referred to as rarefaction and compressibility, respectively. Rarefaction needs to be considered when the particles are very small. The compressibility of the gas becomes important for the particle with $Ma_p > 0.3$. Ma_p is the particle mach number which is a ratio of the particle slip velocity and the speed of sound. When Ma_p increases beyond 0.3 then compression waves are initiated with particle motion which increases the drag at high particle Reynolds numbers (Sommerfeld M. , 2000). Therefore, to take into account both rarefaction and compressibility effects, a following experimental correlation expression proposed by (Carlson & Hoglund, 1964) has been used:

$$C_d = C_{do} \frac{1.0 + exp\left(-\frac{0.427}{{Ma_p}^{4.63}} - \frac{3.0}{{Re_p}^{0.88}}\right)}{1.0 + \frac{Ma_p}{Re_p}\left\{3.82 + 1.28 * exp\left(-1.25\frac{Re_p}{Ma_p}\right)\right\}} \tag{86}$$

C_{do} is the drag coefficient computed in the chapter 2 in equation (28). The compressibility effect is taken into account by the numerator term and the rarefaction effect by the denominator term. The drag coefficient versus particle Reynolds number for Mach number between 0.3 and 1 has been plotted in Figure 35. The small Reynolds numbers represent the small particles and the larger Reynolds numbers represent the larger particles with large slip velocity. The effect of rarefaction is quite obvious until $Re_p$is around 10 where the drag is reduced for all the Mach numbers. However the compressibility effect becomes very prominent for the Mach numbers beyond 0.6.

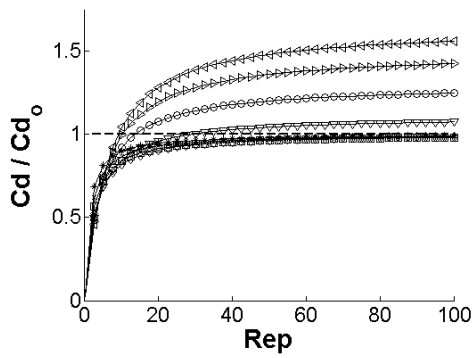

Figure 35: Modification of the drag coefficient due to rarefaction and compressibility effects for small and large particles of (—×—) 0.4 Ma, (—□—) 0.5 Ma, (—◇—) 0.6 Ma, (—▽—) 0.7 Ma, (—○—) 0.8 Ma, (—▷—) 0.9 Ma,(—◁—)1Ma

4.2Numerical Approach

4.2.1 Numerical Solver

The Large Eddy Simulations are performed on an open-source development platform in C programming language, OpenFOAM, with the eulerian approach for the gaseous (carrier) phase and the lagrangian approach for the liquid phase.

For the carrier phase, the solver resolves the filtered compressible Navier-Stokes Equations as described in section 2.1. A second order setup for the space and time discretisation is utilized. Gauss linear scheme, a second order unbounded scheme, is employed for convective operators. Gauss linear corrected scheme, a second order unbounded conservative, is used for diffusion operators. Backward implicit scheme, second order accurate in time and depends on the courant number for the stability is chosen for the time discretisation. All the schemes are described in Appendix C. Pressure velocity coupling of the carrier phase is achieved by PISO (pressure implicit with splitting off operators) like algorithm (Demirdžić, Lilek, & Perić, 1993) with two iterations of PISO loop for the predictor correction. Automatic time step adjustment is included by keeping the local courant number less than 0.1.

4.3 Initial tests

The initial tests are performed in order to investigate different injection models, turbulence models and numerics.

4.3.1 Initial Tests Setup

The setup of these initial test cases is presented below, in detail.

4.3.1.1 Geometry

A rectangular computational domain is used as illustrated, Figure 36. On the sides, the pressure waves at the outlet boundary are controlled by the wave transmission method of (Poinsot & Lele, 1992). The top side has a boundary condition of wall with no slip. This simple geometry allows a straight forward domain decomposition strategy for processors' parallelization by splitting the domain into pieces by direction while guaranteeing an equivalent loading of each processor.

The domain is rectangular with $400D_i$ in width in X and Y directions and $500D_i$ in height in Z direction. D_i represents the diameter of injection surface. An initial rectangular cell size of $5D_i$ is used for the simulations with Adaptative Mesh Refinement (AMR) with 3 levels of mesh refinement corresponding to the maximum cell limit of 8 million. AMR is based on a criterion of refinement based on subgrid scale kinetic energy, k_{sgs} for all the cases except the implicit case which uses magnitude of gas velocity. AMR is mainly used here as a dynamic meshing rather than a localized mesh refinement. The mesh is refined across the whole spray plume; it converges quickly around the jet zone to a constant mesh size, Figure 36. Moreover, once the mesh is refined, the mesh cell size remains constant to the highest level of refinement i.e. no un-refinement of mesh is performed. Therefore, the results are expected to not differ from a a-priori built mesh. The initial cell size after being refined thrice reduces to a minimum cell size of $0.625D_i$. The mesh refinement has to respect the constraints of the lagrangian dispersed phase with point source formalism. For instance, five levels of AMR (cell size= $0.156D_i$) will produce pseudo droplets wakes, pressure and density effects.

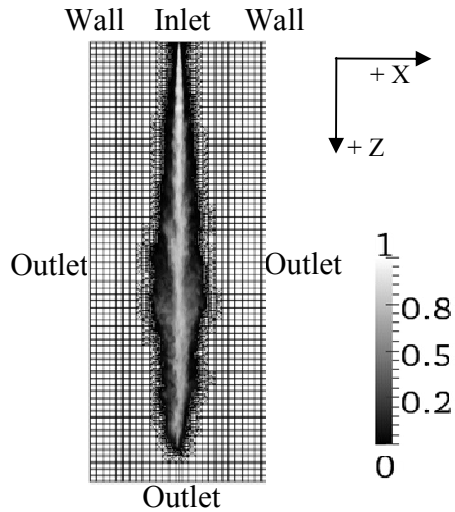

Figure 36: Computational Domain, boundary conditions and mesh with superimposed streamwise gas velocity non dimensioned by the liquid injection velocity. Inside the velocity shape, the mesh cell size remains constant to the highest level of refinement.

4.3.1.2 Liquid injection

The droplets are injected through a defined disk area of diameter Di. The injection area of atomizer nozzle is generally small and corresponds to only a few cells due to the limitation in mesh refinement explained previously. Preliminarily, to avoid any artificial effect of the cells edges, the location of the nozzle has been varied from symmetrical centre at the cell edge, cell centre and non symmetric, and no dependency of the mesh discretisation of the inlet boundary condition was observed. Obviously, the liquid mass load for the cells close to the input conditions is high and can violate the formal constraints of Euler-Lagrange approach for these few cells, where the flow is assumed to not been perfectly modelled. However, no numerical issues were observed with the present settings.

Three different injection profiles, presented in Table 6, are considered. The first shape is a fully random process in terms of position and velocity directions (constant in average). As in reality, atomizers generate a given profile; a Gaussian distribution for position of the droplets in the hole is the second shape. Moreover, as the velocity profile at the nozzle vicinity can also vary, a linear distribution of the direction vector is tested in a third shape category while keeping the injection angle constant to 12°.

Comparison of SGS Models	**Injection Model**		
Standard Smagorinsky	R-R	-	-
One Equation Eddy	R-R	-	-
Dynamic Smagorinsky	Random drop Position & Random angles Case 'R-R'	Gaussian drop Position & Linear angles Case 'G-L'	Gaussian drop Position & Random angles Case 'G-R'
Implicit	R-R	-	-

Table 6 : Subgrid scale models with different injection models

In LES approach, a fully developed turbulent flow in jet simulations can be achieved only by input of flow excitations, for example; introducing a certain amount of excitation at the inlet boundary condition. In this respect, a white noise signal is produced in our simulations by the summation of the sinusoidal waves with different frequencies. This signal is then super-imposed at the inlet as the variation of the injection angles of droplets as presented in Figure 37 (a). In order to remove any artificial numerical effect, only very high frequencies have been generated. These frequencies, in terms of frequency at the inlet f_i which is the ratio of injection velocity and the cell size, range from $0.47f_i$ and $2.8f_i$, where the lower limit corresponding to 5 time steps. Only 5% of droplets are excited by this signal to create sufficient excitations. The sinusoidal signal is expressed as:

$$Ys = n_{rand} \times sin(2\pi f T_{inj}) \tag{87}$$

The variable f denotes the frequency, T_{inj} is the injection time and n_{rand} is the random number.

The fft of the excitation signal is presented in the Figure 37 (b) in terms of strouhal number. Strouhal number (St_h) is useful in characterizes the oscillating behaviour of the flow. At the injection surface strouhal number is defined as $St_h = fD_i/u_i$, where f is the frequency at the inlet, D_i is the inlet diameter and u_i is the injection velocity.

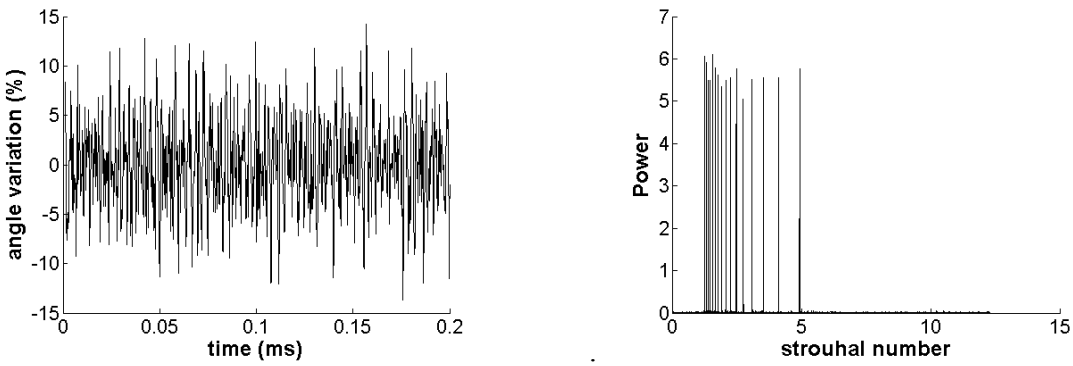

(a) *(b)*

Figure 37: (a) Input excitation signal (b) FFT of the input excitations

A schematic of the methodology of the input excitations is presented in Figure 38. To excite the spray, droplets undergo slight angle variations, generated by the excitation signal, of approximately less than 2°.

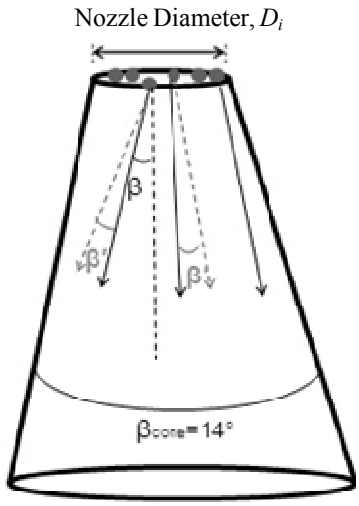

Figure 38: Schematic for the droplet injection Strategy

As it is of primary importance to quantify the level of excitations sufficient to produce a turbulent spray plume at relatively short computational times, the effects of these different levels of input excitations and the duration of excitation injection are studied hereafter. Three different cases presented in Table 6, have been investigated depending on the levels of input excitations of the drops by white noise.

Three cases are dedicated to effect of excitation superimposition at the entrance. The other cases are dedicated to the injection profile. These cases have been realized in the framework of the dynamic Smagorinsky model.

4.3.2 Test cases

Fixed parameters used throughout the study are displayed in Table 7. The subscript 'i' indicates the value at the injection position and conditions. The drops are injected from a geometrical surface of the diameter with a constant diameter of $75 \times 10^{-3} Di$ with an injection velocity, U_i of 0.57 Ma.

"Ma" denotes the mach number which is the ratio of fluid velocity to speed of sound. The injection time scale, T_i is obtained from the injection diameter and injection velocity.

The droplet Reynolds number (Re_p) and the liquid Reynolds number (Re_l) are defined as:

$$Re_p = \frac{|\mathbf{u}_g - \mathbf{u}_p| d_p}{\nu_g}, \qquad Re_l = \frac{\alpha_l |\mathbf{u}_p| D_i}{\nu_l} \tag{88}$$

where, ν_g is the kinematic viscosity of gas and α_l is the ratio of liquid to gas mass at the inlet. Therefore, $\alpha_l D_i$ refers to the liquid outlet section. Droplet Reynolds number at the inlet is 205 and the liquid Reynolds number at the inlet is 48173.

Droplet Weber numbers is a ratio of fluid inertia to surface tension. Weber number defined in two ways based on the density of the gas and liquid:

$$We_p = \frac{\rho_g |\mathbf{u}_g - \mathbf{u}_p|^2 d_p}{\sigma_l}, \qquad We_l = \frac{\rho_p |\mathbf{u}_p|^2 d_p}{\sigma_l} \tag{89}$$

where σ_l is the surface tension of the liquid. At the inlet the liquid We_l is large, therefore, a quasi immediate break process may occur, and that justifies the injection of drops instead of progressive injection based on a large and resolved break up length scale. Since, small drops are injected in present work, hence, the droplet Weber number, We_p is 5 times below the transitional Weber number We_t used in the breakup model.

Droplet Stokes number, St is the ratio of the dispersed phase drag time to a fluid characteristic time. At the inlet of the nozzle, the Stokes number is defined as the ratio of droplet relaxation time to the injection time scale $St_i = \tau_p / T_i$ is 68. The relatively high Stokes number implies that the drops are quite ballistic in the nozzle vicinity.

Injection Parameters	Values
Nozzle diameter $(D_i)/\Delta$	1.6
Droplet size $(d_p)/D_i$	20×10^{-3}
Injection Mach number	0.57
Injection spray plume Angle	14°
Density Ratio $\left({\rho_p}/{\rho_f}\right)$	609.3
Re_p	205
Re_l	4.8×10^4
We_l	47
Oh_p	2.54×10^4
St_i	68

Table 7 : Initial Parameters

4.3.3 Results & discussion

4.3.3.1 Input excitations

The frequency spectra of the velocity field are obtained by the Fourier transform of the numerical data of LES simulation, acquired by the numerical probes at the shear layer of the spray at the various axial downstream locations, in order to understand the role of input excitations in the generation of the transition. The three cases are compared in this regard: continuous input excitation during the fuel injection phase, input excitations limited to only initial transient time of the fuel injection phase and fuel injection without any input excitations.

The frequency of the continuous input excitations induces higher fluctuations in the near nozzle region at $12.5D_i$ and $50D_i$ downstream axial location, as presented in Figure 39. It is seen that forcing

of turbulence is manifested by high frequency excitation of the spray plume. The generation of instabilities with continuous input excitations were observed much earlier in comparison to the case with no excitation and to the case with the excitation was limited to the initial transient time,. It is also observed that only slight input excitations in the beginning of the spray injection make the spray to stay excited even if the excitations are not forced anymore. The case without any input excitation took almost twice the time of the excited jets. The frequency spectra illustrate that the excited spray has a small spread with single high frequency peak as compared to the other cases. This result seems to indicate a high sensibility of the results to input excitations. As "free" spray is studied here, therefore, no supplementary effect of any kind of forcing is allowed. The methodology which is retained for further analysis is the one which excites the injection for a very short time interval of 100Ti. Ti is the injection time scale which is obtained from the ratio of injection diameter and injection velocity. This short input excitation generates well spread frequency spectrum with sufficiently high frequencies within a minimum computational time and allows the flow to evolve further, free of forcing, with a minimum of one convection time in the domain for physical analysis.

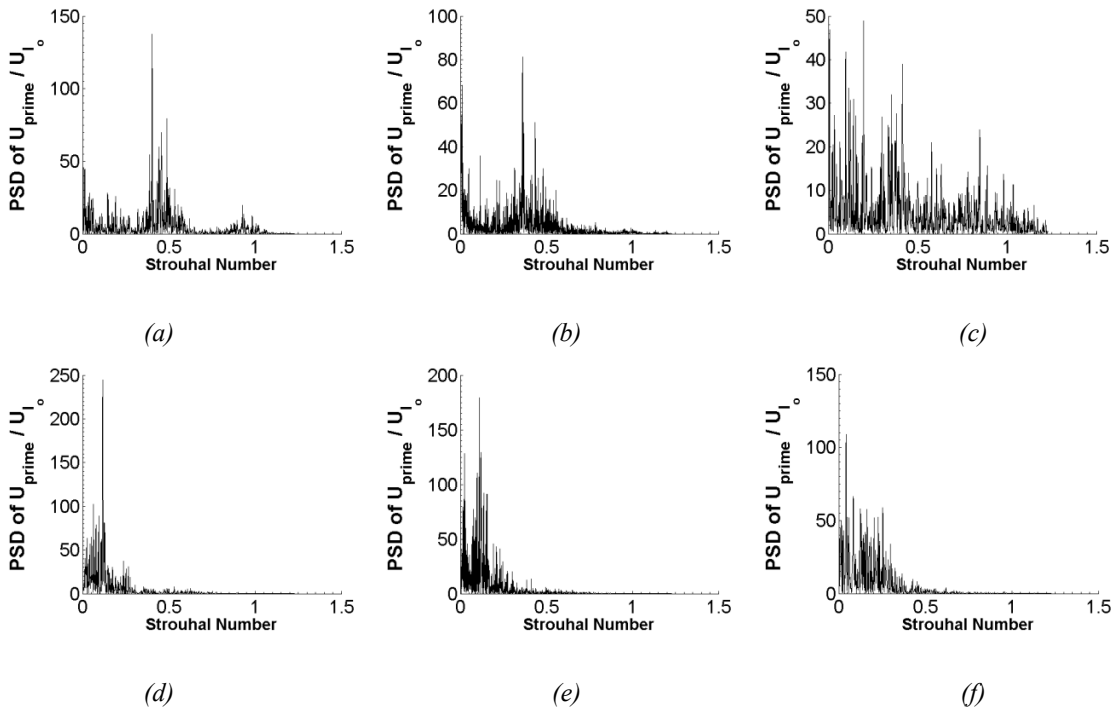

Figure 39: Fourier transform of the normalized velocity field at axial downstream locations of; 12.5D_i (a) Input excitations until the end of injection (b) Input excitations until 100T_i, (c) No Input excitations; 50D_i (d) Input excitations until the end of injection (e) Input excitations until 100T_i, (f) No Input excitations

4.3.3.2 Carrier phase Subgrid model effect:

4.3.3.2.1 Energy Spectra of carrier phase velocity:

The energy spectra in terms of comparison between different subgrid scale models are presented in Figure 40, at a downstream location of $200D_i$. For this comparison, power spectral density (PSD) of fluctuating velocity field normalized by the liquid injection velocity is plotted against the frequency (f) normalized by the frequency at filter scale (f_Δ) , in Figure 40. At this location the spray plume is observed to be sufficiently turbulent, explained more in detail in the next sections. The probes are placed in the shear layer of the spray and the numerical signal is obtained at each time step i.e. approximately every 0.1 T_i, which corresponds to a sampling frequency of $9.3f_i$.

The dynamic Smagorinsky and implicit models follow -5/3 slope of turbulence better than the standard models. The previous works like in LES of particle-laden flows with standard models (Bini & Jones, 2008) have shown a very quick deviation from the -5/3 slope in the inertial range. At high frequency zone, irrespective of the turbulence models, the slope is observed to be sharper than -5/3 due to the enhanced dissipation. However, it is seen that results given by implicit and also by the Dynamic Smagorinsky model exhibit behaviour closely to the classical spectra. Same is the case for standard Smagorinsky model, but compared to two previously referenced approaches, the standard Smagorinsky model is seen to be more dissipative. Concerning the Implicit model, there is a band of frequencies of almost no cascade, and then at higher frequency, the energy decays much faster than the Kolmogorov's spectrum.

It is apparent in Figure 40 that One equation eddy model and Standard Smagorinsky model have much steeper slope than dynamic and implicit models. In the inertial range of the energy spectrum, the one equation model and standard Smagorinsky model show only 0.2 decade and 0.4 decade respectively which are very small in comparison to the dynamic Smagorinsky model which demonstrates 1.2 decade and implicit model with 0.8 decade. It is expected that standard Smagorinsky model is introducing additional viscosity. In inertial range of the dynamic Smagorinsky model, the largest eddy is of the size of approximately 19 cells while the smallest scale before the deviation from the -5/3 slope are about 3.5 cells. The implicit model exhibits a peak near the mesh

cut-off region. This peak near the end of the inertial sub range indicates the inefficiency of the implicit model to dissipate the small scale structures and thus some energy is accumulated before being dissipated. To elaborate this point further, an additional case with coarser mesh (2 levels of AMR) returned a displacement of this small bump by a factor 2, which then seems to be linked to the mesh and could be attributed to energy saturation without sufficient dissipation. Divergence of the results has never occurred with a limited domain size. Moreover, particle Stoke numbers where the peak occurs is 3.5, which means that the particles are not responsible for accumulation of the energy at this spot. However, for this case, a definitive conclusion cannot be drawn from the current observation as the two-phase dynamics is also involved.

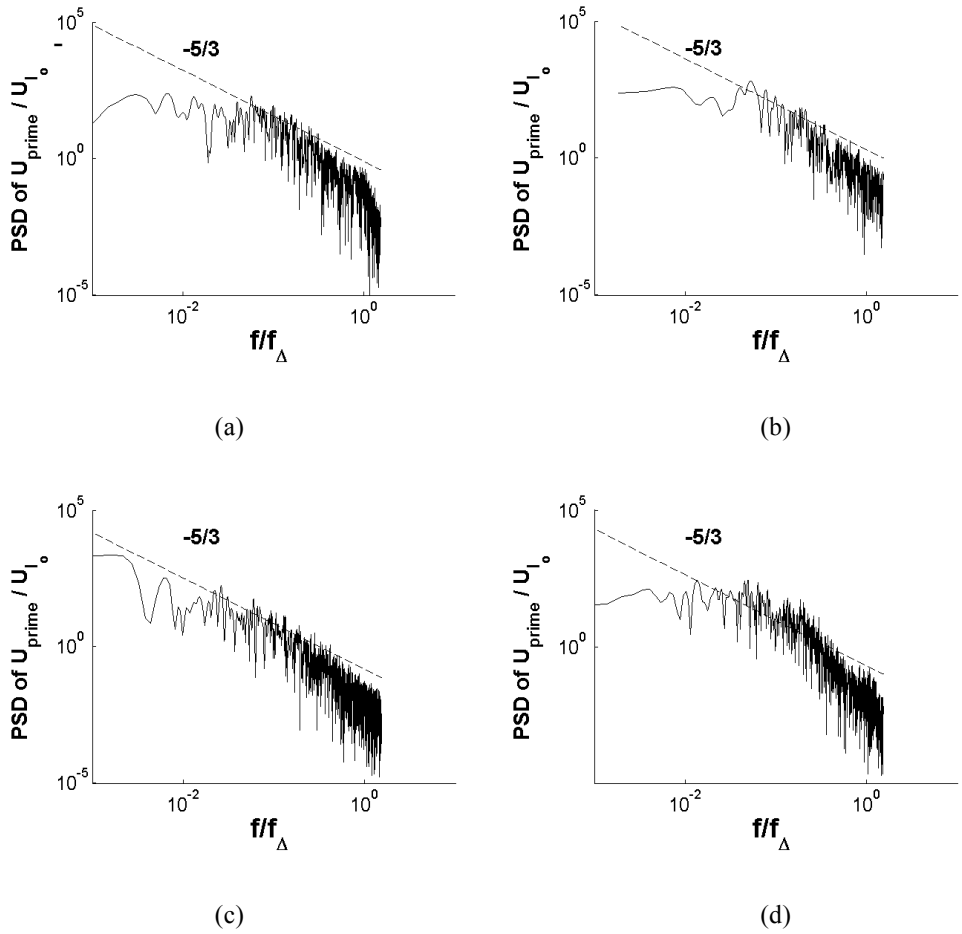

Figure 40: Energy Spectrum using at 200D_i with Input excitations cutoff at 100$T_i$ms for (a) Standard Smagorinsky (b)One equation Eddy (c) Dynamic Smagorinsky (d) Implicit

On the other hand, as two-phase flow can differ from the -5/3 slope due to the phase coupling, the previous results cannot be taken as a quality criterion. Moreover, a large -5/3 forcing effect of the dynamic model close to the cut-off frequency may possibly counterbalance the possible two phase physics, which is still an open question.

4.3.3.2.2 Subgrid scale viscosity fields:

The results of spatial distribution of the subgrid scale viscosity, μ_t normalized by the laminar viscosity are presented in Figure 41. The subgrid scale viscosity for the standard and dynamic models, the normalized subgrid scale viscosity is in reasonable range i.e. between 5 and 20; however the dynamic model returns a very localized subgrid viscosity whereas, the standard model is massively present on the overall shear layers, even at the close-up location where the transition to turbulence did not act. The one-equation eddy exhibits a large area of high dissipation with a value normalized μ_t values between 10 and 27. In case of one equation model, the subgrid scale viscosity over the shear layer appears to be much thicker than that of Standard Smagorinsky model with much higher value especially in the vicinity of the injection region. This indicates high level of dissipation incurred by the one equation model close to the injection region.

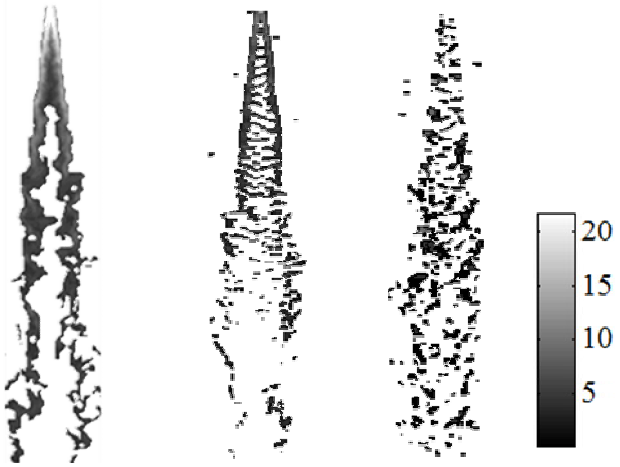

(a) (b) (c)

Figure 41: Streamwise cross-section of Normalized subgrid scale viscosity, isolevels (a) one equation Eddy Model (b) standard Smagorinsky (c) dynamic Smagorinsky

4.3.3.2.3 Shear layer structures:

The second invariant of the vorticity tensor also called Q-criterion, is used to detect the vortical coherent structures present in a flow field (Hunt, Wray, & Moin, 1988)

$$Q = \frac{1}{2}\left(S_{ij}S_{ij} - \Omega_{ij}\Omega_{ij}\right) \tag{90}$$

where S_{ij} is the strain-rate tensor and Ω_{ij} is the rotation-rate tensor and computed as: $\Omega_{ij} = \left(\partial u_i/\partial x_j - \partial u_j/\partial x_i\right)$. When the Q-criterion is positive, the rotational flow is dominant over the strain and shear. Q-criterion isolevels are normalised in the Figure 42 by the rotation-rate tensor (Ghasempour, Andersson, & Andersson, 2012)

$$Q_n = \frac{Q}{\frac{1}{2}\Omega_{ij}\Omega_{ij}} \tag{91}$$

The isosurfaces of normalized Q-criterion are coloured by the helicity level which is defined as the scalar product of velocity and vorticity field normalised by their magnitude (Levy, Degani, & Seginer, 1990), in order to identify at which distance different coherent structures will appear, and at which distance the transition to developed turbulence will occur.

$$helicity = \frac{\boldsymbol{u}.\boldsymbol{\omega}}{|\boldsymbol{u}||\boldsymbol{\omega}|} \tag{92}$$

(a) *(b)* *(c)* *(d)*

Figure 42 : Close up instantaneous view on the top half domain of Iso-surfaces of Q criterium (Qn=0.1) colored by normalized helicity (a) standard Smagorinsky (b) one equation (c) dynamic Smagorinsky (d) implicit

In the Figure 42, clear roll-up instabilities on the upper part, possibly followed by helicoidal instabilities are observable. The one-equation model returns a small level of structure, and the standard Smagorinsky model shows a limited amount of large structure only by comparing to the other models, which can indicate a high dissipation rate. The implicit and dynamic model returns very similar results, with the presence of helicoidal modes and small structures totally aligned with the flow (non dimensional helicity closed to unity). The bottom end of the figure corresponds to the 40% of the domain length.

4.3.3.2.4 Fluctuating velocity profiles:

The results of subgrid scale viscosity are confirmed on the profile of the streamwise velocity fluctuations in Figure 43. The profiles of root mean square (rms) streamwise velocities, at different axial locations, normalized by the mean injection velocity $\langle U_{lo} \rangle$ at the nozzle surface versus the radial distance normalized by the half spray plume width, L_h which is chosen such that $\langle U \rangle / \langle U_c \rangle = 0.5$, (Doudou, 2005). The spray half width evolution in the axial direction is presented in Figure 52 and it will be explained in detail later in this chapter. The fluctuation levels in the streamwise direction increase with distance from the injection nozzle until $250D_i$ from the injection nozzle. Afterwards, the streamwise fluctuations start to reduce and a decreasing trend in turbulent intensity is observed. Typically, the level of fluctuations decrease in the downstream direction, and their maximum is associated with the zone of high shear generation of turbulence. Since we do not have here the reference distribution from measurements, we cannot attribute a favour to one of the model. However, the three first approaches seem to give more realistic distributions, with pronounced "jet-like" profiles of turbulent intensity.

As expected, standard Smagorinsky model and one equation eddy model introduce high dissipation and subsequently delay the development of instabilities, and result in an overall lower level of fluctuations. Even by adding the subgrid contribution to the filtered one which results in the modelled total fluctuations, the standard Smagorinsky and one equation models cannot reproduce the values of fluctuations obtained by the dynamic model where 14% of peak rms values is obtained. Further downstream, even the filtered contribution of the implicit model is higher than the standard Smagorinsky and one equation models.

Finally, it is interesting to note here that relatively high percentages of fluctuations are resolved in comparison to subgrid fluctuations for the present spray settings, with 70% to 90% resolved turbulence. It should also be noticed that to improve the results of the one equation eddy model, some authors (Pomraning & Rutland, 2002; Kajishima & Nomachi, 2006) proposed a dynamic procedure for the estimate of the coefficient. Some other variations of one equation models also do exist e.g. (Fureby, Gosman, Tabor, Weller, Sandham, & Wolfshtein, 1997) which considers subgrid scale stress tensor in the transport equation, whereas, more complex approach could improve the results obtained here, but further modelling of the two-way coupling needs to be introduced.

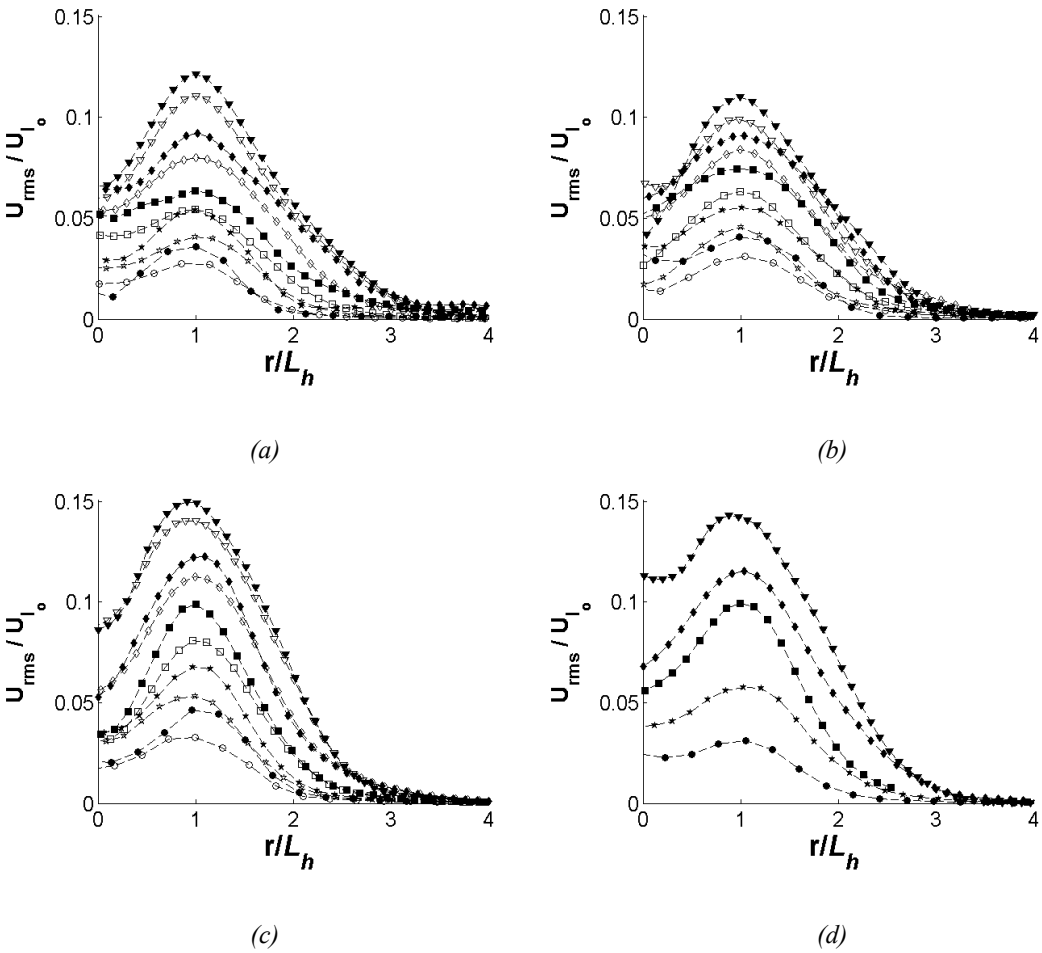

Figure 43: Normalized streamwise radial profiles (hollow) filtered fluctuating velocity (filled) total fluctuating velocity at; $50D_i$ (–○–), $100D_i$ (–☆–), $150D_i$ (–□–), $200D_i$ (–◇–), $250D_i$(–▽–) (a) standard Smagorinsky (b) one Equation Eddy (c) dynamic Smagorinsky (d) implicit

To summarize, the results obtained from the dynamic model indicate that a wide range of dynamics is captured by the numerical solver even in the presence of intense gradients while restricting the

numerical dissipation to acceptable smallest scales. The dynamic model exhibits comparable behaviour close to the implicit and allows the development of the flow instabilities and then turbulence.

4.3.3.3 Injection profile effect:

The radial profiles of liquid to gas mass ratio normalised by the centreline value, obtained from the cases with injection models of random drop position & random angles (referred here as R-R), Gaussian drop position & linear angles(referred here as G-L) and Gaussian drop position & random angles (referred here as G-R) are presented Figure 44. R-R injection model randomly distributes the drops on the injection surface along with random drop injection of the angles, in a fixed spray plume angle β, by limiting the drop injection angle from 0 to β/2. Whereas, G-L injection model uses Gaussian distribution for the positioning of the drops on the injection surface with the linear variation of the drop angles varying 0 to β/2 depending on its position on the injection surface. That means the drops near the centre of the injection surface will have smaller angle and the larger angle towards the periphery while respecting the overall spray plume angle at the same time. In the end, G-R injection combines both R-R and G-L injection models by using the G-L for the drop distribution on the injection surface and R-R for injection angles of the drops.

As expected, a high concentration of the liquid mass is present toward the centre due to the axi-symmetric geometry and the overall dynamics produced by the two way coupling. In both G-R and R-R cases the near nozzle region the jet profile is thinner: more liquid is concentrated in the internal core of the plume. But as spray plume progresses further the liquid phase is spreading less in the case of R-R as compared to G-R case. In Figure 44, the R-R keeps more than 48% of the liquid mass at the centre at $250D_i$. The G-R and G-L are the only profiles which exhibit, after an intermediate stage between $100D_i$ and $150D_i$, a recovery of a self-similar profile inside the jets, and droplets spread out of the jet with radial distance more than twice the jet diameter. Lastly, the G-L profile promotes a higher mass profile spread, as visible in Figure 44 and Figure 45.

The axial and traverse cross-sectional planes provide the visual comparison of the three different injection models in Figure 45. The G-L injection model clearly provides more dispersed flow than the other two injection models. R-R model shows a thin liquid core indicating insufficient dispersion.

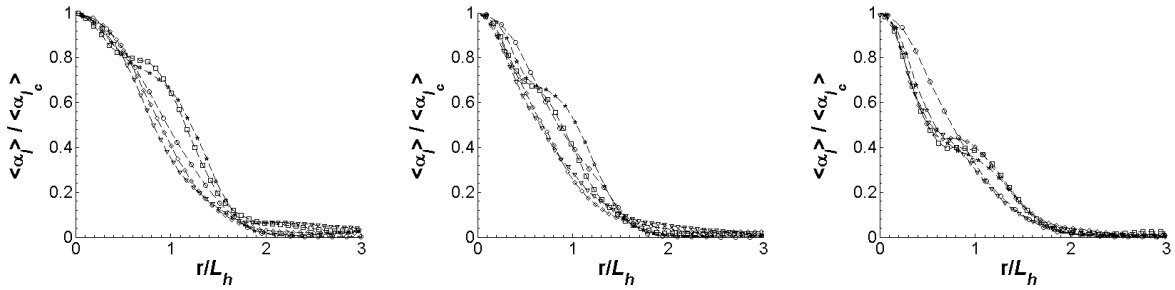

(a) *(b)* *(c)*

Figure 44: Mean radial distribution of Liquid mass normalized by maximum liquid mass at the centreline at; 50D_i (–○–), 100D_i (–☆–), 150D_i (–□–), 200D_i (–◇–), 250D_i(–▽–) with injection models of (a) G-L (b) G-R (c) R-R

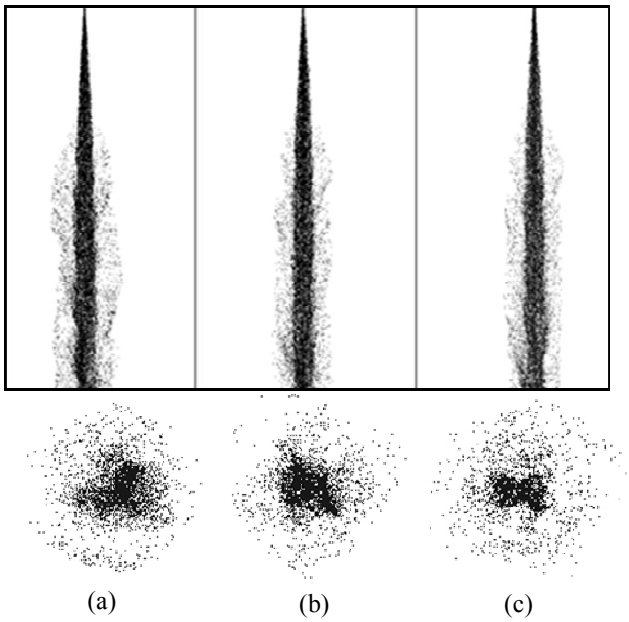

(a) (b) (c)

Figure 45: Spray plumes in the total computational domain with injection models of; (a) G-L; (b) G-R (c) R-R, traverse cross-sectional planes are taken at a downstream location of 200 D_i

As artificial and simplified injection conditions are usually used in spray simulations, it is important to note from the present comparison that the results are largely affected not only by the position of the droplet on the injection surface but also by the injection angle distribution, even for a long distance and after some flow reorganisation. Therefore, the condition G-L is retained for the further analysis.

4.3.3.4 Instabilities and transition

It is important to mention that from this point onwards dynamic Smagorinsky model, which in comparison to the other fixed models performed better, will be used for all the cases.

The overall spray behaviour is close to a gaseous jet. The spray exhibits clearly three main features: an instability development, a transitional phase and lastly a developed turbulent phase. These phases are also driven by the overall characteristic drag time, which allows us to introduce an equilibrium distance that is the result of the individual drops drag time, their global flow and the spray angle. These features are influenced, when exist, by the secondary break-up length and by evaporation.

In the transition zone, the plot of gas velocity at the centreline (U_c) in Figure 46 shows a rapid increase in the velocity of entrained gas flow to its maximum, and around $10D_i$ the mean velocity starts to decrease downstream. Since the drops are injected in the stagnant air, therefore, the spray droplets immediately entrain the air and thus the gas centreline velocity quickly attains the same velocity as the drops.

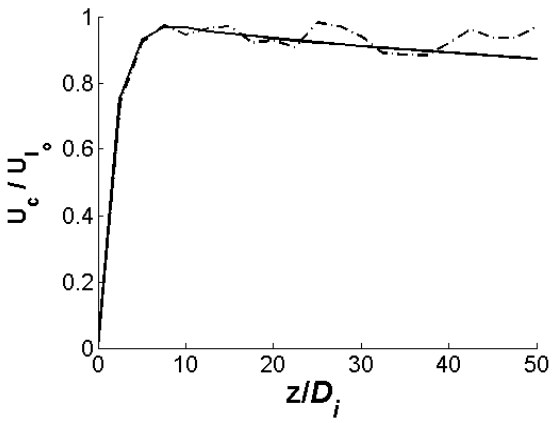

Figure 46: Normalized gas filtered streamwise velocity along the centreline versus distance until $50D_i$ (Solid line) Mean Velocity (dashed line) Instantaneous velocity

The vortical structures represented by vorticity field based on the fluctuating velocity in, Figure 47, indicate the sense of rotation of the vortical structures and their orientation in the space. In the top half part, the vorticity structure confirms the roll up process, with some asymmetry between the two opposite sides.

The potential core in these cases is very small and cannot be resolved with the used mesh size. Further downstream, the helicoidal modes appear again, as observed in Figure 42. The vorticity appears to be diffused in the overall two phase jet cone.

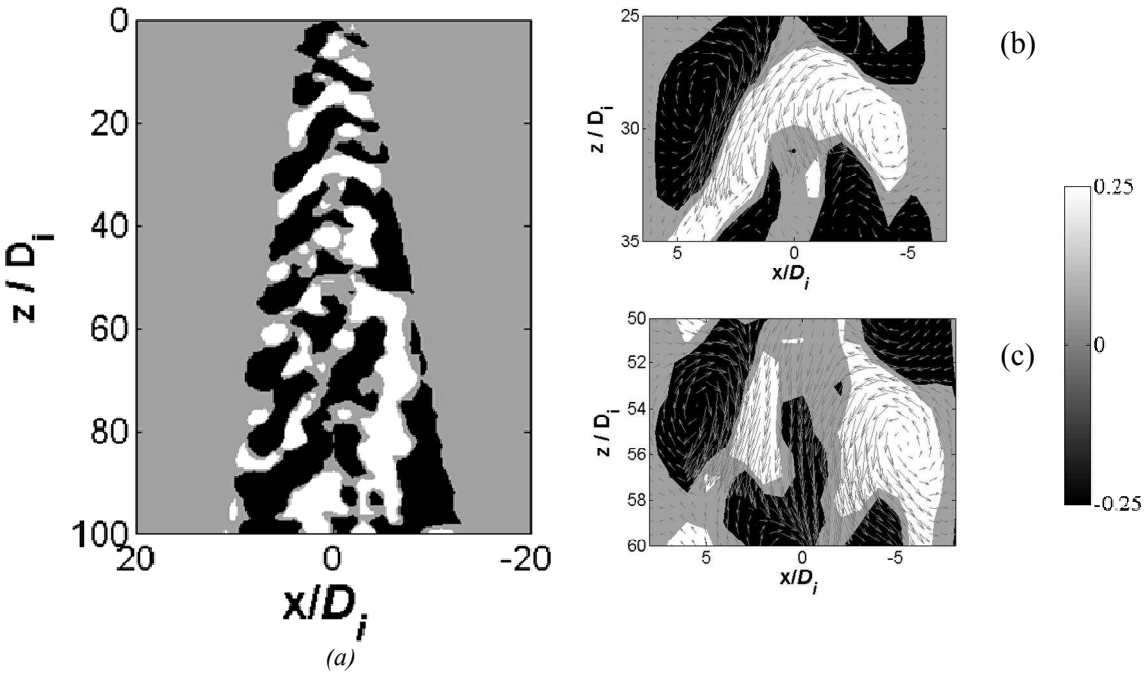

Figure 47 : Normalized vorticity based on the fluctuating velocity (a) Planar cut 100 X/ D_i; (b & c) superimposed by fluctuating velocity vectors

Figure 48: Iso-surfaces of Qn=0.25 colored by helicity

4.3.3.5 Developed turbulence

Based on the theory of turbulent symmetric round jets (Pope S. B., 2000), the turbulence properties of the spray are investigated in this section. Since the spray is round and symmetric, therefore, it is preferable to work in cylindrical coordinates rather than in Cartesian coordinates. The filtered fluctuating velocity components in terms of cylindrical coordinates r, and θ, z are denoted as $\widetilde{u'}$, $\widetilde{v'}$, $\widetilde{w'}$. The spray half width in this section is denoted as the r_h.

The profiles of filtered normal and shear components of Reynolds stress tensor are presented in Figure 49 and Figure 50, respectively. The normalized profiles of all three normal stresses increase steadily before becoming self similar at $200D_i$. The normal stress component in z-direction appears to be the most dominant one which fluctuates about three time more than the other two components.

Similarly, the streamwise profiles of Reynolds shear stress also demonstrate self similarity at $200D_i$. It is clearly observed that the conditions of the isotropy are not reached, as the flow is still directionally dependent as the normal and shear stress components are quite different.

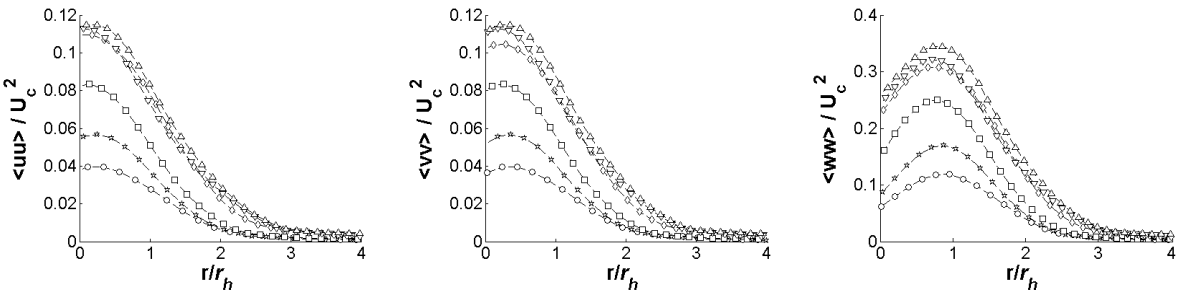

(a) *(b)* *(c)*

Figure 49: Streamwise profiles of filtered normal stress components (a) $\langle\widetilde{u'}\widetilde{u'}\rangle$ (b) $\langle\widetilde{v'}\widetilde{v'}\rangle$ (c) $\langle\widetilde{w'}\widetilde{w'}\rangle$ normalized by the centreline velocity at $50D_i$ (–⊖–), $100D_i$ (–☆–), $150D_i$ (–□–), $200D_i$ (–◇–), $250D_i$(–▽–)

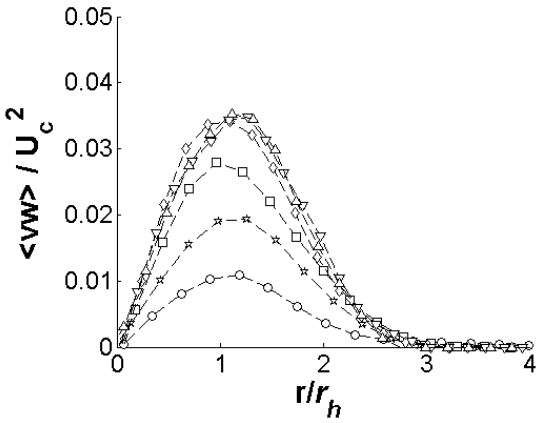

Figure 50: Streamwise profiles of filtered shear stress component $\langle \widetilde{v'}\widetilde{w'} \rangle$ normalized by the centreline velocity $50D_i$ (–○–), $100D_i$ (–☆–), $150D_i$ (–□–), $200D_i$ (–◇–), $250D_i$(–▽–)

The evolution of the velocity and the spray plume half width distance along the centreline presented in Figure 51 and Figure 52 respectively, show a quasi-linear behaviour in average from $25D_i$ to $250Di$ i.e. covering the instability, transition and relaxation to isotropy stages. This behaviour is similar to the gaseous jet behaviour $U_c/\ U_{l_o} = 20\ z/\ D_i$ and as $L_h/Di = 20\ z/\ D_i$ (Wang, Fröhlich, Michelassi, & Rodi, 2008). For the present two-phase simulations, we propose to substitute the liquid velocity to the gas velocity, as the gas velocity centreline slope tends to the liquid value for z = 0.

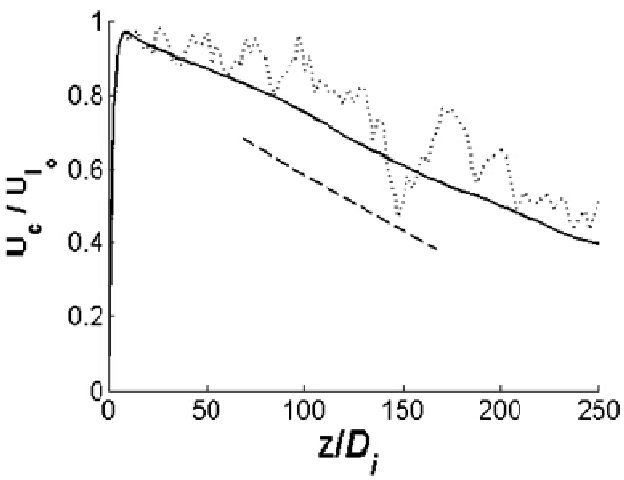

Figure 51 : Normalized velocity along the centrelines versus distance with dynamic Smagorinsky mode, (Solid line) Mean velocity (dotted line) Instantaneous Velocity (dashed line) Wang, Fröhlich, Michelassi, & Rodi, 2008

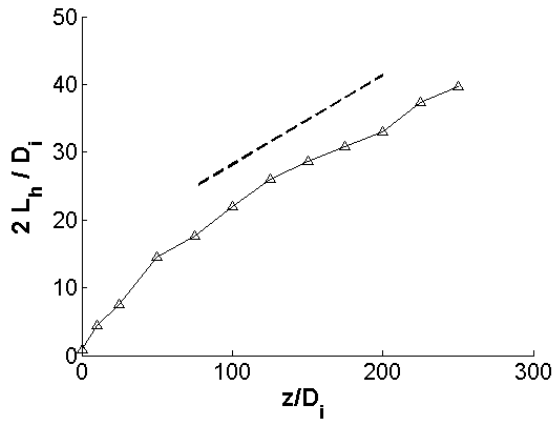

Figure 52: Normalized plume half width along the centrelines versus distance with dynamic Smagorinsky model, dashed line represents the slope of the gas jet half width (Wang, Fröhlich, Michelassi, & Rodi, 2008)

An important aspect which is revealed in Figure 53 is the self similarity of the streamwise velocity similarly as a single phase free jets (Foysi, Mellado, & Sarkar, 2010; Wang, Fröhlich, Michelassi, & Rodi, 2008) which is also confirmed by (Doudou, 2005) for diesel sprays. The self-similarity profiles indicate that the turbulence increases at similar rate in streamwise direction.

Another useful quantity which is needed to be introduced here is the gas Reynolds number. Carrier phase Reynolds number is determined by calculating the diameter of the spray cone at a given downstream position. In this case, the gas Reynolds numbers vary from 35,000 at $50D_i$ to 50,000 at $250D_i$.

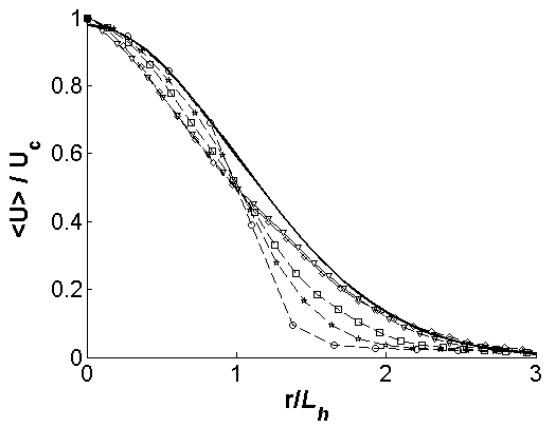

Figure 53: Radial distribution of (a) gas velocity; with dynamic Smagorinsky model downstream at $50D_i$ (–○–), $100D_i$ (–☆–), $150D_i$ (–□–), $200D_i$ (–◇–), $250D_i$(–▽–); solid line, Gaussian fit with mean =0 and standard deviation of 1.

The normalized radial profiles of streamwise rms fluctuations of liquid phase give an insight to the variation trends of droplet fluctuation levels. A continuous increase in the streamwise rms fluctuations is observed with maximum value of rms fluctuation at $250D_i$ of 12%, as presented in Figure 54 (a). Although the streamwise rms fluctuation of the liquid phase follow a similar trend to the rms fluctuations of the gas phase in Figure 43 but dispersed phase is more dominant initially until $100D_i$ but after that the fluctuations reach quasi similar level. The gas phase fluctuations prevail at $200D_i$ and onwards.

It is interesting to note that the liquid phase, unlike carrier phase, does not exhibit a great deal of fluctuations at the centreline of the spray. The levels of fluctuation remain below than 2% of the liquid injection velocity. That means, the spray core remains undisturbed for a long period. However, the streamwise rms fluctuations of the slip velocity show large amount of fluctuations. At $250D_i$ the levels of fluctuations of slip velocity are quite significant. At centreline the rms slip velocity is about 6% of the initial injection velocity and it is about 10% in the shear layer.

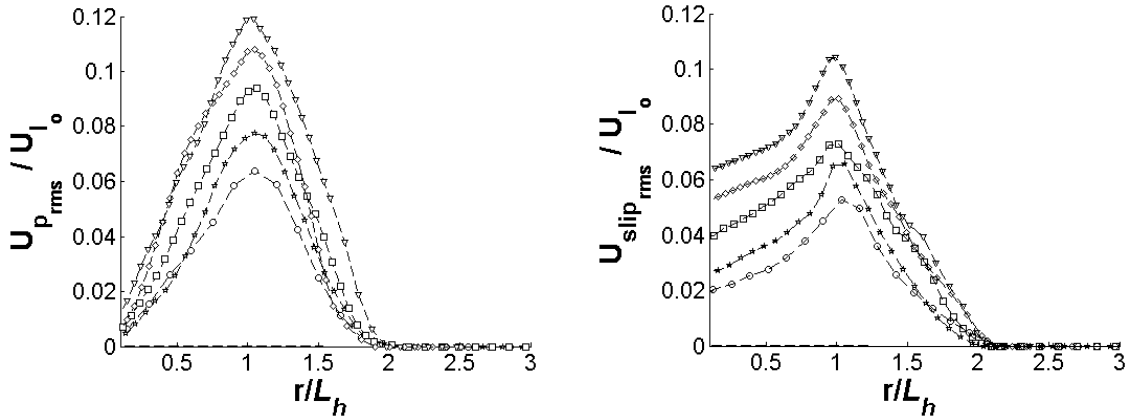

(a) *(b)*

Figure 54: Normalized radial profiles of streamwise fluctuating velocity (a) dispersed Phase (b) Slip velocity; with dynamic Smagorinsky model at downstream locations of; $50D_i$ (–○–), $100D_i$ (–☆–), $150D_i$ (–□–), $200D_i$ (–◇–), $250D_i$(–▽–)

The Stokes numbers at filter scale (St_Δ) and Kolmogorov scale (St_η), at various downstream locations have been presented in Figure 55 (a) and (b) respectively. The stoke numbers are based on the fixed drop size and the filter time scales τ_Δ and the Kolmogorov time scales τ_η are computed (Pope S. B., 2000) as follows:

$$\tau_\Delta = \tau_I \left(\frac{\Delta}{l_I}\right)^{2/3} ; \tau_\eta = \tau_I \left(\frac{\eta}{l_I}\right)^{2/3} \quad (93)$$

where, l_I is the integral length scale and τ_I is the integral time scale which is estimated from the energy spectrum. The highest point in the energy spectrum corresponds to the integral scale.

The Stokes numbers at filter and Kolmogorov scale are quite large at $50D_i$ and $100D_i$. The Stokes number at filter scale decrease further downstream to a value of 1.5. Whereas, the Kolmogorov scale is reduced from a value of 32 to 21.5.

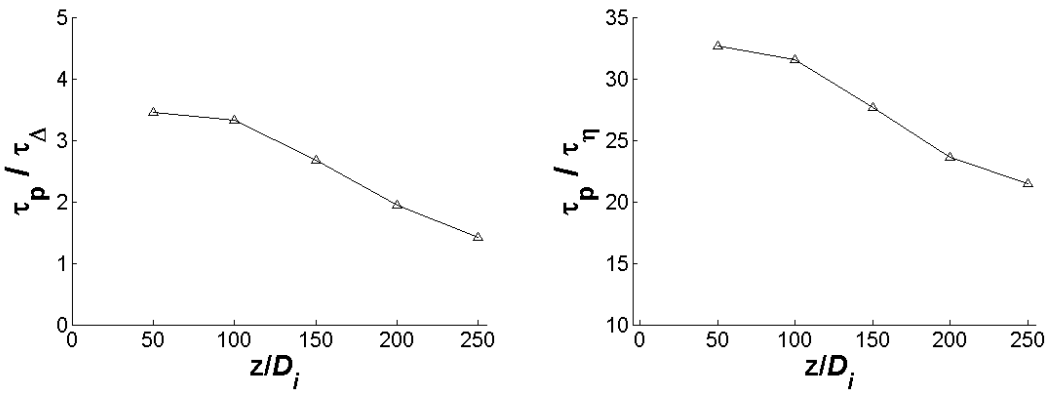

(a) *(b)*

Figure 55: Stoke Numbers at (a) filter scale Δ (b)Kolmogorov scale η ; with dynamic Smagorinsky model in Streamwise direction

Since $St_\eta \gg 1$, therefore, the droplets mainly remain uneffected by the eddies of Kolmogorov size. However at $250D_i$, the Stokes at filter scale is nearly equal to 1 ($St_\Delta \cong 1$) which means that the drops in the developed turbulence region are weakly be effected by the eddies of filter size.

4.3.3.6 Comparison of Simulation and experimental data:

All previous simulation cases in this chapter were performed without considering droplet breakup model which plays an important role in the spray development. As it has been established, from the various simulation tests in this chapter, that the G-L injection model along with dynamic Smagorinsky performs better than the rest of the models, therefore, it becomes important to test these models against the available experimental data. Therefore G-L injection model with dynamic Smagorinsky model and the droplet breakup model of ETAB has been utilized to perform the simulation. It is important to remember that the collision model is not included in this simulation.

The results of the simulation are compared with the PDA data. The setup of experimental PDA measurements is described in detail in the Appendix A. The PDA measurements are performed on a single spray plume injected from a 3-hole GDI injector. It is important to note that the injector is placed vertically in the experiments; consequently, the measured spray plume, unlike the previous simulation, has an angle of 38°. Therefore, in order to compare the results of simulation and experiment, the simulation is performed with inclined spray plume.

The results, in Figure 56, show a reasonable agreement with measurements even in the absence of the collision model. The peak of drop size PDF profile is well captured by the simulation and it suggests that the large numbers of droplets are reduced to about 2% of the inlet or injection diameter. However, the tendency of finding droplets with the size lower than 1% of injection diameter is very scarce in the simulation as compared to the experiments. The axial and radial profiles of the simulation are slightly shifted to the right but the overall trend is predicted correctly.

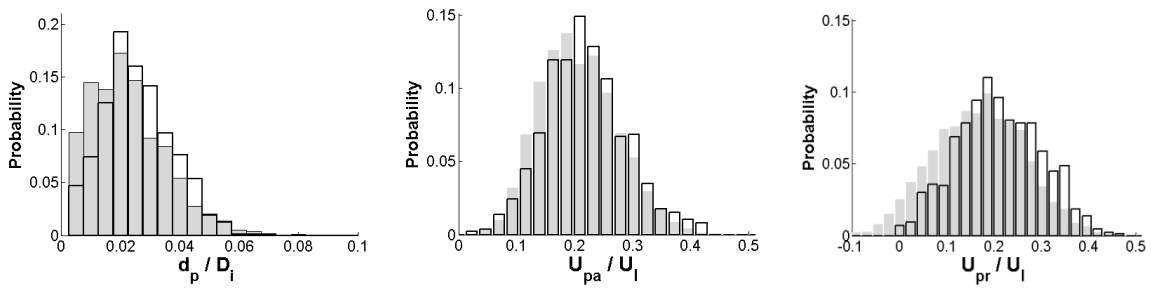

(a) (b) (c)

Figure 56: PDF comparison, 40mm downstream at spray plume centre , (a) Diameter (b) Axial Velocity (c) Radial velocity(filled) experimental (hollow) numerical

In experiments there is some probability of finding drops with negative radial velocities which indicates that the drops actually go inside the spray cone which are not recovered in the simulation results. Finding drops with negative radial velocities at the centre of the spray plume in PDA measurements can be because of the jet flapping.

4.4 Conclusion

In all the test cases, the liquid is injected with a given angle outside of the atomizer. Different classical subgrid models are tested for the carrier phase. The dynamic Smagorinsky and the one-equation model are found to demonstrate a correct ability to capture transitional flow. Most of the spectra ranges are closed to a -5/3 spectrum whatever the subgrid models, even if differences exist between the models.

A small amount of perturbation superimposed at the beginning of the injection during a short initial delay has shown to activate the flow instabilities. Constant injection mass and velocity profiles result in a downstream shear layer flow, whereas, a Gaussian injection profile result in a downstream flow which exhibits characteristic features of measured spray. It is shown that even with two-phase lagrangian limitation, Large Eddy Simulation can capture 90% of the turbulence spectrum. However, in these typical cases, the sensibility of capturing vortical structures depending on the subgrid carrier model is demonstrated. The dynamic model is found to give the more acceptable result. The importance of the subgrid dispersion effect of the carrier phase on the dispersed phase and the reverse subgrid effect of the dispersed phase on the carrier phase is also demonstrated.

Three zones are identified: the round instability development close-up zone, the transitional zone and the self similar turbulent zone. Results of close-up instabilities have been found to be dependent on a limited amount of excitations at the injection. Physically, such excitations are thought to be generated in the internal flow of the injector, from pressure waves, turbulence or detachment of cavitation pockets. In this chapter, different simplified injection models are compared in order to choose the best model which provides reasonably realistic results. A shortcoming which can be associated to such an approach is the lack of any information from the internal flow the injector at the inlet

conditions. Since the GDI sprays are strongly dependent on the internal flow of the injectors therefore it is necessary to develop an approach which could link the information of the internal flow of the injector to the spray inlet conditions. This is approach is discussed in the next chapter.

Chapter 5 LES of Single Spray Plume of GDI Injector

In the previous chapter, a simplified injection model based on the gaussian distribution of the injection position of the drops along with linear variation of the injection angles of the drops, depending on the drop location, have been assumed as an alternative to the random injection of drops. Unfortunately, it is not that simple to predict such a complex flow merely with a simplified model. In reality, the flow arrangement at the exit of the nozzle of an injector is more complex. The liquid is usually not uniformly distributed at the nozzle exit due to the presense of the cavitation inside the metering hole which entrust unpredictability to the sprays. Therefore, the internal flow dynamics of the injector cannot be neglected, as demonstrated in the DNS study of (Sander & Weigand, 2008). (Befrui, Corbinelli, Spiekermann, Shost, & Lai, 2012) demonstrated the effect of nozzle geometry on the spray charecteristics by using LES based Volume of Fluid (VOF) approach.

In VOF approach of two phase flows, typically liquid phase and vapour phase are solved while respecting the compressibility of each phase. The two phase are distinguished by solving a balance equation for the liquid to vapour mass ratio (α). Surface tension is included by reconstructing an interface at prescribed value of α. For more information, the reader should refer to the documentation of OpenFOAM® (http://www.openfoam.org/docs/). The LES-VOF approach of internal flow of the injector has been validated against spray close-up visualizations. Since the topic of LES-VOF simulation is out of scope of the current work therefore no further details are provided.

In the past, (Befrui, Corbinelli, D'Onofrio, & Varble, 2011) coupled the internal nozzle flow from LES VOF to the lagrangian RANS spray simulation but limiting the coupling only to the injection velocity and the turbulent intensities. To our knowledge, there is no detailed coupling of the LES internal flow with LES of lagrangian spray is found in the literature.

A weak coupling approach is developed in this regard to transfer the output results of in-house VOF cavitating nozzle flow simulation to the lagrangian injection as input conditions. This coupling approach introduces the internal flow dynamics in the lagrangian simulation. The VOF simulations corresponds to the real geometry used for validation and has been conducted in FUI-project "MAGIE".

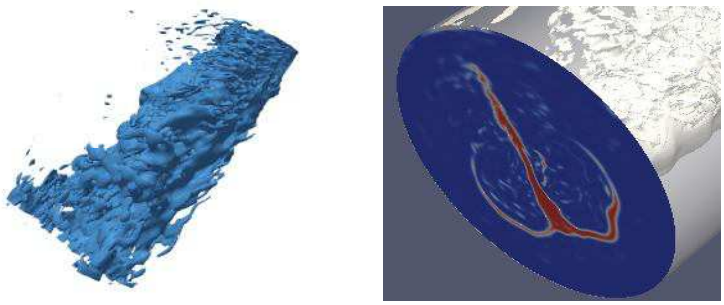

(a) *(b)*

Figure 57: VOF results; (a) iso-surface of liquid; (b) Cross-section of the liquid to gas volume ratio

5.1 Nozzle Flow Dynamics:

The results from an in house volume of fluid simulation, at an injection pressure of 90 bar under the ambient conditions, have been presented here which explains the internal nozzle flow effects. A cross-sectional plane, at a downstream location of $5D_i$, is considered to investigate liquid distribution along with liquid angle, velocity and drop size resulting from the ligament breakup.

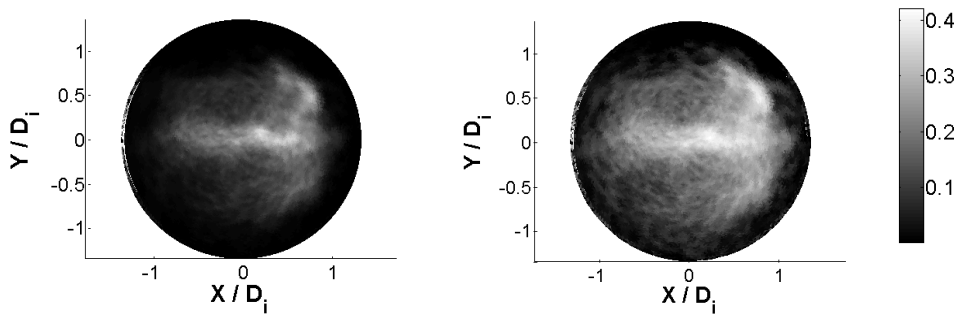

(a) *(b)*

Figure 58: Volume of Fluid simulation, cross-section of liquid to gas ratio at the nozzle outlet (a) Mean (b) rms

The distribution of mean liquid to gas mass ratio $\langle \alpha_l \rangle$, in Figure 58, appears to be far more complex than what a simplified or random profile suggest. An anchor shape of $\langle \alpha_l \rangle$ appears due to presence of cavitation which generates two counter rotating vortices. The RMS or standard deviation of α_l indicates that the liquid is not evenly distributed across the injection hole and injection surface actually reduces.

However, mean liquid velocity distribution seems to be quasi constant irrespective of the liquid density distribution. In Figure 59, both mean liquid velocity and rms liquid velocity are normalized by the maximum liquid velocity at the cross-sectional plane. The rms liquid velocity is around 5% of the maximum liquid velocity at the region where there is high probability of the liquid presence. Although in the periphery of the cavitation side high rms values do exist but α_l in those regions is very low.

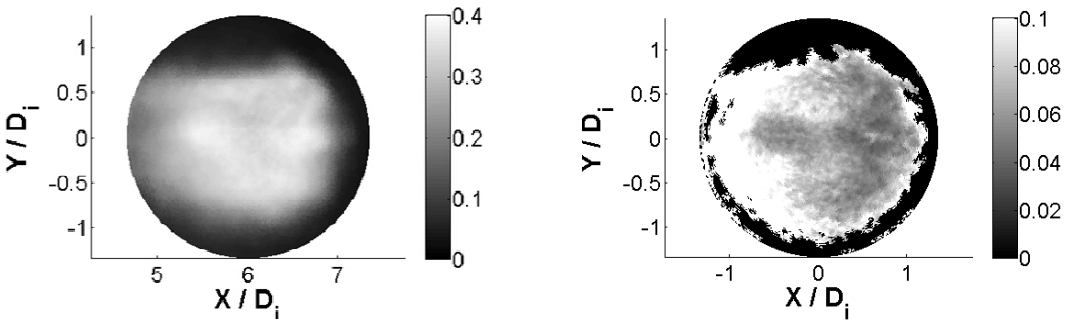

(a) *(b)*

Figure 59: Volume of Fluid simulation, cross-section of mean liquid velocity normalized in terms of Mach number of at the nozzle outlet (a) mean (b) rms

The angle distribution of the liquid, in Figure 60, shows a linear trend and it is simply a function of the radial distance of the hole to the nozzle centre. The angle increases with distance from nozzle centre. The liquid at the centre of the nozzle will have a little angle in comparison to the drops at the periphery of the nozzle. In Figure 60 (a), the angle on the cavitation side $(X/D_i < 0)$ is higher than the non cavitation side $(X/D_i > 0)$.

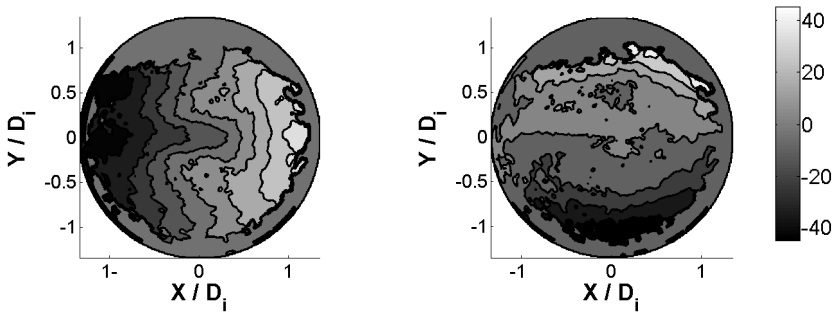

(a) *(b)*

Figure 60: Volume of Fluid simulation, cross-section of the liquid angle from the centreline of nozzle (a) radial (b) azimuthal

The cavitation not only expands the plume angle but also generates some small drops in the nozzle vicinity. In experiments, it is almost impossible to measure the drop sizes very close to the nozzle but from the VOF simulations the drop sizes can be estimated by separating the detached liquid drops from the main liquid core. The drop size distribution on the cavitation side is presented in the Figure 61. There is a high probability of drops with 2μm to 4μm. A lognormal profile from equation (73), with a mean of value of 1.35 and standard deviation of 0.35, fits well with drop size distribution.

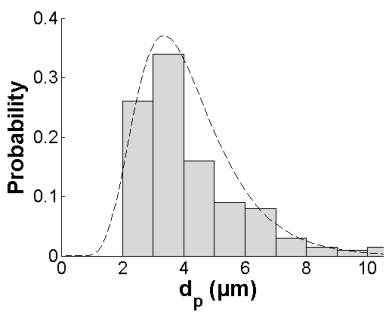

Figure 61: Drop size distribution on the cavitation side, dashed line represents the lognormal distribution with a mean value of 1.35 and standard deviation of 0.375

Since the VOF simulation gives a realistic liquid distribution over the cross-sectional plane but in the form of ligaments. Therefore, a primary breakup model has to be introduced in order to generate the drop size distribution for the lagrangian simulations. The methodology of ligament breakup has been explained in the Appendix B. The thickness of the ligaments has been realised to be in between 3.5%

to 10% of D_i which suggests that the primary breakup has already been resolved by the simulation to a certain extent. The ligament breakup gives the drop sizes of around $0.05D_i$ to $0.15D_i$. The Figure 62 reveals thta there is a high probability of finding largest drop sizes at the centre of the nozzle and smaller drops away from the centre of the nozzle. Moreover, there is some probability of finding the largest drops at the cavitation side as well but here the probability of finding liquid is quite low which means bigger drops will be scarce on cavitation side.

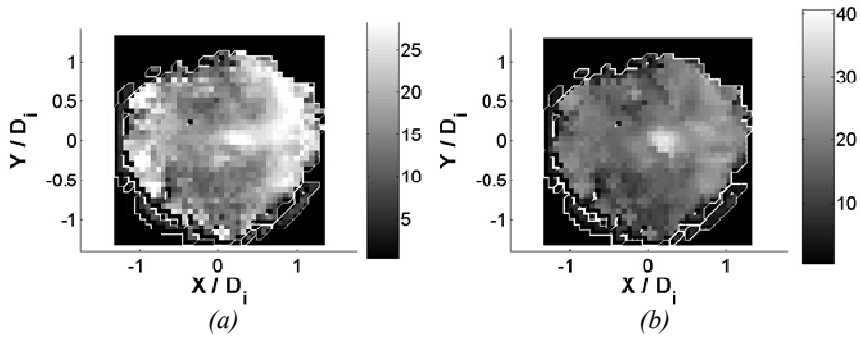

Figure 62: Volume of Fluid simulation, cross-section of drop size distribution (a) D10 (b) SMD

5.2 Coupling of VOF and lagrangian simulation:

The output results of VOF simulations are stored, for a given number of time intervals Δt_i, in form of a database with information of velocity vector (x, y, t), drop size PDF (x, y, d_p, t) and mass load (α). Initially a random integer is generated which locates the coordinates of a point in the nozzle that has some probability of the liquid presence i.e. $\alpha > 0.05$, otherwise a new random integer is generated. Then at a stochastically selected point, a corresponding drop size, velocity magnitude and the injection angle is deduced from the data base. A loop of iterations is performed until a suitable number of points have been stored for each time interval (Δt_i).

The simulation time step (Δt) is smaller than the time interval of the database Δt_i, therefore for a given Δt_i several simulation time steps are performed until $\sum_n \Delta t > \Delta t_i$.

5.3 Studied Cases and numerical setup:

Two cases, under ambient conditions, are investigated in this section, with injection pressure of 100 bar and 200 bar which corresponds to the injection velocities of 0.42 Ma and 0.57 Ma respectively. The injection parameters at the inlet are obtained from the in-house VOF simulation results. The Large Eddy Simulations have been performed with dynamic Smagorinsky subgrid scale model.

The spray sub models, explained in detail in the spray modelling section, include Enhanced TAB droplet breakup model, stochastic dispersion model, trajectory collision model and standard drag model. Evaporation model has been excluded due to non evaporating conditions. Two-way coupling, explained thoroughly in the previous section, has also been included. Compressibility and rarefaction effects on the drag of the particles are also included by using the model presented in the previous chapter.

The numerical schemes used for the simulations presented in this chapter are same as the presented in Chapter 4 in section 4.2.1. All the schemes are described in the Appendix C.

Parameters	Values	
Injection Pressure	100 bar	200bar
Injection Velocity	0.42 Ma	0.57 Ma
Chamber Pressure	1 bar	1 bar
Fuel Temperature	25°C	25 °C
Chamber Temperature	25°C	25 °C

Table 8: Injection parameters

5.4 Steady State Results

The steady state results are presented here in this section.

5.5.1 Comparison of PDA and LES data:

As explained in the previous chapter, the PDA measurements are performed on the inclined spray plume injected from a vertically placed 3-hole injector. Therefore, the simulations are performed according to the experimental conditions. The spray plume is inclined at an angle of 38°.

The comparisons of simulation results with the experimental PDA measurements, for drop diameter, axial velocity and radial velocity, at a downstream location of $250D_i$, at the spray centreline $r/L_h = 0$ and at the periphery $r/L_h = 2$, are presented in Figure 63 and onwards for the cases with injection pressure of 100 bar and 200 bar. Since PDA measurements are performed on a localized point in the spray, therefore, it is necessary to extract the simulation data in a similar way. For this purpose, a cubic measurement volume with a length of size $10D_i$ is taken at the desired locations. The drop sizes and velocities in the control volume are then recorded for a steady state injection interval. It is necessary to mention here that the results presented in this part have not been normalized in order to make it simpler for the design engineers to comprehend the results who usually want to do a quick comparison with the already available data.

5.5.1.1 Probability Density Function comparison of LES and PDA at 100 bar:

The Probability Density Function (PDF) distribution of the drop size diameter at the centre of the plume for an injection pressure of 100 bar at $250D_i$ downstream location, in Figure 63(a), show a peak at 4µm but there is also reasonably high probability of the finding the drops of diameter from 3µm to 9µm. There is a very little probability of encountering the drop size larger than 15µm. The simulation captures the peak and the overall distribution of drop sizes reasonably well. However the probabilities of larger drops are higher in simulation results. In Figure 63(b & c), the experiment

results demonstrate the peak of both axial velocity and radial velocity at 35m/s while simulation results shows these peaks at 35m/s and 30m/s respectively. The slightly higher probabilities of larger drops, in the simulation, effect the drop dispersion and thus the radial velocity.

The simulation also estimates the drop sizes and velocities at the periphery reasonably well. At the periphery of the spray plume the peak of drop size reduces to 3µm. The probability of finding smaller drops (1µm to 2µm) increases at periphery. In comparison to the experiments the simulation again shows similar trends at the periphery of the spray plume. The probability of smaller drops is again slightly lesser in the simulation. At the periphery, the PDA measurements manifest a radial velocity peak at -5m/s where as the simulation has peak slightly shifted to right at 0m/s. Furthermore, the simulation results show slightly higher probabilities of negative radial velocities at the periphery than the PDA measurements.

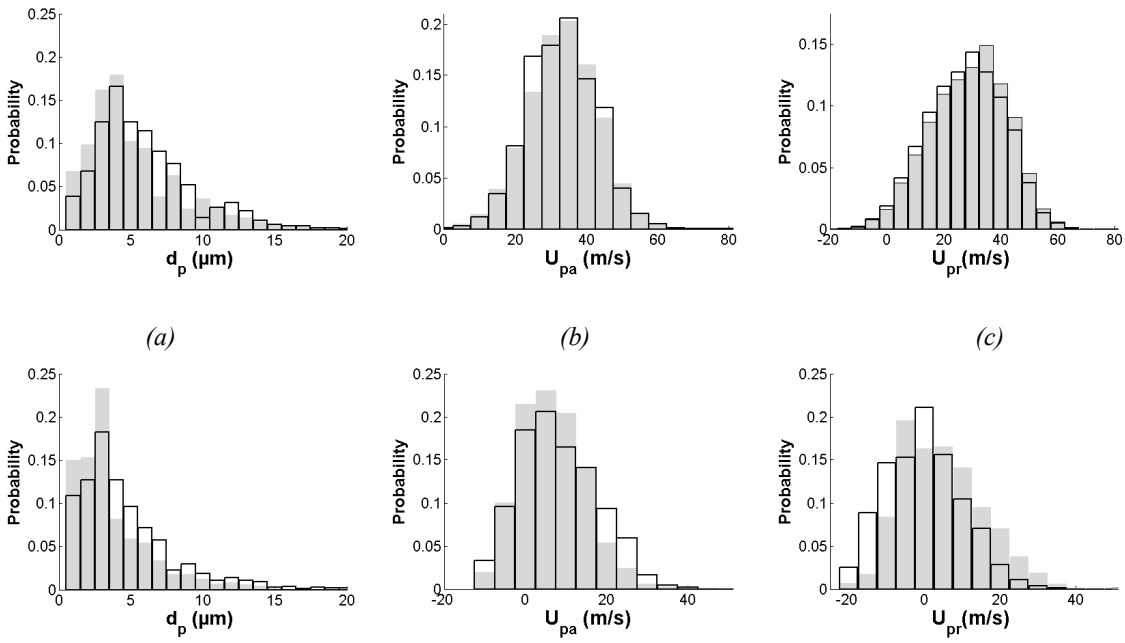

Figure 63: PDF distributions for P_i = 100 bar at a downstream location of $250D_i$; at spray plume centre, (a) diameter (b) axial velocity (c) radial velocity; at periphery (d) diameter (e) axial velocity (f) radial velocity; (filled) experimental (hollow) numerical

In the simulation, the drop sizes in the spray plume are directly linked to the injection conditions which, in our case, are produced VOF simulation. The drop sizes produced by the VOF simulation

are linked to the mesh size. Further mesh refinement in VOF simulation may produce the smaller drops and may eradicate the small mismatch between the experiments and simulations.

5.5.1.2 Joint Probability Density Function comparison of LES and PDA at 100 bar:

The PDF profiles show the drop statistics independently which makes it impossible to identify the drops which move faster or slower. This issue can easily be addressed by the joint PDF which creates a two dimension PDF distribution for given variables. The Joint Probability Density Function (JPDF) of drop diameter and drop velocities at $250D_i$ downstream location, at the spray plume centre and periphery have been displayed in Figure 64 and Figure 65 respectively.

The JPDF profiles show a Gaussian like distribution of axial and radial velocity. The drops with the very small diameter have equal probability of being slowest or fastest both in axial or radial directions. On the other hand, larger drops tend to show less variation in the velocity. The joint PDFs of the axial and radial velocities in Figure 66 depict a linear trend.

The simulations also produce comparable results to PDA measurements. At the centre of spray plume, both experiments and simulations show that mostly the smaller drops with diameter less than 3μm tend to show large variations in the velocity. This variation in the radial velocity seems to be stronger than axial velocity. Moreover a similar trend, in Figure 65, is observed at the periphery but the simulations show a larger spread in the axial and radial velocity. The simple dispersion model is perhaps over dispersing the smaller drops.

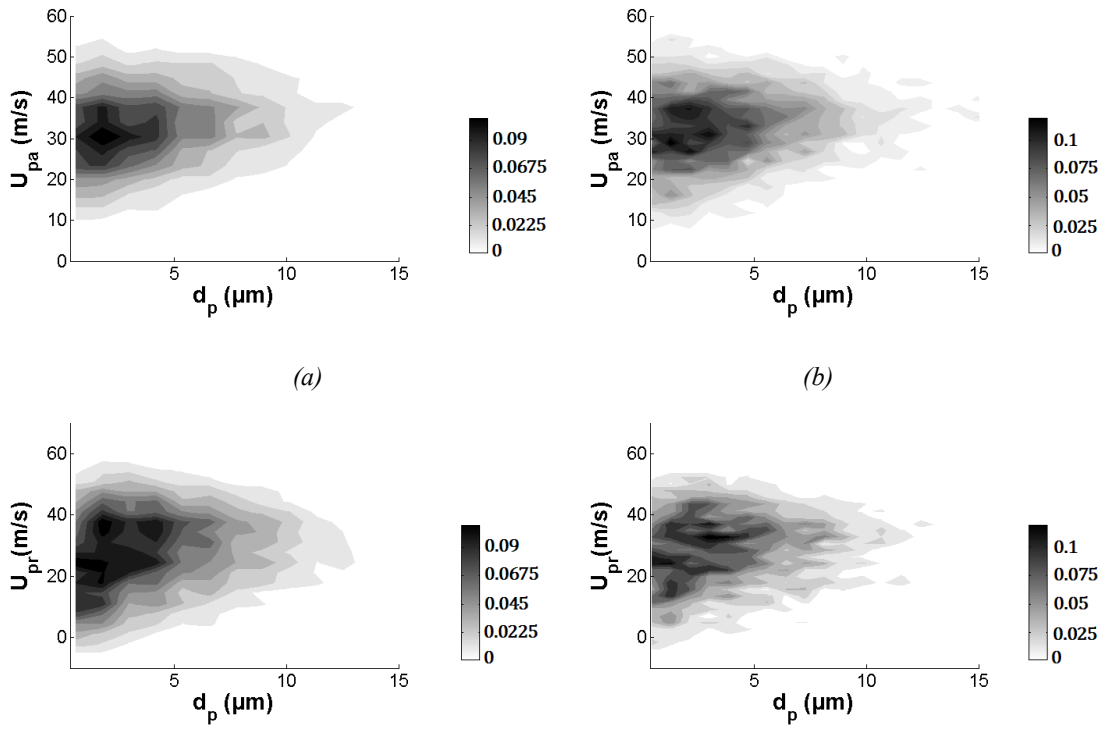

Figure 64: Joint PDF distributions for P_i = 100 bar at a downstream location of $250D_i$; at spray plume centre, for diameter & axial velocity (a) experimental (b) numerical; diameter & radial velocity (c) experimental (d) numerical (gray scale inverted, black denotes maximum)

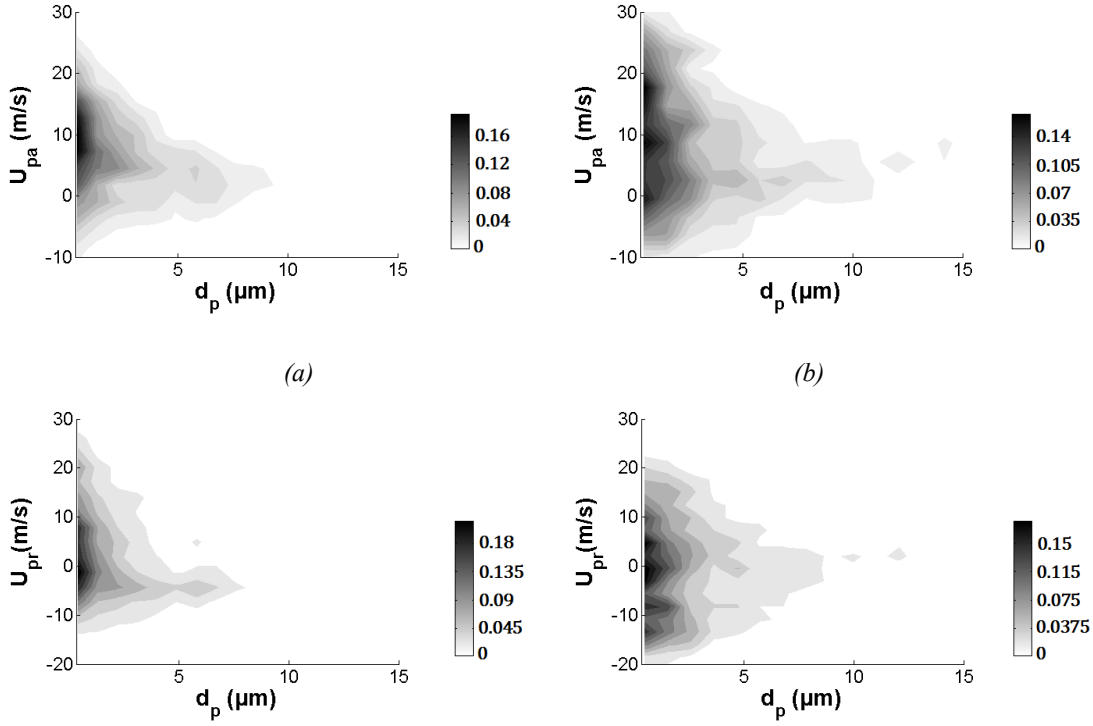

Figure 65: Joint PDF distributions for P_i = 100 bar at a downstream location of $250D_i$; at spray plume periphery, for diameter & axial velocity (a) experimental (b) numerical; diameter & radial velocity (c) experimental (d) numerical (gray scale inverted, black denotes maximum)

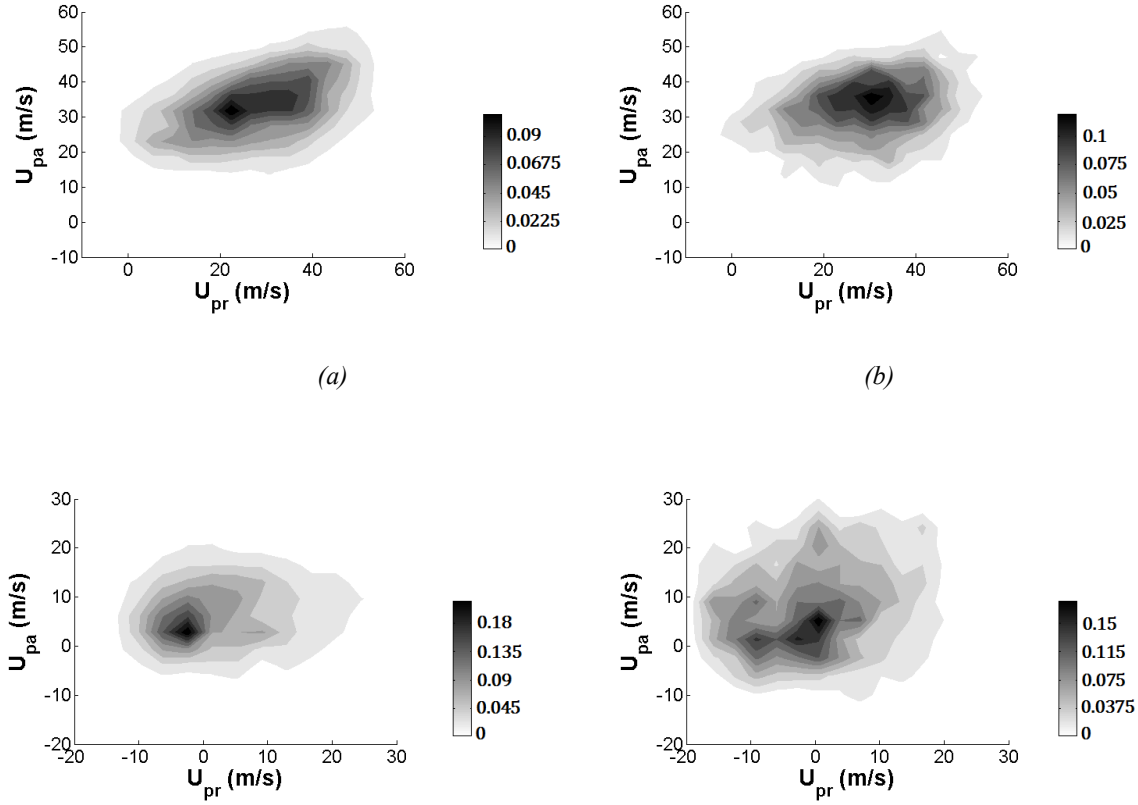

Figure 66: Joint PDF distributions of radial & axial velocity for $P_i = 100\ bar$ at a downstream location of $250D_i$; at spray plume centre, for (a) experimental (b) numerical; spray plume periphery (c) experimental (d) numerical (gray scale inverted, black denotes maximum)

5.5.1.3 PDF comparison of LES and PDA at 200 bar:

The PDF profiles for the injection pressure of 200 bar presented in Figure 67, at a downstream location of $250D_i$, at the spray centreline $r/L_h = 0$ and at the periphery $r/L_h = 2$, also show similar behaviour to the one at lower injection pressure of 100 bar. However the drop sizes are slightly reduced due to higher injection velocity. The experimental data reveals high probability of the existence of drops with diameter of 1µm to 2µm. The simulation results of drop sizes also indicate a similar trend but the probability of very small drops is relatively lower than that of experiments. As expected at the periphery of the spray plume a higher density of smaller drops can be observed.

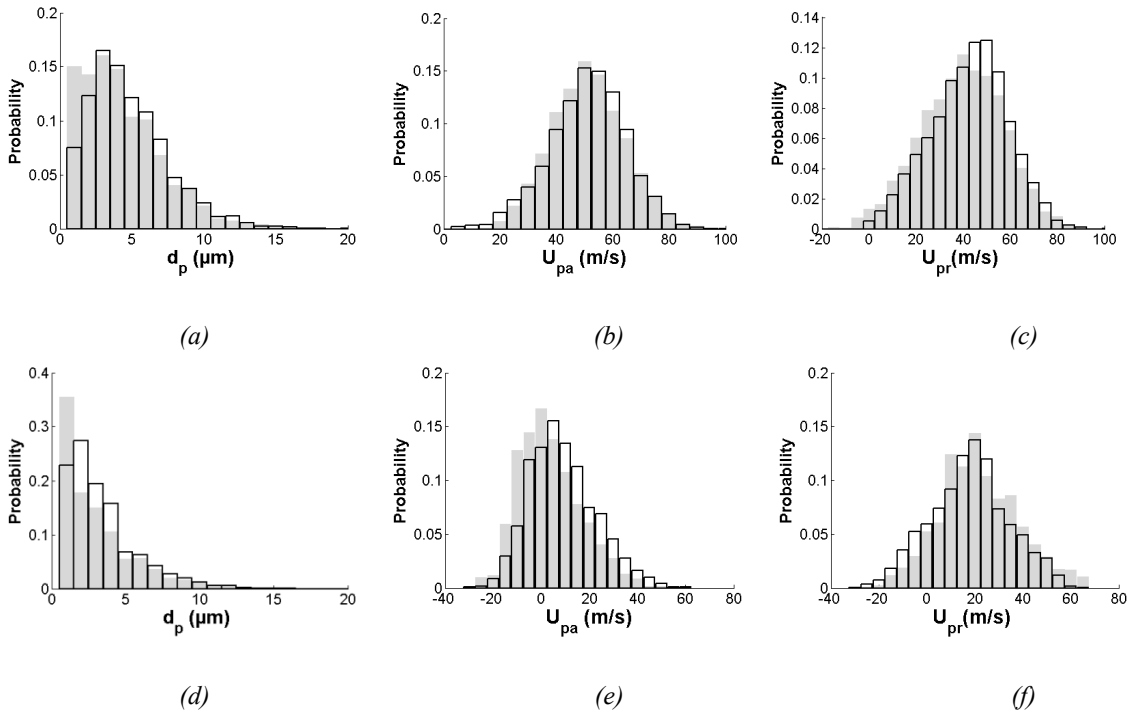

Figure 67: PDF distributions for P_i = 200 bar at a downstream location of $250D_i$; at spray plume centre, (a) diameter (b) axial velocity (c) radial velocity; at periphery (d) diameter (e) axial velocity (f) radial velocity; (filled) experimental (hollow) numerical

The velocity profiles are also captured comparably well by the simulations in comparison to the experiments. In Figure 67 (d) and (e), the axial velocity profile at the periphery of the spray shows a slight shift to the right in comparison to the experimental data. This shift in the axial velocity profile is linked to the lesser number of very small drops found in the simulations which means less probability of drops with negative velocity.

5.5.1.4 JPDF comparison of LES and PDA at 200 bar:

The joint PDFs of axial and radial velocities with drop diameter at the spray centreline are presented in Figure 68 and at the periphery of the spray in Figure 69. The profiles suggest that the smaller drops are more unpredictable in their behaviour. Larger drops have much less variations in the velocities.

The reason for such behaviour is that the smaller drops are very light and have a lower momentum which can easily be influenced by the surrounding conditions.

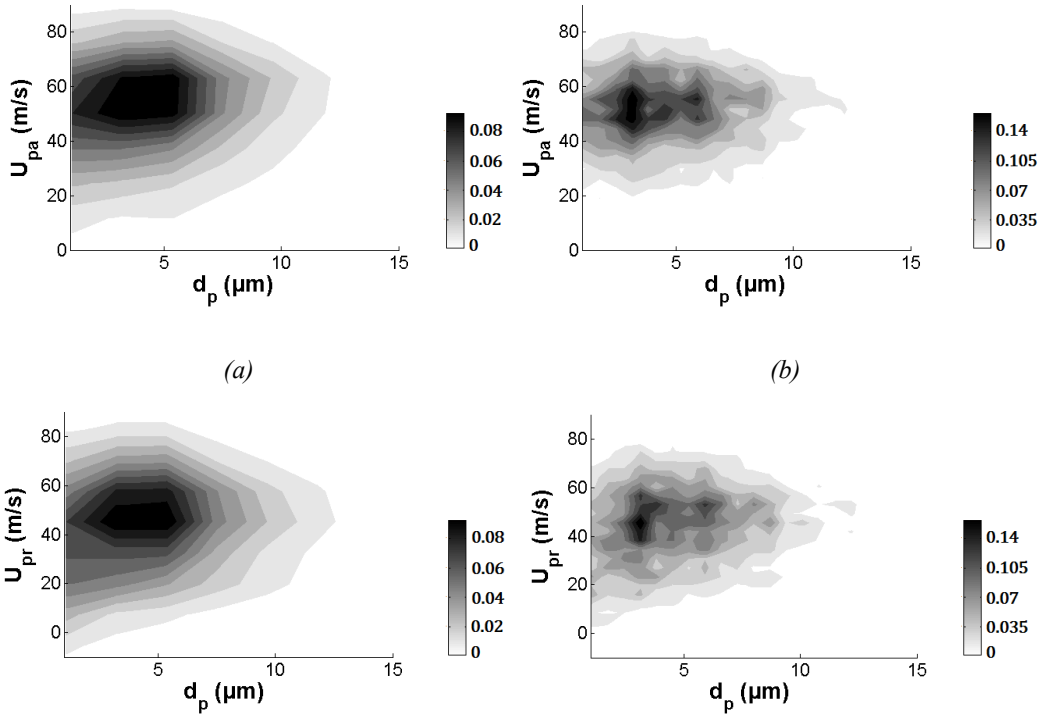

Figure 68: Joint PDF distributions for P_i = 200 bar at a downstream location of $250D_i$; at spray plume centre, for diameter & axial velocity (a) experimental (b) numerical; diameter & radial velocity (c) experimental (d) numerical (gray scale inverted, black denotes maximum)

At the centreline of the spray plume axial velocity in the simulation stays more than 20 m/s whereas in the experiments some of the smaller drops exhibit axial velocity near to zero. Similarly there is no negative radial velocity at the centreline of the spray in the simulation results but the experimental data does show some very small drops with negative radial velocity. This means in the experiments there are some drops which are coming back inside the spray plume while in the simulations the drops do tend slow down or stop but none of the drops is sucked back inside the plume.

The Figure 69 shows the probability of droplets with the negative axial velocity and radial velocity both in experiments and in simulation results at the periphery of the spray. The simulation in

comparison to the experiments, is predicting slightly higher axial velocity for very small drops. Moreover from Figure 70 it can be deduced that the droplets with negative axial velocity and positive radial velocity are entrained away from the spray by the recirculation at the outer region of spray. On the other hand, the drops with negative axial velocity and radial velocity are pushed inside the spray.

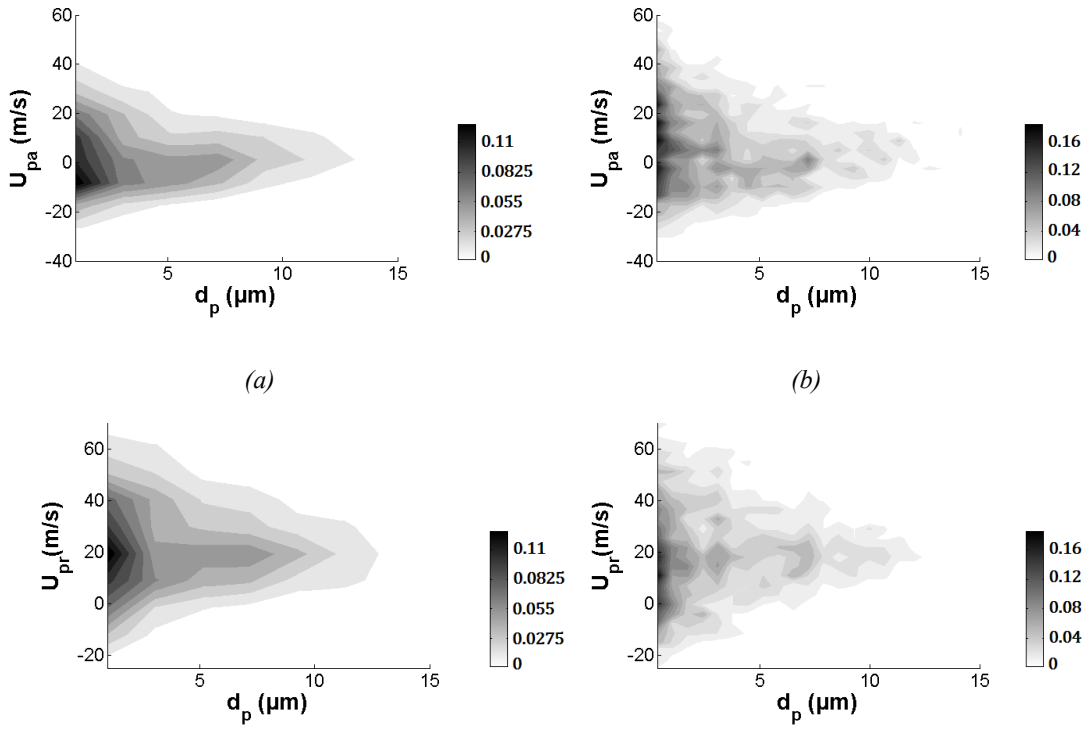

Figure 69: Joint PDF distributions for P_i = 200 bar at a downstream location of 250D_i; at spray plume periphery, for diameter & axial velocity (a) experimental (b) numerical; diameter & radial velocity (c) experimental (d) numerical (gray scale inverted, black denotes maximum)

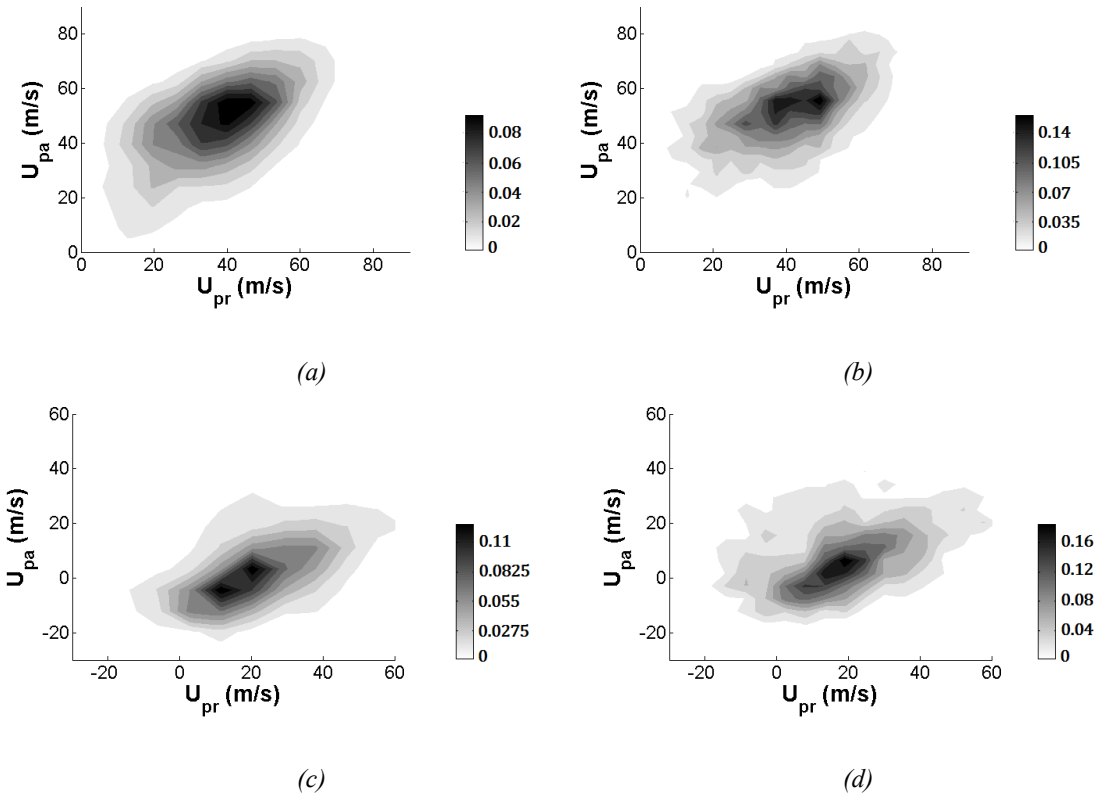

Figure 70: Joint PDF distributions of radial & axial velocity for $P_i = 200\ bar$ at a downstream location of $250D_i$; at spray plume centre, for (a) experimental (b) numerical; spray plume periphery (a) experimental (b) numerical (gray scale inverted, black denotes maximum) Developed turbulence at 100 bar and 200 bar:

5.5.2.1 Centreline gas velocity profile:

Centreline gas velocity profile presented in Figure 71 indicates the rapid decay of the spray plume. When the spray is injected in the stagnant gas environment, an immediate entrainment of the gas in the spray plume occurs. The gas quickly attains the maximum velocity at $z/D_i = 20$ at 100 bar injection pressure and at $z/D_i = 10$ at 200 bar injection pressure. It is important to be noted here that the centreline gas velocity profile in Figure 51 of previous chapter, which corresponds to the 200 bar pressure case without droplet breakup, attains the maximum velocity at $z/D_i = 20$. This shows the droplet breakup strongly affects the spray characteristics. The drop breakup mechanism produces

smaller droplets that experience more drag and interact more with the gas. This is the reason why, the centreline gas velocity in Figure 71 for both 100 bar case and the 200 bar case ends up at 40% of the liquid injection velocity.

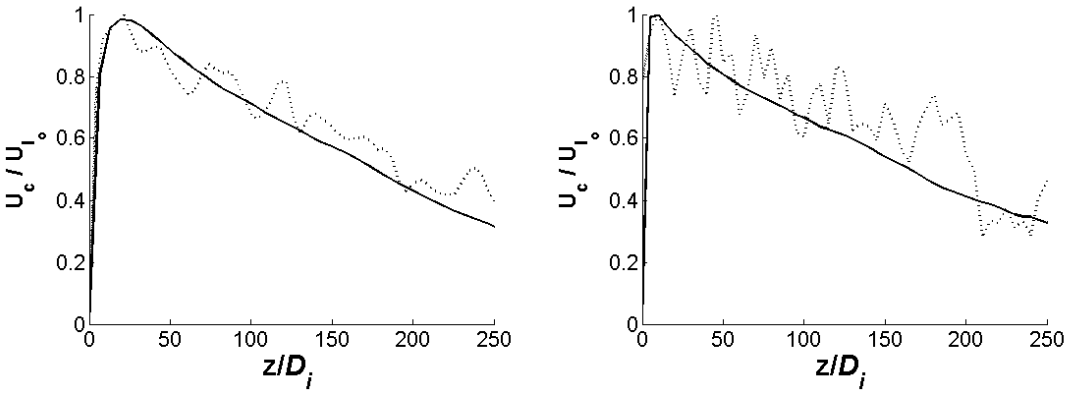

(a) *(b)*

Figure 71 : Normalized gas velocity along the centrelines in downstream direction at the injection pressure of (a) 100 bar (b) 200 bar, (Solid line) Mean velocity (dotted line) Instantaneous Velocity

5.5.2.2 Charecterization of Spray half width:

Before proceeding further, first it is necessary to establish some terminologies which will be used in this chapter from this point onwards. It has been mentioned in the begininnig of this chapter that the injection surface produced by the internal flow of the injector is elliptic due to cavitation. Thus the asymmetry at the injection nozzle may lead to an asymmetric spray plume. A cross-section of spray plume is presented in Figure 72 to distinguishes different zones in the spray which will be useful to understand the further analysis in this chapter. Asymmetric zone is along the x-axis which contains the cavitation side along positive X-axis and non-cavitation side along negative X-axis. The symmetric zone of the spray is along the Y-axis. The horizontal distance of the asymmetric and symmetric zone would be denoted by r_x and r_y respectively.

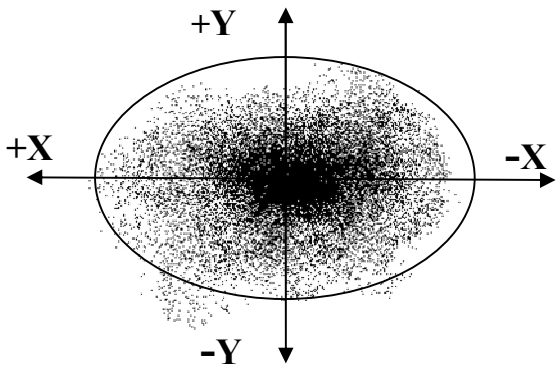

Figure 72: Cross-section of spray plume at 100bar injection pressure

5.5.2.3 Spray half width evolution

Spray half width evolves in a very unique way in comparison to the results from simplified injection models presented in the previous chapter in Figure 52. As, explained before, the cavitation on one side of the injector produces the spray which is asymmetric in horizontal direction (X-axis) and symmetric in the vertical direction (Y-axis). The spray half width of the asymmetric section is larger on the cavitation side (L_{h_c}) than on the non-cavitation side $(L_{h_{nc}})$. The half width profiles are presented in Figure 73, which illustrate that the cavitation side is the more dispersed side. The overall spray half width of the asymmetric side is represented by an average half width profile. (L_{h_a}). The half width in symmetric zone (L_{h_s}) is reduced by one third of the half width of asymmetric cavitating zone.

Initially, all the half width profiles increase linearly until z/D_i = 25 and z/D_i = 20 at the injection pressure of 100 bar and 200 bar respectively before a deviation in the curves occurs. After this deviation, the half width evolves linearly again. Therefore, the profiles can be divided into the two sections namely section 1 (before the change in direction of the curve), section 2 (after the change in direction of the curve). The half width profiles provide very important information about the close up spray plume angle which corresponds to the angle near the injection surface and a far away spray plume angle which relates to the angle to which the spray relaxes to. It is also important to remember

that the angle obtained from the information of the half width only accounts for the mainstream of the spray.

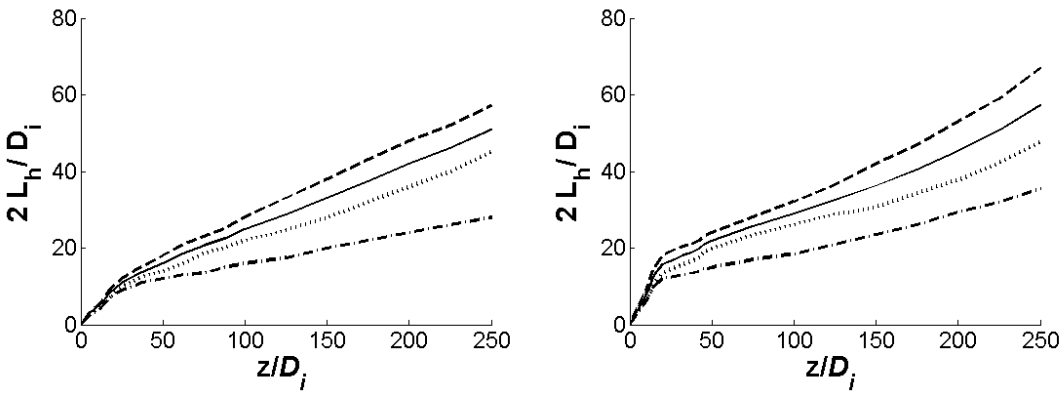

(a) *(b)*

Figure 73: Downstream evolution of normalized half width at the injection pressure of (a) 100 bar (b) 200 bar; (—)L_{h_a} (--) L_{h_c} (•••) $L_{h_{nc}}$ (-·-)L_{h_s}

The main stream spray half angles calculated from the half width are presented in the Table 9 . The angles in the section 1 indicate the large plume angles with which the spray is initially injected. Although the calculated angles only account for the main stream spray but still it is interesting to see that the spray in comparison to very large injection angles settles down to quite small angle. Clearly, the cavitation side as compared to non-cavitation side and the symmetric side exhibits much larger angle near the injection surface

Measurement side	**spray mainstream half angle 100 Bar**		**spray mainstream half angle 200 Bar**	
	Section 1 z/D_i = 25	**Section 2** z/D_i = 250	**Section 1** z/D_i = 20	**Section 2** z/D_i = 250
Cavitation	12.8°	6.3°	20.9°	7.5°
Non-cavitation	10.9°	4.9°	17.2	5.4°
Symmetric	9.8°	3.2°	15.4	4.1°

Table 9: Spray main stream angles

5.5.2.4 Mean velocity profiles:

The profiles of mean velocity are investigated in both asymmetric zone and symmetric zones of the spray.

5.5.2.4.1 Mean gas velocity profiles on Asymmetric zone:

The evolution of radial profiles of streamwise carrier phase mean velocity normalized by the injection velocity and local centreline velocity versus the radial distance (r_x) in the X-axis normalized by half width of non-cavitation and cavitation side $\left(L_{h_{nc,c}}\right)$ for the injection pressures of 100 bar and 200 bar respectively have been presented in Figure 74. A systematic decrease in the mean velocity is observed for the both cases. The asymmetric distribution of the velocity at the centreline indicates the presence of cavitation. Since, the cavitation produces small droplets with larger angle close to the nozzle therefore the spray tends to be a little slower. This is why the non cavitating side becomes quicker as the spray moves downstream.

When velocity profiles are normalized by the centreline velocity (in this case, maxima of the velocity at that location), the overall velocity distribution profiles tend to be a kind of Gaussian distribution but only until a downstream location $100D_i$. Afterwards due to cavitation the centreline velocity becomes distorted but the overall Gaussian shape is retained. A Gaussian profile with a mean of zero and a standard deviation of 0.8 fits well.

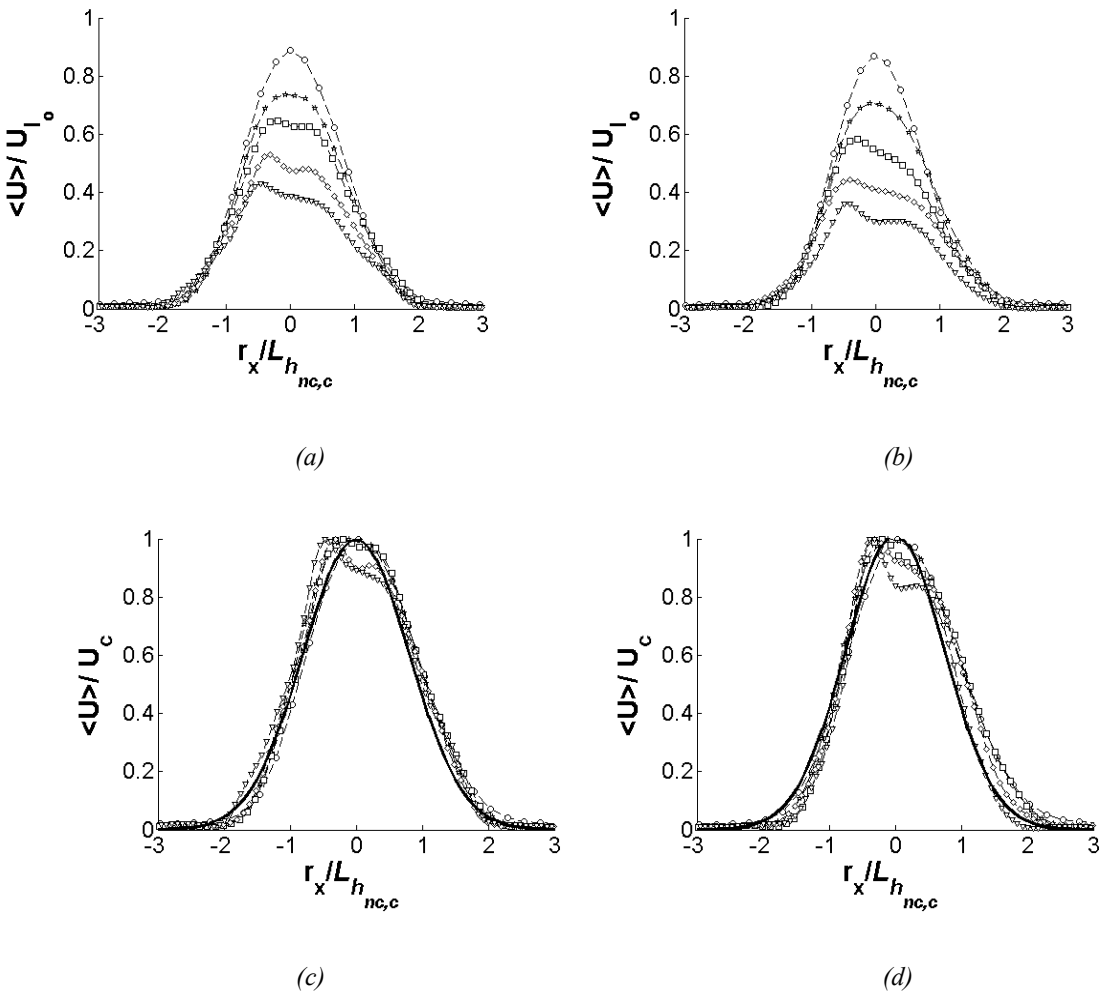

Figure 74: Radial distribution of mean velocity in asymmetric zone, normalized by injection velocity (a) P_i = 100 bar (b) P_i = 200 bar; normalized by centreline velocity (c) P_i = 100 bar (d) P_i = 200 bar; 50D_i (–⊙–), 100D_i (–☆–), 150D_i (–□–), 200D_i (–◇–), 250D_i(–▽–) (dashed line, Gaussian fit with mean =0 and standard deviation of 0.8.

5.5.2.4.2 Mean gas velocity profiles on Symmetric zone:

Orthogonally to the asymmetric zone there is a symmetric zone which remains uninfluenced by the cavitation. The symmetric zone, as the name suggests, show symmetric profiles of the normalized

mean velocity versus the radial distance (r_y) normalized half width of the symmetric zone (L_{h_s}) in the downstream direction.

A continuous decrease in the gas velocity in the downstream direction for both 100 bar and 200 bar injection pressure is observed in Figure 75 (a) and (b) respectively. Unlike asymmetric zone, there is no distortion of the velocity at the centreline of the jet. The velocity profiles normalized with local centreline velocity show a self similar behaviour. A Gaussian profile with a mean of zero and a standard deviation of 0.75 fits well.

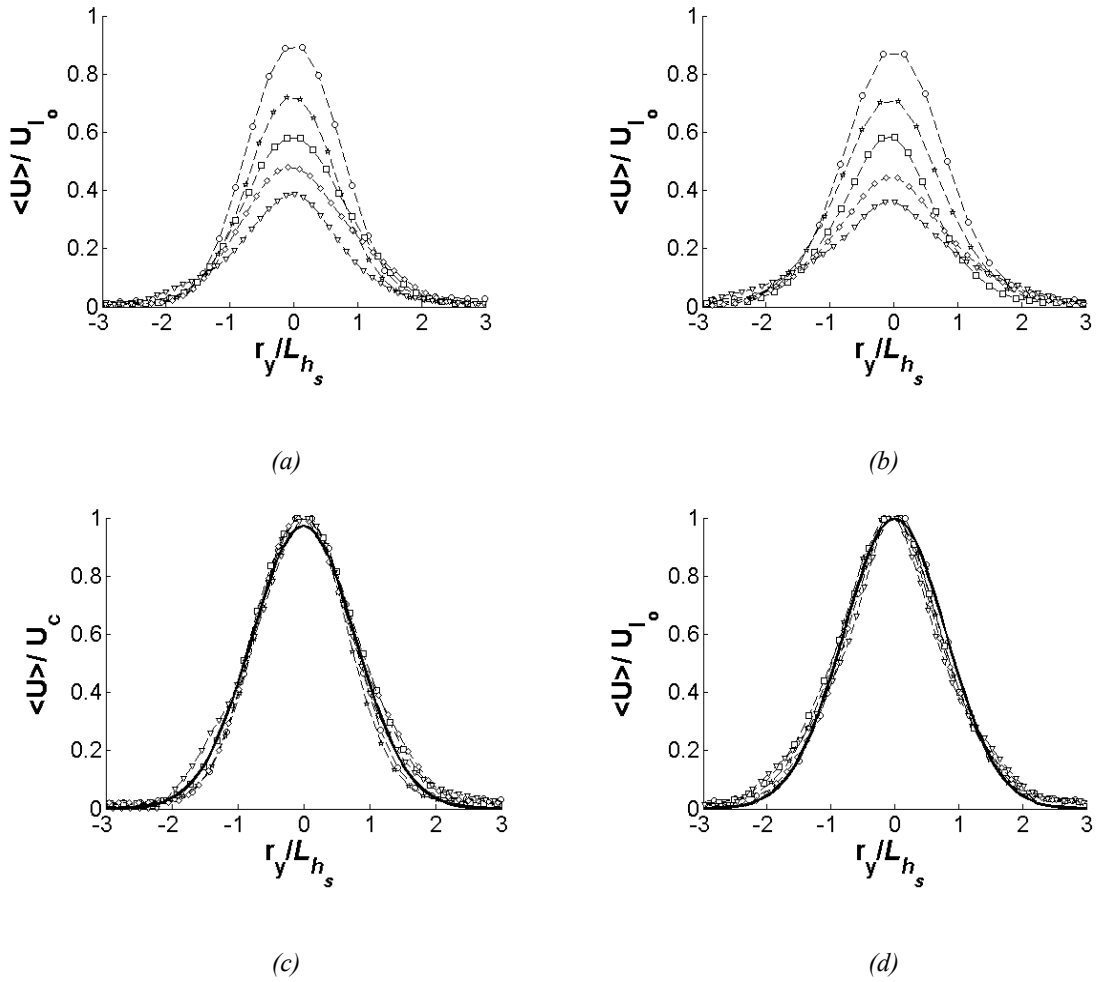

Figure 75: Radial distribution of Mean velocity in symmetric zone; normalized by injection velocity (a) P_i = 100 bar (b) P_i = 200 bar; normalized by centreline velocity (c) P_i = 100 bar (d) P_i = 200 bar; at downstream locations of $50D_i$ (–○–), $100D_i$ (–☆–), $150D_i$ (–□–), $200D_i$ (–◇–), $250D_i$(–▽–) (solid line, Gaussian fit with mean =0 and standard deviation of 0.75.

5.5.2.4.3 Mean liquid velocity profile on Asymmetric zone:

Similar to the gas velocity, the profiles of mean liquid velocity for both 100 bar and 200 bar cases show a lot of distortion at the centreline of the spray due to cavitation as presented in Figure 76. The liquid velocity decay rate in both cases is quite rapid. Interestingly, the normalized liquid velocity at the injection pressure of 200 bar is decaying faster than that of at 100 bar injection pressure. The reason behind this is that the higher pressure promotes the secondary atomization of the drops which leads to increase in the drag and reduction of the drag time of the droplets and thus faster decay.

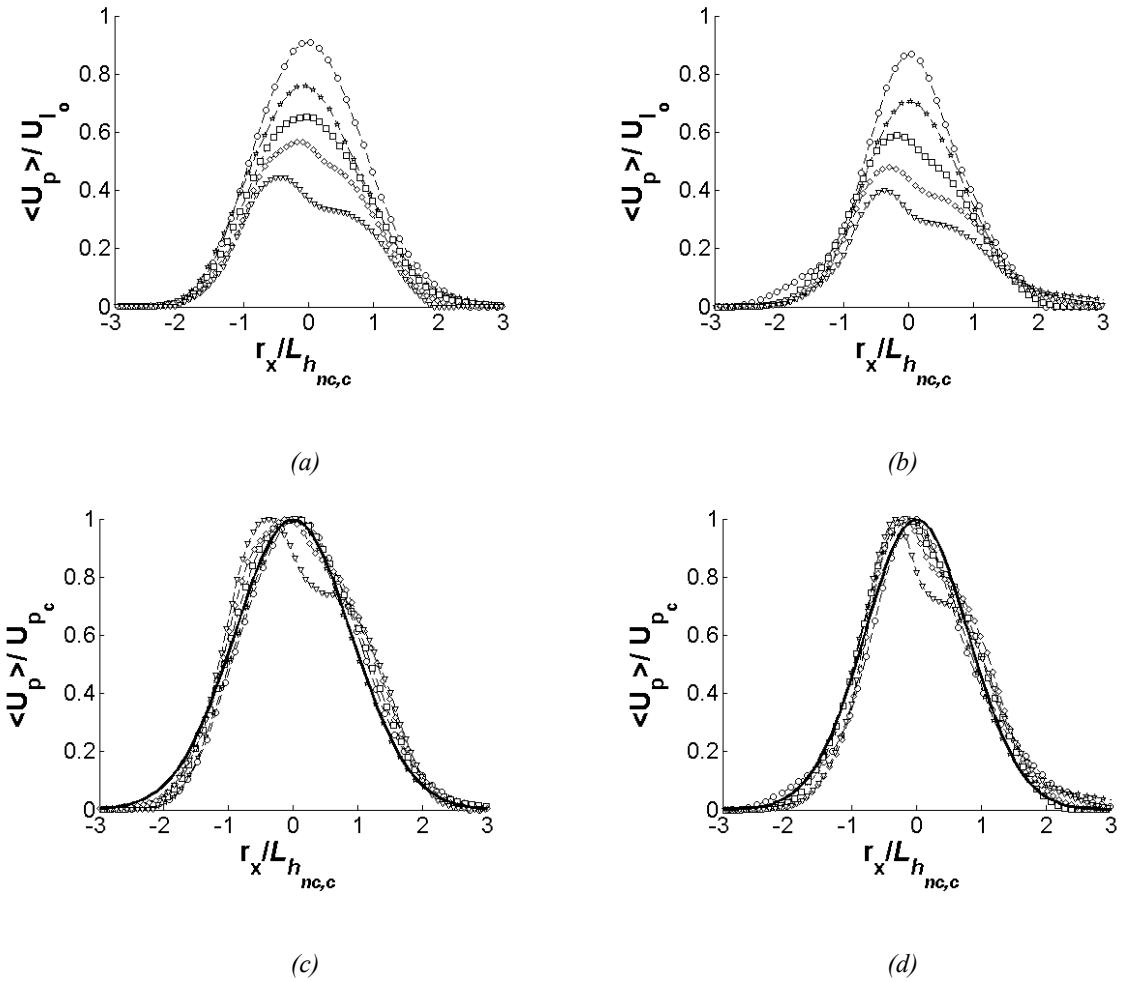

Figure 76: Radial distribution of Mean liquid velocity in asymmetric zone; normalized by injection velocity (a) $P_i = 100\ bar$ (b) $P_i = 200\ bar$; normalized by centreline velocity (c) $P_i = 100\ bar$ (d) $P_i = 200\ bar$; at downstream locations of $50D_i$ (–⊙–), $100D_i$ (–☆–), $150D_i$ (–□–), $200D_i$ (–◇–), $250D_i$(–▽–) (solid line, Gaussian fit with mean =0 and standard deviation of 0.75.

5.5.2.4.4 Mean liquid velocity profile on Symmetric zone:

The liquid velocity profiles, similar to gas velocity profiles, are symmetric in the y-axis. A continuous decrease in the liquid velocity is observed in both 100 bar and 200 bar injection pressure. A self similar behaviour can also be observed in liquid velocity profiles in the symmetric zone. A Gaussian profile with a mean of zero and a standard deviation of 0.75 fits well to the simulation profiles.

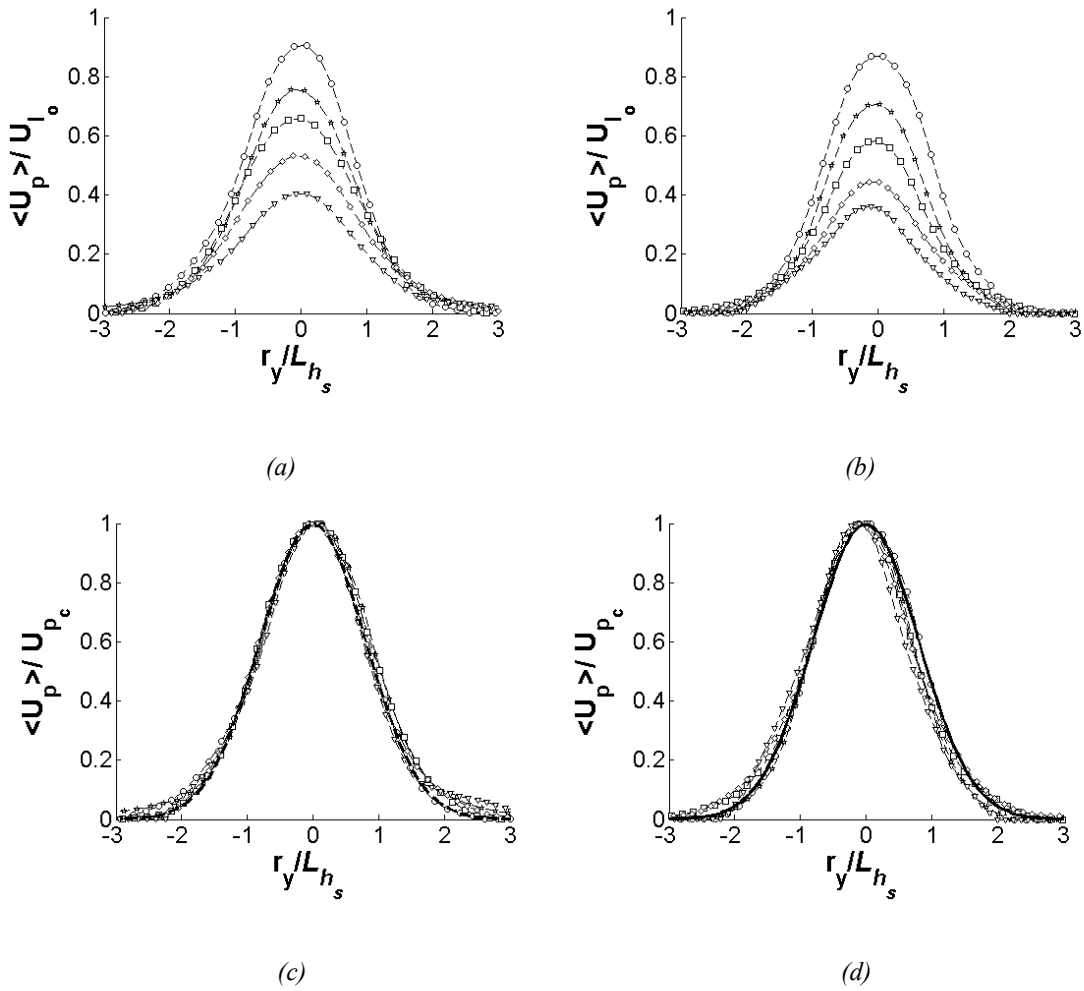

Figure 77: Radial distribution of Mean liquid velocity distribution profiles in symmetric zone; normalized by injection velocity (a) $P_i = 100\ bar$ (b) $P_i = 200\ bar$; normalized by centreline velocity (c) $P_i = 100\ bar$ (d) $P_i = 200\ bar$; at downstream locations of $50D_i$ (–○–), $100D_i$ (–☆–), $150D_i$ (–□–), $200D_i$ (–◇–), $250D_i$(–▽–) (solid line, Gaussian fit with mean =0 and standard deviation of 0.75.

5.5.2.4.5 Liquid Mass distribution:

The profiles of mean liquid to gas density ratio $\langle \alpha_l \rangle$ in Figure 78, show the downstream evolution of liquid mass compared to the gas mass. The results of VOF simulation of the internal flow at 100 bar injection pressure in Figure 58 show maximum $\langle \alpha_l \rangle$ of 0.4 at the injection surface. The maximum $\langle \alpha_l \rangle$ at 200 bar injection pressure is 0.5 which is certainly higher than $\langle \alpha_l \rangle$ at 100 bar injection pressure because the liquid injection rate and mass for a given injector is always higher at a higher pressure. This implies that due to cavitation liquid presence at the injection surface reduces to almost half or even less in 100 bar case.

In the downstream direction, at $50D_i$ $\langle \alpha_l \rangle$ quickly reduces to 0.21 and 0.33 in 100 bar and 200 bar cases, respectively. In the asymmetric zone in Figure 78 (a) and (b), liquid is more concentrated on the non cavitation side whereas the large angle of the spray at the cavitation side reduces the liquid concentration. The profiles of $\langle \alpha_l \rangle$ in symmetric zone are presented in Figure 78 (c) and (d) which show the equal distribution of liquid to gas mass density ratio on both sides.

The liquid mass density ratio in both 100 bar and 200 bar injection pressure cases reduce to less than 0.05 at a distance of $250D_i$ from the nozzle which means that the liquid mass density is reduced by a factor of 10 in comparison to the liquid mass density at the injection surface. Thus the spray plume spreads in the streamwise direction as more gas is engulfed in the spray plume. The asymmetric and symmetric sides both expand with different angles thus different spray shape and different liquid mass distribution is observed on each side.

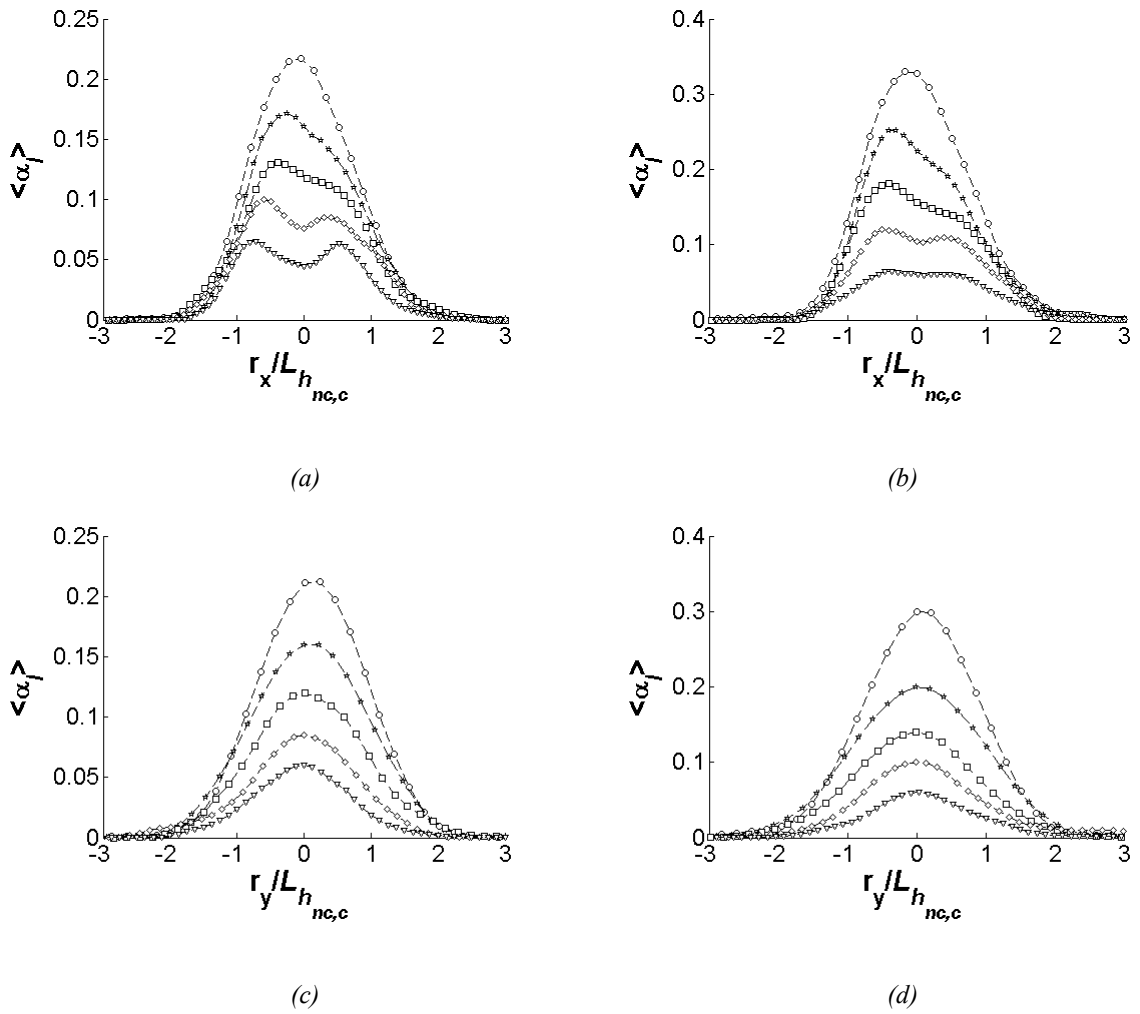

Figure 78: Radial distribution of Mean liquid to gas mass ratio in; asymmetric zone; (a) P_i = 100 bar (b) P_i = 200 bar; symmetric zone; (c) P_i = 100 bar (d) P_i = 200 bar; at downstream locations of 50D_i (—○—), 100D_i (—☆—), 150D_i (—□—), 200D_i (—◇—), 250D_i(—▽—) (solid line, Gaussian fit with mean =0 and standard deviation of 0.75.

5.5.2.5 RMS Fluctuations of Carrier Phase:

Streamwise rms fluctuations without and with subgrid scale fluctuations of the gas field at the injection pressure of 100 bar and 200 bar have been presented in the Figure 79. The resolved and total rms fluctuations continuously increase in the streamwise direction. The resolved rms fluctuations levels increase from a value of 10% at 50D_i to 25% at 250D_i at 100 bar injection pressure and 10% at 50D_i to 30 % at 250D_i at 200 injection pressure. It is also that the rate of

increase in fluctuation levels only occurs to certain point and then it starts to decrease in downstream direction. An interesting point to be noted here is the difference in the evolution of streamwise rms velocity in terms of cavitation $r/L_h > 0$ and non cavitation sides $r/L_h < 0$. The gas on the cavitation side appears to fluctuate more than the non cavitating side. The subgrid scale fluctuations increase the resolved rms fluctuations by about 5% at $250D_i$ and also pronounce the effect of cavitation on the rms fluctuations in Figure 79 (b) and (d) for injection pressures of 100 bar and 200 bar respectively.

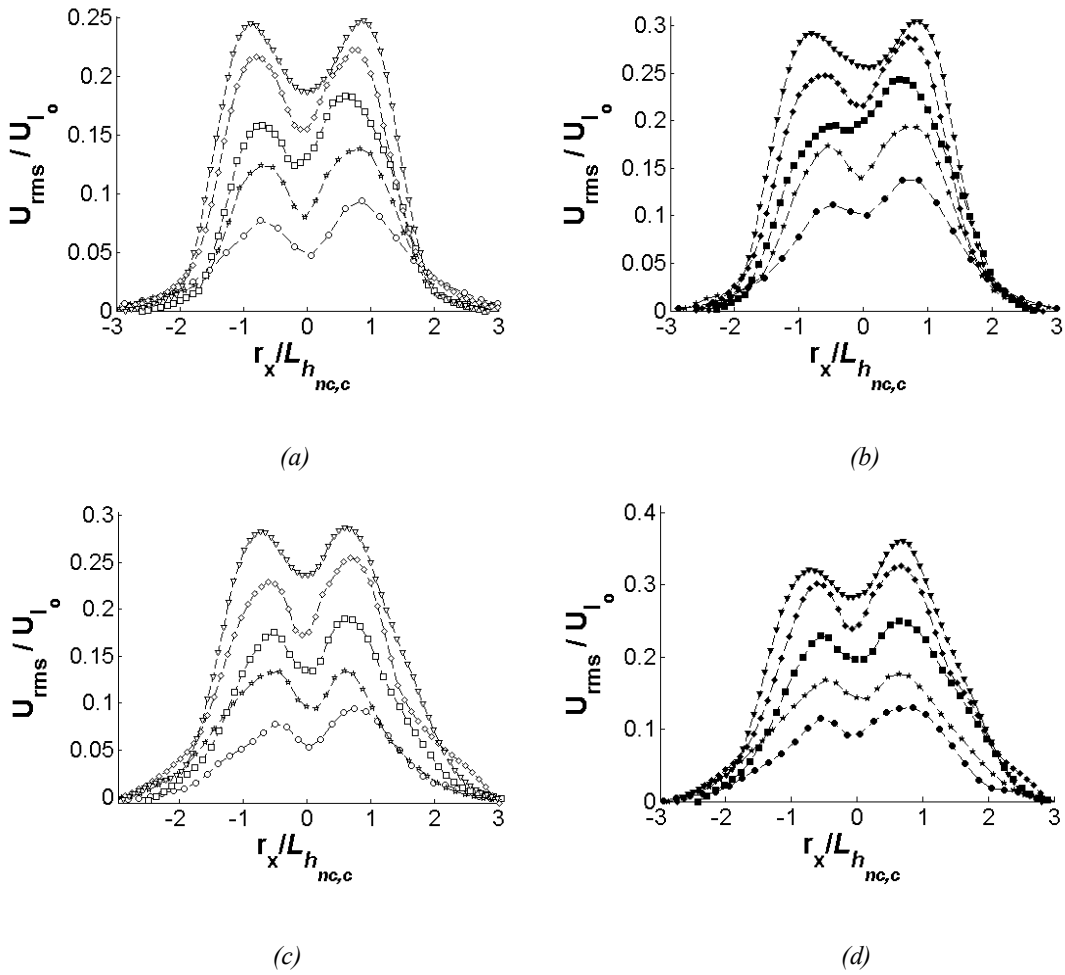

Figure 79: Streamwise rms carrier phase velocity fluctuations at $P_i = 100\ bar$ (a) resolved (b) total; and at $P_i = 200\ bar$ (c) resolved (d) total; at the downstream locations of $50D_i$ (–○–), $100D_i$ (–☆–), $150D_i$ (–□–), $200D_i$ (–◇–), $250D_i$(–▽–)

5.5.2.6 RMS fluctuations of dispersed phase:

The plots of streamwise rms fluctuations of the dispersed phase in Figure 80 illustrate the fact that although rms fluctuations progressively increase with downstream distance but the drops at the centre of the spray plume fluctuate with lesser intensity than the drops in the shear layer of the spray plume. The rms fluctuation levels of dispersed phase appear to dominate the resolved rms fluctuations of gas phase in the beginning at $50D_i$ but after that both phases show similar fluctuation levels and at $250D_i$ the rms fluctuation in the gas and liquid are almost same. Since the cavitation enhances the spray angle and drop dispersion therefore it is bound to change the fluctuation levels of the injected liquid. The effect of cavitation in the Figure 80 for $r/L_h > 0$ shows higher fluctuations levels than the non cavitation side. The rms fluctuations of the dispersed phase initially at 100 bar injection pressure appear to be higher by 2 to 3 % than at the injection pressure of 200 bar until $150D_i$. Further downwards the fluctuation levels of 200 bar case become higher by about 5% than that of 100 bar injection pressure case. This kind of behaviour of the fluctuation levels of dispersed phase is linked to the higher injection velocity which tries to keep the spray plumes undisturbed near the injection region.

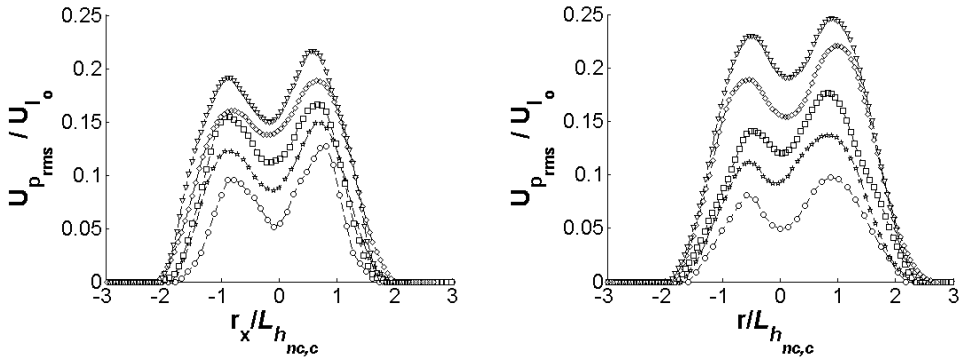

(a) *(b)*

Figure 80: Streamwise rms dispersed phase velocity fluctuations for P_i of (a) 100 bar (b) 200 bar at the downstream locations of $50D_i$ (–⊖–), $100D_i$ (–☆–), $150D_i$ (–□–), $200D_i$ (–◇–), $250D_i$(–▽–)

5.5.2.7 Anisotropy:

The filtered fluctuating velocities $\widetilde{u'}$, $\widetilde{v'}$, $\widetilde{w'}$ in X, Y and Z directions respectively, are utilized to investigate the turbulence development in spray. Since the spray plume is not symmetric, therefore the filtered Reynolds tensor is kept in the Cartesian coordinates. The profiles of filtered normal stress components $\langle\widetilde{u'}\widetilde{u'}\rangle$, $\langle\widetilde{v'}\widetilde{v'}\rangle$, $\langle\widetilde{w'}\widetilde{w'}\rangle$ which give the measure of radial and axial fluctuating velocities are presented respectively from Figure 81 to Figure 83. The filtered shear stress profiles are of$\langle\widetilde{u'}\widetilde{w'}\rangle$ and $\langle\widetilde{v'}\widetilde{w'}\rangle$ are displayed in Figure 84 and Figure 85. The shear component $\langle\widetilde{u'}\widetilde{v'}\rangle$ is dependent only on the radial fluctuating velocity components, which means that it is very weak and therefore it is neglected in current analysis.

Both radial fluctuating velocity and the axial fluctuating velocity initially increase in the streamwise direction until at $150D_i$. However at $200D_i$ the velocities tend to go towards the self similarity. The values of the radial and the axial velocities are quite different in magnitude in both 100 bar and 200 bar cases. Like normal stress components the shear stress components also become self similar at $200D_i$. The shear components are considerably smaller than the normal components. This shows that the isotropic condition is not reached until this point. Some points beyond $250D_i$ were also investigated which are not presented here but no isotropy was observed. This means the spray which demonstrates the self similarity but not isotropy.

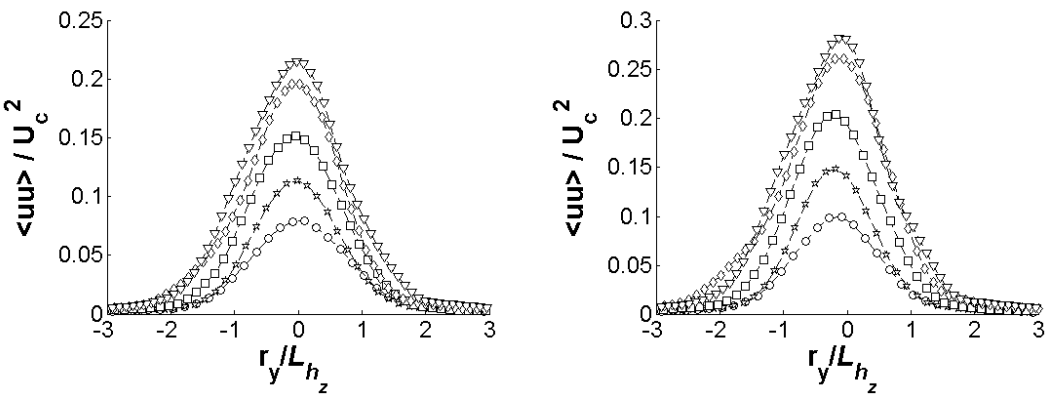

(a) (b)

Figure 81: Streamwise profiles of filtered normal stress component $\langle\widetilde{u'}\widetilde{u'}\rangle$ normalized by centreline velocity at injection pressure (a) 100 bar (b) 200 bar; $50D_i$ (–○–), $100D_i$ (–☆–), $150D_i$ (–□–), $200D_i$ (–◇–), $250D_i$(–▽–)

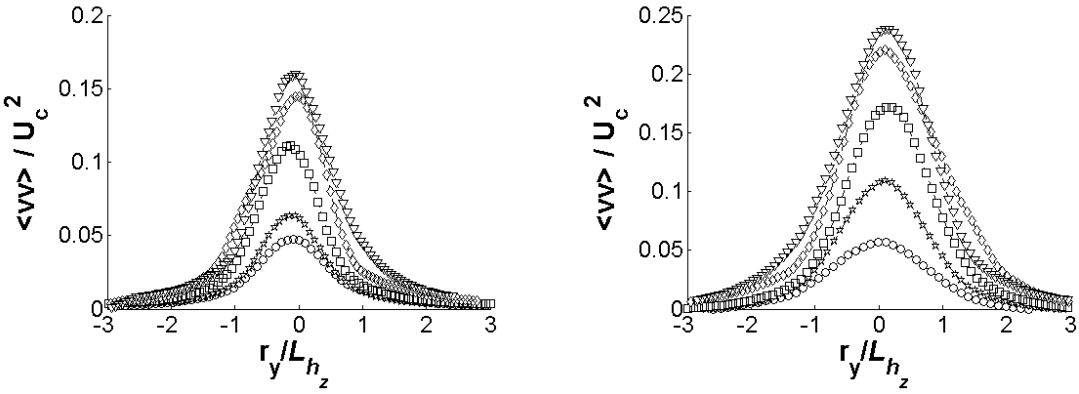

(a) *(b)*

Figure 82: Streamwise profiles of filtered normal stress component $\langle \widetilde{v'}\widetilde{v'} \rangle$ normalized by centreline velocity at injection pressure (a) 100 bar (b) 200 bar; $50D_i$ (–○–), $100D_i$ (–☆–), $150D_i$ (–□–), $200D_i$ (–◇–), $250D_i$(–▽–)

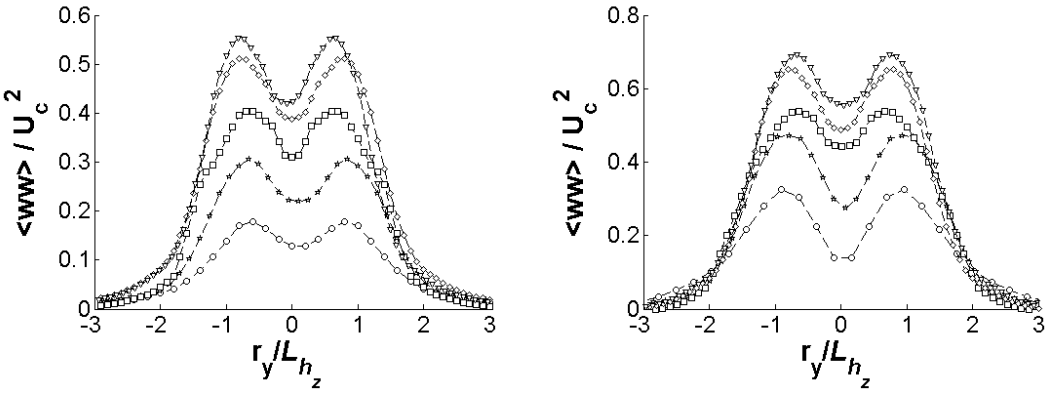

(a) *(b)*

Figure 83: Streamwise profiles of filtered normal stress component $\langle \widetilde{w'}\widetilde{w'} \rangle$ normalized by centreline velocity at injection pressure (a) 100 bar (b) 200 bar; $50D_i$ (–○–), $100D_i$ (–☆–), $150D_i$ (–□–), $200D_i$ (–◇–), $250D_i$(–▽–)

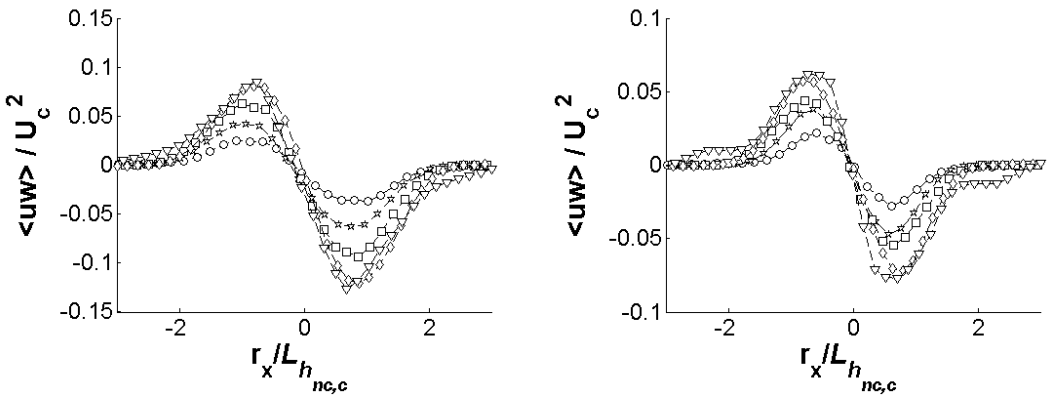

Figure 84: Streamwise profiles of filtered shear stress component $\langle \widetilde{u'}\widetilde{w'} \rangle$ normalized by centreline velocity at injection pressure (a) 100 bar (b) 200 bar; 50D_i (–○–), 100D_i (–☆–), 150D_i (–□–), 200D_i (–◇–), 250D_i(–▽–)

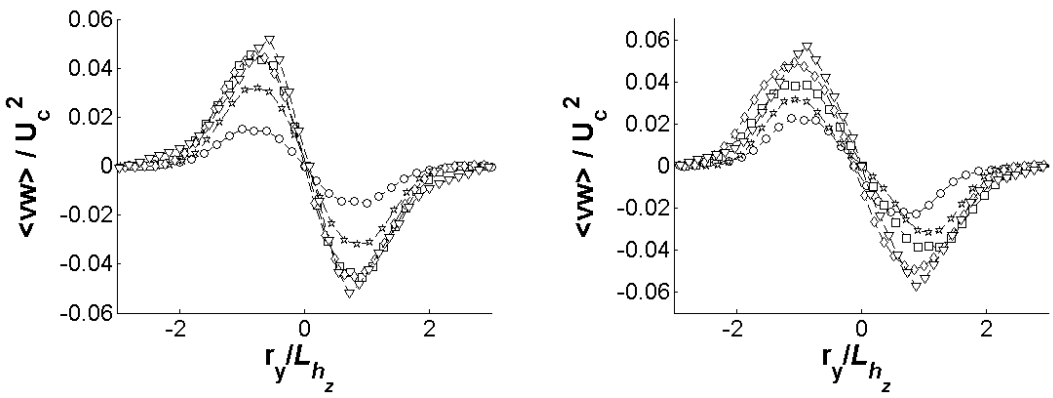

Figure 85: Streamwise profiles of filtered shear stress component $\langle \widetilde{v'}\widetilde{w'} \rangle$ normalized by centreline velocity at injection pressure (a) 100 bar (b) 200 bar; 50D_i (–○–), 100D_i (–☆–), 150D_i (–□–), 200D_i (–◇–), 250D_i(–▽–)

5.5.2.8 Stokes Numbers:

The Stokes numbers at the Kolmogorov scale (st_η) and at the filter scale (st_Δ) at the centreline and the periphery of the spray have been ploted in Figure 86. Large values of Stokes number at komogorov scale at 100D_i suggests that the drops are too inertial to respond to the eddies of the smallest scales. According to (Eaton & Fessler, 1994) small eddies can cause the accumulation of the drops when $st_\eta \sim 1$. This effect becomes weaker when $st_\eta \sim 10$ which means until 300D_i the drops

are inertial and are sightly affected by the eddies of the Kolmogorov size both at centre and shear layers of the spray.

The Stokes numbers at the filter scale illustrates the interaction of the drops with the eddies of filter size Δ are larger than 1 until the downstream location of $100D_i$ which means the drops will be insensitive to the eddies of filter size. However at $150D_i$ $st_\Delta \cong 1$ in the shear layer which indicates that the drops become responsive to the eddies of filter size. Further downstream at $250D_i$, $st_\Delta < 1$ which manifests strong interactions of drops and filter size eddies and also the subgrid scale two way coupling will come into the action at this stage.

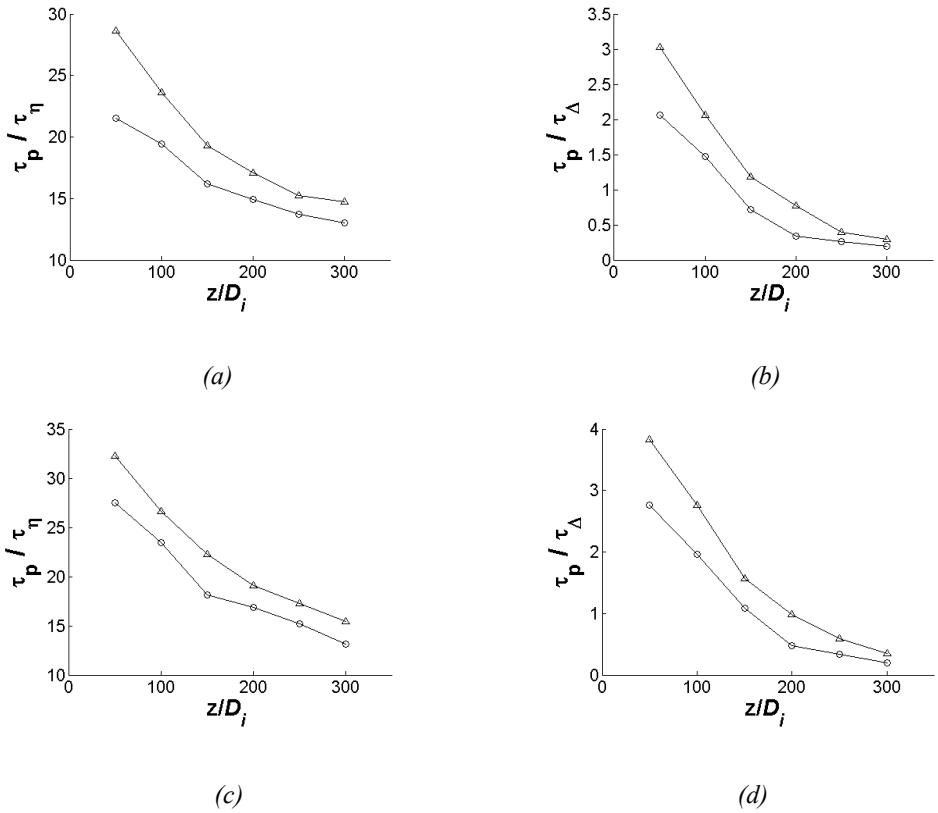

Figure 86: Stoke Numbers at several downstream locations for $P_i = 100\ bar$ (a) Kolmogorov scale η (b) filter scale Δ; and $P_i = 200\ bar$ (c) Kolmogorov scale η (d) filter scale Δ; with dynamic Smagorinsky model in the downstream direction at (—△—) centreline (—□—) shear layer

5.5 Unsteady state results

5.5.1 Temporal spray evolution and dynamics:

Experimental and numerical temporal evolution of a single spray plume from a 3-hole injector is presented in Figure 87. As explained earlier, the spray can be extremely dependent on the internal nozzle flow dynamics. Initially the spray plume appears as if it is a combination of two plumes; one with a larger plume angle on the left and the other one with a thin plume angle on the right hand side. But in reality it is not the case, instead it is the effect of internal nozzle flow dynamics. On the left hand side of the nozzle there is cavitation effect which forces the spray plume to become wider and thus slower. Whereas, on the right hand side of the spray plume there is no cavitation effect but instead there is an intact liquid core which appears inside the injection nozzle. The liquid core on the non cavitation side during the opening phase of the injector slightly bends with angle of 4° from the centreline of the injection nozzle. This inflicts the one half of the spray plume to acquire a kind of slender jet named as "side jet" which penetrates more than the cavitation side from the beginning. Experimentally it has been observed that the side jet does not lose any momentum until the injection time of 1.1ms. After this time the side jet start to slow down and the main stream spray catches up and pushes the side jet to the right. The spray tip recirculation then slowly incorporates the side jet and makes it a part of main stream spray. All these features are very well captured by the simulation. The asymmetric behaviour can never be observed with simplified injection models. Moreover this kind of spray behaviour is quite repeatable and it has been observed for both cases with $P_i = 100\ bar$ and $P_i = 200\ bar$ with different injection times.

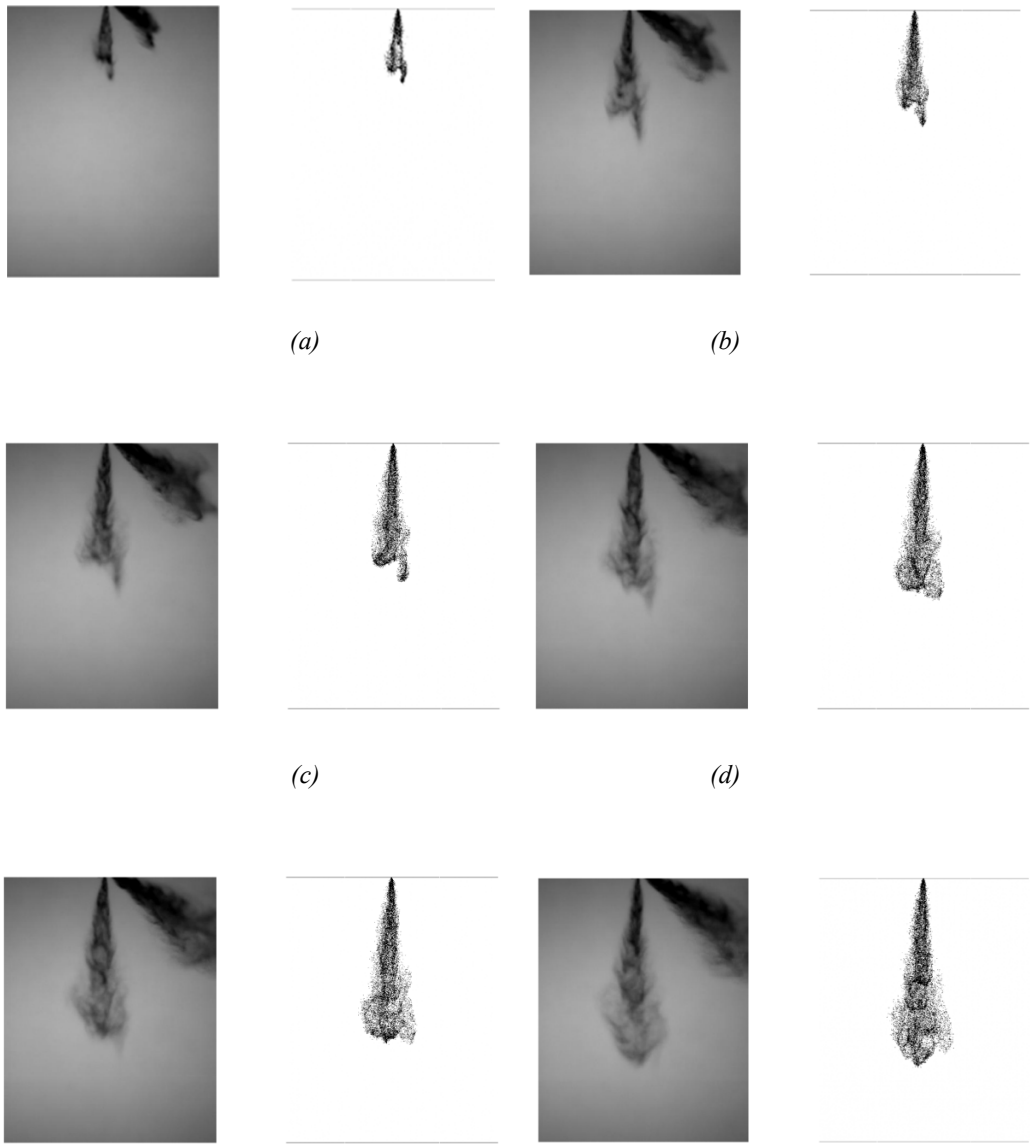

Figure 87: temporal spray evolution of experiment on left and simulation on right; for $P_i = 100\ bar$ at the injection time, T_{inj} of (a) 0.8ms (b) 1.1ms (c) 1.4ms (d) 1.7ms (e) 2 (f) 2.3ms (Including the delay in opening of injector of 0.433ms and 0.490ms for 100 bar and 200 bar respectively)

5.5.2 Spray Penetration and plume angle:

The penetration curves begin at 0.433ms at 100 bar injection pressure whereas 0.492ms for the 200 bar case because of the delay in the opening of the injector and the electrical signal. In the initial

stages, the penetration curve increases steadily in both cases because of the side jet which is very faster than the cavitation side of the spray. In the case of 100 bar injection pressure, at an injection time of 1.1ms, the initial bend in the liquid injection on the non cavitation side which produces the side jet vanishes, the side jets starts to slow down significantly and hence the linear increase in the penetration curve is no longer observed. The liquid penetration curve after 1.1ms gives an impression as if the spray plume starts to slow down but in fact it is not the case. The mainstream jet eventually catches up the side jet at 1.8ms which is illustrated by the flattening of the penetration curve. As soon as the mainstream jet overtakes the side jet the penetration curve start to increase linearly again. This process quite repetitive and is observed in the 200 bar case as well.

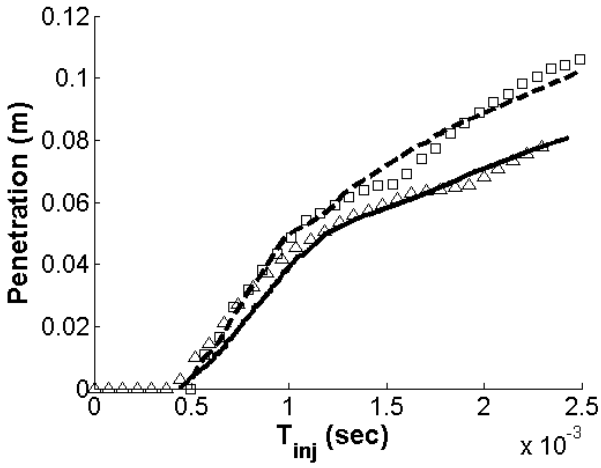

Figure 88: Spray penetration versus injection time (△) Exp 100 bar (□) Exp 200 bar (▬) Num 100 bar (--) Num 200 bar

The spray plume angle is also very well captured by the simulation. The overall spray far plume angle measured from the experiments at 100 bar injection pressure is 24.70°. In comparison to the experiment, simulation predicts the far plume angle of 23.95°.

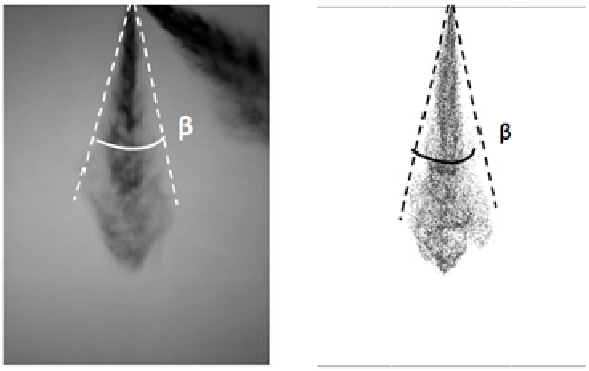

(a) *(b)*

Figure 89: spray plume angle; at 100 bar (a) Experiment (b) Numerical

5.6 Conclusion:

The coupling of internal flow LES-VOF simulation and the external spray LES simulation gives unpredictability to the spray shape and dynamics as seen in the real life scenarios. This unpredictability in the spray arises due to the inhomogeneous distribution of the liquid at the injection nozzle due to cavitation. The cavitation in the nozzle of the injector forces the liquid to attain an anchor shape of the liquid distribution under steady state injection which leads the appearance of the side jet on the non cavitation side and the expansion of the spray with smaller sized droplets at the cavitation side. Moreover the comparison of the simulation data and experimental PDA data show reasonably comparable results both for the drop size and velocity. Spray shape, angle and the dynamics also compare well with the experimental images at 100 bar and 200 bar.

The mean velocity profiles of gas and liquid shows the deviation of maximum centreline velocity towards the non cavitation side where the side jet is observed. This shift in the velocity field appears to be the result of cavitation where the spray plume is expanded. The anisotropy analysis show the spray is anisotropic but with a self similar behaviour of the turbulence at $250D_i$.

Summary & Conclusion:

GDI spray simulations under various conditions were investigated in this thesis. The simulations of 3-hole and 6-hole injector were performed using RANS approach which proved to be an effective tool to study the air entrainment in the multi-hole injectors and also gave a vital insight to the jet-to-jet interactions. The jet-to-jet interactions were found to be a cause of air entrainment inside the spray cone which carried the vapour of the surrounding plumes inside the spray cone. The gas inside the spray cone made sure that the plumes didn't expand and caused the spray collapsing environment. The higher temperature environment amplified the spray collapse due to the trapped vapour inside the cone.

Multi-hole injectors tend to show a sudden collapse under superheated or flashboiling conditions. As soon as the superheated liquid is injected in the low pressure conditions the spray cone immediately expands to an angle of around 80° to 90° followed by an abrupt collapse of spray cone producing a kind of bell shape. Under such intense conditions, the simulations were not able to produce comparable results. A semi-empirical model was introduced in the RANS simulation which systematically allowed the smaller drops to attain larger angle near the injection nozzle. This lead to severe jet-to-jet interactions and hence a full spray cone collapse. Furthermore, several possibilities which could increase or decrease the degree of flashboiling like hole to hole distance, plume angle and spray cone angle, injection velocity etc. The results were very comparable to the experiments. The results showed that the degree of flashboiling increased by decreasing hole to hole distance of the injector due to higher jet-to-jet interaction. On the other hand higher injection velocity decreased the jet-to jet interactions and thus reduced the degree of flashboiling.

The methodology to perform LES of spray simulations were established by comparing results from the different turbulence models such as Smagorinsky, one equation, Dynamic Smagorinsky and Implicit models. Dynamic Smagorinsky model was found to work better than the rest of the models. Moreover, different simplified injection models were also investigated which are usually assumed at inlet of the spray. The simplified injection models at the inlet consisted of random injection positions and random angle variation R-R, Gaussian injection positions and random angle variation G-R, Gaussian injection positions and linear angle variation G-L. In the absence of the any turbulence

dispersion model G-L injection model performed best. However, there is a major drawback of simplified injection models regarding the fixed initial inlet parameters. The initial parameters like, spray angle, injection droplet size usually need to be adjusted empirically in the absence of the experimental data.

Although simplified injection model when compared to experimental data gave comparable results but some percentage of differences in the peak values of diameter and velocity. These kind of discrepancies of simplified models are usually resolved by adjusting the initial conditions empirically from the experiments. But this kind of iterative process to perform number of simulations to get good results can be computationally costly in LES especially in the absence of the experimental results. To overcome this problem, a coupling approach of LES-VOF simulation of the internal flow of the injector and LES of lagrangian simulations was introduced. The inlet conditions to perform LES of lagrangian spray simulation were deduced from the already existing internal flow LES –VOF simulations. The coupling approach of LES-VOF internal flow simulation to the LES external spray provided very comparable results to the experimental results of PDA and shadowgraphy. The appearance of the side jet and the large angle at the cavitation side was predicted very well.

In the end to conclude the current work, it is necessary to mention the important events that were observed in the LES of spray. The spray plume, in the downstream direction, was divided into five main zones:

- The first zone was observed to be as the drag zone where the drag on the droplets was dominant. At 100 bar injection pressure, the drag zones existed until a downstream location of $20D_i$ while it reduces to $10D_i$ at 200 bar injection pressure.
- The second zone identified the instabilities in the shear layer of the carrier phase. These instabilities began as the round vortex rings from near nozzle region and lasted until $100D_i$. In this zone the instabilities were discovered to be quite stable with zero helicity.
- The transition zone was categorized as the third zone which showed the transformation of the round stable instabilities to helical structures. The transition zone occurred between the downstream locations of $100D_i$ and $150D_i$.
- In the fourth zone from $150D_i$ to $200D_i$, the transitional turbulence began to relax to anisotropic self similar turbulence.

Summary and Conclusion

- The fifth zone was observed from $200D_i$ onwards where the quasi self similar anisotropic turbulence was observed. Fully isotropic flow was never observed even at much further downstream locations.

Future Work:

Large Eddy Simulation is promising tool for the study of turbulent flows like sprays. The coupling of internal flow LES-VOF simulation results with external LES spray simulation has shown good comparison with the experimental results. The internal flow simulation results utilized in the current work only deal with the steady state injection i.e. no needle movement. It is observed in the experiments that the unsteadiness in the spray comes from both the initial needle movement and cavitation. In future the LES-VOF simulation of internal flow of the injector can be performed with the needle movement. This would make the spray simulation more susceptible to the initial disturbances caused by the needle movement.

The coupling of internal and external flows can be extended by using Proper Orthogonal Decomposition, POD technique to extract more information about the dominant structures which induces the unpredictability in the spray dynamics and its shape. POD approach has the ability to segregated energetic turbulent structures from the complex turbulent flow field (Khan, Helie, & Burluka, 2011). In future an injection strategy depending on the most energetic structures can be , developed which would allow to investigate the dominant modes which govern the spray dynamics.

In the current work the dynamic Smagorinsky model has been used in LES which performed better in comparison to the fixed models but still dynamic Smagorinsky model forces the carrier phase turbulence spectrum to follow -5/3 slope. But it is still an open question that whether the two phase flows should follow a turbulence spectrum with a slope of -5/3. In future it would be very interesting to investigate this problem which may argue against or in favour of the current model.

Trajectory collision model has utilized in this work with automatic mesh refinement but there are some other models like No Time Counter (NTC) model (Schmidt & Rutland, 2000) which are known to work well with the automatic mesh refinement. Due to lack of time NTC model could not be implemented in OpenFOAM ® but in future it will be intriguing to compare the results between the different collision models which could influence the overall spray dynamics and drops sizing.

Moreover the current work incorporates droplet dispersion model which is based on the eddy turn overtime which is computed from subgrid scale kinetic energy and mean turbulent dissipation. But in

sprays we observed that the flow is quite anisotropic and the presence of large shear and slip velocity make the problem very complex. The comparison of the current simulations with experimental data did show mismatch in the joint PDF of radial velocity profiles where the small drops in the simulations were sometimes dispersed more than what experiments showed. Therefore, more complex approaches like stochastic modelling of the subgrid scales in future may improve the results.

Appendix A Experimental set-up

The experimental setups used to perform the PDA measurements, PIV measurements, high zoom shadowgraphy and high speed spray imaging are presented in this section.

A.1 Experimental set-up of PDA test bench:

The design, construction and application of the Loughborough University two component PDA transmission system to study dense GDI fuel sprays is well documented . The configuration for the 488 and 514 nm laser beam wavelengths at the final focusing lens is: beam diameters of 5mm, equal beam pair separations of 50mm, laser powers of 100 and 200 milli-watts per beam with a horizontal polarisation. With a focal length lens of 300mm this produces coincident measurement volumes of diameters of 37 and 39 microns with fringe spacing of 2.94 and 3.10 microns respectively for the two wavelengths. The 514 nm beam pair is in the vertical plane to measure the axial droplet velocity and size with the 488 nm beam pair in the orthogonal plane to measure the radial droplet velocity.

The Dantec 57X10 receiver is positioned at a scattering angle of 70 degrees with the polariser set to collect only scattered light in the horizontal plane and an aperture micrometer setting of 0,5mm. This optical configuration results in an effective measurement volume length of 0,1mm. In-conjunction with the Dantec processor the transmitter and receiver set up produces a droplet velocity bandwidth of -30 to 110 m/s with a drop size measurement range of up to 100 microns.

The 3-holes GDI injector is supported from a gantry incorporating a rotation stage and three precision orthogonal linear traverses to orientate and position the spray in three dimensions relative to the static PDA measurement volume. Each radial scan starts from the geometric vertical axis through the nozzle tip and traversed out to the periphery of the spray stream. The measurement co-ordinates in the vertical plane are Z = 10, 20, 30, 40, below the nozzle tip. The horizontal traverse is computer controlled and programmed with a radial step increment of nominally 7 - 10% of the Z value in order to resolve local high velocity gradients across the cone of the spray stream in the horizontal plane.

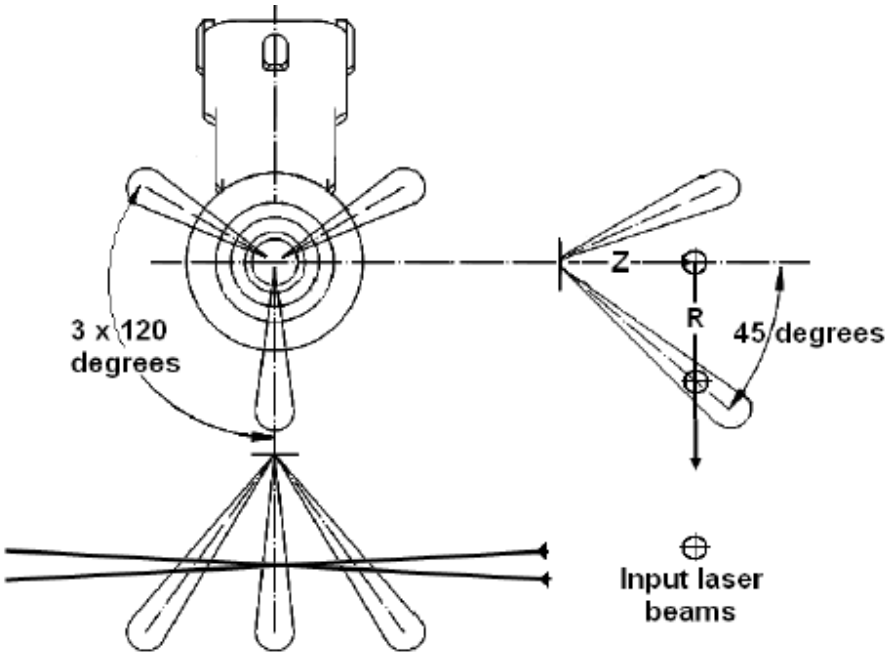

Figure 90: Injector spray geometry and PDA laser beam alignment (Mojtabi, Wigley, & Helie, 2010)

A.2 Experimental set-up of PIV test bench:

The measurements are performed in a constant volume chamber of 112mm × 112mm cube capable of reproducing the high pressure (0-150 bar) and high temperature (20- 200°C) conditions that are encountered in internal combustion engines. The chamber is equipped in such a way as to enable accurate control of the ambient pressure and temperature conditions. The injector fuel temperature and nozzle temperature are also controlled by specific cooling circuits. The test cell includes five 70mm diameter sapphire windows providing significant optical access.

Two injectors XL 3-holes 90° CA and XL 6-holes 60° CA are mounted in such a way that the measurement plane is between the two jets as shown in figure 1. The Xl 3-holes injector is tilted at an angle of 35° to z-axis to separate the two plumes with the third plume resting in the middle. Similarly two plumes from XL 6-holes injector are separated by tilting the injector 35° to z-axis. The laser light source used for the PIV experiments is a PIV 400 SPECTRA PHYSICS laser. The double cavity of the laser generates two pulsed beams with the energy of 200mJ each at a wavelength of 532nm. The Laser frequency is 10 Hz and the two laser pulses are separated by a time delay (Δt) which is adapted

according to the measured velocity range (the Δt value typically used in this study was 20 µs). The two beams are transformed into a 2D laser sheet by a diverging and a converging lens. To get the PIV plane in between the two jets, a laser sheet enters the test cell by the window in the base of the chamber by using a 45° mirror. The laser sheet illuminates a vertical plane in the test cell from the base of the chamber to the chamber roof in the direction of the injector tip, as shown in figure 1.

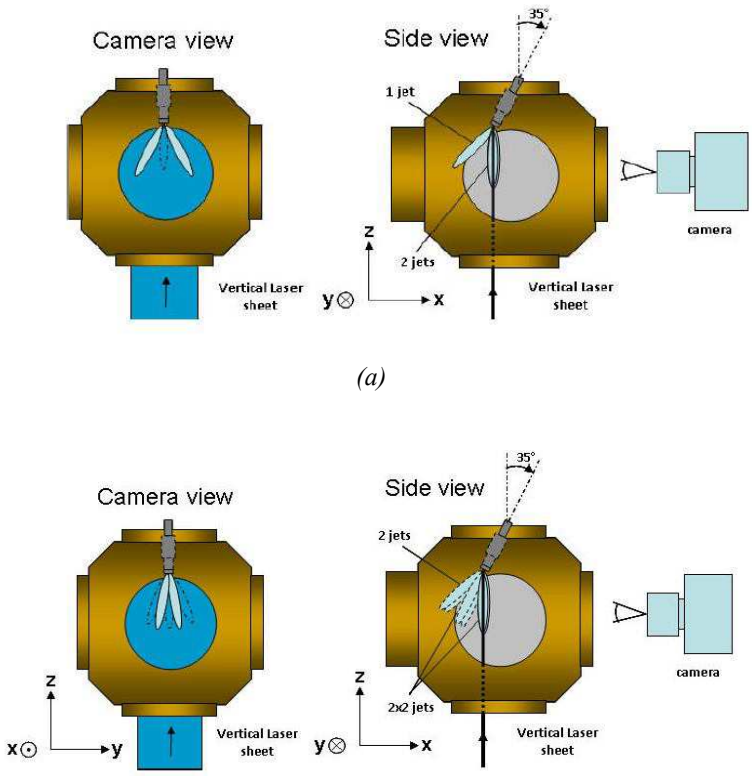

Figure 91: PIV setup of the air entrainment between the two jets for (a) XL 3-holes injector (b) 6-holes injector [courtesy IFPEN]

A.3 Experimental setup high zoom shadowgraphy

Spray images are captured by a Fuji S5 Pro CCD camera - the field of view is 24x36mm - recording shot to shot images with a resolution set to 2 µm/pixel. The illumination lamp is a nanolite with around 20 mJ of energy at each pulse, controlled by a driver, and aligned on the optical axis of the camera. Its flash duration is about 11ns, which is short enough to avoid image blurring. The injector is fixed in between by precise NewPort micrometrics actuation and a lens focuses the light beam on the injector tip. The fuel used is N-heptane and is injected into ambient conditions (temperature

~18°C). A hydraulic system feeds the fuel from the tank to the injector. The pump speed is controlled with a computer and the injection pressure is measured by a transducer. The injection event is controlled by a SDI drivebox Continental. All parts are connected and synchronized thanks to a National Instrument card. Commands are given from the computer using LabView software programmed by Assystem Company. The camera is equipped by 3 sets of 3 rings each and a 105mm objective to reach a magnification of 5.5. Finally, pictures are taken after 2ms from the injector's needle opening command; hence the quasi-steady conditions are reached. (Makhlouf, et al., 2012)

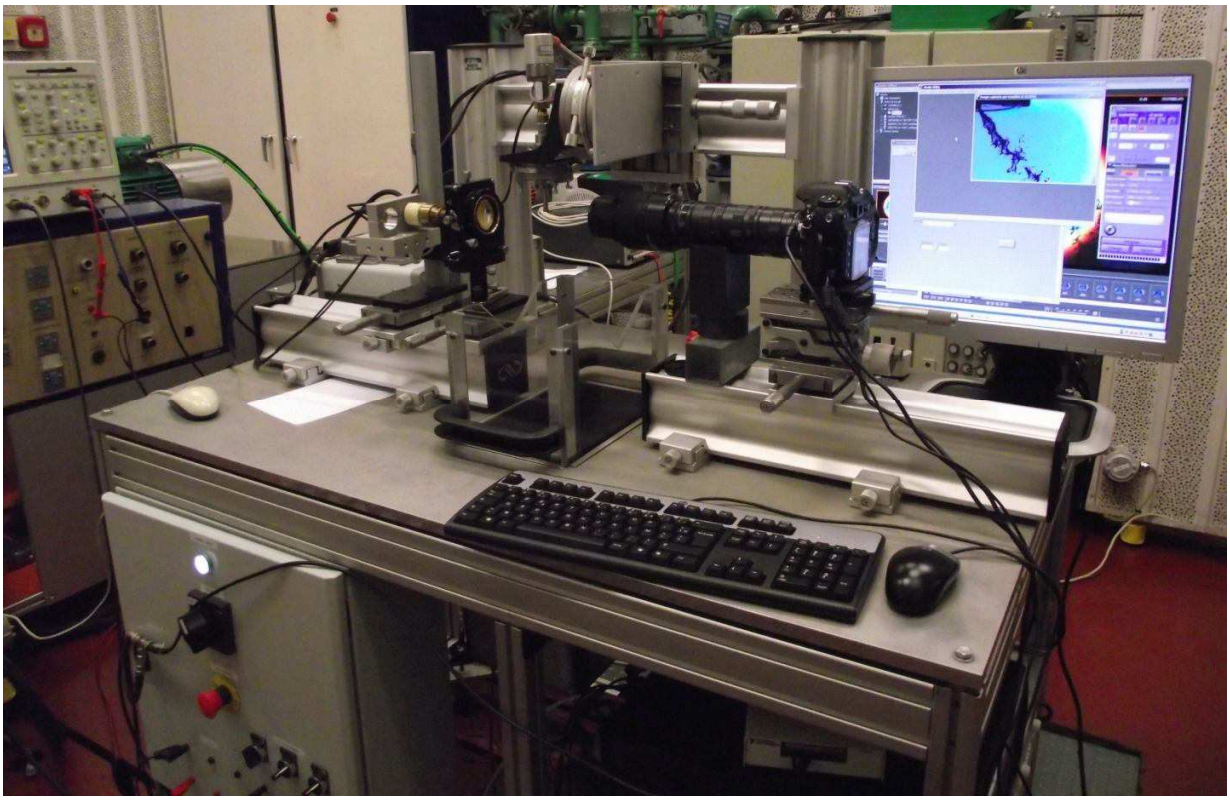

Figure 92: Spray test bench set-up for close-up spray imaging [courtesy Samir Makhlouf, PhD Student]

Appendix B Input Quantities from Separate Existing LES-Volume Of Fluid Simulations

Volume Of Fluid Large Eddy Simulations were realized by Continental engineers during the MAGIE project on the same nozzle geometry. Results of Volume Of Fluid simulations are used as inputs of the dispersed spray LES. The present appendix does not describe the simulations, for which the reader will be able to refer to (Chesnel & Helie, 2013). Quite equivalent simulations are also described in (Befrui, Corbinelli, Spiekermann, Shost, & Lai, 2012). The appendix describes shortly the analysis of these primary atomization results, analysis done by Continental engineers. The methodology of injection quantities are described in Chapter 5.

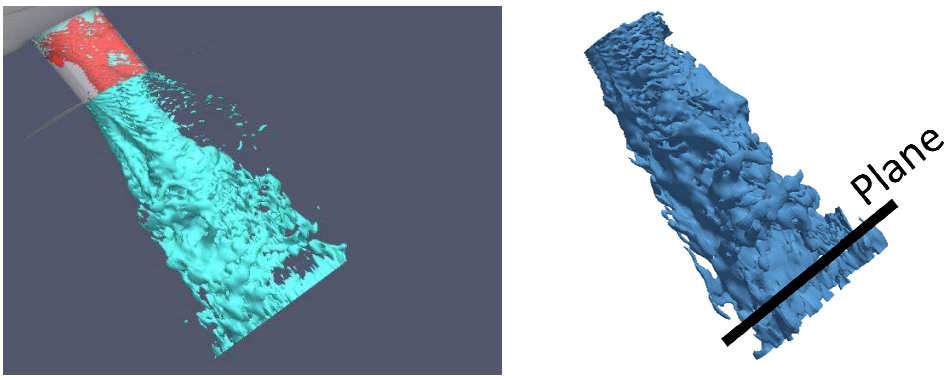

(a) *(b)*

Figure 93: (a) typical simulation, red: cavitation surface in the metering hole red ; light blue: atomization surface in the external domain. (b) Plane used for primary atomisation analysis of the continuous core.

The results are separated in (1) isolated drops and (2) atomizing continuous core.

Firstly, a side jet toward the injector body exterior is clearly observed Figure 93. It contains mainly already atomized individual, not connected, liquid element. These drops are analyzed and their probability density function shows the existence of drops from 2 to 4 µm. That means the droplets are atomized well due to cavitation effect which creates a dense fog of drops but without high

momentum. Moreover, some isolated drops are also present in the main spray cone area. In total, their mass corresponds to about 10 % at 100 bar of the overall liquid flow.

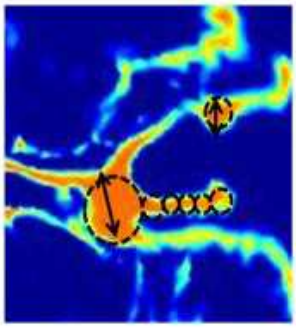

Figure 94: Ligaments analysis rough principle

Secondly, the atomizing continuous core exhibits mainly bidimensional (wrinkled) ligaments. The ligaments are extracted from a plane at short distance on the different instantaneous realizations as in Figure 94. A subgrid projection is operated. The local thickness is defined as the minimum distance across the ligament (around its centreline). The liquid contour determination is based on the Volume-Of-Fluid principal quantity, and a level-set rebuilding regenerates a continuous distance function. Its derivative location edge determinates the centreline, where the contour distance is interpolated. Lastly, this result is projected on a coarse mesh 40*40 to post-treat the probability density function of ligament size, with a projection filter size equal to the interpolated edge. The process captures local thickness evolution, complex shape and the value at the limit of the ligament as presented in Figure 95.

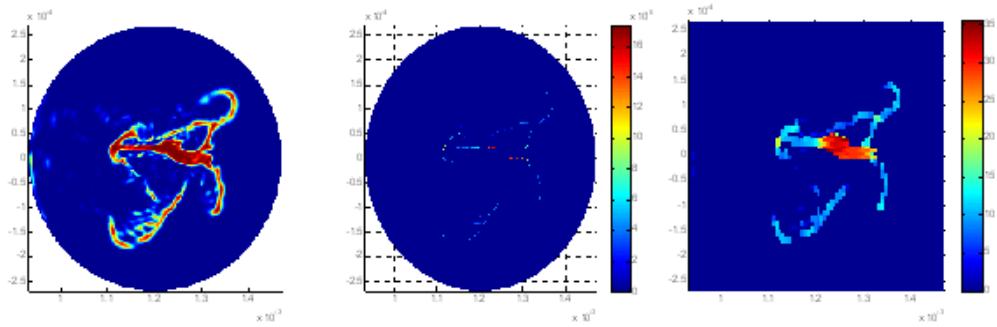

(a) *(b)* *(c)*

Figure 95: Ligaments analysis process. (a) Initial instantaneous filed (b) distance function (c): deduced arithmetic average of the expected drop size on this field (before wave analysis here)

Lastly, as the continuous core is not fully atomized, and the main flow stretches these ligaments. A classical waves analysis, as in (Senecal, Schmidt, Nouar, Rutland, Reitz, & Corradini, 1999), is introduced on a second modelling step to account for this latest atomization process from planar stretched ligaments to rounded ligaments and then into isolated drops. To simplify such approach, the present LES VOF-dispersed spray assumes a constant size relationship factor of 0.5 at 100 bar and 200 bar between the ligaments thickness and final drop size.

Appendix C A Reminder to the Numerical Schemes

The numerical computations require discretisation of the ensemble averaged Navier-Stokes equations in RANS and averaged Navier-Stokes equations over a presumed filter in LES. All the numerical schemes, used in this thesis for RANS and LES, are presented here as reminder to the reader because all these schemes are widely used. For more details, the reader is referred to (Jasak, 1996) and (Villiers, 2006).

The governing equations are solved on the computational mesh which is produced by the domain discretisation. The domain discretisation can be split in to temporal and spatial discretisation. Temporal discretisation is achieved by the subdivision of time into small time steps. The solution is obtained by time marching from the initial boundary condition. (Jasak, 1996). Whereas, spatial discretisation subdivides the domain into small control volumes, and these control volumes completely fill the domain without overlapping. A classic example of control volume is presented in Figure 96 shows the cell centroids P and N, connecting vector d, face f and an outward pointing "face area vector" $\mathbf{S}_f$ perpendicular to the cell face and magnitude equal to the cell face. The cell averaged dependent variables like **u**, p, e, etc are defined at the cell centres and the derived properties (flux densities) on cell faces (Villiers, 2006).

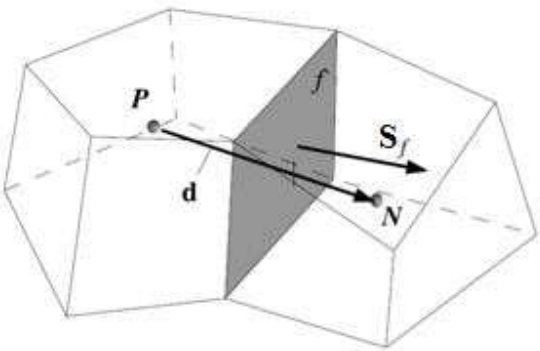

Figure 96: Control volume for finite volume discretisation; adapted from (Villiers, 2006)

Appendix C A Reminder to the Numerical Schemes

A global description of the numerical schemes based on a generalized transport equation has been presented here. A standard transport equation of a general quantity ϕ can be represented by (Ferziger & Perić, 1995).

$$\underbrace{\frac{\partial \rho\phi}{\partial t}}_{Temporal\ derivative} + \underbrace{\nabla.(\rho\mathbf{U}\phi)}_{\text{Covenction term}} - \underbrace{\nabla.\left(\rho\Gamma_\phi\nabla\phi\right)}_{\text{Diffusion term}} = \underbrace{S_\phi(\phi)}_{Source\ Term} \tag{94}$$

where, Γ is the diffusivity coefficient. It is a second order equation because of the diffusion term which involves a second derivative. Particularly in case of LES in order to maintain the high accuracy of the solution, it is necessary to use the discretisation scheme of same order than the order of the equation. Discretisation also produces some error or inaccuracy which directly depends on the size and quality of mesh. A finer and better quality mesh reduces the discretisation errors.

Different numerical methods are usually used in the computational analysis such as; Finite Difference Methods (FDM), Finite Element Methods (FEM) or Finite Volume Methods (FVM), FVM methods are the most widely used in CFD codes due to its versatility and stability. The FVM approach solves the equation over a control volume (V_p) around a point P in the integral form of equation (95) is:

$$\int_t^{t+\Delta t}\left[\frac{\partial}{\partial t}\int_{V_p}\rho\phi\, dV + \int_{V_p}\nabla.(\rho\mathbf{U}\phi)dV - \int_{V_p}\nabla.\left(\rho\Gamma_\phi\nabla\phi\right)dV\right]dt = \int_t^{t+\Delta t}\left(\int_{V_p}S_\phi(\phi)\, dV\right)dt \tag{95}$$

All the terms in the equation (95) are treated separately.

C.1 Spatial Discretisation of the terms:

In order to examine the discretisation of each term, first step is to convert the volume integrals to the surface equivalents. For this purpose, Gauss theorem is utilized throughout the discretisation process involving the identities:

$$\begin{aligned}\int_V \nabla.\boldsymbol{\phi}\, dV &= \oint_{\partial V} d\mathbf{S}.\boldsymbol{\phi}\\ \int_V \nabla\phi\, dV &= \oint_{\partial V} d\mathbf{S}\,\phi\end{aligned} \tag{96}$$

where ∂V is the closed surface bounding volume, $d\mathbf{S}$ is the infinitesimal surface element outward pointing to the surface ∂V.

In OpenFOAM® numerical integration of the divergence operator over the cell surface generates the second order accurate discretised form of Gauss theorem which reads:

$$\int_{V_p} \nabla.\boldsymbol{\phi}\, dV = \oint_{\partial V_p} d\mathbf{S}.\boldsymbol{\phi} = \sum_f \left(\int_f d\mathbf{S}.\boldsymbol{\phi} \right) \cong \sum_f \mathbf{S}_f.\boldsymbol{\phi}_f \tag{97}$$

where the subscript f symbolizes face centred indexing and $\mathbf{S}_f$ denotes the outward pointing face area vector. The face values, $\boldsymbol{\phi}_f$ of the variables need to be computed by some sort of interpolation scheme which will be described later.

C.1.1 Convection term:

The convection scheme can quite simply be deduced by using discretised form of Gauss theorem from equation (97) as:

$$\int_{V_p} \nabla.(\rho\mathbf{U}\phi)\, dV \cong \sum_f \mathbf{S}_f.(\rho\mathbf{U}\phi)_f = \sum_f \mathbf{S}_f.(\rho\mathbf{U})_f \phi_f = \sum_f F_f\, \phi_f \tag{98}$$

where F_f represents the mass flux through the face and it is calculated from the interpolated values of ρ and **U**. Now, in order to evaluate the value on the face ϕ_f from the values of ϕ at cell centres an interpolation scheme is need to be introduced.

C.1.2 Convection differencing scheme:

By using a linear interpolation of ϕ between the cell centres P and N, in Figure **97**, the face value ϕ_f is calculated according to the central difference (CD) method:

$$\phi_f = f_x \phi_P + (1 - f_x)\phi_N \tag{99}$$

where f_x is the interpolation factor which is the ratio of the ratio of the distances $\overline{fN}$ and $\overline{PN}$:

$$f_x = \frac{\overline{fN}}{\overline{PN}} \tag{100}$$

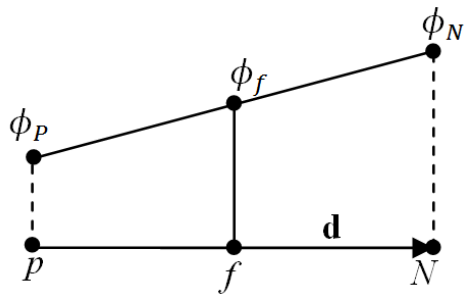

Figure 97: Face interpolation

This scheme is second order accurate even over non uniform meshes (Ferziger & Perić, 1995). The major drawback which is generally associated with this method is the production of spurious oscillations in the solution with convection dominated problems. But if the mesh is fine enough then the solution remains under control. This scheme is used for the LES simulation, which uses sufficiently finer mesh.

However it becomes problematic when the mesh is not sufficiently fine enough. This issue is addressed by using a slope limiter which makes this scheme bounded, thus more stable. The limiter used with the central difference scheme is the Sweby limiter (Sweby, 1984) presented more in detail in (Jasak, 1996). This scheme is used for the RANS simulations of full injector.

C.1.3 Diffusion Term:

The diffusion term in equation (95) is discretised in a similar way to the convection term by assuming the linear variation of ϕ.

$$\int_{V_p} \nabla.(\rho\Gamma_\phi \nabla\phi) dV = \sum_f \mathbf{S}_f.(\rho\Gamma_\phi \nabla\phi)_f = \sum_f (\rho\Gamma_\phi)_f \mathbf{S}_f.(\nabla\phi)_f \tag{101}$$

For an orthogonal mesh, a simple relationship can be used

$$\mathbf{S}_f.(\nabla\phi)_f = |\mathbf{S}_f|\frac{\phi_N - \phi_p}{|\mathbf{d}|} \tag{102}$$

Alternative to this approach, reconstruction based on cell-centred gradients be obtained but it is less accurate than the more compact formulation presented in the equation (102).

$$\nabla\phi_P = \frac{1}{V_P}\sum_f \mathbf{S}_f\phi_f \tag{103}$$

The face interpolation can quite simply be represented in a similar way to the one in equation presented in equation (102)

$$(\nabla\phi)_f = f_x(\nabla\phi)_P + (1 - f_x)(\nabla\phi)_N \tag{104}$$

In the case of non-orthogonal mesh, equation (102) is no longer second order accurate in space and thus a splitting operation of the term $\mathbf{S}_f.(\nabla\phi)_f$ is applied, which can be represented by:

$$\mathbf{S}_f.(\nabla\phi)_f = \underbrace{|\mathbf{S}_\Delta|\frac{\phi_N - \phi_P}{|\mathbf{d}|}}_{orthogonal} + \underbrace{\mathbf{S}_\mathrm{k}.(\nabla\phi)_f}_{non-orthogonal} \tag{105}$$

In the above equation, the first part is the orthogonal contribution whereas the second part denotes the non-orthogonal contribution which makes it as a second order accurate scheme.

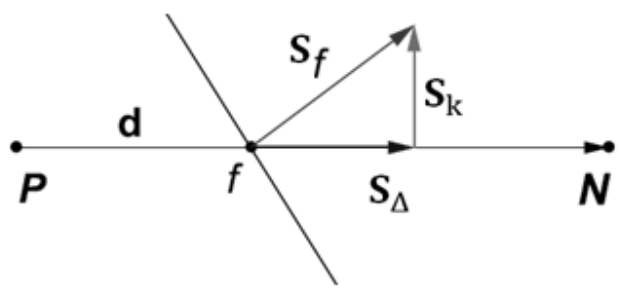

Figure 98: Decomposition of face area vector in orthogonal and non-orthogonal parts.

The vectors in the equation (105) must satisfy the equality condition:

$$\mathbf{S}_f = \mathbf{S}_\Delta + \mathbf{S}_\mathrm{k} \tag{106}$$

C.1.4 Source Terms:

All the terms, which are not possible to be considered as a part of temporal, convection or diffusion terms are classified separately under the name of source terms. Here, for the sake of a general definition, a source term is assumed to be a function of ϕ, which is initially linearised in order to be incorporated in the solution matrix:

$$S_\phi(\phi) = S_u + S_p(\phi) \tag{107}$$

where, both S_u and S_p can be the dependent on ϕ. The calculation of the volume integral of the above equation can be expressed as:

$$\int_{V_p} S_\phi(\phi)\, dV = S_u V_p + S_p V_p \phi_p \tag{108}$$

C.2 Time Discretisation:

Considering the integral form of the generic transport equation (95) can be expressed as in a semi discretised way (Hirsch, 1991):

$$\int_t^{t+\Delta t} \left[\left(\frac{\partial \rho \phi}{\partial t} \right)_P V_p + \sum_f F_f \phi_f - \sum_f \left(\rho \Gamma_\phi \right)_f \mathbf{S}_f . (\nabla \phi)_f \right] dt = \int_t^{t+\Delta t} \left(S_u V_p + S_p V_p \phi_p \right) dt \tag{109}$$

Temporal integrals and the derivates can be computed in straight forward way:

$$\left(\frac{\partial \rho \phi}{\partial t}\right)_P = \frac{\rho_P^n \phi_P^n - \rho_P^o \phi_P^o}{\Delta t} \tag{110}$$

$$\int_t^{t+\Delta t} \phi(t)\, dt = \frac{1}{2}(\phi_P^o + \phi_P^n)\, \Delta t \tag{111}$$

where,

$$\phi_P^n = \phi(t + \Delta t), \quad \phi_P^o = \phi(t) \tag{112}$$

Therefore the by using the equations (96) and (97), the equation (109) can be written in the form of:

$$\frac{\rho_P^n \phi_P^n - \rho_P^o \phi_P^o}{\Delta t} V_p + \sum_f \mathbf{S}_f \phi_f^m - \sum_f \left(\rho \Gamma_\phi\right)_f \mathbf{S}_f . (\nabla \phi)_f^m = S_u V_p + S_p V_p \phi_P^m \tag{113}$$

The resulting equation is a first order accurate in time. The subscript "m" determines the implicit or the explicit method to calculate the values at the face ϕ_f and $\nabla\phi$. Explicit method uses the old time levels (m=o) and implicit method uses new time levels (m=n).

C.2.1 Euler Implicit Scheme:

The explicit method is usually stable only if diffusion terms are not small in comparison to the convection term. Therefore, explicit method becomes unstable for the face CFL numbers (Courant, Friedrichs, & Lewy, 1928) larger than 1, which is a very strict restriction. The CFL number is defined as:

$$CFL = \frac{\mathbf{U}_f \mathbf{d}}{\Delta t} \tag{114}$$

where $\mathbf{U}_f$ is the velocity at the face of the cell. On the other hand, the implicit method for calculating face values in time is stable at even at Co > 1. Implicit method although is also a first order accurate in time but it is preferred over explicit method because of stability

$$\phi_f = f_x \phi_P^n + (1 - f_x)\phi_N^n \tag{115}$$

Euler implicit scheme is thus the choice for the RANS simulation.

C.2.2 Backward Implicit Scheme:

Backward implicit scheme provides second order accuracy in time. The temporal derivatives in equation (113) can be obtained by the Taylor series expansion of ϕ in time with $\phi(t + \Delta t) = \phi^n$

$$\phi(t) = \phi^o = \phi^n - \frac{\partial \phi}{\partial t}\Delta t + \frac{1}{2}\frac{\partial^2 \phi}{\partial t^2}\Delta t + O(\Delta t^3) \tag{116}$$

For achieving the second order accurate derivative another Taylor series expansion is applied once again for an old time, $\phi(t - \Delta t) = \phi^o$

$$\phi(t - \Delta t) = \phi^{oo} = \phi^n - 2\frac{\partial \phi}{\partial t}\Delta t + 2\frac{\partial^2 \phi}{\partial t^2}\Delta t^2 + O(\Delta t^3) \tag{117}$$

Now, combining terms in equation (116) and (117) to eliminate $\frac{\partial^2 \phi}{\partial t^2}$ terms lead to

$$\frac{\partial \phi}{\partial t} = \frac{\frac{3}{2}\phi^n - 2\phi^o - \frac{1}{2}\phi^{oo}}{\Delta t} \tag{118}$$

The final discretised equation takes the form:

$$\frac{\frac{3}{2}\phi^n - 2\phi^o - \frac{1}{2}\phi^{oo}}{\Delta t}V_p + \sum_f F\phi_f^n - \sum_f \left(\rho\Gamma_\phi\right)_f \mathbf{S}.(\nabla\phi)_f^n = S_u V_p + S_p V_p \phi_p^n \tag{119}$$

Backward differencing scheme is less accurate than other classical 2nd order schemes like crank-Nicolson tie marching (Villiers, 2006). However, it is cheaper and especially much more robust. For these reasons, this scheme has been used in this thesis for LES.

Appendix D Research Papers

Research Paper # 1

(Presented at International European Conferencing of Liquid Atomization and Spray, Estoril, Portugal, 2011)

POD Application for the Flow Characterization at the Exit of a Low Pressure Gasoline Nozzle

M. M. Khan[†5], Dr. J. Helie[†], Dr. A.A. Burluka [‡]

[†] Continental Automotive SAS, BP 1149 Toulouse Cedex 1, France, [‡] School of Mechanical Engineering, University of Leeds, United Kingdom

Abstract

A methodology, based on Proper orthogonal decomposition (POD), is developed to identify and characterize coherent structures of fluctuating velocity fields at the exit of a *Gasoline* Low Pressure nozzle. Large numbers of data sets, obtained from already published Large Eddy Simulations (LES) of a gasoline nozzle flow at 10 bar pressure [1], are used to establish a valid correlation matrix. The dominant POD modes identify the big recirculation zones subjected to strong axial and radial pulsations. The coherent structures in the later modes tend to break away into smaller ones carrying less energy. Flow reconstruction, by the linear combination of energetic POD modes, gives a clear understanding of the role of dominant fluctuation patterns and large scale coherent structures in the temporal development of turbulent flow field at the nozzle exit.

Introduction

In automotive industry, sprays are very widely studied with the main emphasis on liquid fuel atomization to produce better combustion. The spray atomization and shape are strongly linked to the

[5] Corresponding Author: Muhammad.2.Khan@continental-corporation.com

flow structure variations at the start of the injection [2, 3]. And the flow structure in the near region is heavily dependent on the injection pressure. Low injection pressure increases the prospects of ligaments and coherent structures whereas high injection pressure produces smaller droplets [1]. Therefore in order to expand the current knowledge of the sprays, in depth experiments along with the detailed simulations are needed to be performed. There are several experimental techniques developed specifically to analyse sprays thoroughly e.g. shadow-graphy, PDA, X-Ray measurement techniques etc. But when it comes to simulation, near injection region is very difficult to simulate because of high instabilities. In this region primary atomization occurs and most of the primary atomization models try to fit several parameters to match particular experimental results. In this regard, Large Eddy Simulation (LES) which resolves large part of the flow can predict better atomization. But a similar study with low pressure injector done with LES in [4] shows the production of large number of droplets with relatively high velocity just after the start of the injection which is contradictory to experiments. Thus to develop more understanding and to achieve better atomization, internal flow simulation of an injector is needed to be coupled with the spray simulation. But it is very difficult to gain any solid understanding from fluctuating quantities (velocity, vorticity, pressure) of LES simulation. In the present study, the data sets obtained from the Large Eddy Simulation of internal flow of three holes special XL2 injector of continental already published in [1], are analysed with Proper orthogonal decomposition (POD). The current work focuses only on the resolved, filtered scales.

POD Methodology

POD is a very powerful method for post-treatment of experimental and simulation data [5]. The classical POD was first introduced in the context of fluid mechanics by Lumley [6, 7] to identify deterministic features of turbulent flows. Data analysis using the POD is often conducted to extract 'mode shapes' or basis functions, from experimental data or detailed simulations of high-dimensional systems, for subsequent use in Galerkin projections that yield low-dimensional dynamical models. It uses the basic principles of earlier available models such as, Principal Component Analysis, the Karhunen–Loéve Decomposition, and the Singular Value Decomposition [8]. These orthogonal eigen-functions are highly correlated in average sense and therefore may be sometimes referred to the coherent structures [8].

Although POD methodology was introduced many years ago but it is being used more and more in order to understand complex phenomena in almost every branch of the fluid mechanics. Earlier, in going further with this methodology, many researchers felt as if their hands are tied down because of its huge computational requirements. But the introduction of the Snapshot POD method in 1985 by Sirovich [10], made its application possible even to the large amount of data sets produced by the simulations now days. The snapshot POD has been extensively used to study the results of LES in detail.

Snapshot POD becomes more efficient than classical POD because of considerable reduction in the resolution of spatial domain by using M snapshots of size N, where (M<<N) [10]. Snapshot POD is applied to a non-homogeneous, fluctuating velocity field, $\mathbf{u}'(\mathrm{x_j}, \mathrm{y_j}, \mathrm{z_j}, \mathrm{t_i})$ represented by a matrix $\mathbf{u}'$ of size M x N. Index i represents the number of snapshots which runs through M and $\mathrm{t_i}$ is the time at which snapshots are taken. Also, index j represents the number of grid points of size N and the coordinates x_j, y_j & z_j symbolize the position of the grid points. A detailed methodology for the flow decomposition to different modes i.e. dominant to the weak modes is given below:

Average velocity $(\overline{\mathbf{u}})$ can be calculated as

$$\overline{\mathbf{u}} = \frac{1}{\mathrm{M}} \sum_{\mathrm{i}=1}^{\mathrm{M}} \mathbf{u}(x_j, y_j, z_j, t_i) \qquad (1)$$

where $\mathbf{u}\ (x_j, y_j, z_j, t_i)$, is the total instantaneous velocity field.

The fluctuating velocity $\mathbf{u}'(x_j, y_j, z_j, t_i)$ can simply be represented as

$$\mathbf{u}'(x_j, y_j, z_j, t_i) = \mathbf{u}(x_j, y_j, z_j, t_i) - \overline{\mathbf{u}} \qquad (2)$$

A general aim of POD is to find the optimal correlated feature from a given fluctuating field. This is achieved by a correlation matrix of M x M resolution.

$$\mathbf{C}_{\mathrm{MxM}} = \frac{1}{M} \langle \mathbf{u}'^T \mathbf{u}' \rangle \qquad (3)$$

This induces a simple eigenvalue problem

$$\mathbf{C}\mathbf{A}^n = \lambda^n \mathbf{A}^n \qquad (4)$$

Here, C is the covariance matrix, λ is the eigenvalue and $\mathbf{A}^n$ is the eigenvector which can be written as $\mathbf{A}^n = A_l^n$. A_l^i corresponds to the *ith* component of eigenvector corresponding to λ^i. Moreover, eigenvalue (λ) is the measure of energy of each mode and arranged in such an order that ($\lambda^1 > \lambda^2 > \lambda^3 > \ldots\ldots\ldots\ldots\ldots\lambda^M$). The sum of eigenvalues is equal to the kinetic energy of the flow.

POD mode (φ) which are simply the orthogonal projection on the original fields. These are determined in the following fashion:

$$\varphi^n = \sum_{l=1}^{M} A_l^n \, \mathbf{u}'^l \quad n = 1 \ldots\ldots M, \qquad (5)$$

Snapshot method is based on the fact that the data vectors $\mathbf{u}'^{\boldsymbol{l}}$ and the eigenfunctions φ^n share the same amount of linear space [7]. This methodology is valid for vector fields like velocity, vorticity or scalar fields like pressure etc.

Furthermore, any snapshot can be reconstructed from a given number of modes in following way

$$\mathbf{u}'^i = \sum_{n=1}^{K} a_n^i \, \varphi^n \qquad (6)$$

Here, each value of a_n represents the POD temporal coefficients and these coefficients can simply be determined by projecting POD modes on the fluctuating velocity field, $a_n = \varphi^T \mathbf{u}'$.

The above mathematical formulation gives an in-depth flow analysis. The eigenvalues are the indicator of the energy content in each mode and POD modes ($\boldsymbol{\varphi^n}$) reveal the turbulent structures present in the flow field. Since POD process is a decomposition procedure, therefore, we can certainly reconstruct the flow field by using only the dominant modes. This feature allows us to understand the affect of the dominant modes on the flow arrangement.

Large Eddy Simulation of Nozzle Flow

POD methodology is applied to the fluctuating velocity field produced by LES simulation of the internal nozzle flow at the exit of the hole. The LES simulation was performed on a complex internal geometry of the injector including needle, seat, sac and hole with low pressure non-cavitating conditions [1]. An example of brut, instantaneous, fluctuating axial velocity at the nozzle exit in

figure 1 (a) is extracted from the velocity field of 3D internal flow simulation presented in figure1 (b). The nozzle is at an angle of approximately 42° to the horizontal plane. The velocity components (U, V, W) in the snapshots, are stored in the main flow direction (X_L, Y_L, Z_L) [6] respectively. But for the sake of better visualization all the figures are plotted in the coordinates, vertical to the exit plane i.e. (X_G, Y_G, Z_G)[7], as shown in figure 1 (c).

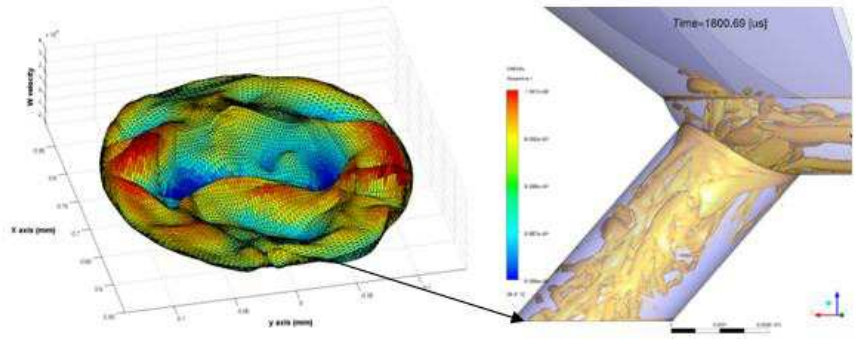

(a) (b)

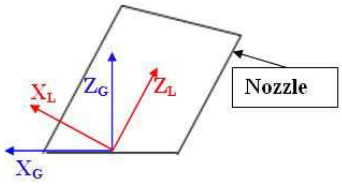

(c)

Figure 1: (a) Instantaneous fluctuating axial velocity (W) (mm/s) (b) internal flow simulation, velocity snapshot taken from [1] (c) coordinate system used for the flow analysis

The reason of choosing a three-hole injector is because a real multi-hole injectors with 5, 6 or 7 holes have been found to be very complex for the not only simulations but also the optical experiments [11]. Therefore injectors with fewer nozzles are suitable for the research and development point of view. For this purpose mono-hole injector and two holes injectors have been examined in detail [12]. However single-hole injector is not a very good representative of the multi-hole injector as the spray angle and vapour to mass ratio can be very different than the multi-hole sprays [12, 13] and also a

[6] *(X_L, Y_L, Z_L) are the local coordinates, in the stream-wise direction of the flow.*
[7] *(X_G, Y_G, Z_G) are the global coordinates, vertical to the exit plane. For simplicity the terms x, y, z are used in the plots to represent these coordinates.*

dual-hole injector can exhibit strong pulsations due to the parity of the sprays producing unstable flow [14]. Therefore three-hole injector is a good compromise *in* this regard.

Two different grids, one with 1.6 million and the other with 3 million cells are used. Although both of the cases are analysed using POD but the results from the simulation with 3 million cells are presented here. Overall results from both simulations are found to be quite similar with minor differences in the velocity pulsations. This certainly indicates that the mesh independence was achieved at 1.6 Million cells. Since with finer grid more fluctuations are visible but it is really difficult to deduce any meaningful result hidden in the instabilities. This is where POD is extremely handy, i.e. it not only identifies the energetic modes but also allows us to rebuild the flow field by reusing the energetic modes. This gives a free hand to the user to reconstruct a flow field using as many modes as he wants and analyze the effects of these modes on the temporal development of the flow.

Results and Discussion

POD decomposes the fluctuating velocity field into a number of different modes with first few modes carrying the most of the energy using equation 4 & 5. As mentioned before the eigenvalues determine the energy content of the flow and therefore pin point the most important modes. The energy analysis of the nozzle flow is presented in figure 2 (a) reveals that the first 10 modes carry 40% of the total energy. A total number of 80 modes accumulate 99% of total energy. The convergence is quite rapid for the earlier modes but it tends to slow down for the later ones as the mode become less and less energetic [15]. The log plot is a better indicator of the convergence of the modes presented in figure 2 (b). The modes after the first 20 modes carry less than 1% of the energy which makes these modes relatively passive in effecting the development of the turbulent flow field. We assume that the first few energetic modes are the best candidates to dictate the flow behaviour and thus their features are examined in detail.

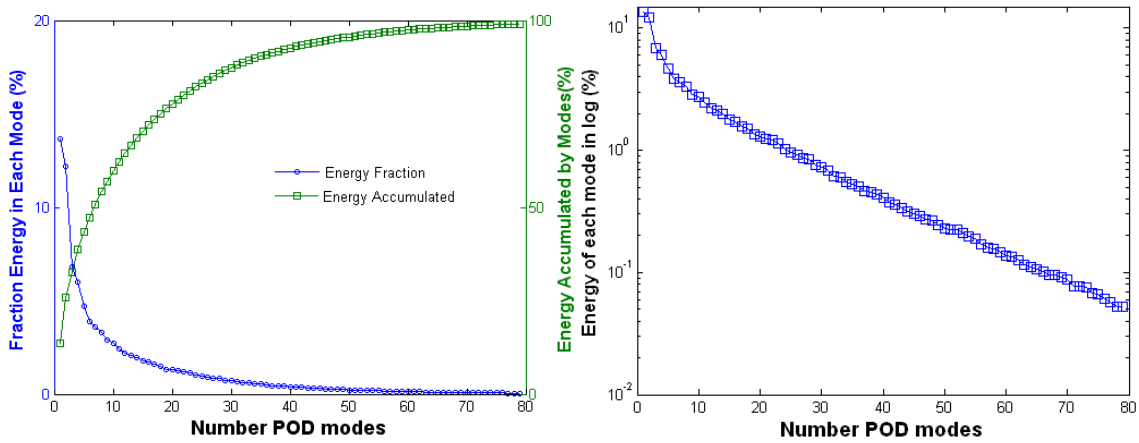

(a) (b)

Figure 2: Energy Analysis of Velocity Field, (a) Energy Analysis (b) Energy Spectrum (log plot)

Axial Velocity Streamlines of Dominant Modes

The streamlines plots, in figure 3, identify the big recirculation zones for the first four modes. The mode 1 carrying 14 % of the total energy of the flow shows a large vortex near the centre of the hole. Two big vortices appear with some small structures near the edges in Mode 2 and 3. Mode 4 shows a large vortex interacting with some small and less energetic vortices. These large scale structures in first four modes are very important not only because they carry 40 % of the total energy but also the way these structures arrange themselves. These hidden structures unveiled by POD means that 40% of flow tends to have these four types of recirculations which are not directly visible in the LES. At every instant, the flow will organize itself through a superimposition of these modes, which changes in time. Strong radial fluctuations are depicted in pairs, Mode 1 with Mode 4, and Mode 2 with Mode 3.

For instance mode 4 is closed to a mirror view of the mode 1, with a large recirculation at the left in the mode 1 and at the right side in mode 4. Mode 2 and 3 exhibit also opposite strong recirculations: bottom-right for mode 2, top-left for mode 3.

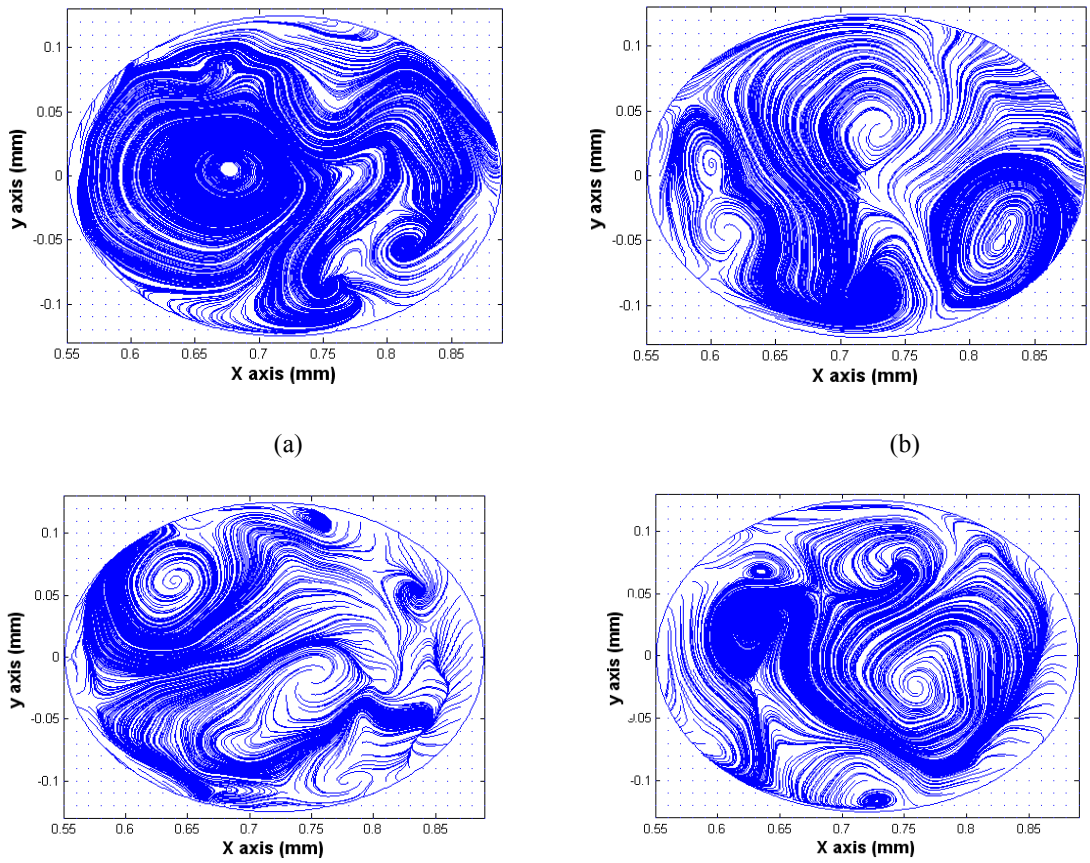

(a) (b)

(c) (d)

Figure 3: X-Y plane of axial velocity field constructed by using artificial 2D streamlines visualisation of (a) Mode1 (b) Mode2 (c) Mode3 & (d) Mode4

A comparison of the location and coupling of recirculation zones in the streamline plots is given below in table1 explaining the properties of the first four modes along with the coupling of these modes.

Mode 1	Mode 2	Mode 3	Mode 4
One Large recirculation mode at right side (including small & minor vortices).	2 counter-rotating vortices, plus 2 small vortices co-rotating vortices and one extra vortex coming from the shear layer on bottom side	2 counter-rotating vortices, plus 2 small vortices co-rotating vortices	Almost complementary physical structure to Mode 1 with mainly one large recirculation at right side and smaller co-rotating vortices on the left.
It carries 14% of the total energy.	The energy content in this mode is 12% of the total energy.	Almost complementary physical structure to Mode2, but lower in energy (7%).	Similar but opposite structure to Mode1 with 6% of the total energy.
Coupled axial/radial fluctuations.	Coupled axial/radial fluctuations.	Coupled axial & radial fluctuations with Mode 2.	Coupled axial fluctuations and radial fluctuations with Mode 1.

Table 1: Comparison of the of the first 4 modes

Strength of Vortices of Axial Velocity

Although large structures are visible in the streamline plots but the strength of these vortices is unknown. Since we have the velocity field, so by using the definition of the vorticity we take the curl of a velocity field denoted Curl $(\mathbf{u})$ or $(\nabla \times \mathbf{u})$. This gives us a vector field having magnitude equal to the maximum "circulation" at each point and to be oriented perpendicularly to this plane of circulation for each point. More precisely, the magnitude of $(\nabla \times \mathbf{u})$ is the limiting value of circulation per unit area. The velocity field will be irrotational where ever $\nabla \times \mathbf{u} = 0$.

$$\nabla \times \mathbf{u} = \left(\frac{\partial w}{\partial y} - \frac{\partial v}{\partial z}\right)\hat{\mathbf{x}} + \left(\frac{\partial u}{\partial z} - \frac{\partial w}{\partial x}\right)\hat{\mathbf{y}} + \left(\frac{\partial v}{\partial x} - \frac{\partial u}{\partial y}\right)\hat{\mathbf{z}} \qquad (7)$$

The following figures show the strength of the vortices. The magnitude of recirculation in mode 1 & 2 is very high as compared to other mode 3&4. In addition some of the small vortical structures are

relatively strong. Mode 1 and Mode 2 have more concentrated energy but the energy in Modes 3&4 is diffused. The velocity shear at the bottom of Mode 2 is also comparatively strong. The velocity vectors are superimposed to see the vortical structures.

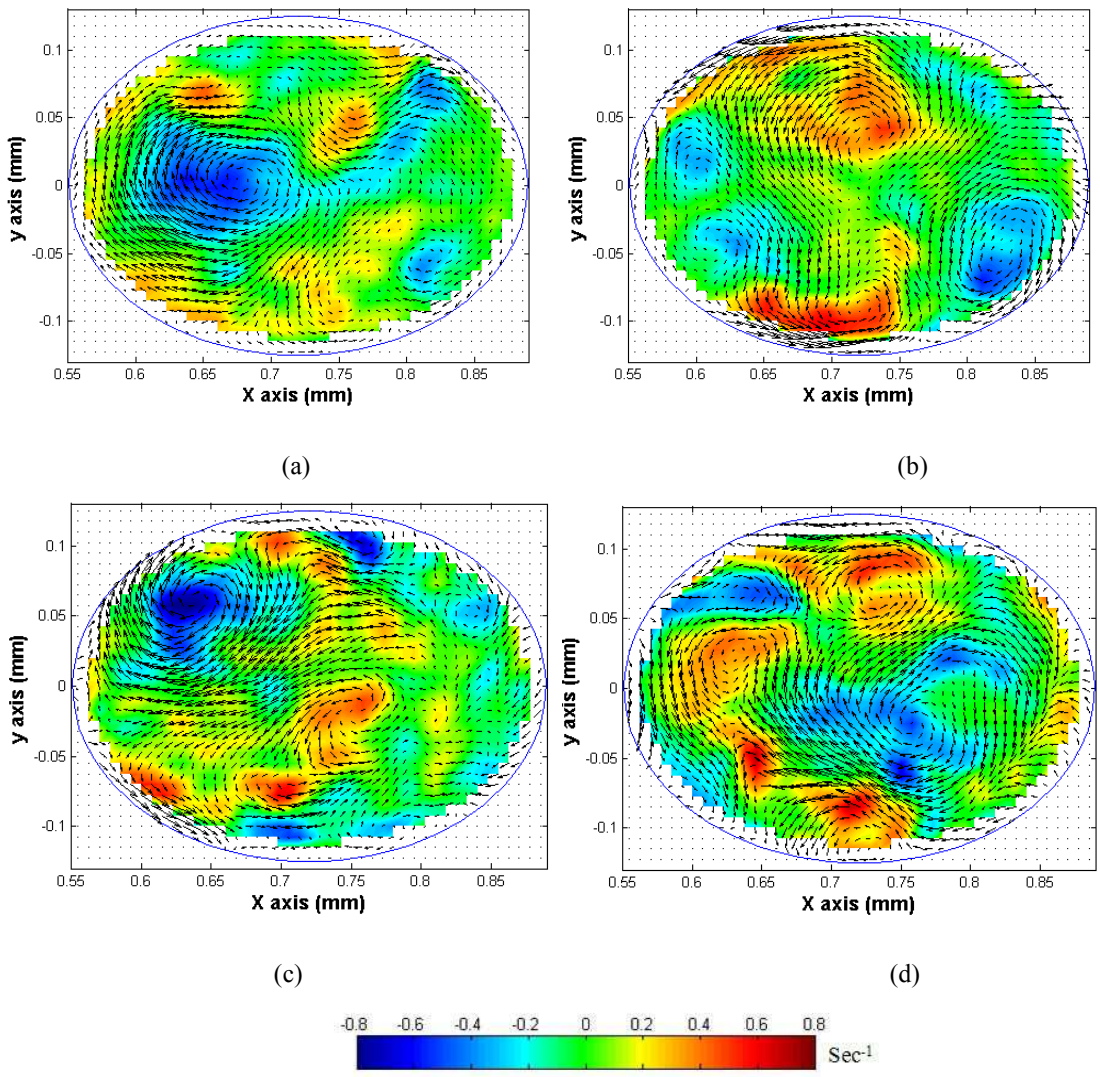

Figure 4: Contour plot of velocity curl showing strength of vortices with velocity vectors superimposed (a) Mode1 (b) Mode2 (c) Mode3 & (d) Mode4

Flow Pulsation in Axial Direction

The contour plots of the fluctuating axial velocity (W) of these four modes in figure 5, demonstrate the simultaneous axial and radial pulsations of the coherent structures in parity i.e. Mode 1 appears to be an inverse of Mode 4 and Mode 2 is the inverse of Mode3. The differences between the

asymmetrical modes in energy and locations are linked to the organization of the main flow in the nozzle hole.

Strong pulsations appear at the same locations where the big coherent structures are found. This will probably make these structures highly unstable. So, the liquid coming out of the nozzle will be dictated by these pulsating coherent structures.

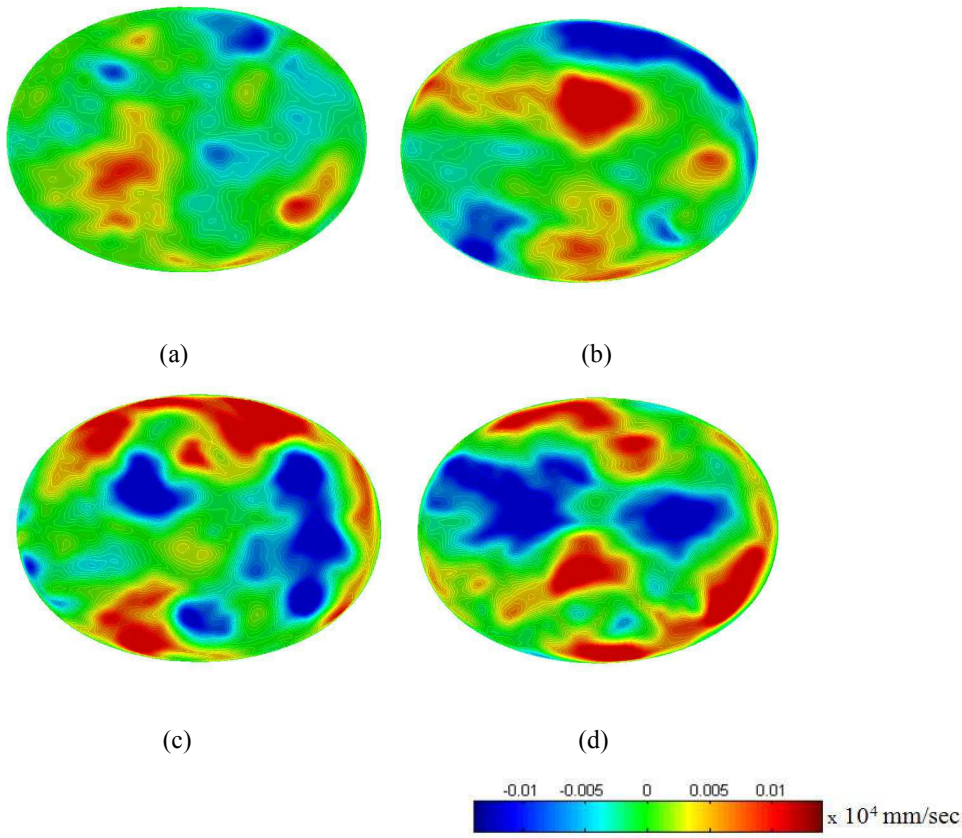

Figure 5: Contour plot of fluctuating axial velocity field (a) Mode1 (b) Mode2 (c) Mode3 & (d) Mode4

Reconstructed Velocity

The axial fluctuating velocity snapshot of figure 1 (a) is reconstructed according to equation 6, by using 10, 20 and 50 Modes has been presented in figure 6. It confirms that the large coherent structures present in first few modes are the most influential ones in the temporal development of turbulent flow at the injector exit. The flow reconstructed from higher number of modes only increases some details of fluctuations but the overall flow structure is kept. The flow reconstructed from 50 modes gives back the original snapshot as 50 modes carry 95 % of energy.

The truncated POD flow reconstruction generates the data sets with the dominant modes can significantly change the behaviour of the spray coming out of the nozzle. Although these data sets will certainly have some errors because of the truncation but then again these data sets will give us uniqueness of the different type of nozzles geometries. From these results it is concluded that the shifting of recirculation zones can be an important factor in primary atomization observed in Gasoline Low length-to-diameter ratio sprays

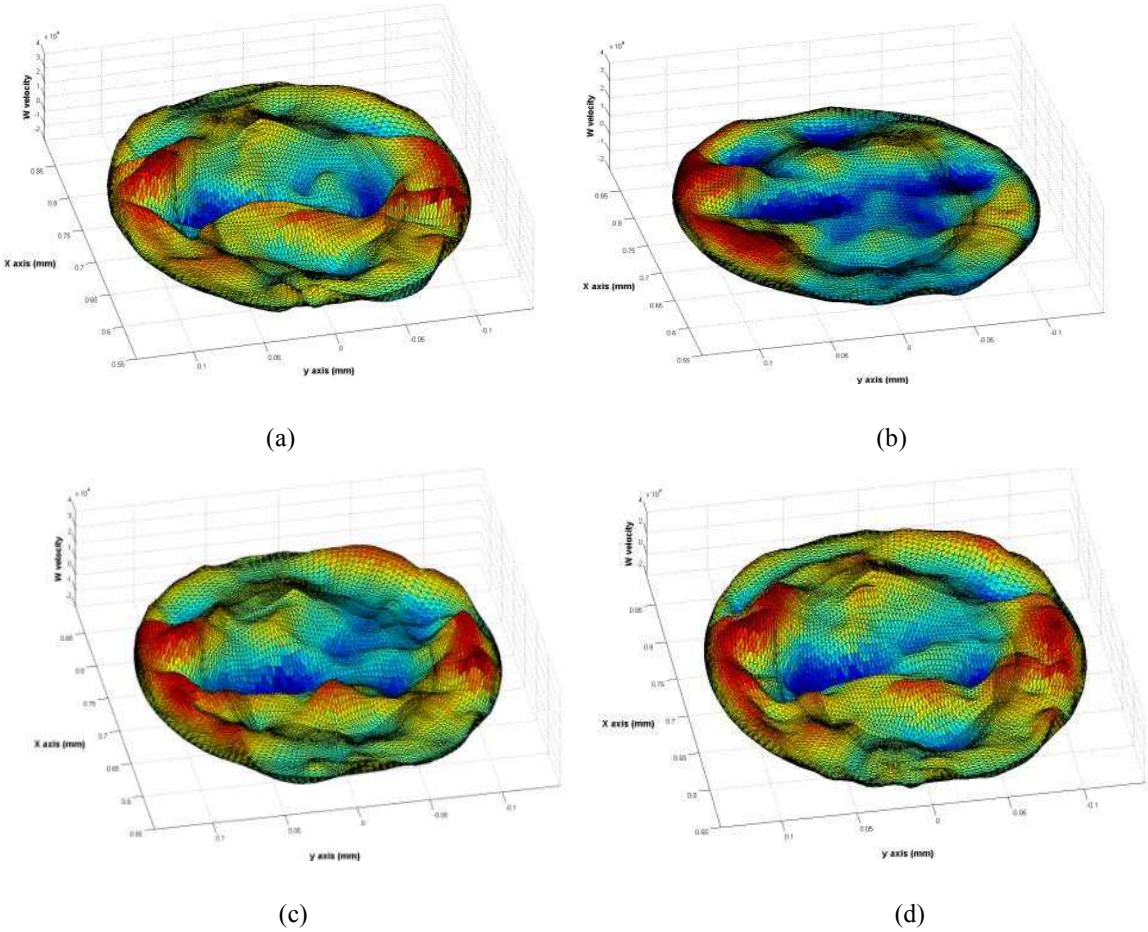

Figure 6: (a) Original axial velocity snapshot, reconstructed axial velocity snapshots (mm/s) from (b) 10 Modes (c) 20 Modes (d) 50 Modes

Superposition of the Axial Fluctuating Velocity on the Mean Flow

Since, all the analysis is done on the fluctuating velocity but the instantaneous differences produced by the dominant modes on the fluctuating velocities have yet to be seen on the overall flow. Therefore, axial fluctuating velocity is superimposed on the mean flow. The figure 7 shows the impact of axial velocity fluctuations on the mean flow (reconstructed from first 15 modes). This

pulsating effect will determine the shape of the flow structure at the exit of the hole at each instant. The axial velocity is reconstructed at two different times, 287µs and 301µs in figure 7 clearly shows the influence of POD temporal coefficients (a_n) in equation 6, on the flow development.

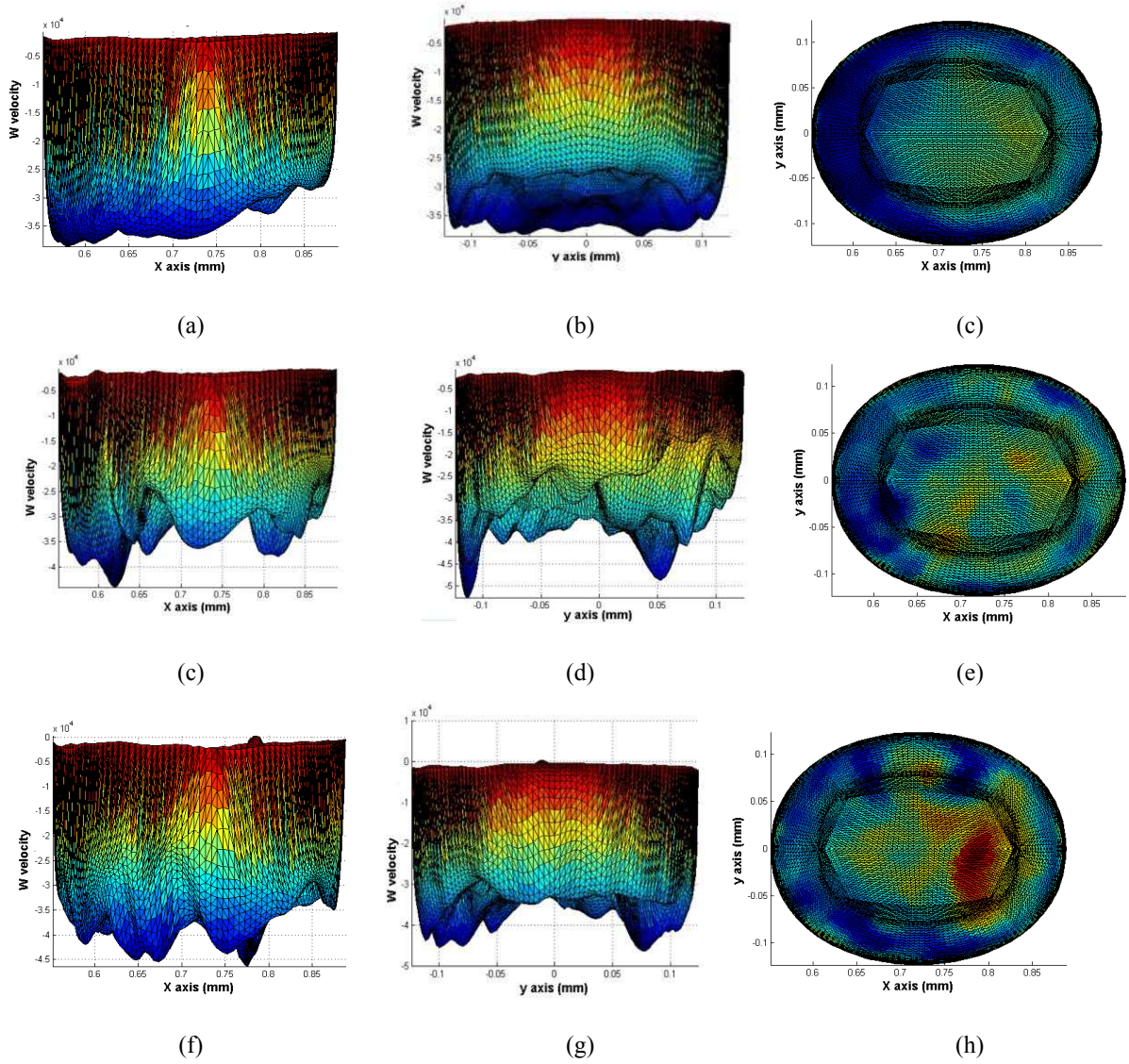

Figure 7: (a, b, c) Mean flow, axial velocity (mm/s) superimposed at (d, e, f) T=287µs,(g, h, i) T=301µs

The strong pulsations of first few modes change the shape of the flow at the exit drastically, e.g. at T= 287µs the flow has a sharp peak in the outer region with a big pulsation in the centre of the hole.

Also, at T=301μs there are two strong pulsations at either side of a big pulsation in middle of the hole. Although fluctuating velocity is relatively small in magnitudes but the fluctuations shown in time, mainly coming from the first modes are not negligible. These fluctuations can dramatically influence the atomization process.

Summary and Conclusion

The results show that first four modes identify the big recirculation zones. Mode 1 carries 14 % of the total energy of the flow shows a large vortex near the centre of the hole. Large vortices appear with some small structures near the edges in Mode 2 and 3. Mode 4 shows a large vortex interacting with some small and less energetic vortices. These large scale structures in first 4 modes are very important not only because they carry 40 % of the total energy but also the way these structures arrange themselves. Strong radial fluctuations are depicted in pairs, Mode 1 with Mode 4, and Mode 2 with Mode 3. Pulsation of these big recirculation zones are also predicted in contour plots of axial velocity along with radial fluctuations. Flow reconstruction with 10 modes has shown to have a strong influence on the mean flow.

POD analysis gives detailed features of the flow which are hidden in the LES data. Big recirculation zones occur in the first few modes carry large part of the energy. These not only pulsate axially but also fluctuate radially. The recirculations appear both simulation with 1.6 million and 3 million cells. Such recirculations have been found to be important for the better atomization because the vortical structures coming from the nozzle will expand as soon as these come out of the nozzle i.e. forcing the plume to spread out radially [3, 4]. Therefore these structures identified by POD can play a big role in the atomization and spray plume angle.

Nomenclature

a POD temporal coefficient

A Eigenvector

C Auto-covariance Matrix

M Number of Snapshots

Appendix D Research Papers

N Number of Grid points

u Total instantaneous velocity[$m \cdot s^{-1}$]

$\bar{u}$ Fluctuating instantaneous velocity [$m \cdot s^{-1}$]

u' Fluctuating instantaneous velocity[$m \cdot s^{-1}$]

λ Eigenvalue

φ Mode

References

1. J.-M. Shi□, K. Wenzlawski, J. Helie, H. Nuglisch, J. Cousin. 2010. URANS and SAS analysis of flow dynamics in a GDI nozzle, *ILASS – Europe, 23rd Annual Conference on Liquid Atomization and Spray Systems, Brno, Czech Republic.*
2. J. Helie. 2010. *The role of unsteadiness and coherent structures in the internal flow of automotive injectors: URANS & LES improving the understanding of the atomization,* Int. Conference for Internal Combustion Engines, Paris, France.
3. *C. Dumouchel. 2008. On the experimental investigation on primary atomization of liquid streams,* Experiments in Fluids, 45 371-422.
4. *Berlemont, J. Cousin, S. Grout, T. Menard. 2010. A numerical investigation of the coupling between Primary Breakup and Internal Flow. Study of the behavior of a triple disk nozzle,* ASME, 8th Int. Conference Nanochannels, Microchannels and Minichannels.
5. J. Kostas, J. Soria, M. S. Chong. 2005. A comparison between snapshot POD analysis of PIV velocity and vorticity data, *Experiments in Fluids 38 146–160*
6. J. L. Lumley. 1967. The structure of inhomogeneous turbulent flow, *Atmospheric Turbulence and Radio Wave Propagation*, *166–178.*
7. P. Holmes, J. L. Lumley, and Gal Berkooz. 1998. Turbulence, coherent structures, dynamical systems and symmetry. *Cambridge Monographs on Mechanics. Camb. Uni. Press.*
8. Knud Erik Meyer, Dalibor Cavar and Jakob M. Pedersen. 2007. POD as tool for comparison of PIV and LES data, *7th International Symposium on Particle Image Velocimetry, Rome, Italy.*

9. R. Gurka, A. liberzon, G. Hetsroni. 2006. POD of Vorticity fields: A method for spatial characterization of the coherent structure, *International Journal of Heat and Fluid Flow, 27 416-423.*
10. L. Sirovich. 1987. Turbulence and the dynamics of coherent structures. Part I: Coherent structures. *Quarterly of Applied Mathematics*, *45(3) 561–571.*
11. K. Nishida, J. Tian, Y. Sumoto, W. Long, K. Sato, M. Yamakawa. 2009. An experimental and numerical study on sprays injected from two-hole nozzles for DISI engines, *Fuel, 88 1634-1642*
12. J. Samad, H. Vahied. 2011. Numerical studies of spray breakup in a gasoline direct injection (GDI) engine, *Thermal Science, Online First 00 47-64.*
13. K. Sato, T. Tadokoro, M. Yamakawa, H. Yokohata, K. Nishida, Y. Sumoto, J. Tian. 2009. Spray and Evaporation Characteristics of Multi-Hole Injector for DISI Engines - Effect of Diverging Angle Between Neighboring Holes, *SAE World Congress, Detroit, Michigan, USA, Paper ID 2009-01-1500.*
14. M. Lai, Y. Zheng, X.-B. Xie, S. Moon, Z. Liu, J. Gao, X. Zhang, K. Fezzaa, J. Wang, J. Shi. 2011. Characterization of the Near-Field Spray and Internal Flow of Single-Hole and Multi-Hole Sac Nozzles Using Phase Contrast X-Ray Imaging and CFD, *SAE World Congress Paper ID 2011-01-0681.*
15. *M. H. Ahmed, T. J. Barber.* 2004. POD Convergence Criterion For Numerically Solved Periodic Fluid Flows, *WASE Transactions on Computer, 5 1167-1172.*

Appendix D Research Papers

Research Paper # 2

(Presented at International Conferencing of Liquid Atomization and Spray, Heidelberg, Germany, 2012)

Numerical Analysis of Multihole Gasoline Direct Injection Sprays

M. M. Khan[1*], J. Helie[*], M. Gorokhovski[†], A. Wood[+], G. Wigley[+], J. Kashdan[‡], J. P. Dumas[‡], M. Mojtabi[**], P. Guibert[**]
* Continental Automotive SAS, BP 1149 Toulouse Cedex 1, France
[†] Ecole Centrale de Lyon, Lyon, France, [+]Loughborough Universty, Leicestershire, UK
[‡]IFP Énergies nouvelles, 1-4 avenue de Bois Préau, 92852 Rueil Malmaison, France,
[**] Université Pierre et Marie Curie, Paris France
[1]Muhammad.2.Khan@continental-corporation.com

Abstract

Multi-hole gasoline direct injection (GDI) injector sprays have been studied numerically and experimentally. This study is an extension of previous work performed by Rossella Rotondi [1]. The main part of this work focuses on air entrainment and droplet size prediction in the spray plumes under non-evaporating and evaporating conditions, which can have a significant effect on jet to jet interactions, spray propagation and mixture formation. For this purpose, several Continental's special XL gasoline direct injector geometries have been studied including a 3-hole 90° Cone Angle (CA) and 6-hole 60° CA injectors. The droplet size distributions of 3-hole injector under non-evaporating conditions show sufficient droplets' breakup. Spray penetrations and the air entrainment fields of 3-hole and 6-hole injectors from simulation and experiments under evaporating conditions are quite comparable. Furthermore, the vapour and the air entrainment fields of the 6-hole spray suggest that the vapour is accumulated in the central region of the spray because the air entrained near the nozzle region is pushed downstream. The air pushed at the tips of the plumes is entrained inside the spray cone and it counters the downstream motion of the gas at a certain location. This generates a stagnation point and produces a radial flow which forces the spray plumes to bend from their original path.

Introduction

* Corresponding author: Muhammad.2.Khan@continental-corporation.com

A typical advantage of a multi-hole GDI injector is to increase the fuel efficiency by reducing fuel injection timing, penetration and increasing the fuel-air mixture quality with sufficient vapor homogeneity for better combustion in the engines. These goals are only possible if the intended spray cone angle, desired spray plumes' path and optimum atomization of the droplets are achieved [2]. But since in multi-hole GDI injectors mostly jet to jet interactions are present which make these tasks very difficult to be fulfilled and thus cause the spray to miss the intended targeting or sometimes even make the spray collapse under certain conditions. To avoid these spray plume interactions a deep understanding of the air entrainment of the spray plumes needs to be developed.

Multi-hole GDI injectors have been studied in some detail in [1] in terms of spray plume angle variations and droplet sizing. The effects of gas entrainment on the mixture formation of GDI hollow cone injector sprays under various injection pressures have been investigated experimentally using Particle Image Velocimetry (PIV) in [3]. Another interesting experimental investigation using PIV was performed in order to study air entrainment variations induced by injection fluctuations in [4]. Numerical and experimental analysis of a GDI annular orifice spray with the effects of air entrainment on the spray structures has been done in [5]. Multi-hole evaporating sprays were studied experimentally in [6] which revealed the air entrainment and vapor accumulation inside the cone but did not enable an explanation of the phenomena of air entrainment and its effects on spray behavior.

Therefore in order to gain a more detailed insight into the performance of multi-hole GDI injectors, Phase Doppler Anemometry (PDA) measurements of droplet sizes were performed by Loughborough University under non-evaporating conditions for the 3-hole nozzle. Also high-speed (Mie scattering) imaging of the liquid phase and PIV measurements were performed at IFP Energies Nouvelles (IFPEN) in order to quantify the spray development and air entrainment characteristics respectively for both the 3 and 6 hole injectors in evaporating conditions. Experimentally it proved particularly challenging to perform air entrainment measurements on the 6-hole nozzle due to its narrow cone angle. The high droplet concentrations between adjacent plumes resulted in significant laser elastic and multiple scattering effects. For such complicated nozzle geometries, numerical studies are therefore particularly useful.

1. Experimental setup and operating conditions:

The experimental setups used to perform the PDA measurements and PIV measurements are described below:

1.1 Experimental set-up of PDA test bench:

The design, construction and application of the Loughborough University two component PDA transmission system to study dense GDI fuel sprays has been well documented [7] and the configuration has been kept constant from previous experiments (reference to my ILASS 2011 paper).

The three-hole GDI injector was supported from a gantry incorporating a rotation stage and three precision orthogonal linear traverses to orientate and position the spray in three dimensions relative to the static PDA measurement volume. Each radial scan started from the geometric vertical axis through the nozzle tip and traversed out to the periphery of the spray stream. The measurement co-ordinates in the vertical plane were Z = 10, 20, 30, 40, 50 and 60mm below the nozzle tip. The horizontal traverse was computer controlled and programmed with a radial step increment of nominally 7 - 10% of the Z value in order to resolve local high velocity gradients across the cone of the spray stream in the horizontal plane.

1.2 Experimental set-up of PIV test bench:

PIV measurements and high-speed spray (Mie scattering) imaging were performed by IFPEN in the high pressure, high temperature constant volume chamber [8, 9, 10]. The chamber has a total volume of 1,4 L 112mm × 112mm and is capable of reproducing the high pressure (0-150 bar) and high temperature (293- 1000 K) conditions that are encountered in gasoline and diesel internal combustion engines. The chamber is equipped in such a way as to enable accurate control of the ambient pressure and temperature conditions. The injector fuel temperature and nozzle temperature are also controlled by specific cooling circuits. The test cell includes five 70mm diameter sapphire windows providing significant optical access for the application of laser diagnostic techniques.

Two Continental XL gasoline direct injectors were studied including a 3-hole 90° CA nozzle and a 6-hole 60° CA nozzle. The injectors were mounted in such a way that the measurement plane is between the two jets. The 3-hole injector was inclined at an angle of 35° with respect to the z-axis in

order to separate the two spray plumes from the third plume which is positioned in the middle and further behind the other two plumes. In a similar manner, two plumes from the 6-hole nozzle were studied by inclining the injector at an angle of 35° with respect to the z-axis. The light source used for the PIV experiments was a PIV 400 Spectra Physics laser. The double cavity of the laser generates two pulsed beams with the energy of 200mJ each at a wavelength of 532nm. The laser frequency was 10 Hz and the two laser pulses were separated by a time delay (Δt) which was adapted according to the measured velocity range (the Δt value typically used in this study was 20 μs). The laser beams were transformed into a 2D laser sheet by diverging and converging lenses. In order to align the PIV measurement plane in between the two jets, a laser sheet entered the test cell through a sapphire window in the base of the chamber by using a 45° mirror. The laser sheet illuminated a vertical plane in the chamber between the floor of the chamber and the chamber roof in the direction of the injector tip.

1.3 Operating conditions:

The operating conditions for both the XL 3-hole 90° CA and XL 6-hole 60° CA injectors are presented in the table below:

Conditions and Experiment type	Injectors	Injection Pressure (P_i) (bar)	Fuel Temperature (T_f) (°C)	Chamber Pressure (P_c) (bar)	Chamber Temperature (T_c) (°C)	Injection Duration (ms)	Total Injected Mass (mg)	Fuel Type
Non-evaporating-PDA	3-hole	100	20	1	20	2.0	15	Gasoline
Evaporating-PIV	3-hole	200	90	1.54	33	3.32	24.9	Iso-Octane
Evaporating-PIV	6-hole	200	90	1.54	33	3.387	49.8	Iso-Octane

Table 1: Operating conditions for PDA and PIV

2. Numerical simulation setup:

The Reynolds Average Navier Stokes (RANS) simulations were performed on OpenFOAM ® [11] version 1.7.1, where the gaseous phase was modeled by the standard K-Epsilon approach and the liquid phase was modeled by the Lagrangian approach. A compressible reacting spray solver based on the standard dieselFoam solver and automatic mesh refinement (AMR) of interDyMFoam was used. This solver was implemented in OpenFOAM ® with the help of [12] which gives the solver a capability of AMR. The PISO (pressure implicit with splitting off operators) algorithm [13] was implied with 2 iterations of the PISO loop for the predictor correction. A second order setup for the space discretisation and first order setup for time discretisation was utilized. Gauss limited linear scheme is a second order bounded scheme which is utilized for the divergence scheme. Gauss linear corrected scheme is applied which is the second order unbounded conservative scheme. Euler Implicit scheme which is first order accurate in time and is dependent on the courant number for the stability is used. Automatic time step adjustment is also included to keep local courant number to be less than 0.5 with initial time step of $10^{-7} sec$. Preconditioned bi-conjugate gradient method [14] with Diagonal incomplete-Cholesky (symmetric) preconditioner (DIC) for pressure equation and Diagonal incomplete-LU (asymmetric) for the equations of the rest of the quantities like velocity, kinetic energy etc are used with a local accuracy of 10^{-7} at every time step.

A computational domain of size 112mm x 112mm x 112mm with an initial cell size of 1.5mm was used for the simulations with a mesh refinement interval of 2 and maximum cell limit of 5 million. The initial cell size after being refined twice reduced to a minimum cell size of 0.375mm. Maximum limit of cells ensures the cell size doesn't increase beyond the computational resources. AMR is based on a scalar field i.e. kinetic energy and vapour mass fraction for non-evaporating and evaporating conditions respectively.

2.1 Spray models:

A spray is sometimes referred to as a cluster of small droplets moving at high velocity in a continuum because when a pressurized liquid jet enters a gaseous environment it exchanges momentum with the slow moving or quiescent gas and thus causes breakup of the liquid jet into smaller droplets. Therefore for high pressure cases blob injection is preferred for the fuel injection which eliminates the need of a primary atomization model and requires only the use of a secondary atomization model.

As the spray plume moves further downstream the effect of drag, inter-droplet collisions, evaporation and heat transfer become prominent and the spray becomes more complex to predict and model. One of the most important features of the sprays is the air entrainment rate which has a main influence on the motion of the droplets. Therefore several sub models need to be included in spray modeling. The library of OpenFOAM covers large number of different spray sub-models which have been used in the simulations.

2.1.1 Blob injection model:

A Rosin Rammler droplet distribution function was utilized for the blob injection with 12° angle for each of the spray plumes was assumed. The coefficients of Rosin Rammler distribution used in the simulations were n= 3, d= 100μm and 1μm < x< 150μm.

2.1.2 Droplet breakup model:

For the secondary atomization Enhanced TAB (Taylor Analogy Breakup) was used. The ETAB model uses the same concept of droplet deformation as a standard TAB model but with different relations for the breakup of parent droplet to child droplets [15]. The relationship of child droplet radius (*Rc*) to parent droplet radius (*Rp*) relationship is given below as:

$$\frac{R_c}{R_p} = e^{-K_{br}t} \;;\; K_{br} = \begin{cases} k_1 w & We \leq We_t \\ k_2 w\sqrt{We} & We > We_t \end{cases} \qquad (1)$$

K_{br} is a constant depending on the regime of droplet breakup. There are two droplet breakup regimes which can occur i.e. either bag breakup or stripping breakup. k_1 and k_2 are the constants which was set to 0.2 and We_t is the transition Weber number which distinguishes the two regimes and was set to 100 for all cases.

2.1.3 Dispersion, collision, evaporation and drag models:

Droplet dispersion is caused by the turbulent gas motion. A stochastic dispersion model which is based on [16] was used in the simulation. It uses the turbulence correlation time relationship from [17].

Trajectory model of Nordin [18] is used in the simulations, which is based on the O'Rourke collision model [19] with some modifications. The short coming of the original model of O'Rourke is that it

only considers the probability of the parcels to be found in the same cell for the collision without any dependence of parcel directions. This problem is addressed in the trajectory model which calculates the trajectory of the parcel and allows collision where these trajectories coincide otherwise droplets do not collide.

The evaporation model is based on simple D^2 law and it uses the Sherwood number calculated from Ranz-Marshal correlation to calculate evaporation relaxation time. This model is well explained in [20].

As the droplets move downstream they experience drag force which slows down these droplets. In order to incorporate drag force in the spray simulation standard drag law with the values based on the coefficient of drag (C_d) is used and it is dependent on the value of droplet Reynolds number (Re).

3. Results and discussion:

The results are discussed below for both non-evaporating and evaporating conditions in detail.

3.1 Non-evaporating conditions:

The simulation results of droplet size distributions of 3-hole injectors are compared with experimental PDA results, under non-evaporating conditions presented in the *Table 1*. The plot in figure 1 (left) shows a comparison between the simulation and experimental results for the average droplets size (D_{10}) at different axial locations at the centre of a single plume for a time interval of 1.6 to 2ms. The mean droplet sizes at 10mm downstream location at the centre of the plumes are 7.55µm and 7.43µm for the experiment and simulation respectively. The mean droplet size reduces to 5.89µm at 40mm location in the experiments where as in simulation it is 6.55µm in figure 1 (right). The probability density function (PDF) of droplet size distribution at 40mm downstream location at the centre of a single separated plume also show good agreement.

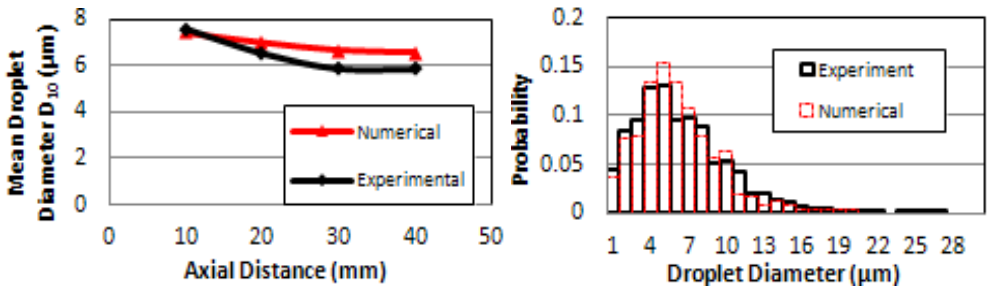

Fig 1: Experimental and simulation results of 3-hole injector (left) Mean droplet diameter (D_{10}) at different axial locations (right) PDF of droplet distribution at 40mm axial location

3.2 Evaporating conditions:

3.2.1 Axial liquid penetration of the spray:

Axial liquid penetration rates of the spray are compared for both the 3-hole and 6-hole injectors experimentally and numerically under evaporating conditions listed in Table 1. The results in figure 2 reveal that both injectors have similar penetration rates despite the fact that the nominal nozzle geometries differ significantly between the two injectors. The numerical prediction of the global spray penetration is comparable with the experimental data. A delay of 400µs was observed for the experiments between the electrical start (injector trigger) and the physical start of injection (first appearance of liquid at the nozzle exit). This delay incorporates the electrical delay (solenoid activation) and hydraulic delay (internal nozzle fluid flow). This delay is also included in the simulations to have the same starting time of fuel injection.

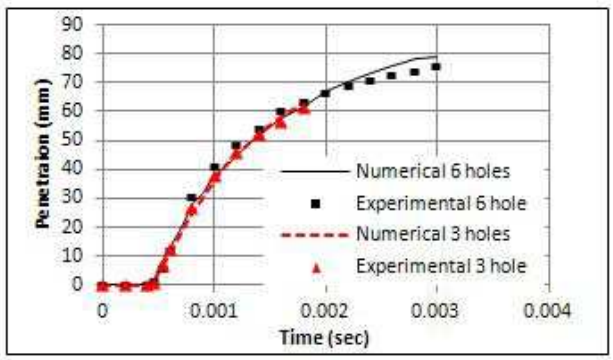

Fig 2: Comparison of penetration curves under evaporating conditions for 3 and 6 hole injectors

3.2.2 Air entrainment between the two jets:

A comparison of the 2D flow fields measured experimentally and simulated numerically under the evaporating conditions has been presented below. The air entrainment characteristics for the 3-hole and 6-hole injectors are shown in figures 3 on top and bottom respectively, at a time 1.4ms *After Start Of Injection* (ASOI). In both cases the numerical results show satisfactory agreement with the experimental data. The air entrainment is relatively high in the near nozzle region and at the spray tip leading edge as a result of the high spray momentum for both the 3 and 6-hole injectors.

On the contrary, the 6-hole injector reveals a quite different structure. Experimental measurements show that the spray collapses compared to the 3-hole injector. The spray collapse is believed to be linked to the more significant jet-jet interactions which modify the air entrainment characteristics. Unfortunately PIV data could not be acquired in the inter-jet spacing for the 6-hole injector due to spray collapse and the resulting formation of what appears to be a continuous spray plume. The air entrainment in between the jets is discussed in more detail in the section entitled "jet to jet interactions". The resulting difference between the experimental and computational results as shown on figure 3 (top left, bottom left) does not exceed 2.5m/s and mostly the error appears to be local or linked to the main direction of the flow more than the absolute value i.e. the error vectors are mainly perpendicular to the main direction from experimental.

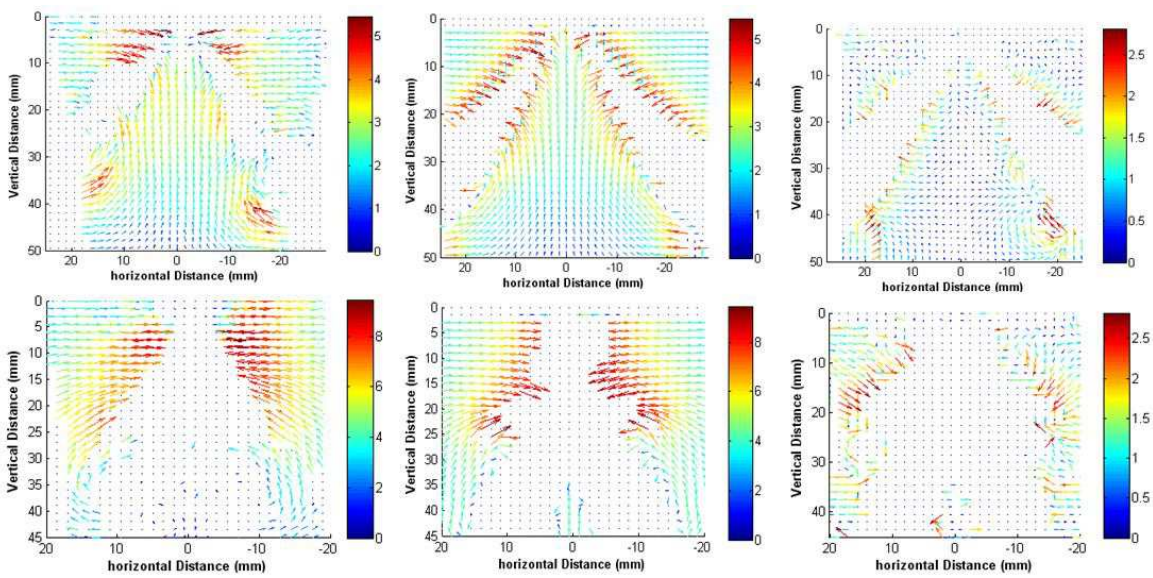

Fig 3: 2D vector flow fields showing air entrainment at 1.4ms ASOI for the (top) 3 hole injector and (bottom) 6 hole injector; (left) Experimental (middle) Numerical (right) Difference between Exp & Num (color map in m/s)

3.2.3 Jet to jet interactions:

Jet to jet interactions can be significant for multi-hole injectors and as a result have an effect on the global spray structure. The simulation results obtained for the 6-hole injector under the evaporating conditions presented in *Table 1*, reveals the presence of what appear to be jet to jet interactions causing a modification in terms of the trajectory of the individual spray plumes as shown in figure 4. In contrast, the spray plumes are well separated in the case of the 3-hole injector. However, the 6-hole injector reveals a continuous spray structure, due to the presence of droplets and it becomes difficult to identify individual plumes. One would expect that significant interactions occur between adjacent jets, modifying the air entrainment and subsequently the fuel-air mixture distribution. Such aspects are studied in more detail by performing numerical simulations.

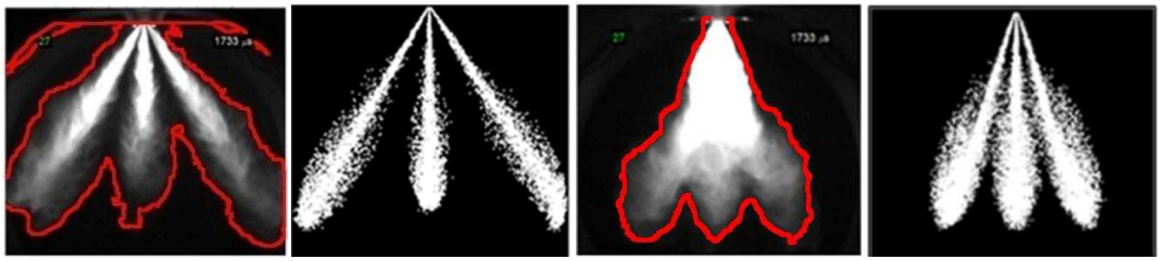

Fig 4: Liquid phase spray images of the 3-hole and 6 injector under evaporating conditions at time=1.75ms (from left); (1st) Experimental data (high-speed Mie scattering) (2nd) Simulation data, (3rd) experimental data (high-speed Mie scattering) (4th) Simulation data

3.2.3.1 Spatial evolution of vapour phase:

The simulation results of the vapour phase of 6-hole injector under evaporating conditions provide further insight to the process involved in the spray propagation, structure and mixture formation. A sequence of images containing various cross-sectional planes of the vapor mass fraction along the axial direction of the spray plumes is presented below in figure 5 at time step of 3.10ms ASOI. The

cross-sections near the nozzle spray region reveal a star shape of the spray plumes which are well separated from one another. The images also divulge vapor phase fuel in the central region of the spray. Moving further downstream the vapor phase fuel surrounding the plumes tends to merge into one other. At this point the star shape transforms into a closed ring structure and the spray reveals a hollow cone spray structure. It is at this stage where the spray plumes tend to deflect resulting in a notable change in spray angle. This process takes places throughout the spray propagation. In order to better understand the observed behavior, an analysis of the air entrainment characteristics has been performed.

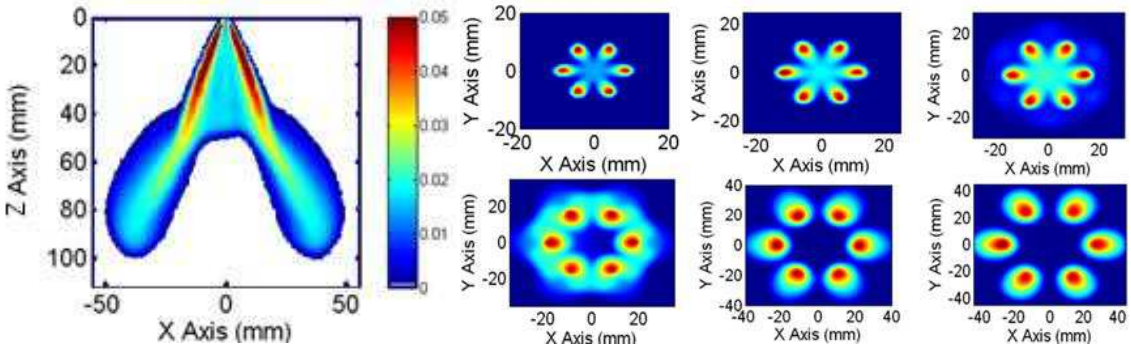

Fig 5: Numerical fuel vapor mass fraction at time 3.1ms ASOI, (on left) 2D axial cross-sectional plane (x, z); (on right) 2D horizontal cross-sectional planes (x, y) with (top left) 20mm, (top middle) 30mm, (top right) 40mm, (bottom left) 50mm, (bottom middle) 60mm, (bottom left) 70mm

3.2.3.2 Axial gas velocity:

The gas entrainment between two adjacent plumes (vertical cross-sections (x-z)) of 6-hole injector at 1.75ms and 3.10ms ASOI is presented in figure 6. Typically gas entrainment into the spray plumes can be divided into two sections (1) air sucked into the near nozzle region and (2) air and vapor pushed downwards in the direction of the spray at the spray tip [3, 6]. These two phenomena can be observed with vapor being sucked in towards the injector tip and pushed out at the spray tip as shown in figure 6.

A new feature is also revealed, whereby air between the two jets is pushed downwards in the upper half of the spray cone (close to the injector tip). This is usually not observed in the sprays with

spatially well separated plumes and wide cone angles as is the case for the 3-hole injector with results shown in figure 6.

The internal downward gas flow in the upper half of the spray cone encounters an inverse flow, originating from the lower downstream region of the spray which is the usual internal air entrainment. When the two flows hit each other at 30mm at 1.75ms and 50mm at 3.10ms, they form a stagnation plane resulting in a very high radial flow toward the external side as seen in the figure 6. This radial flow forces the spray plumes to deviate suddenly from their original paths with a noticeable change in the angles. In our operational conditions, the collapsing tendency then vanishes here and the plumes separated from each other which can be seen in figure 5.

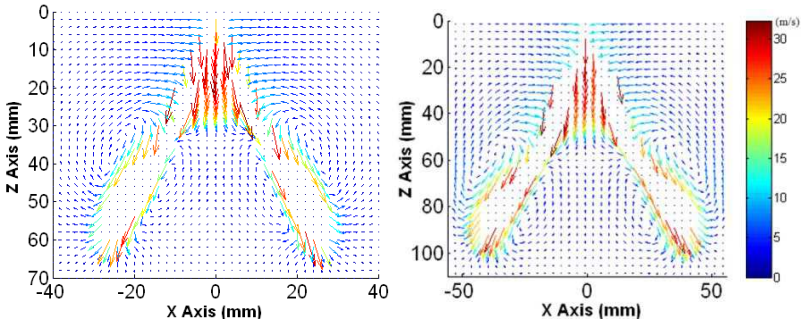

Fig 6: 2D velocity vector plots of air and gas entrainment at time (left) 1.75ms ASOI and, (right) 3.10ms ASOI

However, a second difference observed on the 6-hole compared to 3-holes is on bottom half part of the spray cone (far away from the injector needle). Here the spray tip recirculation area is strongly reduced in its central part. This reduction is approximately compensated by an increased recirculation area on the external side. This asymmetry external/internal is observed where the jet plumes are widely separated.

3.2.3.3 Comparison of spray angles:

A modification of the global spray angle was observed experimentally from high-speed spray imaging performed in the HPHT chamber at IFPEN on the XL 6-hole 60° CA injector. The simulation and experimental data is shown in figure 7 for this particular case. The spray cone can be divided into two regions corresponding firstly, to a close-up, near nozzle zone and secondly, to a downstream region where one observes a modification of the spray angle as shown in figure 7 (left).

The angles are measured by capturing images of the simulated spray in the y-z plane. These spray images at two time steps corresponding to 1.75 and 3.10ms ASOI are analysed by "imageJ" software which is a simple java based image processing. The angle of the near nozzle zone (α_c) at 1.75ms and at 3.10ms ASOI is approximately 42°.

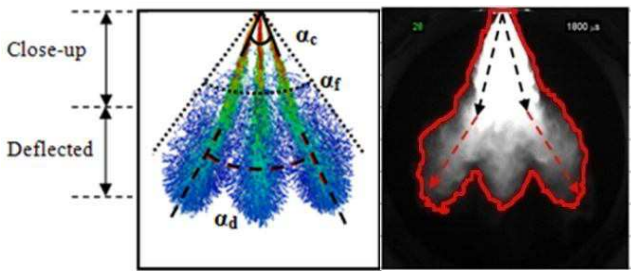

Fig 7: Comparison of spray plumes at 1.8ms ASOI (left) Numerical result (right) experimental result.

These near nozzle angles suggest that the measured spray cone angle is in fact narrower than the nominal cone angle of 60°. The near angles are measured from plume centre to plume centre which implies that taking account of the half plume angle (6°) of each of the two spray plumes, the total cone angle will be approximately 54°. A difference of approximately 6° between the nominal angle and the measured, near nozzle angle indicates the spray collapse in the close up (upper) region. In the downstream zone of the spray, at 1.75ms ASOI, the deflected spray angle (α_d) is approximately 48° which increases to 51° at 3.10ms ASOI. The spray cone is thus deflected by 6 ° and 9 ° at 1.75ms and 3.10ms ASOI respectively. Although the spray far cone angles (α_f) of both experimental and numerical results show very good agreement but the spray plumes propagate with two different angles near and far from the injector nozzle. That means the overall spray cone angle is not a pure indicator of the spray directions when there are strong jet to jet interactions present.

Time (ms)	**Simulated Close up Angle (α_c)**	**Simulated Deflected Part Angle (α_d)**	**Simulated Far cone angle (α_f)**	**Experimental Far cone angle (α_f)**
1.75	42°	48°	66°	65°
3.10	42°	51°	65°	65°

Table 2: Angles of close-up and deflected part of the spray at time 1.75ms and 3.10ms

3.2.3.4 Radial gas velocity:

Horizontal planes showing radial velocity vector plots of air entrainment at different axial locations at time =3.10ms are shown in figure 8. The vector plots show that until 40mm downstream air is sucked from the outer region and pushed out afterwards. The air entrainment in the inner side of the spray plumes infect comes from the accelerating flow in between the jets. A part of the air movement in between the jets which misses its target is pushed downstream because there is almost no time for this air to turn towards the plumes due to the high speed of spray plumes.

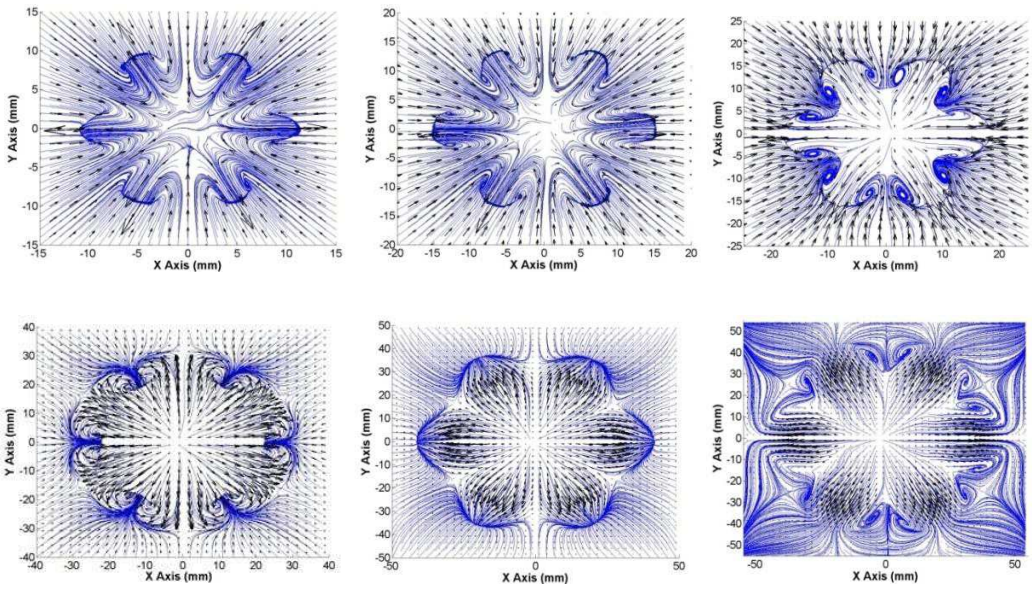

Fig 8: Radial velocity vector plot of the air entrainments (time =3.10ms) at downstream locations (top left) 20mm, (top middle) 30mm, (top right) 40mm, (bottom left) 50mm, (bottom middle) 60mm,(bottom right) 70mm

As explained earlier the air in the core of the spray is opposite in directions at 40mm and 60mm and when the gas being pushed downwards and the air being sucked upwards hit each other a stagnation point is created and thus a radial flow is generated causing the spray to bend. This is visible in the figure 8 (bottom left) at 50mm downstream where there is a ring of gas pushing outwards produced by the interactions of opposite gas velocity in the core of spray cone. This radial flow as presented in figure 11 (b) is relatively larger than the air entrainment from outside the spray cone. Hence this

radial flow blocks the air from the outer region of the spray cone completely and causes the spray plumes to bend from their original path.

As expected at 70mm downstream position the radial velocity is a projection of the air entrained in the spray, with a large external recirculation around the jets – the process of jet-to-jet interaction is finished and the jets propagates linked to its previous (bent) direction.

Conclusions:

Numerical results with standard spray models and AMR approach show a good agreement for the both 3 and 6-hole GDI injectors compared to high-speed Mie scattering, PDA and PIV experimental data which have been performed in non-evaporating and evaporating conditions. The droplet size comparison between the experiments and numerical results at the center of the spray plume reveals a difference of less than 1μm in D_{10}. PDF of droplet distribution shows a good agreement. The penetration and vector fields of air entrainment for both injectors are very well captured. The air entrainment effects on the spray jets are observed and appear to be very pronounced. Jet to jet interaction appears to be linked with the reorganization of the flow due to the compact geometry. The narrow spray cone angle causes the air near the nozzle to be pushed downwards. This phenomenon occurs continuously during the spray propagation. The air which is pushed downwards doesn't allow the spray cone to expand until this air interacts with the air opposite in direction which is entrained from the lower region of the spray. The interactions of both positive and negative velocities result in outward radial velocity, which makes the spray plumes to deflect from their original path. At the deflection point a ring of vapor appears which is pushed along with the radial flow from the centre of the spray cone. The cone deflection angle in the simulations is measured roughly to be between 6° to 9°.

Acknowledgements

This work has been financially supported by the French Government within the framework of the FUI Magie project. The PDA measurements were supported by the excellence grant of Continental to Loughborough University.

Appendix D Research Papers

References

1. Rotondi R., Hélie J., Leger C., Mojtabi M., Wigley G., *ILASS Europe, Czech Republic, (2010).*
2. Befrui B., Corbinelli G., D'Onofrio M., Varble D., *SAE Paper, 2011-01-1211, (2011).*
3. Prosperi, B., Helie, J., Bazile R., *ILASS – Europe, Turkey, (2007).*
4. Delay, G., Bazile, R., Charnay, G., Nuglisch, H. J., *12th International Symposia on Applications of Laser Techniques to Fluid Mechanics, Portugal, (2004).*
5. Seibel C., Gartung K., Arndt S., Weigand B., *ICLASS, Italy, (2003).*
6. Skogsberg, M., Dahlander, P., Lindgren, R., and Denbratt, I., *SAE Paper, 2005-01-0097, (2005).*
7. Wigley G., Pitcher G., Nuglisch H., Helie J., Ladommatos N., *AVL 8th International Symposium on Combustion Diagnostics, Baden-Baden, Germany (2008).*
8. *Le Coz, J-F., Lemenand, C., Bruneaux, G., SAE paper, 2003-01-3108, (2003).*
9. *Bruneaux, G., Causse, M., Omrane, A., ". SAE paper, 2011-01-1828, (2011).*
10. *Malbec, L-M., Bruneaux, G., SAE paper, 2010-01-0342, SAE Int. J. Engines, 3(1):107-123, (2010).*
11. Weller H, Tabor G, Jasak H, Fureby C. *J Comput Phys, 12(6):620–31, (1998).*
12. Kosters A., "*Dynamic mesh refinement in dieselFoam*", *CFD with OpenSource software, project report, Division of Combustion, Chalmers University of Technology (2010).*
13. Issa R., *J Comput Phys; 62:40–65, (1986).*
14. Hestens M., Steifel E., *J Res Nat Bur Stand, 29:409–36, (1952).*
15. Tanner F.X., *SAE Transactions Journal of Engines, 106 (3): 127-140, (1998).*
16. O'Rouke P. J., *J. Comput. Physics, 83(2), 345–360*, (1989).
17. Dukowitz J. K., *J. Comput. Physics, 35, 229, (1980).*
18. Macpherson G. B., Nordin N., Weller H. G., *Commun. Numer. Meth. Engg; 25:263–273,* (2009).
19. O'Rourke, P., "Collective Drop Effects on Vaporizing Liquid Sprays". *PhD thesis, Princeton University, (1981).*
20. Karrholm F P, "Numerical Modeling of Diesel Spray Injection, Turbulence Interaction and Combustion". *PhD thesis, Chalmers University of Technology, (2008).*

Bibliography

Abramoff, M. D., Magalhaes, P. J., & Ram, S. J. (2004). Image processing with ImageJ. *Biophotonics International , 11* (7), 36-42.

Ahmed, A. M., & Elghobashi, S. (2000). On the mechanism of modifying the structure of turbulent homogeneous shear flows by dispersed particles. *Physics of Fluids , 12*, 2906–2930.

Alkidas, A. C., & El-Tahry, S. H. (2003). Contributors to the fuel economy advantage of DISI engines over PFI engines. *SAE Paper* , 2003-01-3101.

Apte, S. V., Mahesh, K., Gorokhovski, M., & Moin, P. (2009). Stochastic modeling of atomizing spray in a complex swirl injector using large eddy simulation. *Proceedings of the Combustion Institute , 32*, 2257-2266.

Apte, S. V., Mahesh, K., Moin, P., & Oefelein, J. C. (2003). Large-eddy simulation of swirling particle-laden flows in a coaxial-jet combustor. *International Journal of Multiphase Flow , 29*, 1311-1331.

Ashgriz, N. (2011). *Handbook of atomization and sprays.* New York: Springer.

Bakker, A. (2006). *Course on computational fluid dynamics.* Dartmouth College.

Befrui, B., Corbinelli, G., D'Onofrio, M., & Varble, D. (2011). GDI multi-hole injector internal flow and spray analysis . *SAE Technical Paper* .

Befrui, B., Corbinelli, G., Spiekermann, P., Shost, M., & Lai, M. C. (2012). Large eddy simulation of GDi single-hole flow and near-field spray. *SAE International Journal of Fuels and Lubricants , 5*, 620-636.

Bharadwaj, N., Rutland, C. J., & Chang, S. (2009). Large eddy simulation modelling of spray-induced turbulence effects. *International Journal of Engine Research* , 97-119.

Bini, M., & Jones, W. (2008). Large-eddy simulation of particle-laden turbulent flows. *Journal of Fluid Mechanics* , 207-252.

Bibliography

Boivin, M., Simonin, O., & Squires, K. D. (1998). Direct numerical simulation of turbulence modulation by particles in isotropic turbulence. *Journal of Fluid Mechanics , 375*, 235–263.

Boivin, M., Simonin, O., & Squires, K. D. (2000). On the prediction of gas–solid flows with two-way coupling using large eddy simulation. *Physics of Fluids , 12*, 2080-2090.

Boivin, M., Simonin, O., & Squires, K. D. (2000). On the prediction of gas–solid flows with two-way coupling using large eddy simulation. *Physics of Fluids , 12*, 2080.

Boussinesq, J. (1903). *Theory analytique de la chaleur. Paris 2, 224.* Paris.

Carlson, D. J., & Hoglund, R. F. (1964). Particle drag and heat transfer in rocket nozzles. *AIAA Journal , 2*, 1980-1984.

Chang, D. L., Lee, C., & Fon, F. (2005). Development of a simplified bubble growth model for flash boiling sprays in direct injection spark ignition engines. *Proceedings of the Combustion Institute , 30*, 2737-2744.

Chesnel, J., & Helie, J. (2013). Gasoline multihole atomization process. *in preparation for Atomisation and Spray* .

Courant, R., Friedrichs, K. O., & Lewy, H. (1928). Über die partiellen differenzengleichungen der mathematischen Physik. *Mathematische Annalen , 100*, 32-74.

Crowe, C. T. (1982). Review—numerical models for dilute gas particle. *Journal of Fluids Engineering , 104*, 297-303.

Crowe, C. T., Chung, J. N., & Troutt, T. R. (1993). Particle dispersion by organized turbulent structures. *Particulate Two-Phase Flow* , 626.

Crowe, C., Sommerfeld, M., & Tsuji, Y. (1998). *Multiphase flows with droplets and particles.* CRC Press LLC.

Dahlander, P., & Lindgren, R. (2009). Multi-hole injectors for DISI engines: nozzle hole configuration influence on spray formation. *SAE International Journal of Engines , 1* (1), 115-128.

Dejoan, A., & Schiestel, R. (2002). Les of unsteady turbulence via a one-equation subgrid-scale transport model. *International Journal of Heat Fluid Flow , 23*, 398.

Delay, G., Bazile, R., Charnay, G., & Nuglisch, H. (2004). Temporal dependency of air entrainment to liquid flow rate variations for gazoline direct injection sprays. In: Temporal dependency of air of laser tecniques to fluid mechanics. *International Symposia on Applications of Laser Techniques to Fluid Mechanics.* Lisbon.

Demirdžić, I., Lilek, Ž., & Perić, M. (1993). A collocated finite volume method for predicting flows at all speeds. *International Journal for Numerical Methods in Fluids , 16*, 1029-1050.

Doudou, A. (2005). Turbulent flow study of an isothermal diesel spray injected by a common rail system. *Fuel , 84*, 287-298.

Druzhinin, A. (1994). Recent developments in PDF methods. In *Turbulent Reactive Flows* (pp. 375–474). Academic.

Dukowitz, J. K. (1980). A particle-fluid numerical model for liquid sprays. *Journal of Computional Physics* , 35, 229.

Dukowitz, J. K. (1980). A particle-fluid numerical model for liquid sprays. *Journal of Computational Physics , 35*, 229.

Eaton, J. K., & Fessler, J. R. (1994). Preferential concentration of particles by turbulence. *International Journal of Multiphase Flow , 20* , 169-209.

Elghobashi, S., & Truesdell, G. C. (1993). On the two way interaction between homogeneous turbulence and dispersed solid particles. I: Turbulence modification. *Physics of Fluids A* , 1790–1801.

Ferrante, A., & Elghobashi, S. (2003). On the physical mechanism of two way coupling in particle laden isotropic turbulence. *Physics of Fluids , 15*, 315–330.

Ferziger, J. H., & Perić, M. (1995). *Computational methods for fluid dynamics.* Berlin-New York: Springer Verlag.

Bibliography

Foysi, H., Mellado, J. P., & Sarkar, S. (2010). Large-eddy simulation of variable-density round and plane jets. *International Journal of Heat and Fluid Flow , 31*, 307-314.

Fureby, C., Gosman, D. A., Tabor, G., Weller, H. G., Sandham, N., & Wolfshtein, M. (1997). Large eddy simulation of turbulent channel flows. *Turbulent shear flows , 11*.

Germano, M., Piomelli, U., Moin, P., & Cabot, W. H. (1991). A dynamic subgrid-scale eddy viscosity model. *Physics of Fluids A , 3* (7), 1760–1765.

Ghasempour, F., Andersson, R., & Andersson, B. (2012). *Multidimensional turbulence spectra-properties of turbulent vortices.* Maastricht, Netherlands: ISCRE 22.

Godsave, G. A. (1953). Studies of the combustion of drops in a fuel spray—the burning of single drops of fuel. *Symposium (International) on Combustion* (pp. 818-830). Elsevier.

Gore, R. A., & Crowe, C. T. (1989). Effect of particle size on modulating turbulent intensity. *International Journal of Multiphase Flow , 15*, 279-285.

Hahn, F., Olbricht, C., & Janicka, J. (2008). Large eddy simulation of an evaporating spray based on an Eulerian–Lagrangian approach. Proceedings of ILASS, Como Lake, Italy,. *ILASS.* Como Lake, Italy.

Hestens, M. R., & Stiefel, E. (1952). Methods of conjugate gradients for solving linear systems. *Journal Research National Bureau of Standards , 49*, 409-436.

Hinze, J. O. (1975). *Turbulence.* New York: McGraw-Hill Publishing Co.

Hirsch, C. (1991). *Numerical computation of internal and external flows.* John Wiley& Sons.

Holmes, P., Lumley, J. L., & Berkooz, G. (1998). *Turbulence, coherent structures, dynamical systems and symmetry.* . Cambridge University Press.

http://www.openfoam.org/docs/. (n.d.).

Hunt, J. C., Wray, A., & Moin, P. (1988). *Eddies, stream, and convergence zones in turbulent flows.* 193-208: Center for turbulence research report, CTR-S88.

Jasak, H. (1996). *Error analysis and estimation in the Finite Volume method with applications to fluid flows.* London: Imperial College.

Jenny, P. R. (2012). Modeling of turbulent dilute spray combustion. *Progress in Energy and Combustion Science , 38*, 846–887.

Johnson, N. L., Kotz, S., & Balakrishnan, N. (1994). *Lognormal distributions. Continuous Univariate Distributions* (Vol. 1). John Wiley & Sons.

Kajishima, T., & Nomachi, T. (2006). One equation subgrid scale model using dynamic procedure for the energy production. *Journal of Applied Mechanics , 73*.

Kaufmann, A., Moreau, M., Simonin, O., & Helie, J. (2008). Comparison between Lagrangian and mesoscopic Eulerian modelling approaches for inertial particles suspended in decaying isotropic turbulence. *Journal of Computational Physics , 227*, 6448-6472.

Kawano, D., Ishii, H., Suzuki, H., Goto, Y., Odaka, M., & Senda, J. (2006). Numerical study on flash-boiling spray of multicomponent fuel. *Heat Transfer—Asian Research , 35*, 369-385.

Khan, M. M., Helie, J., & Burluka, A. A. (2011). POD Application for the flow characterization at the exit of a low pressure gasoline nozzle. *ILASS.* Estoril.

Khan, M. M., Helie, J., Gorokhovski, M., Wood, A., Wigley, G., Kashdan, J., et al. (2012). Numerical analysis of multihole gasoline direct injection sprays. *ICLASS.* Heidelberg, Germany.

Kobayashi, H., Masutani, S. M., Azuhata, S., Arashi, N., & Hishinuma, Y. (1988). *Transport phenomena in turbulent flows.* (M. Hirata, & K. N, Eds.) Hemisphere.

Kosaka, H., & Kimura, S. (2006). LES of diesel fuel spray. *ICLASS.* Kyoto, Japan.

Kostas, J., Soria, J., & Chong, M. S. (2005). A comparison between snapshot POD analysis of PIV velocity and vorticity data. *Experiments in Fluids , 38* , 146–160.

Kosters, A. (2010). *Dynamic mesh refinement in dieselFoam.* Division of Combustion. Chalmers University of Technology.

Krajnović, S., & Davidson, S. (2002). A mixed one equation subgrid model for large-eddy simulation. *International Journal of Heat Fluid Flow , 23*, 413-425.

Lain, S., & Grillo, C. A. (2007). Comparison of turbulent particle dispersion models in turbulent shear flows . *Brazilian Journal of Chemical Engineering , 24*, 351–363.

Launder, B. E., & Spalding, D. B. (1972). *Lectures in mathematical models of turbulence.* London, England: Academic Press.

Lazaro, B. J. (1989). Particle dispersion in a turbulent, plane, free shear layer. *Physics of Fluids , 1*, 1035–1044.

Lazaro, B. J. (1992a). Particle dispersion in the developing free shear layer. Part 1. *Journal of Fluid Mechanics , 235*, 135–178.

Lazaro, B. J., & Lasheras, J. C. (1989). Particle dispersion in a turbulent, plane, free shear layer. *Physics of Fluids A , 1*, 1035–1044.

Lazaro, B. J., & Lasheras, J. C. (1989). Particle dispersion in a turbulent, plane, free shear layer. *Physics of Fluids , 1*, 1035–1044.

Lazaro, B. J., & Lasheras, J. C. (1992). Particle dispersion in the developing free shear layer. Part 1 Unforced flow. *Journal of Fluid Mechanics* , 135-178.

Lazaro, B. J., & Lasheras, J. C. (1992a). Particle dispersion in the developing free shear layer. Part 1. *Journal of Fluid Mechanics , 235*, 135–178.

Lazaro, B. J., & Lasheras, J. C. (1992b). Particle dispersion in the developing free shear layer. Part 2. *Journal of Fluid Mechanics , 235*, 179–221.

Lefebvre, A. H. (1989). *Atomization and sprays.* New York: Hemisphere Publishing Corporation.

Lefebvre, A. H. (1989). *Atomization and Sprays.* Hemisphere.

Leonard, A. (1975). Energy cascade in large-eddy simulations of turbulent fluid flows. *Advances in Geophysics , 18*, 237-248.

Levy, Y., Degani, D., & Seginer, A. (1990). Graphical visualization of vortical flows by means of helicity. *AIAA* , 1347-1352.

Lilly, D. K. (1992). A proposed modification of the Germano subgrid-scale closure model. *Physics of Fluids , 4*, 633–635.

Lin, H., Storey, B. D., & Szeri, A. J. (2002). Inertially driven inhomogeneities in violently collapsing bubbles: the validity of the Rayleigh–Plesset equation. *Journal of Fluid Mechanics , 452*, 145-162.

Longmire, E. K., & Eaton, J. K. (1992). Structure of a particle-laden round jet. *Journal of Fluid Mechanics , 236*, 217-257.

Loth, E. (2008). *Computational fluid dynamics of bubbles, drops and particles.*

Lumley, J. L. (1967). The structure of inhomogeneous turbulent flow and radio wave propogation. In J. L. Lumley, *Atmospheric Turbulence and Radio Wave Propagation* (pp. 166–178).

M, S., P, D., R, L., & Denbratt, I. (2005). Effects of injector parameters on mixture formation for multi-hole nozzles in a spray-guided gasoline DI engine. SAE.

Macpherson, G. B., Nordin, N., & Weller, H. G. (2009). Particle tracking in unstructured, arbitrary polyhedral meshes for use in CFD and molecular dynamics. *Communications in Numerical Methods in Engineering , 25*, 263-273.

Macpherson, G. B., Nordin, N., & Weller, H. G. (2009). Particle tracking in unstructured, arbitrary polyhedral meshes for use in CFD and molecular dynamics. *Communications in Numerical Methods in Engineering , 25*, 263-273.

Makhlouf, S., Hélie, J., Grimoux, O., Gestri, L., Cousin, J., Wood, A., et al. (2012). Spray resulting from high pressure atomization with low L over D multihole injectors and the role of the cavitation. *ICLASS.* Hidelberg.

Marcu, B., & Meiburg, E. (1996). The effect of streamwise braid vortices on the particle dispersion in a plane mixing layer. I. Equilibrium points and their stability. *Physics of Fluids , 8*, 715–733.

Marcu, B., & Meiburg, E. (1996). Three-dimensional features of particle dispersion in a nominally plane mixing layer. *Physics of Fluids , 8*, 2266–2268.

Martin, E., & Meiburg, E. (1994). The accumulation and dispersion of heavy particles in forced two-dimensional mixing layers. i. The fundamental and sub harmonic cases. *Physics of Fluids , 6*, 1116–1132.

Maxey, M. R. (1987). The gravitational settling of aerosol particles in homogeneous turbulence and random flow fields. *Journal of Fuid Mechanics , 174*, 441–465.

Maxey, M. R., & Riley, J. J. (1983). Equation of motion for a small rigid sphere in a nonuniform flow. *Physics of fluids A , 26*, 883-889.

Meldi, M., Lucor, D., & Sagaut, P. (2011). Is the Smagorinsky coefficient sensitive to uncertainty in the form of the energy spectrum? *Physics of Fluids , 23*, 125109-125109.

Meyer, K., Cavar, D., & Pedersen, J. (2007). POD as tool for comparison of PIV and LES data. *7th International Symposium on Particle Image Velocimetry.* Rome.

Minier, J., & Peirano, E. (2001). The PDF approach to turbulent polydispersed two-phase flows. *Physics Reports , 352*, 1-214.

Mojtabi, M. (2011). *Optical analysis of multi-stream GDI sprays under various engine operating conditions.* Lougborough, UK: Lougborough University.

Mojtabi, M., Chadwick, N., Wigley, G., & Helie, J. (2008). The effect of flash boiling on breakup and atomisation in GDI sprays. In Proceedings of the 22nd European Conference on Liquid Atomization and Spray Systems. *ILASS Europe.* Como Lake, Italy.

Mojtabi, M., Wigley, G., & Helie, J. (2010). A comparison between one and two component velocity size measurements in a dense spray. *ILASS.* Brno.

MOREAU, M., BEDAT, B., & SIMONIN, O. (2005). From euler-lagrange to euler-euler large eddy simulation approaches for gas-particle turbulent flows. *10th ASME Fluids Engineering Summer Conference.* United States.

Moreau, M., Simonin, O., & Bédat, B. (2010). Development of gas-particle euler-euler LES approach: a priori analysis of particle sub-grid models in homogeneous isotropic turbulence. *Flow, turbulence and combustion , 84*, 295-324.

Negro, S., Brusiani, F., & Bianchi, G. M. (2011). A numerical model for flash boiling of gasoline-ethanol blends in fuel injector nozzles. *SAE International Journal of Fuels and Lubricants , 4*, 237-256.

Nordin, N. (2001). *Complex chemistry modeling of diesel spray combustion.* PhD thesis, Chalmers University of Technology, Dept. of Thermo and Fluid Dynamics, Göteborg.

O'Rouke, P. J. (1989). Statistical properties and numerical implementation of a model for droplet dispersion in a turbulent gas. *Journal of Computational Physics , 83*, 345–360.

O'Rourke, P. J., & Amsden, A. A. (1987). The TAB method for numerical calculation of spray droplet breakup. *SAE Technical Paper* , 872089.

O'Rourke, P., & Bracco, F. (1980). Modeling of drop interactions in thick sprays and a comparison with experiments. *Proceedings of the Institution of Mechanical Engineers , 9*, 101-106.

Park, B. S., & Lee, S. Y. (1994). An experimental investigation of the flash atomization mechanis. *Atomization and Sprays , 4*, 159-179.

Pilch, M., & Erdman, C. A. (1987). Use of breakup time data and velocity history data to predict the maximum size of stable fragments for acceleration-induced breakup of a liquid drop. *International Journal of Multiphase Flow , 13*, 741-757.

Poinsot, T. J., & Lele, S. K. (1992). Boundary conditions for direct simulations of compressible viscous reacting flows. *Journal of Computational Physics , 101*, 104-129.

Pomraning, E., & Rutland, C. J. (2002). Dynamic one-equation nonviscosity large-eddy simulation model. *AIAA Journal , 40*, 689-701.

Pope, B. S. (2004). Ten questions concerning the large-eddy simulation of turbulent flows. *New Journal of Physics , 6*.

Pope, S. B. (2000). *Turbulent flows.* Cambridge university press.

Prosperi, B., Helie, J., & Bazile, R. (2007). PIV measurements of injection pressure effect on gas entrainment in GDI engines. Turkey: ILASS Europe.

Radhakrishnan, S., & Bellan, J. (2012). Influence of computational drop representation in LES of a mixing layer with evaporating drops. *Computers & Fluids , 58*, 15-26.

Raju, N., & Meiburg, E. (1995). The accumulation and dispersion of heavy particles in forced two-dimensional mixing layers. Part 2: The effect of gravity. *Physics of Fluids , 7*, 1241–1264.

Ranz, W. E., & Marshall, W. R. (1952). Evaporation from drops. *Chem. Eng. Prog , 48*, 141-146.

Reitz, R. D. (1990). A photographic study of flash-boiling atomization. *Aerosol Science and Technology , 12*, 561-569.

Rosin, P., & Rammler, E. (1933). The laws governing the fineness of powdered coal. *Journal of the Institute of Fuel , 7*, 29–36.

Rotondi, R., Hélie, J., Leger, C. M., & Wigley, G. ". (2010). Multihole gasoline direct injection spray plumes. *ILASS* . Brno.

Sagaut, P. (2006). *Large eddy simulation for incompressible flows: an introduction.* Springer.

Samimy, M., & Lele, S. K. (1991). Motion of Particles with Inertia in a Compressible Free Shear Layer. *Physics of Fluids A , 3*, 1915-1923.

Sander, W., & Weigand, B. (2008). Direct numerical simulation and analysis of instability enhancing parameters in liquid sheets at moderate reynolds numbers. *Physics of Fluids , 20*, 053301 .

Schmidt, D. P. (1997). *Cavitation in diesel fuel injector nozzles.* UNIVERSITY OF WISCONSIN.

Schmidt, D. P., & Rutland, C. J. (2000). A new droplet collision algorithm. *Journal of Computational Physics , 164* (01), 62-80.

Schumann, U. (1975). Subgrid-scale model for finite difference simulations of turbulent flows on plane channels and annuli. *Jounal of Computational Physics , 18*, 376-404.

scoltock, J. (2012, March). Gasoline solinoid direct injector. Automotive Engineer.

Seibel, C., Gartung, K., Arndt, S., & Weigand, B. (2003). Detailed analysis of spray structure and air entrainment in GDI sprays using a tomographic approach. *ICLASS.* Sorrento.

Senecal, P. K., Schmidt, D. P., Nouar, I., Rutland, C. J., Reitz, R. D., & Corradini, M. L. (1999). Modeling high-speed viscous liquid sheet atomization. *International Journal of Multiphase Flow* , 1073–1097.

She, J. (2010). Experimental study on improvement of diesel combustion and emission using flash boiling injection. Detroit, Michigan: SAE.

Sher, E., Bar Kohany, T., & Rashkovan, A. (2008). Flash-boiling atomization. *Progress in Energy Combustion Science , 24*, 417–439.

Shi, J. M., Wenzlawski, K., Helie, J., Nuglisch, H., & Cousin, J. (2010). URANS and SAS analysis of flow dynamics in a GDI nozzle. *ILASS.* Brno.

Sirignano, W. A. (2000). *Fluid dynamics and transport of droplet and sprays.* Cambridge University Press.

Sirovich, L. (1987). Turbulence and the dynamics of coherent structures. Part I: Coherent structures. *Quarterly Applied Mathematics , 45*, 561–571.

Skogsberg, M., Dahlander, P., Lindgren, R., & Denbratt, I. (2005). Effects of injector parameters on mixture formation for multi-hole nozzles in a spray-guided gasoline DI engine. *SAE* .

Smagorinsky, J. (1963). General circulaton experiments with the primitive equations. *Montly Weather Review* , 99–164.

Sommerfeld, M. K. (1993). Some open questions and inconsistencies of lagrangian particle dispersion models. *9th Symposium on Turbulent Shear Flows.* Kyoto, Japan.

Sommerfeld, M. (2000, April 3-7). Theoretical and experimental modelling of particulate flows. Germany: von Karman Institute for Fluid Dynamics.

Spalding, D. B. (1953). The combustion of liquid fuels. *In Proceedings of the Fourth Symposium (lnternational) on Combustion* (pp. 847-864). Elsvier.

Squires, K. D., & Eaton, J. K. (1991). Preferential concentration of particles by turbulence. *Physics of Fluids A , 3*, 1169–1178.

Stokes, G. C. (1850). On the effect of the internal friction of fluids on the motion of pendulums. *Transactions of the Cambridge Philosophical Society , 9*, 8.

Suma, S., & Koizumi, M. (1977). Internal boiling atomization by rapid pressure reduction of liquids. *Trans JSME , 43*, 4608-4617.

Sweby, P. K. (1984). High resolution schemes using flux limiters for hyperbolic conservation laws. *SIAM Journal on Numerical Analysis , 21*, 995–1011.

Tanner, F. (1997). Liquid jet atomization and droplet breakup modeling of non-evaporating diesel fuel sprays. *SAE Technical Paper* , 970050.

Villiers, E. d. (2006). *The potential of large eddy simulation for the modeling of wall bounded flows.* London: Imperical College.

Vinkovic, I., Aguirre, C., Simoens, S., & Gorokhovskhi, M. (2005). Large-eddy simulation of droplet dispersion for inhomogeneous turbulent wall flow. *International Journal of Multiphase Flow , 32*, 344–364.

Vuorinen, V. (2010). *Les of Certain Droplet Size Effects in Fuel Sprays.* Helsinki: Aalto University.

Wang, P., & Maxey, M. R. (1993). Settling velocity and concentration distribution of heavy particles. *Journal of Fluid Mechanics , 256*, 27-68.

Wang, P., Fröhlich, J., Michelassi, V., & Rodi, W. (2008). Large-eddy simulation of variable-density turbulent axisymmetric jets. *International Journal of Heat and Fluid Flow , 29*, 654-664.

Weller, H. G., Tabor, G., Jasak, H., & Fureby, C. (1998). A tensorial approach to computational continuum mechanics using object-oriented techniques. *Computers in physics , 12*, 620.

Wen, F., Kamalu, N., Chung, J. N., Crowe, C. T., & Troutt, T. R. (1992). Particle dispersion by vortex structures in plane mixing layers. *Journal of Fluids Engineering , 4*, 657.

Wood, A., Wigley, G., & Helie, J. (2013). Analysis of Multi-hole GDI Injectors under Flash Boiling Conditions. *ILASS – Europe.* Chania, Greece.

Xu, M., Zhang, Y., Zeng, W., Zhang, G., & Zhang, M. (2013). Flash Boiling: Easy and better way to generate ideal sprays than the high injection pressure. *SAE International Journal of Fuels and Lubricants , 6*, 137-148.

Yoshizawa, A. (1985). A statistically-derived subgrid-scale kinetic energy model for the large eddy simulation of turbulent flows. *Journal of the Physical Society of Japan , 54*, 2834–2839.

Zeng, W., Xu, M., Zhang, G., Zhang, Y., & Cleary, D. J. (2012). Atomization and vaporization for flash-boiling multi-hole sprays with alcohol fuels. *Fuel , 95*, 287-297.

Zhang, M., Xu, M., Zhang, Y., & Zhang, G. (2010). High-speed PIV evaluation of fuel sprays under superheated conditions. *ILASS-ASIA.* Jeju, Korea.